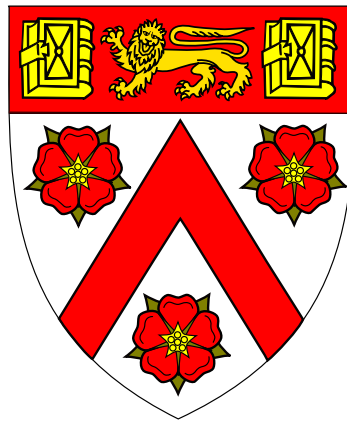




**Spatio-temporal variability  
and energy-balance implications  
of surface ponds on Himalayan  
debris-covered glaciers**



**Evan S Miles**

Scott Polar Research Institute  
University of Cambridge

This dissertation is submitted for the degree of  
*Doctor of Philosophy*

Trinity College

November 2016



## Dedication

I would like to dedicate this thesis to the villagers of the Langtang Valley in Nepal, who have kindly hosted myself and my collaborators over the past few years, along with many other glaciologists over the past few decades. So many acquaintances and friendships were built through shared labour, laughter, and music: the joy in simple, unhurried life is infectious. How strange it must seem to see scientists scampering all over the glaciers and mountains in pursuit of modern knowledge; their knowledge blends science with strands of pragmatic old-world belief. To these villagers the Valley was simply home, although it was not isolated from the outside world: villagers widely acknowledged growing problems of deforestation and waste management, the loss of traditional lifestyles, and the retreat of the local glaciers from their recollection. Change was also a part of life: most of the population were descended from Tibetan refugees, and had only resettled in the mythical refuge of Tibetan Buddhism due to persecution. How unfitting, then, that these villages should suffer so greatly from the 25 April 2015 Gorkha Earthquake, in their place of refuge. Now, as the survivors rebuild, they exemplify one of the old world's great lessons: joy in resilience.



Fig. 1 Langtang (left) and Kyanjing (right) Villages in May 2013. Both villages were severely damaged by the 24 April 2015 Gorkha earthquake and subsequent avalanches. Langtang Village suffered a particularly high mortality rate.



## **Declaration**

I hereby declare that except where specific reference is made to the work of others, the contents of this thesis are original and have not been submitted in whole or in part for consideration for any other degree or qualification in this, or any other university. This thesis is my own work and contains nothing which is the outcome of work done in collaboration with others, except as specified in the text and Acknowledgements. This thesis is 228 pages long including text, illustrations, tables, and references.

Evan S Miles  
November 2016



## Acknowledgements

First and foremost, I would like to thank my PhD supervisors, Ian Willis and Neil Arnold, for their patient encouragement and kind support throughout my time at the Scott Polar Research Institute (SPRI). They have directed this research to a productive conclusion in spite of my many peripheral research ventures and personal passions.

Secondly, I am extremely grateful for my colleagues ETH-Zürich, the University of Utrecht, and the International Centre for Integrated Mountain Development (ICIMOD), whose support, collaboration, and friendship has been invaluable personally, professionally, and for this thesis. I would especially like to thank Francesca Pellicciotti, who integrated me within her scientific group and has closely mentored much of my work on debris-covered glaciers. I have also greatly benefited from scientific discussions with Jakob Steiner, Pascal Buri, Silvan Ragettli, Lene Petersen, Walter Immerzeel, Philip Kraaijenbrink, Joseph Shea, and Patrick Wagnon, among others. Without these relationships, both the thesis and my PhD experience would have been entirely different. My research activities during the PhD have also enjoyed productive collaborations with scientists working on other topics, and I would like to thank Przemek Zelazowski, Fanny Brun, Ed Pope, Allen Pope, Thomas Chudley, Marc Girona-Mata, and Martin Heynen for their stimulating discussions, hard work, and, occasionally, patience.

To some degree, this thesis represents the culmination of several opportunities and discussions which took me first from Oregon State University (OSU) to the University of British Columbia (UBC) and then onto Cambridge, and I am very thankful for the encouragement and opportunities given to me by several scientists along that journey. Specifically, I would like to acknowledge Anne Nolin, who fostered my connection with Garry Clarke, whose enthusiasm and generosity created an opportunity for me. At UBC, I was stimulated by research with Valentina Radić and frequent discussions with Garry, Valentina, Christian Schoof, Ian Hewitt, Mauro Werder, and Gwenn Flowers, as well as students Camilo Rada, James Ferguson, Marianne Haseloff, and Flavien Beaud, which encouraged me onto a PhD.

The primary costs of my PhD were borne by the Gates Cambridge Trust, without which I would not have been able to undertake my work at Cambridge. Fieldwork and research travel during the course of my PhD has been supported by a variety of sources, and I would

specifically like to acknowledge the Rouse Ball and Eddington Fund (at Trinity College), the Scandinavian Studies Fund (at the Department of Anglo-Saxon, Norse, and Celtic), the B.B. Roberts Fund (at SPRI), the Cambridge Philosophical Society, the Cambridge Society for the Application of Research (CSAR), the Philip Lake and William Vaughn Lewis Fund (at the Department of Geography), and the Royal Geographical Society's Geographical Fieldwork Grant.

Fieldwork in Nepal requires manpower, and my collaborators and I are indebted to Tek Rai and his staff at Himalayan Trekking Dreams, who maximised the success of our expeditions by minimising the logistical hassle. I am additionally thankful to Peter Hill, Ibai Rico, and Simon Wicki for their easygoing attitudes, efficiency, technical knowledge, and endurance at various stages of the project.

Finally, and more fundamentally, I am deeply grateful for the daily support of my wife, Hannah, who has loved me through many travels and late nights at work, and for the unfaltering encouragement and support from my parents, Michael and Elizabeth, and my sister, Danielle.

## Abstract

Surface ponds play a key role in transferring atmospheric energy to the ice for debris-covered glaciers, but as the spatial and temporal distribution of ponds is not well documented, their effect on glacier ablation is unknown. This thesis uses remote sensing and field methods to assess the distribution of supraglacial ponds in the Langtang Valley of Nepal, then develops and applies numerical models of pond surface energy balance to determine energy receipts at the pond, glacier, and basin scales.

172 Landsat TM/ETM+ scenes are analysed to identify thawed supraglacial ponds for the debris-covered tongues of five glaciers for the period 1999-2013. There is high variability in the incidence of ponding between glaciers, and ponds are most frequent in zones of low surface gradient and velocity. The ponds show a pronounced seasonality, appearing rapidly in the pre-monsoon as snow melts, reaching a peak area in the monsoon of about 2% of the debris-covered area, then declining in the post-monsoon as ponds drain or freeze. The satellite observations are supplemented by diverse field observations on Lirung Glacier in the Langtang Valley made in 2013 and 2014, confirming that overall pond area is markedly higher in the pre-monsoon than post-monsoon. Four ponds are observed in detail showing pond drainage, stability, and growth.

The thesis then advances efforts to develop a model of mass and energy balance for supraglacial ponds, using field data from a small pond on Lirung Glacier. Sensitivity testing is performed for several key parameters and alternative melt algorithms. The pond acts as a significant recipient of energy, and participates in the glacier's local hydrologic system during the monsoon. The majority of absorbed energy leaves the pond via englacial conduits, delivering sufficient energy to melt 2612 m<sup>3</sup> of ice (~5.3 m ablation for the pond area).

Energy receipts for all Lirung Glacier ponds for 2014 are then determined, using the full model and simpler approaches based on data availability. The partition of absorbed energy between pond-proximal and englacial melt is inconsistent between ponds, and the shortwave energy balance alone is not adequate to represent pond energy absorption. The model results suggest that ponds absorbed sufficient energy to account for ~10% of Lirung Glacier's ablation in 2014.

Finally, a simplified pond surface energy-balance model is applied to assess pond energy absorption for the entire Langtang catchment, using local meteorological data for 2013 and mean monthly pond distributions from the Landsat observations. Supraglacial ponds are found to absorb sufficient atmospheric energy to account for 5-16% (mean ~12%) of the debris-covered area's volume loss in 2013 (equivalent to 0.11 m thinning for this area). Less absorption occurs in the pre-monsoon and post-monsoon than in the monsoon due to decreased latent heat exchange. Altitude is an additional control, but seasonal surface energy balance remains positive at the ELA of 5400 m.

This research suggests that due to the efficiency of supraglacial ponds as vectors of atmospheric energy to the glaciers' interior, they may account for a considerable portion of the debris-covered area's ablation (~10%) in spite of their low aerial coverage (1-2%), and ponds must be accounted for in studies of debris-covered glacier ablation and evolution.

# Table of contents

<b>List of figures</b>	<b>xv</b>
<b>List of tables</b>	<b>xix</b>
<b>Nomenclature</b>	<b>xxi</b>
<b>1 Introduction</b>	<b>1</b>
1.1 Motivation . . . . .	1
1.2 Study Objectives . . . . .	2
1.3 Thesis Structure . . . . .	2
<b>2 Background</b>	<b>5</b>
2.1 Glaciology in the HKKH mountains: an overview . . . . .	5
2.1.1 Significance of the HKKH . . . . .	6
2.1.2 Glaciers in the HKKH mountains . . . . .	7
2.1.3 Debris-covered glaciers . . . . .	9
2.2 Supraglacial ponds of debris-covered glaciers: a summary . . . . .	16
2.2.1 Pond appearance and dynamic processes . . . . .	18
2.2.2 Modelling efforts . . . . .	23
2.2.3 Pond distributions and controls . . . . .	26
2.3 Key objectives relating to supraglacial ponds . . . . .	27
2.3.1 Pond observations . . . . .	27
2.3.2 Pond-associated ablation . . . . .	28
2.4 Site Description: Langtang Valley, Nepal . . . . .	29
<b>3 Spatial and temporal variability of supraglacial ponds in the Langtang Valley</b>	<b>33</b>
3.1 Executive Summary . . . . .	33
3.2 Specific Objectives . . . . .	34
3.3 Methods . . . . .	34

3.3.1	Identification of ponds . . . . .	34
3.3.2	Glacier characteristics . . . . .	42
3.3.3	Analysis of pond controls . . . . .	44
3.4	Results and Discussion . . . . .	44
3.4.1	Summary of pond observations for the basin . . . . .	44
3.4.2	Uncertainty . . . . .	46
3.4.3	Glacier characteristics and pond cover . . . . .	48
3.4.4	Pond spatial distributions and controls . . . . .	51
3.4.5	Pond seasonality . . . . .	53
3.4.6	Pond persistence, recurrence, and evolution . . . . .	55
3.4.7	Interannual variability . . . . .	58
3.5	Summary . . . . .	61
<b>4</b>	<b>Field observations of Lirung Glacier ponds, 2013 and 2014</b>	<b>65</b>
4.1	Executive Summary . . . . .	65
4.2	Specific Objectives . . . . .	66
4.3	Methods of pond observation . . . . .	66
4.3.1	Instrumentation . . . . .	68
4.3.2	Orthoimages and DEMs . . . . .	69
4.4	Results . . . . .	70
4.4.1	Observed pond areas . . . . .	70
4.4.2	Changes at individual ponds . . . . .	72
4.4.3	Pond temperatures . . . . .	85
4.4.4	Pond albedo . . . . .	88
4.4.5	Wind speed . . . . .	88
4.5	Discussion . . . . .	89
4.5.1	Ponded area seasonality . . . . .	89
4.5.2	Pond size and Landsat observations . . . . .	90
4.5.3	Behaviour and interaction of ponds . . . . .	91
4.5.4	Pond-related phenomena . . . . .	99
4.6	Summary . . . . .	105
<b>5</b>	<b>Modelling the energy balance of a supraglacial pond</b>	<b>107</b>
5.1	Executive Summary . . . . .	107
5.2	Specific Objectives . . . . .	108
5.3	Methods . . . . .	108
5.3.1	Model setup . . . . .	108

5.3.2	Model evaluation . . . . .	115
5.4	Results . . . . .	119
5.4.1	Standard run results . . . . .	119
5.4.2	Configuration tests . . . . .	120
5.5	Discussion . . . . .	123
5.5.1	Pond geometry . . . . .	123
5.5.2	Pond temperature . . . . .	125
5.5.3	Subaqueous melt . . . . .	125
5.5.4	Hydrologic activity . . . . .	127
5.5.5	Cliff/lake system propagation . . . . .	128
5.5.6	Limitations . . . . .	129
5.5.7	Differences to prior efforts . . . . .	129
5.6	Summary . . . . .	130
<b>6</b>	<b>Supraglacial pond associated ablation for Lirung Glacier</b>	<b>133</b>
6.1	Executive Summary . . . . .	133
6.2	Specific Objectives . . . . .	134
6.3	Methods and Approach . . . . .	135
6.3.1	Data: empirical relationships of environmental conditions . . . . .	135
6.3.2	Reducing model complexity . . . . .	144
6.3.3	Input meteorological data . . . . .	145
6.3.4	Specification of pond geometry . . . . .	147
6.4	Results and Discussion . . . . .	147
6.4.1	Summary of energy-balance results, A1-A5 . . . . .	147
6.4.2	Comparisons for common period . . . . .	152
6.4.3	Effects of pond geometry: Levels B-D . . . . .	159
6.4.4	Glacier-scale estimates of pond-absorbed energy . . . . .	164
6.5	Efficiency of ponds and cliffs as vectors of atmospheric energy . . . . .	166
6.6	Summary . . . . .	166
<b>7</b>	<b>Idealised SEB modelling of ponds, all Langtang Valley glaciers</b>	<b>169</b>
7.1	Executive Summary . . . . .	169
7.2	Specific Objectives . . . . .	170
7.3	Model setup . . . . .	170
7.3.1	Spatial and seasonal pattern of ponds . . . . .	170
7.3.2	Meteorology . . . . .	171
7.4	Results and Discussion . . . . .	174

7.4.1	Pond energy absorption by glacier . . . . .	176
7.4.2	Spatial patterns and energy partition . . . . .	179
7.4.3	Seasonal accumulation of energy . . . . .	182
7.4.4	Comparison with other studies . . . . .	184
7.5	Summary . . . . .	185
<b>8</b>	<b>Summary and conclusions</b>	<b>187</b>
8.1	Outcomes of Research Objectives . . . . .	187
8.1.1	Determine the spatial, seasonal and interannual variability of ponds in the Langtang Valley (Chapter 3) . . . . .	187
8.1.2	Document Lirung Glacier supraglacial pond physical characteristics, behaviour, and meteorological forcing (Chapter 4) . . . . .	189
8.1.3	Develop an improved model of energy balance for a supraglacial pond (Chapter 5) . . . . .	190
8.1.4	Model ablation due to ponds at Lirung Glacier (Chapter 6) . . . . .	191
8.1.5	Assess the pond-associated ablation for the entire Langtang catch- ment (Chapter 7) . . . . .	192
8.2	Synthesis . . . . .	193
8.3	Future directions of research . . . . .	195
8.3.1	Pond seasonality . . . . .	195
8.3.2	Pond persistence, drainage, and recurrence . . . . .	195
8.3.3	Pond density for an increased sample of glaciers . . . . .	196
8.3.4	Internal ablation and conduit collapse . . . . .	196
8.3.5	Pond surface conditions and near-surface meteorology . . . . .	196
8.3.6	Pond energy-balance modelling . . . . .	196
8.4	Conclusion . . . . .	197
	<b>References</b>	<b>199</b>
	<b>Appendix A Supplemental Tables and Figures</b>	<b>217</b>

# List of figures

1	Langtang and Kyanjing Villages, May 2013 . . . . .	iii
2.1	Glacier distribution across the HKH . . . . .	8
2.2	Debris-covered glacier response to climate change . . . . .	17
2.3	Examples of supraglacial ponds . . . . .	19
2.4	Ponds in a hydrologic context . . . . .	21
2.5	Pond self-propagation through conduit collapse . . . . .	23
2.6	Glaciers of the Langtang Valley . . . . .	31
2.7	Lirung Glacier surface . . . . .	32
3.1	Pond identification image analysis workflow . . . . .	35
3.2	Temporal distribution of Landsat TM/ETM+ scenes, 1999-2013 . . . . .	36
3.3	Size distribution of observed ponds . . . . .	45
3.4	May-October spatial distribution of supraglacial ponds . . . . .	46
3.5	Comparison of Landsat ETM+ and Cartosat-1 pond observations . . . . .	48
3.6	Annual velocity and surface gradient of study glaciers . . . . .	50
3.7	Distribution of local surface gradient and velocity for all observed ponds . . . . .	51
3.8	Seasonal pattern of thawed pond cover . . . . .	54
3.9	Pond filling and draining on Langtang Glacier, May 2013 . . . . .	56
3.10	Pentadal pond spatial distributions . . . . .	57
3.11	Interannual patterns of supraglacial ponding . . . . .	59
4.1	Observed ponds on Lirung Glacier, 2013 and 2014 . . . . .	67
4.2	Pond areal changes from orthoimages, 2013 and 2014 . . . . .	71
4.3	Pond C photographs in May and October of 2013 and 2014 . . . . .	73
4.4	Pond C pressure transducer records, 2013 and 2014 . . . . .	73
4.5	Pond C outlines, profiles, and surface change . . . . .	75
4.6	Pond D in May and October of 2013 and 2014 . . . . .	77
4.7	Pond D pressure transducer record, 2014 . . . . .	78

4.8	Pond D outlines, profiles, and surface change . . . . .	79
4.9	Pond I in May and October of 2013 and 2014 . . . . .	80
4.10	Pond I pressure transducer record, 2014 . . . . .	81
4.11	Pond I outlines, profiles, and surface change . . . . .	82
4.12	Pond J pressure transducer records, 2013 and 2014 . . . . .	83
4.13	Pond J outlines . . . . .	83
4.14	Pond J in May and October of 2013 and 2014 . . . . .	84
4.15	Diurnal air and water temperatures at ponds C and D . . . . .	86
4.16	Observed hourly pond temperature gradients . . . . .	87
4.17	Albedo observations . . . . .	88
4.18	AWS wind speeds . . . . .	89
4.19	On-glacier wind speeds . . . . .	90
4.20	Post-monsoon 2013 pond C temperature decay . . . . .	95
4.21	Winter 2013-2014 pond C freeze-over . . . . .	96
4.22	Pre-monsoon 2014 pond C thaw-out . . . . .	96
4.23	Pond surface ice . . . . .	98
4.24	Thermo-erosional notches . . . . .	99
4.25	Supraglacial calving and ice cliff crevasse opening . . . . .	103
4.26	Englacial conduit exposures . . . . .	104
4.27	Pond-related data availability . . . . .	105
5.1	A supraglacial pond as a conceptual control volume . . . . .	109
5.2	Geometry for view factors . . . . .	110
5.3	Location of test pond on Lirung Glacier . . . . .	115
5.4	The study pond in May and October, 2013 . . . . .	116
5.5	Observed hourly pond temperature gradients . . . . .	118
5.6	Key model outputs in the pre-monsoon and monsoon . . . . .	124
5.7	Observed and modelled thermo-erosional notching . . . . .	126
6.1	$T_{ws}$ regression development scatter plots . . . . .	137
6.2	Performance of $T_{ws}$ models M3 and M4 . . . . .	139
6.3	Albedo model performance . . . . .	140
6.4	Pond D wind speeds . . . . .	142
6.5	Kyanjing AWS $u_a$ adjustment to Lirung Glacier . . . . .	143
6.6	Conceptual diagram of useful numerical modelling trade-offs . . . . .	145
6.7	Pond surface energy-balance partition . . . . .	149
6.8	Surface energy-balance results, levels B1-D2 . . . . .	159

---

6.9	Pond-associated energy flux, pond C . . . . .	160
6.10	Pond-associated energy flux, pond D . . . . .	161
6.11	Pond-associated energy flux, pond J . . . . .	163
7.1	Debris-covered glacier 50 m elevation bands . . . . .	171
7.2	Pond densities by 50 m elevation bands . . . . .	172
7.3	Supraglacial pond hypsometry for Langtang Glacier . . . . .	173
7.4	Response of EB components to elevation . . . . .	175
7.5	Pre-monsoon and monsoon SEB . . . . .	177
7.6	Pond energy absorption by 50 m elevation band . . . . .	180
7.7	Pond energy absorption by 50 m elevation band . . . . .	181
7.8	Seasonal pond surface energy absorption for each glacier . . . . .	183
A.1	Pond-associated energy flux, pond A . . . . .	225
A.2	Pond-associated energy flux, pond F . . . . .	226
A.3	Pond-associated energy flux, pond G . . . . .	226
A.4	Pond-associated energy flux, pond H . . . . .	227
A.5	Pond-associated energy flux, pond I . . . . .	227
A.6	Pond-associated energy flux, ponds K-P . . . . .	228



# List of tables

3.1	Study glacier characteristics and pond observations . . . . .	42
3.2	Comparison of Landsat ETM+ and Cartosat-1 pond observations . . . . .	47
3.3	Landsat pond identification errors . . . . .	47
3.4	Distribution of ponds within categorised terrain . . . . .	52
4.1	Lirung Glacier pond and meteorological instrumentation . . . . .	69
4.2	Summary of Lirung Glacier orthoimages, 2013 and 2014 . . . . .	70
4.3	Pond areal changes from orthoimages, 2013 and 2014 . . . . .	72
4.4	Summary of pond behaviours, 2013 and 2014 . . . . .	93
5.1	Energy-balance model configurations and results . . . . .	121
6.1	Seasonal definitions and lapse rates for the study . . . . .	136
6.2	$T_{ws}$ regression coefficients and performance . . . . .	138
6.3	Albedo model performance . . . . .	141
6.4	Energy-balance model complexity structure . . . . .	146
6.5	Summary of modelled melt for the level A runs . . . . .	150
6.6	Summary of A4 energy-balance results for common period . . . . .	154
6.7	Modelled melt for A4 runs, for common period . . . . .	155
6.8	Effects of DEM changes on energy balance . . . . .	155
6.9	Effects of meteorological data changes on energy balance . . . . .	156
6.10	Surface energy balance and total melt comparison . . . . .	157
6.11	Summary of results for model levels B-D . . . . .	158
6.12	Glacier-wide surface energy-balance scaling . . . . .	165
7.1	Glacier size and energy-balance model discretisation . . . . .	172
7.2	Mean pond view-factors . . . . .	174
7.3	Pond-associated ablation, Langtang Valley glaciers . . . . .	178
A.1	Summary of Landsat scenes analysed in Chapter 3 . . . . .	218

A.2	Summary of Landsat scenes analysed in Chapter 3, part 2 . . . . .	219
A.3	Summary of Landsat scenes analysed in Chapter 3, part 3 . . . . .	220
A.4	Summary of Landsat scenes analysed in Chapter 3, part 4 . . . . .	221
A.5	Summary of A level energy-balance results for common period . . . . .	222
A.6	Modelled melt for all level A runs, for common period . . . . .	222
A.7	Summary of $\alpha = 0.12$ energy-balance results for common period . . . . .	223
A.8	Modelled melt for all level A runs with $\alpha = 0.12$ , for common period . . . . .	223
A.9	Full results for model levels B-D . . . . .	224

# Nomenclature

## Roman Symbols

$\Delta S$	Rate of change in pond internal energy, [W]
$\Sigma Ex$	Total pond-associated ablation, [m <sup>3</sup> icemelt equivalent]
$\Sigma Q_n A_p$	Cumulative pond surface energy balance, [m <sup>3</sup> icemelt equivalent]
$A$	Total pond area, [m <sup>2</sup> ]
$A_d$	Area of pond subaqueous saturated debris interface, [m <sup>2</sup> ]
$A_i$	Area of pond subaqueous bare-ice interface, [m <sup>2</sup> ]
$A_p$	Pond area, [m <sup>2</sup> ]
$A_{miss}$	Total area of ponds too small to be observed, m <sup>2</sup>
$b$	Coefficient for regression fit
$c_w$	Specific heat of water, [J kg <sup>-1</sup> K <sup>-1</sup> ]
$D$	Rate of energy advection out of pond by discharge, [W]
$d$	Index of agreement between two datasets
$d_d$	Subaqueous debris thickness [m]
$D_l$	Mean vertical subaqueous bare-ice contact length [m]
$D_s$	Diffuse shortwave radiation incident upon the pond surface, [W m <sup>-2</sup> ]
$D_t$	Terrain-reflected shortwave radiation incident upon the pond surface, [W m <sup>-2</sup> ]
$g$	Standard acceleration due to gravity at the Earth's surface, 9.81 m s <sup>-2</sup>
$H$	Sensible turbulent energy flux at the pond surface, [W m <sup>-2</sup> ]
$h_i$	Mean coefficient of heat transfer [W m <sup>-2</sup> K <sup>-1</sup> ]
$I$	Rate of energy advection into pond, [W]
$I_n$	Net shortwave radiation flux at the pond surface, [W m <sup>-2</sup> ]
$I_s$	Direct shortwave radiation incident upon the pond surface, [W m <sup>-2</sup> ]
$k_r$	Bulk thermal conductivity for rock, [W m <sup>-1</sup> K <sup>-1</sup> ]
$k_w$	Bulk thermal conductivity for water, [W m <sup>-1</sup> K <sup>-1</sup> ]
$k_{eff}$	Bulk thermal conductivity for saturated debris, [W m <sup>-1</sup> K <sup>-1</sup> ]
$L_f$	Latent heat of fusion for ice [J kg <sup>-1</sup> ]
$L_n$	Net longwave radiation flux at the pond surface, [W m <sup>-2</sup> ]

---

$L_o$	Emitted longwave radiation flux from the pond surface, [ $\text{W m}^{-2}$ ]
$L_d$	Debris-emitted longwave radiation flux incident upon the pond surface, [ $\text{W m}^{-2}$ ]
$L_{in}$	Atmospheric longwave radiation flux incident upon the pond surface, [ $\text{W m}^{-2}$ ]
$LE$	Latent turbulent energy flux at the pond surface, [ $\text{W m}^{-2}$ ]
$MW_d$	Cumulative subaqueous subdebris melt volume, [ $\text{m}^3$ ]
$MW_i$	Cumulative subaqueous bare-ice melt volume, [ $\text{m}^3$ ]
$N$	Number of ponds
$p$	Statistical strength of regression
$P_0$	Observed barometric pressure [kPa]
$Q_d$	Net energy flux at pond subaqueous saturated debris interface, [ $\text{W m}^{-2}$ ]
$Q_i$	Net energy flux at pond subaqueous bare-ice interface, [ $\text{W m}^{-2}$ ]
$Q_n$	Net pond-atmosphere surface energy flux, [ $\text{W m}^{-2}$ ]
$Q_r$	Energy flux advected into the pond by rain, [ $\text{W m}^{-2}$ ]
$q_r$	Rate of rainfall, [ $\text{m s}^{-1}$ ]
$R^2$	Coefficient of correlation
$rH$	Relative Humidity [%]
$RMSE$	Root-Mean-Squared-Error between two datasets
$S$	Pond internal energy, [J]
$S_0$	Smallest possible pond diameter, 0 m
$S_p$	Pond diameter [m]
$S_{lim}$	Maximum pond diameter [m]
$S_{min}$	Minimum observable pond diameter [m]
$T_a$	Air temperature at 2 m above the surface, [K]
$T_f$	Film temperature for natural convection of water [K]
$T_i$	Temperature of ice, [K]
$T_p$	Mean pond temperature, [K]
$T_{2m}$	Pond temperature at a depth of 2 m [K]
$T_{50cm}$	Pond temperature at a depth of 0.5 m [K]
$T_{deb}$	Debris surface temperature [K]
$T_{wb}$	Temperature of the pond at the saturated debris interface, [K]
$T_{ws}$	Temperature of the pond surface, [K]
$u_a$	Wind speed at 2 m height [ $\text{m s}^{-1}$ ]
$u_w$	Vertical pond velocity at bare-ice contact [ $\text{m s}^{-1}$ ]
$v_d$	Melt rate for the subaqueous subdebris ice surface, [ $\text{m s}^{-1}$ ]
$v_i$	Melt rate for the subaqueous bare-ice surface [ $\text{m s}^{-1}$ ]
$V_p$	Pond volume, [ $\text{m}^3$ ]

$x_i$	Horizontal subaqueous bare-ice contact length [m]
$z_0$	Aerodynamic roughness length, or surface roughness, [m]
Gr	Grashof number [dimensionless]
LR	Air temperature lapse rate [ $^{\circ}\text{C m}^{-1}$ ]
Nu	Nusselt number [dimensionless]
Pr	Prandtl number [dimensionless]
Ra	Rayleigh number [dimensionless]
SSC	Suspended sediment concentration [ $\text{mg L}^{-1}$ ]
$\Delta V$	Changes in pond volume [ $\text{m}^3 \text{s}^{-1}$ ]
$\dot{V}_d$	Mean pond discharge, [ $\text{m}^3 \text{s}^{-1}$ ]
$\dot{Q}_{LE}$	Total energy flux of due to latent heat exchange at the pond surface [W]
$\dot{V}_{dmax}$	Maximum pond discharge, [ $\text{m}^3 \text{s}^{-1}$ ]
$\dot{V}_{LE}$	Volumetric flux of water vapour at the pond surface [ $\text{m}^3 \text{s}^{-1}$ ]
$\dot{V}_d$	Pond discharge, [ $\text{m}^3 \text{s}^{-1}$ ]
$\dot{V}_i$	Water input to a pond, [ $\text{m}^3 \text{s}^{-1}$ ]
$\dot{V}_R$	Rain input to a pond, [ $\text{m}^3 \text{s}^{-1}$ ]
$\nabla T$	Vertical temperature gradient in pond, [ $^{\circ}\text{C m}^{-1}$ ]
$\bar{v}_d$	Mean subaqueous subdebris melt rate, [ $\text{m d}^{-1}$ ]
$\bar{v}_i$	Mean subaqueous bare-ice melt rate, [ $\text{m d}^{-1}$ ]

### Greek Symbols

$\alpha$	Pond albedo
$\beta$	Coefficient of thermal expansion of water, $6.8 \times 10^{-5} \text{ K}^{-1}$
$\beta$	Exponent for pond size power-law fit
$\varepsilon_w$	Emissivity of water, [ $\text{W m}^{-2}$ ]
$\kappa_l$	Thermal diffusivity of water [ $\text{m}^2 \text{s}^{-1}$ ]
$\mu()$	Mean of a variable
$\nu$	Kinematic viscosity of water, $1.75 \times 10^{-6} \text{ m}^2 \text{ s}^{-1}$
$\nu_0$	Broadband refractive index of water
$\nu_f$	Film kinematic viscosity for natural convection of water [ $\text{m}^2 \text{s}^{-1}$ ]
$\phi$	Debris porosity, [%]
$\rho_w$	Density of water, [ $\text{kg m}^{-3}$ ]
$\rho_0$	Water density at the freezing point [ $\text{kg m}^{-3}$ ]
$\rho_f$	Film water density for natural convection [ $\text{kg m}^{-3}$ ]
$\rho_{ws}$	Water density at the pond surface [ $\text{kg m}^{-3}$ ]
$\sigma()$	Standard deviation of a variable
$\sigma$	Stefan-Boltzmann constant, [ $\text{W m}^{-2}$ ]

$\theta_s$  Solar elevation, [ $^\circ$ ]

### Acronyms / Abbreviations

6S Second Simulation of a Satellite Signal in the Solar Spectrum radiative transfer code

AOD Aerosol Optical Depth

ASTER Advanced Spaceborne Thermal Emission and Reflection Radiometer

AVNIR-2 Advanced Visible and Near Infrared Radiometer, type 2

AWS Automated Weather Station

BR24 Band 2 to Band 4 Ratio (green to near-infrared)

BR45 Band 4 to Band 5 Ratio (near-infrared to middle-infrared)

BT Brightness temperature

CGIAR-CSI Consultative Group for International Agricultural Research - Consortium for Spatial Information

CNES Centre national d'études spatiales, the space agency of France

DEM Digital Elevation Model

DGM Difference in height between Glacier surface and Moraine [m]

DOY Numerical day of the year

EB Energy Balance (model)

ETH Swiss Federal Institute for Technology

ETM+ Enhanced Thematic Mapper

HMA High Mountain Asia

ICIMOD International Centre for Integrated Mountain Development

LEDAPS NASA Landsat Ecosystem Disturbance Adaptive Processing System

NASA United States National Aeronautics and Space Administration

NDSI Normalised Difference Snow Index

NDWI Normalised Difference Water Index

SEB Surface Energy Balance (model)

SfM Structure-from-Motion photogrammetry

SLC Scan Line Corrector for the ETM+ sensor

Spot6 CNES Satellite Pour l'Observation de la Terre 6th satellite

SRTM Shuttle Radar Topography Mission

TM Thematic Mapper

TOMS Total Ozone Mapping Spectrometer

TWV Total Water Vapour

UAV Unmanned Aerial Vehicle

USGS United States Geological Survey

WRS-2 Worldwide Reference System, used for Landsat 5 and 7

# Chapter 1

## Introduction

### 1.1 Motivation

As debris-covered glaciers in the Hindu Kush-Karakoram-Himalaya mountain chain respond to sustained climate warming, their low-gradient tongues are stagnating and heterogeneously downwasting (e.g. Gardelle et al., 2013; Kääb et al., 2012; Benn et al., 2012). Differential ablation due to spatially-varying debris thickness combines with collapses of englacial void roofs to produce a karst-like appearance of surface depressions and bare ice outcrops, and leads to a fragmented hydrological network (e.g. Iwata et al., 1980; Sakai et al., 1998; Wessels et al., 2002; Gulley, 2009). At depressions with inefficient surface-subsurface connectivity, water is likely to collect as a supraglacial pond perched above the local hydrological base-level until it drains by exploiting a weakness or void within the nearby ice (Gulley et al., 2009b).

The ponds absorb and transfer atmospheric energy to the ice surface much more efficiently than the widespread debris layer (Sakai et al., 2000; Röhl, 2008). Surface ponds accelerate local ice wastage through subaerial ice-cliff backwasting, subaqueous melt at the ice-water interface, and subaerial calving, leading to basin expansion (Benn et al., 2001; Röhl, 2008). Importantly, the ponds' eventual drainage leads to delivery of the absorbed energy to englacial conduits (Sakai et al., 2000). This promotes down-glacier conduit collapse and could contribute to the heightened rates of downwasting observed for these glaciers, in spite of reduced surface ablation. Ponds may therefore play a strong role in determining the evolution of debris-covered tongues (Benn et al., 2012).

Studies have determined glaciological controls of surface ponding (e.g. Reynolds, 2000; Quincey et al., 2007), and have developed a firm conceptual model to understand the role that ponds play in the development of large, hazardous glacial lakes (e.g. Kirkbride, 1993; Benn et al., 2012). However, spatial distributions of supraglacial ponds have been developed

for few glaciers, and understanding of seasonal and interannual variability of ponded areal extent is limited (Gardelle et al., 2011; Liu et al., 2015; Watson et al., 2016). At the same time, few studies have quantified the ablation attributable to ponds at even the local scale. Consequently, few assessments exist of the energy balance and associated ablation due to supraglacial ponds at the glacier scale (e.g. Sakai et al., 2000; Röhl, 2008; Thompson et al., 2016), and current understanding of these features and their effects is not included in numerical models of debris-covered glacier ablation (Reid et al., 2012; Fyffe et al., 2015; Ragettli et al., 2015).

## 1.2 Study Objectives

The overarching goal for the study is to determine the ablation that may be attributed to supraglacial ponds, focusing on the debris-covered glaciers of the Langtang valley of Nepal as a case study. To achieve this goal, several key objectives will be addressed spanning multiple spatial scales and methodologies. On one hand, the targeted research requires investigation of individual features through *in-situ* instrumentation and repeat surveys to develop a numerical model of supraglacial pond ablation. At the same time, the goal requires basin-scale observation of the spatial and temporal variability of ponds. Finally, the outcomes must be reasonably extended to assess the role of ponds across the entire catchment. Thus, the study's specific objectives are to:

1. Determine the spatial, seasonal and interannual variability of supraglacial ponds in the Langtang Valley
2. Document Lirung Glacier supraglacial pond physical characteristics, behaviour, and meteorological forcing through field observation
3. Develop an improved model of energy balance for a supraglacial pond
4. Model ablation due to supraglacial ponds for an entire glacier with *in-situ* data
5. Assess the ablation due to supraglacial ponds across the entire Langtang catchment

## 1.3 Thesis Structure

The thesis is structured into 8 chapters to address the above aims. Following this Introduction, a more comprehensive Background describes the state of knowledge of debris-covered glaciers and supraglacial ponds in High Mountain Asia, and describing the Langtang valley

study site (Chapter 2). Chapter 3 details a Landsat-based remote sensing study of supraglacial pond spatio-temporal variability for the debris-covered glaciers of the Langtang valley. Field observations of supraglacial ponds and meteorological conditions on Lirung Glacier in 2013 and 2014 are summarised in Chapter 4, specifically targeting the input data necessary to run the pond energy-balance model. Chapter 5 describes and tests a refined version of the supraglacial pond energy-balance model of Sakai et al. (2000); this material also appears in published form as Miles et al. (2016). Using the field observations, Chapter 6 evaluates the energy-balance model with a range of configurations for all ponds on Lirung Glacier in 2014 to arrive at a whole-glacier estimate of energy inputs attributable to ponds. In Chapter 7, a simplified energy-balance model is evaluated for all of the debris-covered glaciers of the Langtang valley, integrating the results of Chapters 3 and 6. Finally, Chapter 8 presents a summary of the principal outcomes of the analyses.

Each of the body Chapters (3-7) tries to follow a common structure for ease of the reader. First, a brief Executive Summary summarises the methodology and key results of the chapter. A short section then summarises the Specific Objectives for the chapter, before the chapter's analytical Methods are described, followed by Results and Discussion. Last, a Summary of the analyses and outcomes is made.



# Chapter 2

## Background

This chapter will first provide a summary of the relevance and state of knowledge of glaciology in High Mountain Asia, then will focus on the current understanding of supraglacial ponds on debris-covered glaciers. The chapter will then consider open questions relating to the observation and energy-transfer of supraglacial ponds, and will conclude by introducing the Langtang Valley, the study site for all analyses in the thesis.

### 2.1 Glaciology in the HKKH mountains: an overview

The glaciers of the Hindu Kush-Karakoram-Himalaya (HKKH) mountain chain have not been a strong focus of scientific research until recent years (Bolch et al., 2012). Occasional observations were made by scientific members of expeditions during the Golden Era of Exploration and during attempts to conquer the 8000 m peaks, but only a handful of glaciers were studied in a systematic manner. This lack of historical data is not unique to glaciology; there is a similar regional shortage of observations for hydrology and ecology, among other fields, until the later part of the 20th century. Similarly, the absence of historical data is not unique to the Himalaya and Karakoram, or more broadly to High Mountain Asia; most of the world's glaciers were not extensively documented until recently (Pfeffer et al., 2014). However, the scientific understanding of glaciers in these mountains was sufficiently limited that in the International Panel on Climate Change's Fourth Assessment Report (2007), an erroneous statement that Himalayan Glaciers could disappear by 2035 made its way into the final text (Cogley et al., 2010).

The relative shortage of glaciology studies in the HKKH and throughout High Mountain Asia is not without reason. First, the glacierised catchments are generally situated on political borders, some of which are contested to this day, and many of these countries were closed to foreigners until recent years. These political limitations to access are exacerbated

by logistical challenges. The mountains and glaciers of the region occur at the highest altitudes of the world, and the high altitude creates a physical challenge and medical risk for any fieldwork. Further, road and helicopter access are limited by the extremely rugged terrain, often requiring approach to the glaciers on foot, with supplies for the duration of the research campaign. In spite of these challenges, the region's glaciers and climate have been increasingly studied in the past decade, filling gaps in knowledge at the global scale and attempting to understand the behaviour of ice at the altitudinal extremes of the world (Bolch et al., 2012).

### **2.1.1 Significance of the HKKH**

The HKKH mountain chain extends over 3000 km in length, forming the border region of eight South and Central Asian countries. Formed by uplift due to the tectonic convergence of the Indian plate with the Eurasian plate, this region contains all 14 mountains greater than 8000 m in altitude in the world. The region remains tectonically very active, experiencing three earthquakes >M7.0 in 2015 alone, and these earthquakes typically have significant death tolls (Jackson, 2006; Elliott et al., 2016; Kargel et al., 2016).

The HKKH mountains form the headwater catchments of many of the great rivers of Asia. The Indus, Ganges, and Brahmaputra all drain to the south and support the livelihoods of over 800 million people (Immerzeel et al., 2010) by providing drinking water, increasing irrigation capacity, and enabling hydroelectric power generation. The dependence of settlements on mountain streamflows varies with altitude, longitude, and season (Immerzeel et al., 2010; Lutz et al., 2014). Hydrologic studies of streamflow partitioning suggest a significant cryospheric contribution for drier seasons and regions, and for increasing altitudes (Lutz et al., 2014; Ragettli et al., 2015; Wilson et al., 2016). Seasonal snow is a major contribution to streamflow (Immerzeel 2009), and the region is one of the most extensive glacierised areas outside of the poles (Pfeffer et al., 2014).

Climate varies longitudinally along the mountain chain. In the west, the Karakoram is characterised by warm, dry summers and cold winters bringing two-thirds of annual precipitation, and storm tracks are determined by westerly and southwesterly flows (Hewitt, 2011; Ragettli et al., 2013; Mölg et al., 2014). To the east, the climate of Himalayan mountains is dominated by the warm, wet Indian monsoon in the summer months, bringing the majority of annual precipitation between June and September (Bookhagen and Burbank, 2010; Immerzeel et al., 2014b). A mild gradient of climatic conditions exists between these two extremes in the Ladakh and Zaskar regions (Shukla and Qadir, 2016). The high mountains provide a very strong orographic obstacle for storms sourced from the south and west, and lead to a North-South precipitation gradient across the zone (Galewsky, 2009;

Ménégoz et al., 2013). Prevailing cold, dry conditions characterise the climate of the Tibetan Plateau and glaciers north of the HKKH range, although these, too, are affected by the monsoon (Mölg et al., 2012). Across the entire HKKH range, annual precipitation averages 880 mm (Shrestha et al., 2015).

Ten major river systems are sourced in the HKKH mountains, whose basins cover a total area of 9 million km<sup>2</sup> and provide sustenance to more than 1.4 billion people (Immerzeel et al., 2010; Shrestha et al., 2015). The population within the Hindu Kush Himalayan region is approximately 210 million, and 31% of this population lives below the official poverty line (Shrestha et al., 2015). These communities are largely agrarian, relying heavily on local natural resources and employing subsistence farming on small plots of land. The population is vulnerable to both rapid environmental and socio-economic changes, and they depend on sustained streamflow for domestic use, agriculture, hydropower and industry (Xu et al., 2009; Shrestha et al., 2015), motivating research to assess the impact of climate change on streamflows across the region through numerical modelling (e.g. Immerzeel et al., 2011; Lutz et al., 2014).

Recent temperature increases have been stronger for mountainous areas such as the HKKH relative to other land surfaces (Rangwala and Miller, 2012; Mountain Research Initiative EDW Working Group, 2015). Few long-term meteorological records exist in the HKKH region, making direct assessment of change in temperature or precipitation difficult (Bolch et al., 2012). The widespread and often rapid loss of glacier mass suggests serious imbalance between local climate and the cryosphere over the last few decades (Fujita and Nuimura, 2011; Käab et al., 2012; Gardelle et al., 2013; Gardner et al., 2013).

### 2.1.2 Glaciers in the HKKH mountains

High Mountain Asia as a whole is one of the most extensively glacierised areas outside the poles. Only considering the HKKH mountain chain, there are approximately 35,000 individual glaciers covering 55,000 km<sup>2</sup> and estimated to contain 4100-5000 Gt of mass (Pfeffer et al., 2014; Frey et al., 2014). These glaciers are also notable for their low latitude (30-37°N); the only significant glacierised areas of the globe more equatorial are the glaciers of the High Andes, although individual glaciers occur in Mexico, Africa, and Indonesia at high altitudes. As with these tropical glaciers, glaciation in South Asia is only possible due to the mountains' high altitude. Although glaciers in the HKKH occasionally extend below 3500 m.a.s.l., the mean glacier elevation is ~5350 m.a.s.l. (Bolch et al., 2012; Bajracharya et al., 2015). The glaciers are not distributed uniformly across the range; those in the West Himalaya and Karakoram are more likely to extend to lower elevations. Additionally, the

Karakoram glaciers are more often connected via ice divides to form large ice fields, while the glaciers of the Central and Eastern Himalaya are more often disconnected features.

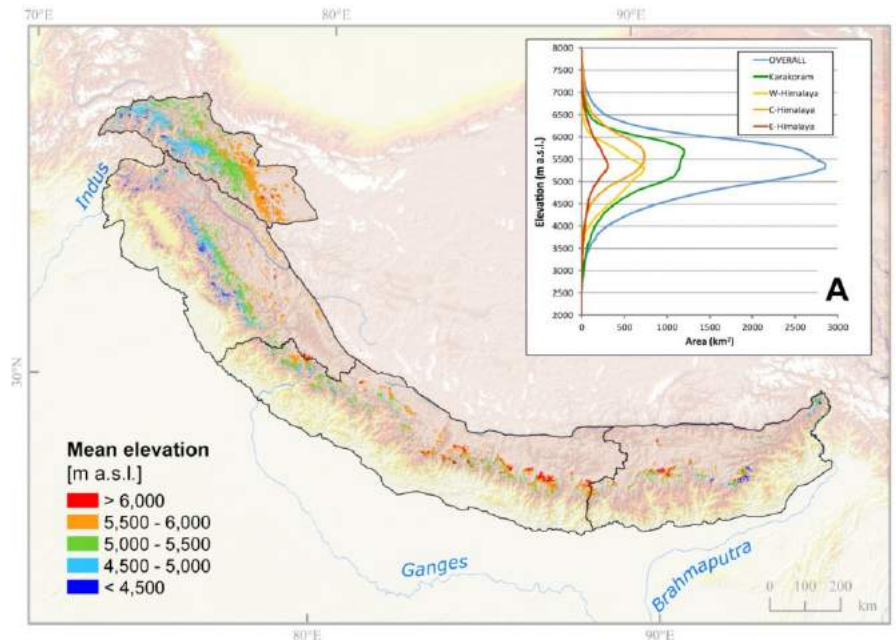


Fig. 2.1 Zonal distribution of glacier area and elevation across the Hindu Kush-Karakoram-Himalaya mountain chain. Figure reproduced from Bolch et al. (2012).

Most of the region's glaciers are responding actively to climate change, exhibited by widespread observations of glacier thinning and terminus retreat. Glacier thinning has been observed from satellites via optical photogrammetry (e.g. Bolch et al., 2012; Gardelle et al., 2013; Pellicciotti et al., 2015) and laser altimetry (Kääb et al., 2012), and is frequently in the range of  $0.2\text{-}0.75\text{ m a}^{-1}$ . Glacier thinning is inconsistent in the Karakoram, where some glaciers are surging, some are losing mass rapidly, and others are stable or even growing (Kääb et al., 2012). Glacier area and length has been routinely monitored for a large number of glaciers across the mountain chain and predominantly shows a strong decrease in glacier size, with the exception of the Karakoram (Bolch et al., 2012; Bajracharya et al., 2015). The mixed climate response of the Karakoram glaciers has led to focused investigation of the climate sensitivity of these glaciers (Hewitt, 2005, 2011; Janes and Bush, 2012) and the timing, causes, and consequences of their surge behaviour (Quincey et al., 2011; Paul, 2015). Gravimetric studies of High Mountain Asia are in general agreement with the spatial variability and magnitudes of change (Jacob et al., 2012), and consensus estimates suggest that glaciers across the whole region are losing  $26 \pm 12\text{ Gt}$  of mass per year, accounting for  $\sim 10\%$  of total cryospheric contribution to sea level rise in recent years (Gardner et al., 2013).

The response of the region's glaciers to 21<sup>st</sup> century climate change has been assessed through numerical modelling with models of varied complexity in recent years, usually focusing on glacier mass balance with a simplified representation of glacier dynamics (e.g. Marzeion et al., 2012; Radić et al., 2014; Wiltshire, 2014; Zhao et al., 2014; Huss and Hock, 2015). Most such studies have examined the HKKH glaciers only as a component of global glacier mass balance calculations (Marzeion et al., 2012; Radić et al., 2014; Huss and Hock, 2015), but recently models have focused on regional assessments with increased model complexity, both for the HKKH region (Wiltshire, 2014; Zhao et al., 2014) and other regions of the globe (e.g. Clarke et al., 2015). All models suggest a very strong decline in HKKH glacier area and volume through the 21<sup>st</sup> century, between 34% and 90% depending on zone, climate scenario, and model, but with the greatest specific mass losses in the Central and Eastern Himalaya (e.g. Radić et al., 2014). Generally, results indicate increasing rates of glacier mass loss in the short term, before levelling off and decreasing by the end of the 21<sup>st</sup> century as the glacierised area decreases (Radić et al., 2014). The results with lowest confidence are for the Karakoram, where limited understanding of current glacier behaviour leads to large uncertainties in the response of those systems to future climate.

More advanced numerical models have been developed and applied for select well-characterised catchments to understand the response of their glaciers to climate change (Immerzeel et al., 2013; Rowan et al., 2015; Shea et al., 2015a; Ragettli et al., 2016). Here, better documentation of glacier geometry, more refined ice-dynamics models, and explicit representation of the debris-covered surface has enabled understanding of the evolution of the region's glaciers through the 21<sup>st</sup> century. Results indicate increasing rates of glacier mass loss leading to a peak in meltwater production in the mid-21<sup>st</sup> century, before decreasing glacier melt production as the glacierised area decreases (Immerzeel et al., 2013). Glacier area losses in the 21<sup>st</sup> century could be 33-54% by 2100 depending on region and glacier size (Immerzeel et al., 2013), or even greater (Shea et al., 2015a). However, debris cover may play an important role in extending these glaciers' longevity, and understanding the response of these glacier systems to climate change may depend on improved characterisation of the dynamic processes of debris-covered glaciers (Rowan et al., 2015).

### 2.1.3 Debris-covered glaciers

Debris-covered glaciers (also called 'debris-mantled' or 'rubble-covered') have been a focus of glaciological interest in recent years (e.g. Benn et al., 2012; Bolch et al., 2012; Ragettli et al., 2015; Rowan et al., 2015). Unlike the bare ice surface commonly associated with glaciers, the ice surface of a debris-covered glacier is mantled by a layer of granular rock. Surface debris layers commonly found in a glaciological context range across a spectrum

from dust or scattered pebbles near a glacier's terminus to rock glaciers with minimal interstitial ice (Janke et al., 2015; Bosson and Lambiel, 2016). As many alpine glaciers exhibit some debris cover near the terminus, and others have exposed surface debris as medial moraines, the definition of a 'debris-covered glacier' varies in the scientific literature. For this thesis, a 'debris-covered glacier' refers to the case of a nearly-continuous layer of debris mantling the glacier's ice surface. Such layers are generally exposed below the equilibrium line altitude (ELA) and are most common for valley glaciers. The debris layer can vary in thickness ranging from a few centimetres to several metres, and generally increases in thickness down-glacier (e.g. Zhang et al., 2011). Individual grains within the debris layer can range in size from dust to boulders, spread heterogeneously across the glacier (Fushimi et al., 1980). The surface of a debris-covered glacier can be very smooth in certain cases, but is often very rugged, characterised by large boulders, closed surface depressions, supraglacial ponds, and exposed cliffs of bare ice (e.g. Iwata et al., 1980; Benn et al., 2000).

Debris-covered glaciers occur in nearly all glacierised mountain ranges globally: High Mountain Asia (e.g. Bolch et al., 2012), the European Alps (e.g. Brock et al., 2010), the Southern Alps (e.g. Kirkbride, 1993) the Caucasus (e.g. Lambrecht et al., 2011), the Andes (e.g. Emmer et al., 2015; Janke et al., 2015), Alaska (e.g. Kienholz et al., 2015), and Antarctica (e.g. Mackay et al., 2014). A global estimate of debris-covered glacier area has yet to be formulated, but this type of glacier area represents a distinctive minority of total glacier area that varies by region and subregion. For many mountain ranges, debris covers a very small portion of total glacier area, and debris-covered glaciers are often associated with tectonically active, younger mountain ranges with significant vertical relief, where headwall erosion and avalanches sustain a strong supply of rock debris onto glaciers (Benn et al., 2000; Hambrey et al., 2008; Bolch et al., 2012). Thus, patterns of debris cover are heterogeneous at both the global and regional scale. In Alaska, for example, debris-covered glaciers comprise 11% of total glacier area, but this varies zonally from 5% to 28% (Kienholz et al., 2015). Latitudinal differences span the full spectrum of debris cover in the Andes of Chile, suggesting climatic controls as well (Janke et al., 2015). In the Himalaya-Karakoram, debris-covered glaciers make up ~10% of the glacierised area, covering a slightly larger portion of total glacier area in the East (16.6% in the Ganges basin) than in the West (9.6% in the Indus basin) (Bolch et al., 2012).

### **Surface ablation calculation and challenges**

Early scientific interest focused on the debris' role to amplify or reduce ablation based on surface thickness. As observed by field (e.g. Ostrem, 1959; Fujii, 1977; Nakawo and Young, 1982; Adhikary S., M. Nakawo, K. Seko, 2000) and laboratory (e.g. Reznichenko et al.,

2010) experiments, the thickness of supraglacial debris exerts a critical control on glacier surface ablation. For thin debris cover, the low albedo of the debris results in an increase in absorption of radiation and an increase in melt as compared to a clean ice surface. Beyond a critical thickness, however, the debris instead has an insulating effect that overcomes the increased radiative absorption, resulting in reduced ablation relative to clean ice. Commonly referred to as the Östrem curve, this empirical relationship is not numerically transferable between glaciers as it depends on the climatic setting and debris composition at any particular site (e.g. Nakawo and Rana, 1999; Conway and Rasmussen, 2000; Reznichenko et al., 2010). The typical result is that, following a flowline down-glacier, cumulative surface ablation leads to increasing debris thickness as debris accumulates at the surface. The increased debris-cover in turn inhibits ablation, and debris-covered glaciers are generally found to have decreasing surface ablation approaching the terminus (e.g. Juen et al., 2014).

Numerical modelling of surface ablation for ice covered by debris has advanced remarkably in recent years. The importance of conduction through the debris layer was realised by initial studies, but results were only achieved for idealised, steady-state situations (Kraus, 1975; Bozhinskiy et al., 1986). The concept of thermal resistance was employed to account for the reduced and lagging delivery of heat through a debris layer within a surface energy balance model, enabling direct application to field observations, but at the point scale (Nakawo, Masayoshi Takahashi, 1982). Later work enabled numerical representation of conduction within the debris layer by using a multilayered modelling domain, both on daily (Nicholson and Benn, 2006) and hourly timescales (Reid and Brock, 2010). More recent model development efforts have incorporated the effects of surface snow layers (Lejeune et al., 2013), moisture fluxes and phase changes within the debris (Collier et al., 2014), and air flow through porous debris (Evatt et al., 2015).

Point energy balance models are not easily applied for a distributed domain due to data requirements (e.g. Collier et al., 2014), so interest in modelling ablation at the glacier scale initially focused on developing simplified representations of subdebris ablation. Degree-day and temperature-index models have been applied to debris-covered glaciers (e.g. Kayastha et al., 2000; Mihalcea et al., 2006), and intermediate-complexity models incorporating partial representation of surface energy fluxes (Ragettli et al., 2015; Carenzo et al., 2016) or debris conduction (Han et al., 2006) have also been advanced. These and similar models have the advantage of easy distribution over a larger spatial extent (e.g. Hagg et al., 2008; Lambrecht et al., 2011; Zhang et al., 2011; Immerzeel and Bierkens, 2012; Fujita and Sakai, 2014; Juen et al., 2014; Ragettli et al., 2015; Carenzo et al., 2016). Unfortunately, these approaches seem to be limited in transferability between sites, as they depend heavily on site-specific calibration (Ragettli et al., 2015; Carenzo et al., 2016).

Recently, fully-distributed energy-balance models have emerged to estimate subdebris surface ablation (e.g. Reid et al., 2012; Fyffe et al., 2014; Collier et al., 2015). While such models may produce the most robust distributed estimates of surface ablation, they have spatially-extensive data requirements (especially meteorology and debris thickness), which even point-scale models find challenging to develop (Reid et al., 2012; Fyffe et al., 2014). Debris-covered glaciers exhibit higher temperature lapse rates than clean-ice glaciers, but these vary between glaciers (Brock et al., 2010; Shaw et al., 2016; Steiner and Pellicciotti, 2016). Spatial representation of other meteorological variables is even more challenging, so a modelling approach coupling atmosphere and glacier surface processes seems like a step forward (Collier et al., 2015). For this approach, the limitation for model application is due to the composition of the debris itself, as observations are limited for debris thickness, thermal conductivity, albedo, and surface roughness (e.g. Nicholson and Benn, 2013; Rounce et al., 2015), and these each need to be represented in a distributed manner.

As the debris thickness exerts principal control over subdebris melt rates, efforts to understand its spatial variability have received the most attention. Spatial variability of debris thickness is a major problem for distributed models, as it is heavily under-sampled (Ragettli et al., 2015). Efforts to map supraglacial debris thickness include *in-situ* physical measurement (e.g. Brock et al., 2010; Kellerer-Pirklbauer et al., 2008; Zhang et al., 2011; Kirkbride and Deline, 2013; Nicholson and Benn, 2013; Mackay et al., 2014; Pratap et al., 2015; Rounce et al., 2015) and scans with ground-penetrating radar (e.g. Gades et al., 2000; Singh et al., 2010; Wu et al., 2013), but may be biased in terms of site selection.

Taking advantage of the distinct thermal signal of debris-covered glaciers as compared to ice-free terrain (e.g. Taschner and Ranzi, 2002; Ranzi et al., 2004), fully-distributed maps of supraglacial debris thickness or thermal resistance have been developed by inverting thermal observations from satellite sensors using an energy-balance or simplified model (e.g. Nakawo and Rana, 1999; Suzuki et al., 2007; Mihalcea et al., 2008; Foster et al., 2012; Fujita and Sakai, 2014; Rounce and McKinney, 2014; Schauwecker et al., 2015). These methods work when calibrated to particular study sites, but are limited by coarse resolution, mixed pixel composition, and calibration requirements (Schauwecker et al., 2015). A similar idea was extended to invert geodetic differences and surface velocities to calculate spatially-distributed effective degree-day factors for Lirung Glacier (Immerzeel et al., 2014a; Ragettli et al., 2015).

The spatial heterogeneity of the debris surface extends beyond debris properties. The hummocky rock mantle of many debris-covered glaciers is interrupted by exposures of bare ice (both ‘ice cliffs’ and ‘ice sails’; e.g. Sakai et al., 1998) and by ponded surface water accumulations in depressions (e.g. Iwata et al., 1980; Sakai et al., 1998; Wessels et al., 2002). The ponds will be discussed in more detail shortly (Section 2.2), but ice cliffs have been

documented to ablate much more rapidly than the surrounding debris-covered surface (e.g. Sakai et al., 1998, 2002; Benn et al., 2001; Thompson et al., 2016). Due to the spatial variability of topography-dependent surface fluxes (Buri et al., 2016b), the features have an orientation-dependent life cycle (Sakai et al., 2002; Benn et al., 2012), but eventually reduce in slope and become progressively reburied by debris (Brun et al., 2016). Progressively more sophisticated models of ice-cliff backwasting have been developed and validated with field measurements for several study sites (Sakai et al., 1998, 2002; Han et al., 2010; Reid and Brock, 2014; Steiner et al., 2015; Buri et al., 2016b).

According to models and observations, ablation from ice cliffs can contribute a considerable portion of a glacier's meltwater production: Sakai et al. (2000) found that ice cliffs of Lirung Glacier accounted for 20% of the glacier's melt in 1996, while Immerzeel et al. (2014a) attributed 24% of observed volume loss to the 8% areal coverage of ponds and cliffs in 2013. Based on an assumption of the average ice-cliff slope and melt rate, Han et al. (2010) attributed a more moderate 7.3% of melt to ice cliffs at the Koxcar Glacier, a similar value to that calculated for Miage Glacier with a more sophisticated model by Reid and Brock (2014). Observations by Juen et al. (2014) for the Koxcar Glacier attributed 7-16% of the debris-covered area's ablation to ice-cliff backwasting, although these features occupied only 1.7% of glacier area. The analysis of Thompson et al. (2016) found that ice cliffs occupied ~5% of the stagnant debris-covered area of Ngozumpa Glacier, but account for 40% of ablation in this zone. Although the distribution of cliffs varies greatly between glaciers, and their melt rates vary based on climate, the overall picture is clear: these features play a significant role in the overall mass balance of debris-covered glaciers. Consequently, although debris surface energy balance models have become increasingly advanced for the point scale (e.g. Reid and Brock, 2010), and may be applied in a distributed manner to estimate subdebris melt (e.g. Reid et al., 2012; Fyffe et al., 2014), they do not yet provide a complete picture of debris-covered glacier ablation, even accounting only for surface changes.

### **Debris sources and dynamics**

The surface debris, itself the defining characteristic of debris-covered glaciers, is also largely responsible for their morphometry: by reducing surface ablation, the formation of a debris layer promotes development of long, low-gradient glacier tongues which typically exhibit low surface velocities approaching the terminus (Anderson and Anderson, 2016). These effects have been observed through natural experiments: large supraglacial landslides have widely been observed to lead to glacial advance by inhibiting surface ablation (e.g. Crandall and Fahnestock, 1965; Hewitt, 2011; Shugar and Clague, 2011; Deline et al., 2015).

The high concentration of debris-covered glaciers in the HKKH is therefore a direct consequence of extreme vertical relief and high erosion rates in the region, which combine to provide concentrated mass and debris inputs to glaciers via avalanching (Scherler et al., 2011a). Prominent headwalls are not necessary for debris-covered glacier development (Anderson and Anderson, 2016), but snow, ice, and rock avalanches are major mechanisms of ice and debris transfer from headwalls to the valley glaciers (Benn et al., 2000; Hambrey et al., 2008; Bolch et al., 2012). Notably, neither the total mass or debris supply by avalanching is particularly well-constrained, yet these two inputs control the long-term evolution of debris-covered glaciers (Scherler et al., 2011a; Rowan et al., 2015; Anderson and Anderson, 2016). Debris may also be supplied from other sources, including alluvial fans (Watanabe et al., 1998), moraine debuitressing (Hugenholtz et al., 2008) and even the subglacial environment (Hambrey et al., 2008). In Bhutan, erosion rates have an aspect dependence due to solar forcing, leading to southwest-facing slopes as a primary control for debris-covered glaciers (Nagai et al., 2013).

Debris supplied below the ELA is deposited directly onto the glacier's surface, but debris falling above the ELA will often have an englacial transport path before emergence below the ELA (e.g. Anderson and Anderson, 2016). Exposure of debris at the surface may be more complicated than simple surface ablation and debris accumulation (as described by, e.g., Swithinbank, 1950). Kirkbride and Deline (2013) identified melt-out of inclined debris septa, such as englacial sedimentary debris bands, as a primary mechanism of englacial-supraglacial debris transfer and surface dispersal. For glaciers with terminus obstructions, this mechanism promotes development of thick debris, as the debris septa are more steeply inclined (Kirkbride and Deline, 2013).

Secondary mechanisms of debris dispersal include fluvial and hillslope mass movement, and rework the debris surface (Kirkbride and Deline, 2013). Importantly, local variations in debris thickness and composition result in spatially-varying effective thermal conductivity, which leads to large differences in glacier ablation over short distances. This differential ablation leads to the development of cones, ridges, and slopes near the angle of repose (e.g. Swithinbank, 1950; Watanabe et al., 1986), and can lead to topographic inversion (Thompson et al., 2016). Differential ablation therefore enhances hillslope processes such as slope creep and rockfall, which further alter local debris thickness and occasionally expose bare ice, and providing feedback to alter the local rate of ablation. The overall picture is of a dynamic debris surface which can exhibit heterogeneous patterns of ablation, composition, and relief.

### Observed thinning and evolution

Due to the long, low-gradient tongue resulting from debris cover (Anderson and Anderson, 2016), debris-covered glaciers undergo a particular evolution in response to climate warming. Firstly, debris-covered glaciers often do not express length changes in response to climate change (Scherler et al., 2011b). However, as the ELA increases the zone of debris emergence expands, and an increase of debris-covered area has been observed for many glaciers in the HKKH since the 1960s (Kirkbride and Deline, 2013; Thakuri et al., 2014; Racoviteanu et al., 2015). Total glacier area, on the other hand, often decreases as larger glaciers fragment and small clean-ice glaciers disappear entirely (Ojha et al., 2016). Glaciers with stable mass balances, including many in the Karakoram, appear to show no change in debris-covered area (Herreid et al., 2015).

Surface thinning is a widespread expression of sustained mass loss for these glaciers, and has been observed through diverse remote sensing methodologies (e.g. Kääb et al., 2012; Nuimura et al., 2012; Gardelle et al., 2013; Immerzeel et al., 2014a; Pellicciotti et al., 2015). This thinning varies regionally across the HKKH, with limited mass loss in the Karakoram but increasing mass losses to the east across the mountain chain (Kääb et al., 2012; Gardelle et al., 2013). Surface thinning has very heterogeneous patterns between glaciers and on a single glacier, but higher thinning rates occur where flow velocities are slow and slopes are low (e.g. Pellicciotti et al., 2015). Thinning rates for debris-covered glaciers appear to be increasing in recent years in some regions (Bolch et al., 2011; Ragettli et al., 2016).

Notably, studies have identified similar or even higher rates of thinning for debris-covered glacier areas than for the debris-free glacier area, both at the regional (Kääb et al., 2012; Gardelle et al., 2013) and individual glacier (Nuimura et al., 2012; Pellicciotti et al., 2015; Ye et al., 2015) scales. The similarity of rates may be due to the elevation bias of debris-covered ice relative to clean ice, as debris-covered glaciers extend to much lower altitudes than clean-ice glaciers (Pratap et al., 2015; Ragettli et al., 2016). Nonetheless, the high rates of thinning do not seem to be in agreement with measured or modelled subdebris ablation, which is heavily reduced under a thick debris cover (Ragettli et al., 2015). Many studies have attributed this apparent discrepancy to mass losses associated with thermokarst features, especially ice cliffs and supraglacial ponds, which may account for a significant portion of the debris-covered area's total mass loss (Basnett et al., 2013; Immerzeel et al., 2014a; Pellicciotti et al., 2015; Thompson et al., 2016). These features commonly occur in low-gradient areas of the glacier, where observed thinning is highest (Nuimura et al., 2012), and appear as areas of pronounced elevation change with high-resolution elevation datasets (Immerzeel et al., 2014a; Thompson et al., 2016).

Another important consideration for thinning in the terminus area is the potential reduced mass supply due to up-glacier thinning. The increased ELA may result in heightened melt rates above the debris-covered area (Rowan et al., 2015; Ragettli et al., 2016). Here, surface gradients may be higher, and glaciers may be thinner (e.g. Anderson and Anderson, 2016), and consequently the enhanced melt eventually leads to a physical disconnect between the bare-ice and debris-covered portions of the glacier (Rowan et al., 2015). Transfer of mass between the separated bodies can occur by serac-fall avalanches, and the newly-fragmented clean-ice glacier may retreat rapidly.

Increased surface ablation also reduces mass fluxes through the debris-covered area, resulting in widespread stagnation in the terminus area (e.g. Kirkbride, 1993; Kirkbride and Warren, 1999; Quincey et al., 2007; Benn et al., 2012; Thompson et al., 2016). Heterogeneous patterns of thinning can occur in this area due to thermokarst features in spite of thick surface debris. If a prominent moraine or other terminus impediment maintains a high hydrological base level, melt may accumulate in the stagnant area, forming surface ponds that coalesce into a base-level lake (see reviews in Benn et al., 2012; Sakai, 2012). Base-level lakes can expand rapidly through freshwater calving (Sakai et al., 2009), leading to rapid terminus retreat (Kirkbride and Warren, 1999; Quincey et al., 2007; Benn et al., 2012).

This transition has been documented in detail at numerous sites, including the Tasman Glacier (Kirkbride, 1993), Imja-Lhotse Shar Glacier (Fujita et al., 2009), Tsho Rolpa (Reynolds, 1999), the Lunana area of Bhutan (Reynolds, 2000), and Ngozumpa Glacier (Benn et al., 2001; Thompson et al., 2012). The expansion of glacial lakes and their effect on glacier retreat has been documented across the HKKH region by many studies (e.g. Ageta et al., 2000; Komori, 2008; Bajracharya and Mool, 2009; Nie et al., 2013; Lutz et al., 2015). Base-level lakes often retain impressive volumes of water (Yao et al., 2012; Fujita et al., 2013), and glacial lake outburst floods (GLOFs) pose considerable hazard for downstream communities (Richardson and Reynolds, 2000). Assessment of GLOF risk (e.g. Meon and Schwahz, 1993; Watanabe et al., 1995; Huggel et al., 2002; Shrestha et al., 2010; Werder et al., 2010; Westoby et al., 2014) and development of mitigation strategies (e.g. Grabs and Hanisch, 1993; Kattelmann, 2003) are ongoing research priorities.

## **2.2 Supraglacial ponds of debris-covered glaciers: a summary**

Considering the framework of debris-covered glacier response to climate change (Figure 2.2), it is useful to distinguish between the surface ponds that occur scattered across the debris-

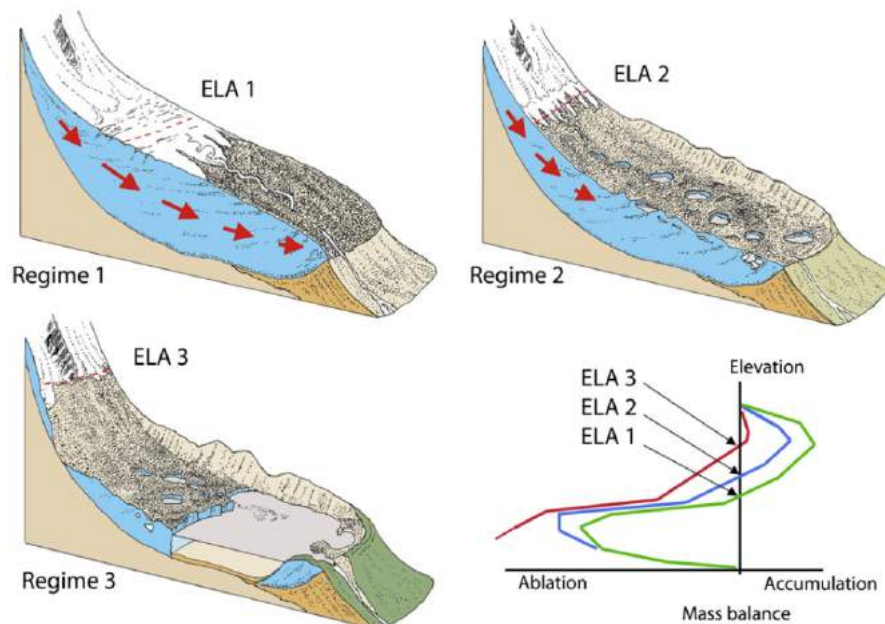


Fig. 2.2 Ponds may be occasional when a debris-covered glacier is in balance with climate, but may become more commonplace as the glacier thins and the debris-covered area expands. Finally, if the base level is reached and a terminal lake forms, the glacier will retreat rapidly. Figure adapted from Benn et al. (2012).

covered surface and the large lakes that occur in the late stage of response, which lead to sudden glacier retreat. A first difference may be made based on size: supraglacial ‘ponds’ are nearly always small, while glacial ‘lakes’ that pose a hazard grow to large extents (Cook and Quincey, 2015). A better distinction between these features is the water level: water features at the base level cannot drain further, and are likely to expand until drainage is possible. Water features which are perched above this level may also expand, but only until connection with an efficient drainage route is reached. Consequently the distinction between ‘perched’ and ‘base-level’ ponds also represents the difference between isolated and hydrologically connected features (Benn et al., 2012). In this context ‘terminal’ lakes specifically refer to base-level lakes in a configuration leading to glacier retreat, while ‘supraglacial’ lakes refers to base-level features away from the terminus, and perhaps at an earlier stage of expansion. The development of base-level supraglacial lakes (e.g. Wessels et al., 2002) is possible for debris-covered glaciers. Terminal and proglacial lakes have received significant treatment in the literature (see review in Carrivick and Tweed, 2013), and this thesis is focused on supraglacial ponds, but the distinction between ‘perched’ and ‘base-level’ ponds is useful for understanding pond behaviour. This section will first describe typical supraglacial ponds and summarise the role that they play in surface ablation, then will consider the role of surface

ponds in the hydrology of debris-covered glaciers, and finally satellite observations of ponds in High Mountain Asia.

### 2.2.1 Pond appearance and dynamic processes

Surface water bodies are well-documented features for clean-ice surfaces, where they form in topographic lows during periods of positive surface temperature by collecting surface runoff, a process that has been successfully modelled to a high degree of spatial and temporal accuracy (e.g. Banwell et al., 2012). While present, they are responsible for locally-enhanced atmospheric and radiative energy absorption and melt driven by natural convection (Luthje and Pedersen, 2006). Such water bodies can grow to large sizes for ice sheets (Liang et al., 2012). The surface water drains either superficially by dam overtopping or breakthrough (Kingslake et al., 2015) or englacially through hydrofracture (e.g. Das et al., 2008). This results in a seasonal evolution of most surface water features, with ponds and lakes increasing in size due to meltwater supply before drainage or freeze-over (McMillan, 2007; Sundal et al., 2009).

The low gradient and dense undulations typical of debris-covered glaciers greatly impede the flow of water, leading to frequent ponding in surface depressions (e.g. Iwata et al., 1980; Benn et al., 2001; Wessels et al., 2002). Although the hydrological system of debris-covered glaciers exhibits strong parallels to that of clean-ice glaciers, the debris surface presents several challenges for a direct analogy (Fyffe et al., 2015). Supraglacial ponds observed on debris-covered glaciers vary in size from several metres to a few hundred metres across and exhibit a variety of shapes (e.g. Watson et al., 2016), while also varying in suspended sediment content (e.g. Wessels et al., 2002; Takeuchi et al., 2012). They are often bordered by extensive ice cliffs (e.g. Sakai et al., 2000; Benn et al., 2001), leading to a variety of appearances for ponded water at the surface of a debris-covered glacier (Figure 2.3). The structure and evolution of individual supraglacial ponds has been assessed in detail by several authors through basic observations, repeat surveys (e.g. Benn et al., 2001; Röhl, 2008; Werder et al., 2010; Watson et al., 2016; Thompson et al., 2016), and numerical modelling (Kääb and Haeberli, 2001; Werder et al., 2010). Understanding of key processes occurring in supraglacial ponds has advanced conceptually to include conduit-collapse formation (e.g. Kirkbride, 1993; Sakai et al., 2000), subaqueous and waterline melting (e.g. Sakai et al., 2000; Röhl, 2006), calving (e.g. Benn et al., 2001; Sakai et al., 2009), and englacial drainage (e.g. Gulley and Benn, 2007).



Fig. 2.3 Typical supraglacial ponds on debris-covered glaciers, exhibiting variable suspended sediment content and size. Note that many ponds are associated with outcrops of bare ice. a) A supraglacial pond on Lirung Glacier showing small icebergs and exfoliation at the ice-cliff. b) A large ( $> 150$  m diameter) circular pond surrounded by ice-cliffs on Langtang Glacier. c) A very large pond on Langtang Glacier which filled and drained over a 10-day period (see Section 3.4.5). d) A small perched pond on Langtang Glacier showing settling of suspended sediments.

### Hydrology of debris-covered glaciers and pond formation

Glacier hydrology is not the focus of this thesis (excellent reviews of various aspects are available, e.g. Fountain and Walder, 1998; Clarke, 2005; Gulley et al., 2009b; Cuffey and Paterson, 2010; Chu, 2014), but a basic summary of glacier hydrology is necessary to understand the supraglacial pond formation process, which is inextricably tied to englacial conduits (Benn et al., 2012). In the standard model of glacier hydrology, there are three primary drainage systems: 1) meltwater can pass over surface through firn aquifers and supraglacial channels, 2) it may route through the interior of the glacier through englacial conduits or voids, and 3) it may reach the bed of glacier to flow to the terminus through channels or a variety of less efficient drainage configurations (e.g. Fountain and Walder, 1998; Gulley et al., 2009b). Each of these systems (surface, englacial, subglacial) stores water over various timescales (Jansson et al., 2003). A variety of models have been developed to represent surface, englacial and subglacial processes (e.g. Jarosch and Gudmundsson,

2012; Werder et al., 2013; Kingslake et al., 2015), and to reproduce the behaviour of the system as a whole (e.g. Flowers and Clarke, 2002). Although many questions remain, current conceptual understanding has been widely substantiated through numerical modelling and field investigations (e.g. Nienow et al., 1998; Gulley et al., 2009b).

The hydrologic system of debris-covered glaciers closely echoes that of clean-ice glaciers: the englacial and subglacial hydrological networks are regulated by the same physics. Above the debris line, the glacier's supraglacial hydrology also follows that of a clean glacier. However, the presence of surface debris alters the lower glacier's surface hydrology in several important ways. Debris represents a much more permeable surface than ice, potentially allowing the formation of shallow groundwater lenses if the surface slope is low; wetted and even saturated debris is commonly encountered at the debris-ice interface (Collier et al., 2014). On the other hand, the high surface slopes common to rugged debris-covered glaciers should encourage rapid downslope transport of meltwater (Benn et al., 2012). From a practical standpoint, debris masks small surface channels and moulins, making dye-tracer experiments difficult to accomplish and leading to a paucity of studies (Hasnain et al., 2001; Pottakkal et al., 2014; Fyffe et al., 2015).

Within this basic framework of glacier hydrology, supraglacial ponds represent one aspect of debris-covered glaciers' surface storage capacity (Watson et al., 2016), where the rugged debris surface routes water into hydrologically-closed surface basins. The debris layer also promotes supraglacial stream formation: investigations by Gulley et al. (2009a) suggested that supraglacial streams will persist wherever incision due to turbulent heat dissipation is greater than surface ablation, and found this condition satisfied on the Khumbu Glacier. These surface channels may then rapidly downgrade and become enclosed as efficient cut-and-closure conduits (e.g. Fountain and Walder, 1998; Gulley, 2009; Jarosch and Gudmundsson, 2012). The dye-tracing study of Fyffe et al. (2015) found that supraglacial streams are more common in areas of shallower debris cover, but tended to be rarer down-glacier in thick debris cover. This essentially agrees with the distribution proposed by Gulley et al. (2009b).

The study of Fyffe et al. (2015) also found that the areas without supraglacial streams had an inefficient connection to the glacier's outlet, resulting in substantial delay in the delivery of meltwater although these zones were in the near-stagnant lowermost portion of the glacier. This is in agreement with Benn et al. (2012), who found that the cumulative downwasting of the debris-covered surface leads to fragmentation of the formerly-efficient superficial streams and englacial conduits. The discontinuous hydrological network that results routes englacial discharge back to the glacier's surface, deactivating some englacial conduits while promoting a rapid feedback of conduit enlargement in other locations (e.g. Gulley and Benn, 2007; Gulley, 2009; Benn et al., 2009).

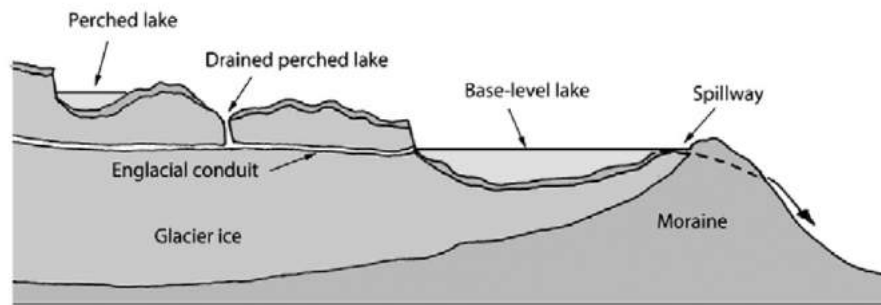


Fig. 2.4 Locations of supraglacial ponds related to the hydrologic base level and englacial conduits. Figure reproduced from Benn et al. (2012).

The englacial melt due to channel incision and migration, combined with low rates of creep closure in stagnant ice, can create large englacial voids and enables structural collapse of weak roofs (Gulley and Benn, 2007). If at a shallow depth within the glacier, such a roof collapse may create a sinkhole-like surface depression (Kirkbride, 1993), leading to common analogy with karst topography and thermokarst processes (e.g. Clayton, 1964; Käab and Haeberli, 2001; Mavlyudov, 2006; Gulley et al., 2009b). As this process of conduit collapse also interrupts the englacial drainage network, it may lead to pond development within the new surface depression (e.g. Benn et al., 2012, Figure 2.5).

Importantly, not all topographically-closed surface depressions are ponded, which suggests a hydrological outlet for those that are not, as the steep topography should rapidly route water down-slope (Gulley and Benn, 2007; Benn et al., 2012). Thus, while ‘perched’ ponds are a consequence of englacial ablation, they also represent a temporary discontinuity between the surface and englacial hydrological networks, forming only in basins that are not efficiently connected to the down-gradient englacial network. This inefficient connection can lead to flooding if the hydrological network routes water into the depression (e.g. Benn et al., 2000, 2001).

### **Pond basin expansion and drainage**

When water is routed into a closed basin flooding ensues, which may then lead to basin expansion and eventual drainage. ‘Perched’ supraglacial ponds are underlain by intact glacier ice with low permeability, suggesting that pond drainage would generally initiate when an efficient connection is established with the englacial system (Benn et al., 2001, 2012; Gulley et al., 2009b), or by a feedback exploiting permeable debris-filled crevasse traces (Gulley and Benn, 2007). Basin expansion is therefore necessary to establish a connection with an englacial outlet (Benn et al., 2012), while the drainage is limited by the position of the connection (Benn et al., 2001).

As an example of basin expansion processes, Benn et al. (2000, 2001) investigated perched ponds in two surface depressions on the Ngozumpa Glacier debris-covered tongue using repeat field surveys between October 1998 and October 2000. At both locations, flooding led to water-level increases (~9 m), exposure and backwasting of marginal ice cliffs, and extensive basin expansion during the flooded period. The flooded debris surface showed minimal change in appearance or topography, suggesting a very low rate of subaqueous subdebris melt. Instead, the pond basins expanded laterally through a combination of subaerial ice cliff backwasting, subaqueous melt at the ice-water interface, and calving (Benn et al., 2000, 2001). These observations have been supported through investigations at other sites (Reynolds, 2000; Röhl, 2006, 2008; Sakai et al., 2009; Thompson et al., 2016).

Subaerial calving has been reported by numerous studies as a particularly rapid growth mechanism for supraglacial ponds (Benn et al., 2001; Diolaiuti et al., 2006; Sakai et al., 2009). This primarily occurs when thermoerosional notches incised at the waterline significantly undercut ice cliffs (Röhl, 2006; Sakai et al., 2009), leading to eventual collapse of the unsupported ice. Such thermo-erosional notches have been commonly observed at supraglacial ponds' bare-ice margins, and are generally attributed to enhanced waterline melting driven by warm currents at the water surface (e.g. Kirkbride and Warren, 1997; Benn et al., 2001; Diolaiuti et al., 2006; Röhl, 2006). A principal driver of such currents is wind, and therefore the pond basin's depression depth and the pond's wind fetch may be important controls, as they describe a pond's exposure to the glacier surface boundary layer (Sakai et al., 2009; Sakai, 2012). Notch development leading to calving and rapid basin expansion is likely to occur for large ponds, where 1) the pond fetch is sufficient to drive strong water circulation (Sakai et al., 2009) and 2) water temperatures are likely to be much higher (Röhl, 2008). For smaller ponds, the thermal regime is less important, and pond circulation and melt is largely driven by natural convection, a kinetic regime leading to lower rates of subaqueous ablation distributed more evenly at the vertical ice surface (Xin et al., 2011).

The subaerial backwasting of marginal ice cliffs accounts for dramatic topographic change in the vicinity of a pond (e.g. Immerzeel et al., 2014b; Thompson et al., 2016), but does not directly enable pond drainage, as this change occurs above the waterline and therefore cannot connect the pond to an englacial conduit. Instead, this backwasting leads to the remobilisation of debris into the pond depression (Thompson et al., 2016) to produce new debris mounds, displace water, and further reduce pond-bottom melt rates. If the subaerial backwasting rate exceeds the subaqueous melt rate, debris remobilisation leads to a disconnect between the ice cliff and pond, and the basin expansion may slow or stop altogether (Thompson et al., 2016).

The overall picture from the literature is that most 'perched' ponds expand rapidly until drainage is achieved, whereas 'base-level' ponds cannot achieve drainage through basin

expansion and continue to expand until they coalesce and form a lake (Röhl, 2008; Benn et al., 2012). Finally, it is important to note that pond drainage advects significant energy to the glacier's interior, leading to enhanced englacial ablation along flowpaths, and promoting the formation of further surface depressions through conduit collapse. Thus, the formation and drainage of supraglacial ponds provides a feedback of accelerated downwasting for debris-covered glaciers, in spite of reduced rates of surface ablation due to superficial debris (e.g. Benn et al., 2012).

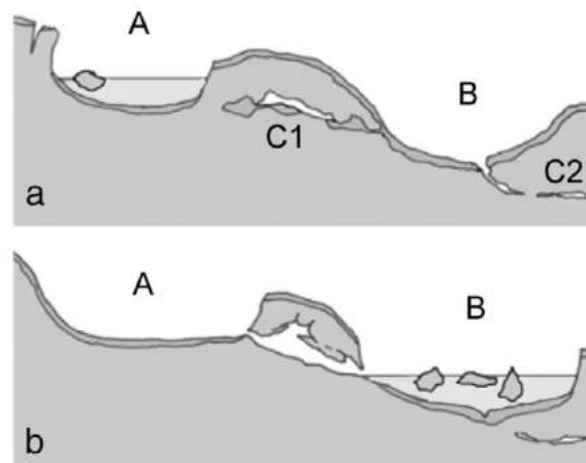


Fig. 2.5 Perched pond drainage is hypothesised to cause down-glacier conduit collapse and potential blockage, forming a new pond. Figure reproduced from Benn et al. (2012).

### 2.2.2 Modelling efforts

Compared to the debris surface, water is a much more efficient medium for atmospheric and radiative energy absorption and transfer to the glacier (Sakai et al., 2000; Xin et al., 2011), motivating quantitative assessments of the ablation attributable to ponds. However, due to the complex processes controlling supraglacial pond growth and drainage, numerical modelling efforts have focused on representation of individual energy fluxes. Only the study of Sakai et al. (2000) has attempted a full energy and mass balance for supraglacial ponds. Here, a summary is provided for each of the principal energy exchanges important for supraglacial ponds.

The surface energy balance of supraglacial ponds on Lirung Glacier in Nepal was modelled by Sakai et al. (2000) using a basic representation of all major fluxes of energy based on observations from a nearby meteorological station. An empirical relationship of albedo and solar elevation, developed at Tsho Rolpa by Yamada (1998), was used to represent pond albedo, which varied from  $\alpha=0.08-0.12$ . Due to the high turbidity of supraglacial ponds,

shortwave radiation was assumed to be absorbed at the pond surface. The study assumed a uniform flux of downwelling longwave radiation across the debris surface. Bulk aerodynamic formulae were used to calculate the sensible and latent heat fluxes, and the study neglected heat inputs due to rainfall and rockfall (Sakai et al., 2000). The surface energy balance was thus calculated for several ponds encompassing much of the monsoon, producing an average energy input of  $\sim 170 \text{ W m}^{-2}$ , although the study acknowledged uncertainties up to  $40 \text{ W m}^{-2}$ .

Other studies have assessed individual components of the pond surface energy balance, but no other study seems to have conducted the full calculation. Based on studies at Ngozumpa Glacier, Benn et al. (2001) report that ponds have low albedo ( $\alpha \sim 0.07$ ) and present shortwave and longwave radiation budgets for a pond surface, but did not assess turbulent fluxes at the ponds. The study of Röhl (2008) had equipped ponds on Tasman Glacier with thermistor strings, but could not assess surface energy exchange as no local meteorological records were available. At the Koxcar Glacier, Xin et al. (2011) had the necessary meteorological data to derive surface energy exchanges, but focused on water temperature at depth. The lack of studies is problematic, as the surface energy exchange provides energy to the pond system to enable all pond-related ablation processes. Sakai et al. (2000) suggested that, overall, supraglacial ponds absorb energy at a rate about 7 times greater than subdebris ablation.

Subaqueous subdebris ablation has received slightly more scientific attention. Sakai et al. (2000) assumed that convection in the saturated debris layer was negligible based on the fine particles commonly encountered in the subaqueous debris, for which they assumed a very low permeability. They thus used a basic conduction model with the thermal conductivity of permafrost. Röhl (2008) used the same method, but with a thermal conductivity between that of rock and water based on an assumption of 50% porosity of the debris layer. For a conduction approach, the subaqueous debris thickness must be known, and both studies used a value from nearby subaerial debris. Regardless, subdebris melt estimated by this method was very low ( $0.15 \text{ m a}^{-1}$  estimated by Röhl, 2008), producing the topographic self-similarity before and after a pond's flood and drainage (Benn et al., 2001).

Melt at subaqueous bare-ice surfaces, however, occurs at much higher rates (Sakai et al., 2000; Röhl, 2008). Sakai et al. (2000) adapted an equation developed for iceberg melt rates (Weeks and Campbell, 1973) to the freshwater situation in ponds. The equation, originally developed for fully turbulent flow over a flat plate, requires specification of the flow speed across the flat surface. Sakai et al. (2000), being unable to measure this rate, assumed a velocity of  $< 0.02 \text{ m s}^{-1}$ . Röhl (2008) adapted an empirical equation (also developed for icebergs; Russell-Head, 1980), based on water temperature but not accounting for water currents. Given the dependence on site-specific conditions, subaqueous melt rates vary

greatly. Röhl (2008) reports an annual-average subaqueous melt rate of  $4.7 \text{ m a}^{-1}$  given conditions on the Tasman Glacier (mean hourly rate of  $0.054 \text{ cm h}^{-1}$ ), while Benn et al. (2001) made hourly observations of  $0.7\text{-}2.7 \text{ cm h}^{-1}$  on Ngozumpa Glacier.

As described by Xin et al. (2011), supraglacial ponds exhibit two distinct kinetic regimes for internal mixing: wind-driven surface currents, and natural convection. Within this framework, the approach of Sakai et al. (2000) is appropriate for the first regime, but it is unclear where the equation used by Röhl (2008) falls, as it is based on empirical measurements from a variety of scenarios. A third relevant approach, applied by Luthje and Pedersen (2006) to supraglacial lakes on the Greenland Ice Sheet, used an idealised parametrisation for natural convection in a turbulent layer (Linden, 2002). Unfortunately, it is not clear if the distinct system geometries would necessitate modification to this equation: lakes on Greenland may be thought of as horizontal tapering lenses with all heat transfer occurring vertically, while ponds on debris-covered glaciers are more like disc-shaped wedges with heat transfer to bare ice only at the margins (Sakai et al., 2000; Kääh and Haerberli, 2001).

When the wind-driven kinetic regime is dominant, subaqueous melt rates can be very high due to the advection of warm surface water to the ice face (e.g. Röhl, 2006), and this leads to subaerial calving (e.g. Diolaiuti et al., 2006). Benn et al. (2001) found that waterline melt rates were generally 2.9 times the subaerial melt rates, and frequently observed calving events. As this type of calving is the consequence of enhanced subaqueous melting, however, it is difficult to model directly. Instead, the rate of thermoerosional notch growth may be the best predictor for this scenario (Röhl, 2006). Sakai et al. (2009) modelled near-surface air currents and water-surface currents for varying lake lengths and temperatures, and found that subaqueous melt exceeds subaerial melt if the fetch is  $> 20 \text{ m}$  and the water temperature is  $2\text{-}4^\circ\text{C}$ , while calving most likely begins when fetch is  $> 80 \text{ m}$ . When calving does occur, basin expansion rates can be  $20\text{-}50 \text{ m a}^{-1}$  (Röhl, 2008).

In addition to the marginal energy exchanges, Sakai et al. (2000) modelled the stored energy within the pond, using water temperature observations and a simple cylinder geometry, representing a major simplification in geometry and thermal structure. Studies of pond internal temperatures suggest high spatial and temporal heterogeneity based on the kinetic regime and pond bathymetry (e.g. Röhl, 2008; Xin et al., 2011). However, this enabled Sakai et al. (2000) to close the energy and mass budgets (albeit with some uncertainty) by assuming that any inflows of water advect negligible energy, and to assess the energy discharged englacially. Their results suggest that the majority of energy absorbed by the pond surface is delivered englacially.

Given the uncertainties and assumptions involved in these modelling efforts, it is little surprise that few studies have assessed the ablation contribution of supraglacial ponds. The analysis of Sakai et al. (2000) suggested that although ponds accounted for only 0.43% of Lirung Glacier's debris-covered area, they absorbed 3.4% of the total energy required for the glacier's ablation. At the Tasman Glacier, supraglacial ponds accounted for 4% of all ice loss in the terminus area, including loss at the terminus lake (Röhl, 2008). Thompson et al. (2016) found that internal ablation accounted for 9% of the mass loss at Ngozumpa Glacier, but this value is difficult to compare as it includes internal ablation due to meltwater runoff not routed through ponds, while it does not include pond-proximal ablation.

### 2.2.3 Pond distributions and controls

The role of ponds for any given glacier is limited by their prevalence, and relatively few studies have assessed the spatial or temporal distribution of ponds (Watson et al., 2016). Several studies have used satellite data to determine pond distributions at a single point in time (Wessels et al., 2002; Panday et al., 2012; Salerno et al., 2012) or their variability across several years or decades (Röhl, 2008; Gardelle et al., 2011; Liu et al., 2015; Watson et al., 2016), but notably not assessing seasonal variability. Ponds seem to take up about 0.5% of the debris-covered area of many glaciers (Sakai et al., 2000; Juen et al., 2014), although this seems to vary greatly between glaciers and over time as the glacier's surface evolves (Watson et al., 2016).

Ponds have been mapped using field surveys (e.g. Sakai et al., 2000; Benn et al., 2001), manipulation of multispectral imagery (e.g. Wessels et al., 2002; Gardelle et al., 2011; Liu et al., 2015), and manual delineation of satellite imagery (e.g. Salerno et al., 2012; Thompson et al., 2016; Watson et al., 2016). The results of Watson et al. (2016) suggest that medium-resolution satellite imagery may induce significant errors in pond identification, but the authors also note that frequent repeat visits made possible by these satellite archives (Landsat, ASTER) are presently the only method of routinely observing temporal changes. Consequently, the high interannual (Liu et al., 2015) and potentially seasonal (Watson et al., 2016) variability of pond cover makes measurement of long-term changes difficult. However, some studies suggest that climate change may be increasing coverage of supraglacial ponds throughout the HKKH (e.g. Gardelle et al., 2011), as for debris-covered glaciers in other parts of the world (e.g. Röhl, 2008).

Some studies have instead focused on the controls of the spatial distribution of ponds, which may be useful to identify zones of 'base-level' lake formation (e.g. Reynolds, 2000; Quincey et al., 2007). Studies have identified glacier slope, velocity, and thinning as controls on supraglacial pond formation and persistence (Benn et al., 2001; Quincey et al., 2007;

Sakai and Fujita, 2010; Salerno et al., 2012) as these influence the surface's intersection with englacial conduits and crevasses (Gulley et al., 2009b). The work of Quincey et al. (2007), building on Reynolds (2000), emphasised the influence of glacier surface gradient and velocity. They suggested that significant glacier velocities ( $> 7.5 \text{ m a}^{-1}$ ) led to the opportunity for the reorganisation of drainage conduits, promoting efficient drainage and limiting lake development. Areas with moderate surface gradient ( $> 2^\circ$ ), on the other hand, discourage the accumulation of water at the surface. Stagnant or near-stagnant ice ( $< 7.5 \text{ m a}^{-1}$ ) with a low surface gradient ( $< 2^\circ$ ), they concluded, were the conditions most conducive to supraglacial lake development. Perched ponds have also been observed outside this zone, even on moderately steep glacier tongues of up to  $9^\circ$  (Emmer et al., 2015), but these features are not likely to persist long.

Both terminus stagnation and low gradients are typical characteristics of debris-covered glaciers (Scherler et al., 2011b; Anderson and Anderson, 2016), but these conditions are enhanced as the glacier surface downwastes in response to sustained climate warming. Consequently, Sakai and Fujita (2010) proposed a measure of this cumulative downwasting, the difference between glacier and moraine altitudes or 'DGM', as an indicator of the likelihood of supraglacial pond coalescence and terminal lake formation. Thus, as cumulative downwasting progresses, ponds forming in the low-gradient terminus areas are more likely to encounter the hydrological base level, coalesce, and form a large glacier lake (Sakai and Fujita, 2010). Unfortunately, debuttressed moraines are constantly eroding (Thompson et al., 2016), confusing measurement of DGM, and a critical value of DGM may depend on each glacier's in-balance thickness. Most importantly for this thesis topic, there is no indication that cumulative downwasting will increase surface ponding until the base level is reached.

## **2.3 Key objectives relating to supraglacial ponds**

The state of understanding of supraglacial ponds has advanced considerably in recent years, but many gaps still remain. Key objectives for this thesis are grouped into two categories: pond observations and pond-associated ablation.

### **2.3.1 Pond observations**

Studies have demonstrated that the supraglacial ponded area changes from year to year (Gardelle et al., 2011; Liu et al., 2015; Watson et al., 2016), which is related to glacier thinning in response to climate warming (Sakai and Fujita, 2010; Benn et al., 2012) and to seasonal meteorology (Liu et al., 2015). Pond filling and drainage is linked to the supply and

timing of rain and meltwater from snow or glacial sources (Benn et al., 2001; Liu et al., 2015), the supraglacial routing of that water, and the opening or collapse of englacial conduits and voids (Gulley et al., 2009b; Benn et al., 2012). In many respects, therefore, the controls on the spatial and temporal distribution of ponds on debris-covered glaciers are similar to those of lakes on clean-ice valley glaciers (Boon and Sharp, 2003) and the Greenland ice sheet (Selmes et al., 2011; Chu, 2014). Understanding the controls on pond filling and draining is important from a mass-balance perspective: pond-associated melt enhancement, which occurs for both clean-ice (Tedesco et al., 2012) and debris-covered (Sakai et al., 2000) glaciers, is possible when ponds are thawed and before they drain, but no observation of the seasonal pattern and magnitude of pond formation and drainage has yet been made.

Controls on the spatial distribution of ponds have been postulated, including surface gradient, mass balance, cumulative surface lowering, and surface velocity (Reynolds, 2000; Quincey et al., 2007; Sakai and Fujita, 2010; Sakai, 2012; Salerno et al., 2012). Several studies have used satellite data to determine pond distributions at a single point in time (Panday et al., 2012; Salerno et al., 2012) or their variability across several years or decades (Gardelle et al., 2011; Liu et al., 2015). However, no attempt has been made to document the seasonal and interannual variability of ponds, even though individual ponds have been observed to fill and drain periodically (Benn et al., 2001; Immerzeel et al., 2014a; Liu et al., 2015) and are known to freeze over winter. For this reason, previous studies may be biased in their assessment of pond cover by not considering the seasonal or year-to-year variability.

There is need for a study focused on spatial and temporal distributions of supraglacial ponds to:

- determine representative pond distributions for a set of glaciers
- improve understanding of pond seasonal variability
- numerically validate the suggested controls of pond spatial distributions
- assess the frequency of pond recurrence and the duration of pond persistence
- make an unbiased assessment of changes in interannual pond density

### **2.3.2 Pond-associated ablation**

Although the insulating effect of thick debris is known to reduce ablation (e.g. Ostrem, 1959; Ragetti et al., 2015), the impact of surface ponds and their associated ice cliffs on the ablation process is much less understood (Nakawo and Rana, 1999; Sakai et al., 2000; Benn et al., 2001, 2012; Röhl, 2006). Supraglacial ponds and ice cliffs are thought to play

a key role in the ablation of debris-covered glaciers (Benn et al., 2012; Immerzeel et al., 2014a; Pellicciotti et al., 2015; Steiner et al., 2015; Buri et al., 2016b; Thompson et al., 2016). Understanding of key processes occurring in supraglacial ponds has advanced conceptually to include conduit-collapse formation (Kirkbride, 1993; Sakai et al., 2000), subaqueous and waterline melting (Sakai et al., 2000; Röhl, 2006), calving (Benn et al., 2001; Sakai et al., 2009), and englacial filling and drainage (Gulley and Benn, 2007). Most process observations have been made on individual features (Benn et al., 2001; Röhl, 2008; Xin et al., 2011).

However, few studies have attempted to quantify the energy exchanges associated with supraglacial ponds, or their effects on glacier ablation. Xin et al. (2011) identified two kinetic types of melt: (1) winds may force currents to drive thermo-erosion and notch development near the lake surface and (2) free convection, due to the density/temperature relationship of water, may drive pond circulation and therefore promote melt along the entire water/ice interface. Sakai et al. (2000) and Röhl (2008) each adapted empirical relationships from iceberg melt observations to examine subaqueous and waterline melting of ice cliffs, while Luthje and Pedersen (2006) adapted a method based on free convection to study basal melting of ponds on the Greenland ice sheet. To date, no effort has been made to compare these algorithms or to apply a melt model based on physical principles to supraglacial ponds on debris-covered glaciers. Perhaps more importantly, the ablation effect of such ponds at the glacier scale is reported for few locations, where it is poorly constrained (Sakai et al., 2000; Röhl, 2008).

Based on the current understanding of pond-related processes and associated mass loss, research is needed to:

- revisit the Sakai et al. (2000) modelling approach with modern instrumentation and numerical modelling approaches
- compare the subaqueous melt modelled using the Sakai et al. (2000); Röhl (2008); Luthje and Pedersen (2006) models and investigate a free-convection algorithm
- assess the surface and subaqueous energy balances of several ponds
- determine the total surface energy balance of all ponds across several glaciers to determine their influence ablation at the glacier scale

## 2.4 Site Description: Langtang Valley, Nepal

The Langtang Valley was selected as a study site based on accessibility, environmental data availability, potential for collaboration, and its heritage of previous scientific studies. Located

60 km north of Kathmandu and just three days' walk from a roadhead, Langtang Valley is exceptionally accessible for a glacierised catchment in the HKKH (Figure 1). The upper Langtang basin borders the Tibetan Autonomous Republic, China to the north and measures 350 km<sup>2</sup> (Figure 2.6a and b). Elevation ranges from 3650 m.a.s.l. at Langtang village to 7234 m.a.s.l. at the peak of Langtang Lirung; they are located only 4.5 km apart, highlighting the extremely steep topography in the basin. The basin has a mean slope of 23° as calculated from a 90 m DEM.

Local climate is primarily influenced by the South Asian monsoon, with the majority of precipitation occurring concurrently with the warmest temperatures, from mid-June to September (Immerzeel et al., 2011). This period also contains the highest daily maximum and minimum temperatures experienced at the site, and consequently the highest rates of ablation occur during these months (Ragetti et al., 2015). Occasional precipitation events occur in the post-monsoon (October to November) and in the much colder winter (December to February). The pre-monsoon (March to mid-June) is characterised by rising temperatures, which are responsible for melting much of the annual snowpack deposited during the post-monsoon and winter months; occasional precipitation events also occur during the pre-monsoon (Collier and Immerzeel, 2015). The rugged topography drives spatial meteorological variability through relief, illumination, and wind channelisation.

Air temperature has been thoroughly studied throughout Langtang Valley, both through *in-situ* observation (Immerzeel et al., 2014b; Heynen et al., 2016) and numerical modelling of atmospheric dynamics (Collier and Immerzeel, 2015), with seasonal lapse rates established over a 3-year record (Heynen et al., 2016). On-glacier lapse rates for debris-covered glaciers are often much steeper than for non-glacier terrain (Brock et al., 2010; Shaw et al., 2016; Steiner and Pellicciotti, 2016), and a network of temperature-loggers was installed on Lirung Glacier to monitor temperature across the glacier, which identified local and general seasonal temperature lapse rates along the debris surface (Steiner and Pellicciotti, 2016).

28% of the glacier area in Langtang Valley is mantled by heterogeneous rock debris, primarily covering the tongues of five valley glaciers (Figure 2.6a). The debris-covered glacier tongues are characterised by extremely variable surface topography, with large depressions occasionally filled by ponds or punctuated abruptly by bare-ice cliffs. The debris mantle varies in thickness from 0.1 to at least 2.5 m (Ragetti et al., 2015), composed of grains ranging in size from sand to large boulders. Lirung Glacier has been the site of numerous field studies of supraglacial ponds (Sakai et al., 2000; Bhatt et al., 2007; Takeuchi et al., 2012; Miles et al., 2016) in spite of its small size and advanced decay (Immerzeel et al., 2014a). The much larger Langtang, Langshisa, and Shalbachum Glaciers have strongly

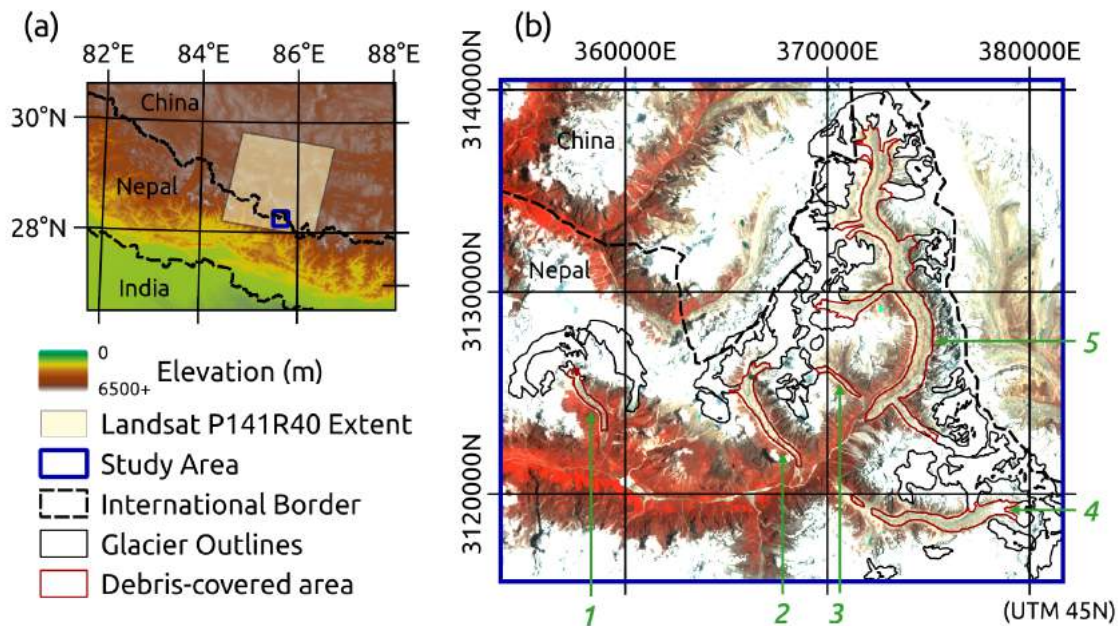


Fig. 2.6 (a) Geographic context of the study area. (b) The study area, showing the upper Langtang basin's principal debris-covered glaciers: 1-Lirung, 2-Shalbachum, 3-Langshisa, 4-Ghanna, 5-Langtang. Backdrop is 6S-corrected Landsat TM false-colour composite from 16 June 2009.

negative surface mass balances and show significant supraglacial ponded areas (Pellicciotti et al., 2015).

The five study glaciers sharply differ in size, debris cover and hypsometry. In terms of size, they range from 1.3 km<sup>2</sup> (Ghanna) to 52.8 km<sup>2</sup> (Langtang), with debris mantling 22-40% of total glacier area. The glaciers also vary in their altitudinal extents, with terminus elevations ranging from 4025 m.a.s.l. (Lirung) to 4718 m.a.s.l. (Ghanna). All five glaciers are rapidly losing mass in response to climate change. Ghanna Glacier is retreating from its terminal moraines, with Lirung and Langshisa Glaciers also retreating to a lesser degree, while Shalbachum and Langtang are downwasting with a nearly stable terminus (Ragettli et al., 2016). Field observations have noted the pronounced disconnect between the debris-covered tongue and clean-ice upper portion for Lirung Glacier, a process which has recently been noted for Shalbachum Glacier as well. Langshisa and Langtang Glacier have both lost connectivity with minor tributaries since the 1970s (Pellicciotti et al., 2015; Ragettli et al., 2016).

Of the five glaciers, Lirung Glacier has received the most scientific attention. The glacier is the most accessible in the valley, and its relatively small debris-covered area (1.03 km<sup>2</sup>) enables a thorough analysis of changes across the glacier's surface. Consequently, fieldwork

has been conducted sporadically at Lirung Glacier for several decades, including repeat surveys (Aoki and Asahi, 1998; Immerzeel et al., 2014a), and investigation of phenomena such as ice cliffs (Sakai et al., 1998, 2002; Steiner et al., 2015; Buri et al., 2016b) and supraglacial ponds (Sakai et al., 2000; Takeuchi et al., 2012).



Fig. 2.7 A view of the debris-covered surface of the terminus area of Lirung Glacier. Ice cliffs, hummocky terrain, and the outwash plain and proglacial lake are typical features for debris-covered glaciers, as is the vegetation growing on less dynamically-active parts of the debris surface.

The glacier's recent retreat in response to climate change has been documented by these studies. Downwasting led to development of a terminal lake in the 1990s which has a naturally-incised outlet and poses minimal hazard. The glacier's terminus quickly retreated from contact with this lake and continues to retreat at a more gradual rate (Ragettli et al., 2016). More recently, the debris-covered tongue disconnected from its source icefalls, and the icefall termini have experienced pronounced retreat in recent years.

Over the past several years, an extensive set of glaciological and meteorological observations has been collected at Lirung Glacier and its surroundings (e.g. Immerzeel et al., 2014b; Shea et al., 2015b; Steiner et al., 2015; Kraaijenbrink et al., 2016; Steiner and Pellicciotti, 2016). These datasets provide an excellent glaciological context for the study of pond-related processes at this site.

## **Chapter 3**

# **Spatial and temporal variability of supraglacial ponds in the Langtang Valley**

### **3.1 Executive Summary**

Supraglacial ponds play a key role in transferring atmospheric energy to the ice of debris-covered glaciers, partially overcoming the ablation-reducing effects of debris cover, but the spatial and temporal distribution of these features is largely unknown, so their overall effect is poorly constrained. 172 Landsat TM/ETM+ scenes are analysed covering the period 1999-2013 to identify thawed supraglacial ponds for the debris-covered tongues of five glaciers in the Langtang Valley of Nepal. I apply an advanced atmospheric correction routine (LandCor/6S) and improve upon previous band-ratio and image morphological techniques to identify ponds, then characterise their spatial, seasonal, and interannual patterns of ponding. Pond cover exhibits high variability between glaciers (May-October means of 0.06-1.69% of debris-covered glacier area), with ponds most frequent in zones of low surface gradient and velocity. The ponds show a pronounced seasonality, appearing rapidly in the pre-monsoon as snow melts, peaking in cover in the monsoon at ~2% of debris-covered area, then declining in the post-monsoon as ponds drain or freeze. Ponds at the study site are highly recurrent and persistent, with 40.5% of pond locations apparent in multiple years. For the whole investigation period, Langtang Glacier shows an increase in April-October total pond cover, while all glaciers show a decline in August-October pond cover for 2009-2013.

## 3.2 Specific Objectives

Characterising the spatial and temporal variability of pond distributions, particularly within the annual melt cycle, is important for improving understanding of the hydrology and ablation processes of debris-covered glaciers, and is the objective for this study. I utilise all available Landsat imagery for the period 1999-2013 to identify thawed supraglacial ponds, in order to consider the spatial, seasonal, and annual patterns of ponds for debris-covered glacier tongues in the Langtang Valley of the Nepalese Central Himalaya. I apply this database of identified ponds to:

1. Measure the density of supraglacial ponding for five glaciers with differing characteristics, and evaluate the dependency of pond density on those glaciers' characteristics.
2. Evaluate the controls that surface gradient and glacier velocity in particular exert on pond occurrence.
3. Document the seasonal cycle of pond thawing and formation followed by freezing and draining.
4. Document pond persistence, recurrence, and evolution over the 15-year period.
5. Determine if surface ponding has increased over time for the study glaciers.

## 3.3 Methods

A thorough pond identification workflow is applied to identify ponds in each Landsat scene. The differences in pond density between glaciers are then assessed with a suite of glacier morphometric characteristics; these characteristics are also used to assess the precise positions of ponds.

### 3.3.1 Identification of ponds

The determination of ponded water from Landsat data required a sophisticated workflow, with the basic steps depicted in Figure 3.1a. An advanced atmospheric transfer code was applied to bring the scenes into close radiometric agreement (Figure 3.1b), then masks for clouds, shadows, and snow/ice were applied to reduce misidentification of ponds (Figure 3.1c). Finally, a set of image morphological operations was developed based on band metrics to classify water objects (Figure 3.1d), which were clipped to the debris-covered glacier area (Figure 3.1e).

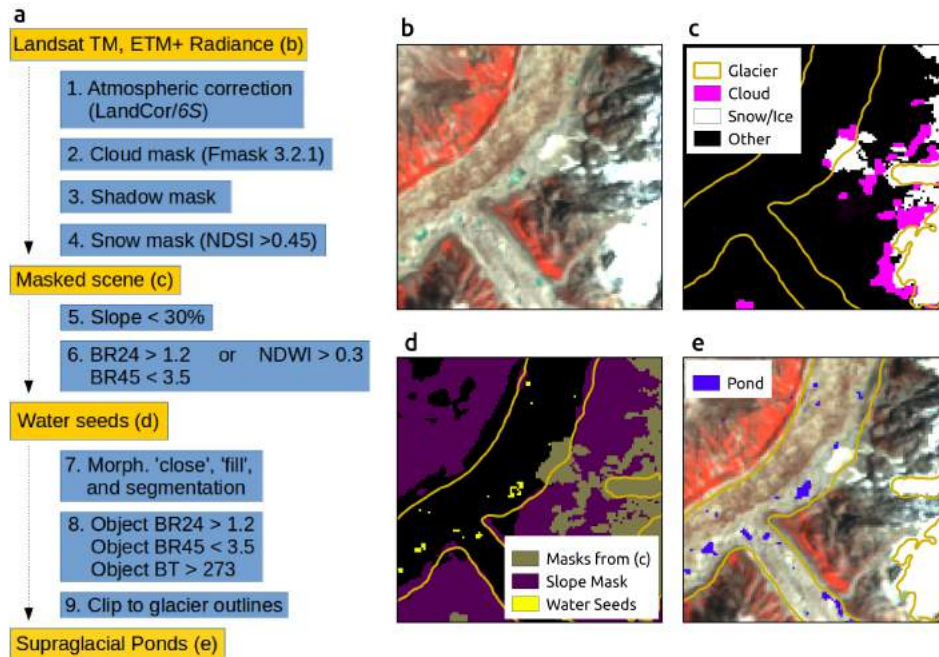


Fig. 3.1 (a) Processing workflow for supraglacial pond classification, with intermediate steps shown in insets (b)-(e). (b) Subset of Landsat TM false-colour composite for 19 August 2009 after LandCor/6S processing. (c) Cloud, snow/ice, and shadow (not shown) masks determined by subroutines. (d) Slope mask and determination of high-probability water seeds. (e) Pond cover output after image morphological operations and reclassification.

#### Data: Landsat TM/ETM+

To examine many relatively small lakes for an extended period, the spatial resolution and temporal frequency of observations must be balanced. Due to their 30 m spatial resolution, long history of repeat visits, and free availability, the Landsat 5 (TM sensor) and 7 (ETM+ sensor) satellites offered the most promise to resolve seasonal and annual patterns of supraglacial ponds. Spectral coverage is nearly identical for the TM and ETM+ sensors (Chander et al., 2009), although the ETM+ sensor also performs broadband panchromatic observations at 15 m ground resolution. All available TM and ETM+ observations for WRS-2 path 141, row 40 within the period 1999-2013 were retrieved from the USGS. Landsat 5 and 7 have a return-period of 16 days, but the sensors are unable to penetrate clouds so data availability for the study site is lower. 198 scenes were identified for processing, although 26 scenes were later removed due to heavy cloud cover obscuring more than 50% of the basin's debris-covered glacier area. The scenes were cropped to the extent of the Langtang valley. The temporal distribution of processed scenes is displayed in Figure 3.2, showing the reduced number of observations during the monsoon due to cloud cover.

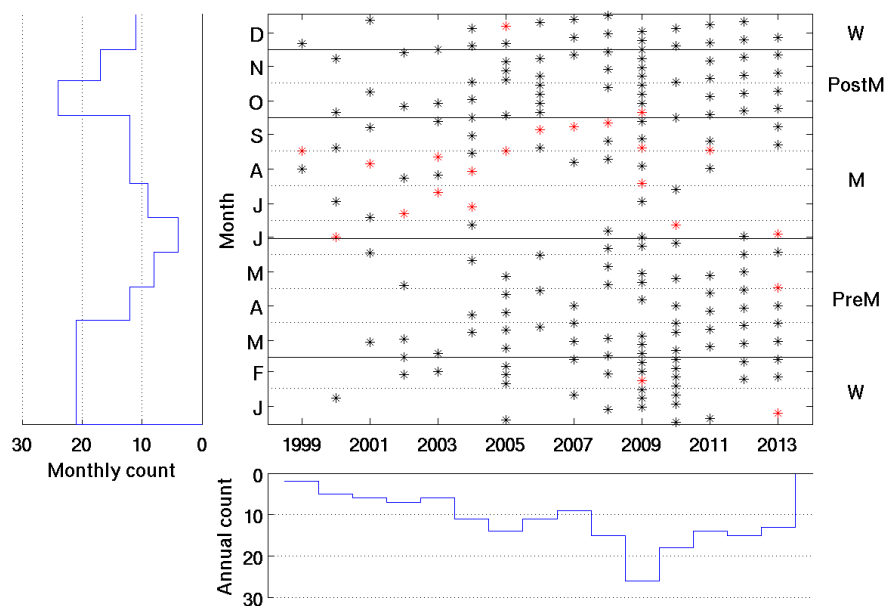


Fig. 3.2 Temporal distribution of scenes processed in the study, with histograms indicating monthly (left) and annual (bottom) counts of observations. Red marks are those scenes with < 50% observable debris-covered area, which were removed from the analysis (26 removed from 198 scenes processed).

Several ancillary datasets were used to analyse and interpret the Landsat data. The hole-filled CGIAR SRTM-CSI 4.1 digital elevation model (SRTM DEM), based on data collected in 2000 and gridded at 90 m resolution (Jarvis et al., 2008), was bilinearly resampled to the Landsat 30 m resolution to describe topography at the study site. The extents of the main glaciers and their debris-covered areas were mapped for 1999 by Pellicciotti et al. (2015). For the present study, these outlines were supplemented by an outline for the smaller Ghanna Glacier based on the same 1999 scene. Glacier surface velocities were provided by Amaury Dehecq; these were derived for 1999-2013 using the Landsat ETM+ panchromatic band to produce annual velocity and error estimates, following the cross-correlation methodology of Dehecq et al. (2015): all available images are preprocessed with principal component analysis and image gradient calculation for feature enhancement, then after cross-correlation image-pairs are fused through a spatio-temporal median filter to produce a robust estimate of surface velocity. These glacier surface velocity measurements were filtered for error, removing pixels with error  $> 7.5 \text{ m a}^{-1}$ .

### Atmospheric correction

Previous efforts to map supraglacial ponds (Gardelle et al., 2011; Xin et al., 2011; Salerno et al., 2012) selected ideal scenes with very clear atmospheric conditions and minimal snow cover to obtain snapshots of pond cover for a few time periods. These studies mapped lakes using manual thresholds of band metrics based on sensor digital numbers or top-of-atmosphere reflectance values, an approach that is straightforward and justified for a few ideal scenes, but inappropriate for a larger number of scenes when atmospheric conditions are variable. In order to take into account all potential pond observations, a robust and semi-automated method was required to bring the range of scenes into radiometric agreement, enabling accurate detection of pond cover changes by accounting for differences in sun-scene-sensor geometry and atmospheric conditions (Chander et al., 2009).

The radiative transfer code 6S (Kotchenova et al., 2006; Kotchenova and Vermote, 2007) has been widely used to correct for atmospheric and geometric differences between datasets (e.g. Burns and Nolin, 2014), but is computationally taxing for an entire scene because it runs on a pixel-by-pixel basis and requires substantial data preparation.

Instead, the version 4.0 LandCor code (<http://www.eci.ox.ac.uk/research/ecodynamics/landcor/>) was applied to the 198 Landsat scenes selected for processing (Step 1 in Figure 3.1a). This code utilises metadata supplied with the raw Landsat data, including fundamental sensor characteristics (e.g. spacecraft identity, swath width, ground resolution, band spectral information) and scene-specific values, to define the illumination characteristics (e.g. scene-centre geographic coordinates, solar position, date and time) across the scene. Supplied with an atmospheric specification, Landcor develops representative lookup tables which are processed with 6S and inverted to distribute corrected top-of-atmosphere reflectance values across the entire scene (Zelazowski et al., 2011).

6S requires specification of an aerosol type and three principal atmospheric constituents aerosol optical depth (AOD), total water vapour (TWV), and ozone ( $O_3$ ). The predefined 6S ‘biomass-burning’-type of aerosol was selected to describe the particle-size distribution at the study site. For AOD and TWV, I used the findings of a previous LandCor project, which uses a topography-dependent background constituent specification and determines constituent anomalies from the scene’s characteristics via an inverse approach (Zelazowski et al., 2011). The value for  $O_3$  was interpolated from a daily 1-degree LEDAPS (Masek et al., 2012) dataset developed from Total Ozone Mapping Spectrometer (TOMS) measurements spanning 1978-2011, with missing values interpolated from monthly averages computed for 2000-2011.

With the full atmospheric composition and illumination geometry described for the entire scene, LandCor routines were used to: 1) prepare representative lookup tables spanning

the multidimensional space of geometry, atmospheric conditions, and top-of-atmosphere spectral reflectance values; 2) run 6S for the representative cases; and 3) invert the 6S results to produce a coverage of ‘corrected’ reflectance values for each band, equivalent to a band-specific albedo. These corrected reflectance values were used for all subsequent calculations (example in Figure 3.1b).

### Cloud, shadow, and snow masks

The Landsat data analysed included several scenes that were affected by cloud cover, deep shadows (Chen et al., 2013), and seasonal snow cover, all of which required masking. Fmask version 3.2.1 (Zhu et al., 2015) was applied to detect clouds spanning several spectral classes semi-automatically (Step 2 in Figure 3.1a).

At sites with very steep terrain, persistent shadows can be problematic for automated classification routines based on thresholding (Chen et al., 2013). For this study, I detected shadows in the scene based on the Fmask results, 6S-corrected Band1 and Band5 reflectances, and terrain slope. The Fmask algorithm consistently classified all terrain-cast shadows as either cloud shadows or clear water. I trimmed these two data categories to the areas satisfying  $B1 < 0.2$  and  $B5 < 0.2$ , then performed morphological fill and close operations on connected pixel groups (more than 20 pixels) to create potential shadow coverages. As terrain-cast shadows cover areas of high-slope (at least exceeding the solar elevation angle), each connected group of pixels was evaluated based on slope values within the coverage. If more than 20% percent of the group’s pixels exceeded a 30% slope, the group was considered a shadow and removed from the potential area for pond identification. (Step 3 in Figure 3.1a). Shadows identified in this manner occupied up to 15% of the study area’s debris-covered glaciers in Dec-Jan, but 0.6% of this area from May-October on average. Conversely, cloud effects were minimal for winter months, but affected 9.2% of the debris-covered glacier area during the May-October period.

Finally, pond surfaces may be obscured by snow for part of the scene. Consequently, the determination of snow cover was a critical step for interpreting the pond distribution maps. The close inter-scene radiometric agreement of 6S-corrected reflectances enabled a uniform threshold of the normalised difference snow index ( $NDSI = \frac{B2-B5}{B2+B5}$ ) to be applied. Based on the cumulative NDSI histogram of all scenes, pixels were classified as snow and ice where  $NDSI > 0.45$  (Step 4 in Figure 3.1a).

### Pond classification

Prior efforts to identify supraglacial ponds on debris-covered glaciers have used band metrics (Huggel et al., 2002; Wessels et al., 2002; Gardelle et al., 2011; Chen et al., 2013) or image morphological operations (Panday et al., 2012; Liu et al., 2013, 2015), while studies of debris-covered glaciers in general also use values of thermal band derived brightness temperature (BT) to classify glacier facies (Mihalcea et al., 2008). This study applies a set of image morphological operations with previously used metrics to identify potential water bodies, then evaluates and classifies them based on these metrics. The spectral metrics used are the Normalised Water Difference Index ( $NDWI = \frac{B1-B4}{B1+B4}$ ), the green-to-near-infrared ratio ( $BR24 = \frac{B2}{B4}$ ), and the near-to-middle-infrared ratio ( $BR45 = \frac{B4}{B5}$ ).

The NDWI and BR24 metrics largely contain the same spectral reflectance information, as both are dependent on at-sensor reflectance in the green (0.52-0.60  $\mu\text{m}$  for Landsat TM) and near-infrared (0.76-0.90  $\mu\text{m}$ ) wavelengths. For consistency with prior approaches (Wessels et al., 2002; Gardelle et al., 2011), both metrics are used, although computationally  $NDWI = \frac{BR24-1}{BR24+1}$ . However, BR24 is only used in conjunction with BR45, while a more restrictive NDWI threshold is used by itself, targeting slightly different groups of pixels. The metrics are used to identify and evaluate objects that may be ponds.

Ponds are known to form only in areas of low surface gradient ( $< 10^\circ$ ), but studies differ in the critical slope threshold to apply to a DEM to determine the area of a debris-covered glacier conducive to ponding (Reynolds, 2000; Quincey et al., 2007; Gardelle et al., 2011; Sakai, 2012; Chen et al., 2013). Due to the coarse spatial resolution of the SRTM DEM and the high topographic variability of the study area's debris-covered glaciers, which is especially pronounced locally in the proximity of supraglacial ponds, I do not use a slope filter to restrict potential pond areas (Figure 1b, Step 5 in Figure 3.1a). I instead use a higher surface slope threshold of 30% to eliminate continuously-steep avalanche fans or icefalls from the debris-covered area eligible to form ponds.

Using the 6S-corrected reflectance values, pond seeds were identified as locations that met the slope threshold as well as  $NDWI > 0.3$ , or the slope threshold and both  $BR24 > 1.2$  and  $BR45 < 3.5$ , following an approach similar to Gardelle et al. (2011). The thresholds were chosen based on investigations into the spectral characteristics of easily recognisable proglacial lakes at the study site, which were often misclassified using the thresholds identified in Wessels et al. (2002) for ASTER data. These high-likelihood pond seeds were morphologically closed (sequential binary dilation and erosion) using a 2-pixel disk, then morphologically filled, to identify connected regions of high pond likelihood. The closing and filling operations connected adjacent areas of high pond probability, which occurred in the larger sediment-laden water bodies and spectrally variable areas of melting snow near the

firm line, but not for the small isolated ponds. Connected groups of pixels were then classified based on the mean metric values for each connected body (same BR24, BR45, and NDWI thresholds as before, and additionally  $BT > 273\text{ K}$ ), eliminating most debris-marginal zones and creating a coverage of thawed water bodies (Figure 3.1e).

Finally, the 1999 glacier coverage of Pellicciotti et al. (2015) was supplemented with the outline of Ghanna Glacier, then trimmed to define the debris-covered area of the basin's glaciers. The full set of classified scenes was used to determine the glacier area that was snow-free for at least 50% of the monsoon observations (between June and August, which exhibits the annual minimum of snow cover). This debris-covered area then defined the area of analysis for supraglacial ponds over the study period. Although the glaciers are undergoing rapid thinning, the areal change of the debris-covered portion has been less than  $0.1\% \text{ a}^{-1}$  in recent years, with the exception of Ghanna Glacier, which is losing area at  $0.4\% \text{ a}^{-1}$  (Ragettli et al., 2016). Therefore, the debris-covered glacier area is treated as fixed for the purposes of this study.

## Uncertainty

The pond classification results presented below contain several potential sources of uncertainty that are difficult to quantify. First, although the 6S radiative transfer code improves the inter-scene radiometric consistency, it relies on extrapolated and modelled atmospheric conditions and is unlikely to result in exact comparability of scenes. Second, the separation of cloud, shadow, snow, and open water relies on several manually-chosen thresholds, resulting in potential misclassification of individual pixels and pond objects. Third, to distinguish between frozen and thawed pond objects, the method utilises brightness temperature data that are of lower spatial resolution than the visible imagery (all data is provided at 30 m resolution, but thermal data is collected at 120 m for TM and 60 m for ETM+) and they are not adjusted by 6S. As ponds occur at smaller scales than these data, this method is likely to increase subpixel and adjacency effects (Gardelle et al., 2011; Salerno et al., 2012; Liu et al., 2015). Finally, most pond identification approaches have difficulty with the high turbidity and variable chemical characteristics of the supraglacial ponds on debris-covered glaciers (Bhatt et al., 2007). These four factors likely lead to errors of commission for features spectrally similar to ponds, omission for ponds that are too small to be resolved by the sensors or are heavily sediment-laden, and mixed edge effects due to the 30 m resolution of the source data.

To roughly bound these errors, I first take advantage of the log-linear size-distributions of ponds (as observed by Liu et al., 2013) to estimate scene-specific uncertainty. For a lower bound of pond cover, I determine the percent cover only for ponds that are at least four pixels in size, comparable to the values reported by Liu et al. (2015). For the upper bound, I fit the

glacier-specific size-distributions for each scene to a power function (Equation 3.1), where  $N$  is the number of ponds in the size class centred at  $S_p$ , and  $b$  and  $\beta$  are the fitted coefficient and exponent. Assuming the ponds are roughly circular, the area  $A$  in each size class may be estimated from Equation 3.3. This is integrated between the minimum observable pond size ( $S_{p,min}$ , 30 m) and the smallest potential pond size ( $S_{p,0}$ , 0 m) to estimate the area of unobserved small ponds,  $A_{miss}$  (Equation 3.4), which reduces to Equation 3.6 since  $S_{p,lim} \gg S_0$ .

A further assessment of pond identification accuracy was conducted with two Cartosat-1 panchromatic orthoimages (2.5 m resolution) available for October 2006 and November 2009 and processed by Ragetti et al. (2016). Each of these occurs in close temporal proximity ( $< 10$  days) to a cloud-free or mostly cloud-free Landsat ETM+ scene, enabling a comparison of the 30 m and 2.5 m pond observations. Pond identification error was analyzed in a 3.3 km<sup>2</sup> area near the terminus of Langtang Glacier, where thawed ponds were easily recognisable in the high-resolution orthoimages. Ponds were manually digitised from the orthophotos, and the resulting coverage of ponds was compared to the Landsat pond locations to assess errors of commission and omission. The Cartosat-1 stereo-pairs were georectified by Silvan Ragetti. The manual pond delineation was carried out by Jakob Steiner and validated by Pascal Buri, both according to my instructions but without reference to the Landsat results.

$$N(S_p) = bS_p^\beta \quad (3.1)$$

$$A(S_p) = (bS_p^\beta) \left( \pi \left( \frac{S_p}{2} \right)^2 \right) = \frac{\pi b}{4} S_p^{\beta+2} \quad (3.2)$$

$$A(S_p) = \frac{\pi b}{4} S_p^{\beta+2} \quad (3.3)$$

$$A_{miss} = \int_{S_p=S_{p,0}}^{S_{p,lim}} A(S_p) \quad (3.4)$$

$$A_{miss}(S_{p,lim}) = \frac{\pi b}{4(\beta+1)} S_p^{\beta+3} \Big|_{S_{p,0}}^{S_{p,lim}} \quad (3.5)$$

$$A_{miss} \approx \frac{\pi b}{4(\beta+1)} (S_{p,lim})^{\beta+3} \quad (3.6)$$

Table 3.1 Comparison of morphometric and dynamic characteristics and pond observations for the five debris-covered glaciers in the study area. Elevation values correspond to the debris-covered area of the glaciers. AAR is the accumulation area ratio, while DRAA is the portion of debris-cover below the ELA. Width and DGM (elevation difference between glacier surface and moraine peaks) values are derived from profiles near the glacier terminus. Surface gradient and velocity values are the mean over the debris-covered area. Pond cover is reported as a percent of the debris-covered area, and calculated as the mean value for May to October for all years.  $R^2$  and  $p$ -values are derived from a linear fit between the variable and pond cover.

	Area (km <sup>2</sup> )		Elevation (m.a.s.l.)		Descriptive Ratios (%)		Width (m)	DGM (m)	Slope (°)	Velocity (m a <sup>-1</sup> )	Pond Cover (%)
	Glacier	Debris	Min	Mean	AAR	DRAA					
$R^2$	[0.93]	[0.86]	[0.01]	[0.10]	[0.01]	[0.56]	[0.85]	[0.04]	[0.77]	[0.26]	[ - ]
$p$ -value	[0.008]	[0.022]	[0.87]	[0.61]	[0.86]	[0.15]	[0.025]	[0.75]	[0.051]	[0.38]	[ - ]
Lirung	6.1	1.2	4025	4287	52%	50%	590	65	10.2	1.5	0.57
Shalbachum	11.7	2.8	4218	4607	15%	53%	430	30	7.1	5.5	0.73
Langshisa	21.7	4.4	4526	4884	49%	40%	760	125	4.9	9.0	0.88
Ghanna	1.3	0.6	4718	4879	52%	70%	295	32	9.5	0.9	0.06
Langtang	52.8	17.8	4468	4944	55%	45%	970	50	3.1	4.9	1.69
Total	93.7	26.8									1.40

### 3.3.2 Glacier characteristics

To help interpret the pond distributions, ten descriptive metrics were evaluated for the debris-covered area of each glacier, which are summarised in Table 3.1.

First, the total area and debris-covered area for the study glaciers is considered, as larger glaciers have potential to grow larger and more numerous ponds, and because size may control the total supply of water. Larger glaciers may also be more complex in terms of hydrologic routing, with a greater likelihood of a discontinuous englacial drainage system as englacial conduits are exposed to intersect the surface due to sustained differential surface ablation. The debris-covered area and total glacier area are computed directly from the glacier outlines. The elevation of the debris-covered tongues may be important as it controls air temperatures and surface mass balance, so minimum and maximum elevations are determined for each study glacier based on the SRTM DEM (third and fourth).

The fifth and sixth metrics describe the distribution of the glacier and debris area relative to climatic forcing. The accumulation area ratio (AAR) is a widely-used metric that describes the portion of glacier area above or below the equilibrium line altitude (ELA) at which zero mass balance is expected. Based on the results of prior studies in Langtang Valley (Sugiyama et al., 2013; Ragettli et al., 2015), I use an ELA of 5400 m. I then determine a ratio describing the portion of glacier area covered by debris below the ELA, the debris ratio in the ablation area (DRAA). Both ratios range from 0 to 100%.

Seventh, I evaluate glacier width, which may limit the size to which ponds can grow, and therefore the extent to which ponds may be observable. Eighth, I determine the cumulative downwasting of the glacier surface (DGM, the elevation difference between glacier surface and moraine peaks as defined by Sakai and Fujita, 2010), which demonstrates the state of response to climate warming of each glacier, and could be a factor if thinning leads to a change in pond cover. Glacier width and DGM are determined as the average based on 5 transects in the lowest third of the debris-covered area, where moraines are most clearly identifiable. DGM approximates the cumulative surface lowering since the Little Ice Age, when the glacier surface was at least as high as present-day lateral moraines. It is difficult to measure due to narrow moraine peaks, coarse elevation data, and topographic variability of the debris-covered glacier surface (Sakai and Fujita, 2010). I use the minimum transect elevation for the glacier surface and the dominant outermost lateral moraine peak elevation to estimate DGM. Each profile therefore produces two estimates (one for each lateral moraine), except in cases where the lateral moraine is not separable from the valley's larger geologic structure (i.e. elevation increases monotonically outwards).

For the ninth metric, I calculate the mean surface gradient of the debris-covered areas, as surface gradient has been identified as a control on surface runoff and pond formation (Reynolds, 2000; Quincey et al., 2007; Salerno et al., 2012). The gradient of a debris-covered glacier surface is difficult to assess due to the high surface topographic variability, so I estimated surface gradient with the SRTM DEM by adapting the approach of Quincey et al. (2007), but automating and iterating their approach for adaptability to glacier tributaries and to better capture changes in surface gradient. First, the lowest elevation of the glacier was identified from the DEM as a starting point. Next, the glacier was divided into segments based on 100 m elevation bands, and the longitudinal gradient calculation of Quincey et al. (2007) was performed from each segment's lowest point. To reduce dependence on the elevation step, the procedure was repeated for 200, 300, 400, and 500 m elevation bands. Finally, the median value for each pixel was determined for the different gradient estimates, producing a composite map of longitudinal surface gradients approximating the glacier's active slope.

Last, I calculate the mean surface velocity for the debris-covered area of each glacier (tenth metric). A glacier's internal ice dynamics control the connectivity of surface and englacial conduits through the opening of crevasses and closure of conduit entrances (Gulley and Benn, 2007). Mean surface velocity is a coarse indicator of the breadth of processes associated with ice creep, but may indicate whether any structural reorganisation occurs, or if the study glaciers are effectively stagnant. High velocities would suggest a very dynamically-active glacier, with zones of crevasse formation inhibiting pond formation (Quincey et al.,

2007; Salerno et al., 2012). Conversely, very low velocities may inhibit pond formation by disabling the reorganisation and closure of internal conduits, or encourage pond formation by reducing the likelihood of drainage.

### 3.3.3 Analysis of pond controls

To determine the roles that surface velocity and gradient play in controlling supraglacial pond formation, all individual pond locations were evaluated with respect to the categorisation adapted by Quincey et al. (2007) from the work of Reynolds (2000). Quincey et al. (2007) segmented debris-covered glacier area into four categories based on local surface gradient and velocity to understand the likelihood of pond formation: A) area with very low surface gradient ( $< 2^\circ$ ) and very low velocity ( $< 7.5 \text{ m a}^{-1}$ ); B) area with very low surface gradient and higher velocity ( $\geq 7.5 \text{ m a}^{-1}$ ); C) area with higher surface gradient ( $\geq 2^\circ$ ) and very low velocity; and D) area with higher surface gradient and higher velocity. I therefore classified each observed pond based on the local glacier velocity and surface gradient. Then, to take into account the debris-covered area in each category, I determined the total debris-covered area, pond area, and pond count for each glacier and category.

## 3.4 Results and Discussion

### 3.4.1 Summary of pond observations for the basin

The spatial pattern of observed ponds is shown for the study glaciers in Figure 3.4. Dark spots indicate distinct pond features that occurred in a large portion of the observations, while light smudges show areas that were occasionally covered by ponds. Langtang Glacier has the greatest ponded surface area and the features with the highest frequency of occurrence. Although some false-positive identification occurred, primarily near snow-debris transitions, my algorithm also reliably identified proglacial lakes not included in the analysis (ellipses in Figure 3.4).

Considering all the study glaciers and years together, ponds cover an average of 1.40% of the basin's debris-covered area (0.39% of the total area of the glaciers with some debris cover) between May and October (Table 3.1). A total of 7138 ponds were observed over the period of record for all scenes and glaciers combined, with the majority and highest density occurring on Langtang Glacier. The pond size distributions show a roughly linear trend on a log-log scale for both individual glaciers and the valley as a whole (Figure 3.3), and the mean observed pond size was  $0.0037 \text{ km}^2$  (4.1 pixels). Most ponds were very small (5525 ponds

with 4 pixels or fewer), but these ponds account for only 31% of the total ponded area over the study period.

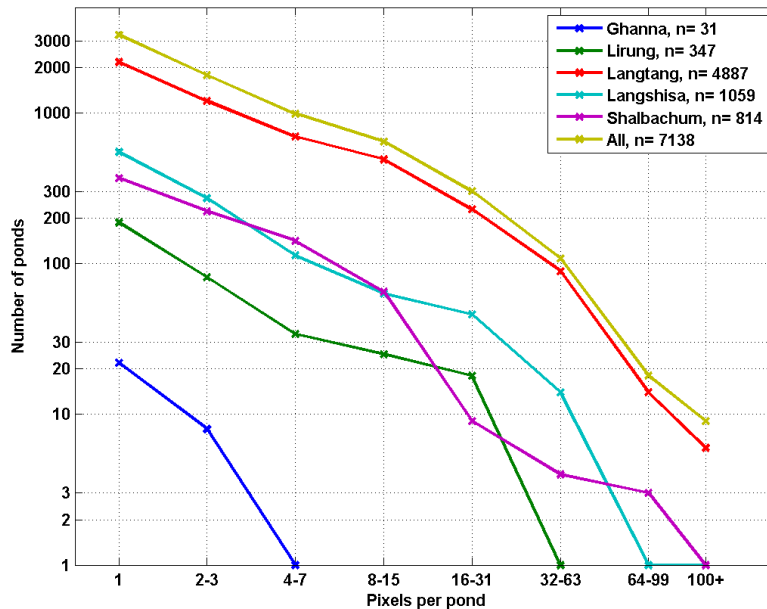


Fig. 3.3 Log-log size distribution of observed supraglacial ponds for each glacier.

The general results are in agreement with previous observations of supraglacial pond density for debris-covered glaciers. Using Landsat data, Gardelle et al. (2011) observed supraglacial ponds covering about 0.4% of glacier area for the Khumbu basin of Nepal, but only 0.05% for basins in the Karakoram of Pakistan, during September-October. Salerno et al. (2012), also studying the Khumbu basin, reported ponds covering 0.3% to 2% of total glacier area for individual glaciers, determined using the 10 m resolution AVNIR-2 sensor during October 2008. In contrast to these findings, that study observed a normal distribution of pond sizes. Liu et al. (2015), considering only ponds greater than 4 Landsat pixels to minimise identification error, reported supraglacial ponds covering between 0.18% (1990) and 0.38% (2005) of debris-covered glacier area for their study basin in the Tian Shan of Central Asia. That study found an average pond size of  $0.01 \text{ km}^2$ , which is almost exactly the value I produce ( $0.011 \text{ km}^2$ , 12.4 pixels) when considering ponds of at least 4 pixels. Limiting the dataset to these larger ponds, ponds cover 0.97% of Langtang Valley's debris-covered area between May and October (0.30% of total glacier area), in very close agreement with the results of Liu et al. (2015) for a very different setting.

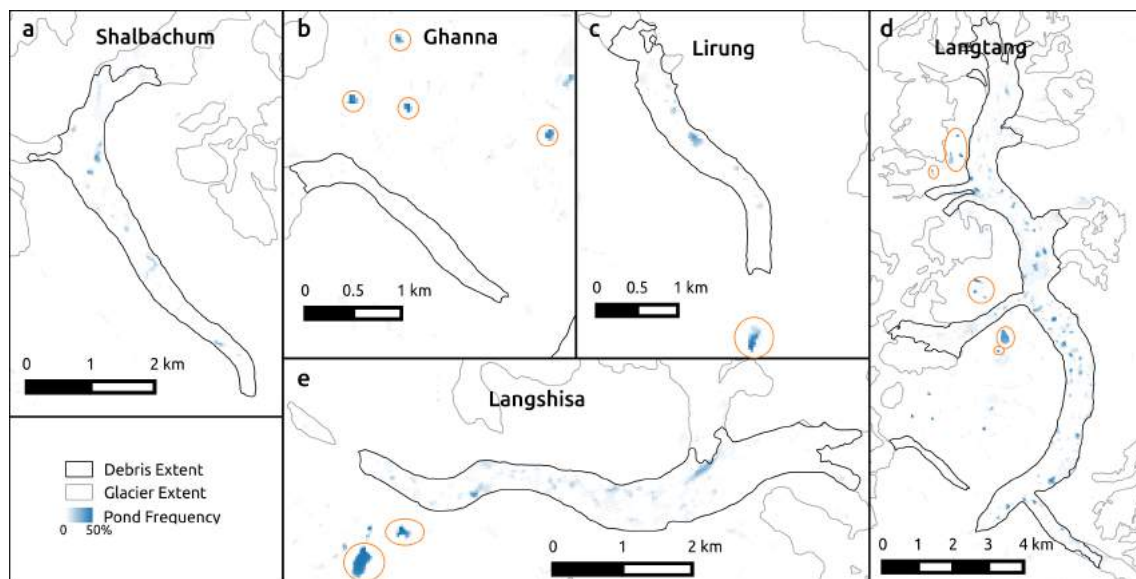


Fig. 3.4 Spatial distribution of supraglacial ponds as percent of May-October observations ( $n=68$ ), also showing results for proglacial lakes outside the debris-covered tongues (orange ellipses), 1999 to 2013.

### 3.4.2 Uncertainty

Applying the statistical approach to uncertainty assessment, the size distribution suggests an overall potential commission error of 31% by area, although individual scenes varied between 0% (i.e. no small ponds were observed) and 100% (i.e. all observed ponds were smaller than 4 pixels). Estimating the omitted pond area by extrapolating and integrating scene-specific pond size distributions, I find an overall omission of less than 1% of pond area. However, this assessment requires that ponds are discretised in 30 m squares, and subpixel and boundary inaccuracies are likely to be larger than 1% (Salerno et al., 2012). Consequently, the study conveys low confidence in pond identification for small features and for individual scenes, but higher confidence for larger features and for distributions of pond frequency, which highlight locations of regular pond observation.

This statistical result was further substantiated by the comparison of available high-resolution imagery with the Landsat results (Figure 3.5, Table 3.2). The pond-identification algorithm struggles to identify small ponds of  $< 900 \text{ m}^2$  visible in the orthoimage (44% of features, but 7% of pond area). The algorithm performs well for ponds greater in area than 1 pixel ( $900 \text{ m}^2$ ), in agreement with the error assessment of Salerno et al. (2012), but overestimates the area of these features by 30-50%, largely due to resolution effects. The algorithm occasionally misidentified features as thawed ponds (16% of Landsat features, 2.1% of observed area): these were recognisable as exposed ice cliffs or frozen pond surfaces in

Table 3.2 Landsat ETM+ and Cartosat-1 pond observations for a 3.03 km<sup>2</sup> area of Langtang Glacier (Figure 3.5). Ponds observed in the Cartosat-1 images but obscured by SLC-error stripes are omitted. Pond sizes are reported for ponds common to both images (Observed) and for ponds not identified by the Landsat routines (Missed). Pond density for the area of comparison falls into the overall range observed by Landsat for October-November (Figure 3.8).

Date	Sensor	<i>N</i> ponds	Ponded area (m <sup>2</sup> )	Mean pond size (m <sup>2</sup> )		Pond Density
				Observed	Missed	
6 Oct 2006	Landsat ETM+	16	100,088	5,125	–	3.03%
15 Oct 2006	Cartosat-1	53	60,910	3,425	182	1.85%
30 Oct 2009	Landsat ETM+	14	58,610	3,907	–	1.78%
9 Nov 2009	Cartosat-1	17	41,752	2,982	286	1.27%

Table 3.3 Landsat commission and omission rates of pond features and size for each scene comparison, and the overall error in pond area for each scene.

Date	Pond features		Pond size		Overall
	Commission	Omission	Commission	Omission	
Oct 2006	+25.0%	-69.8%	+49.6%	-11.7%	+39.1%
Nov 2009	+7.1%	-17.6%	+31.0%	-2.0%	+28.8%
Mean:	+16.1%	-43.7%	+40.3%	-6.8%	+34.0%

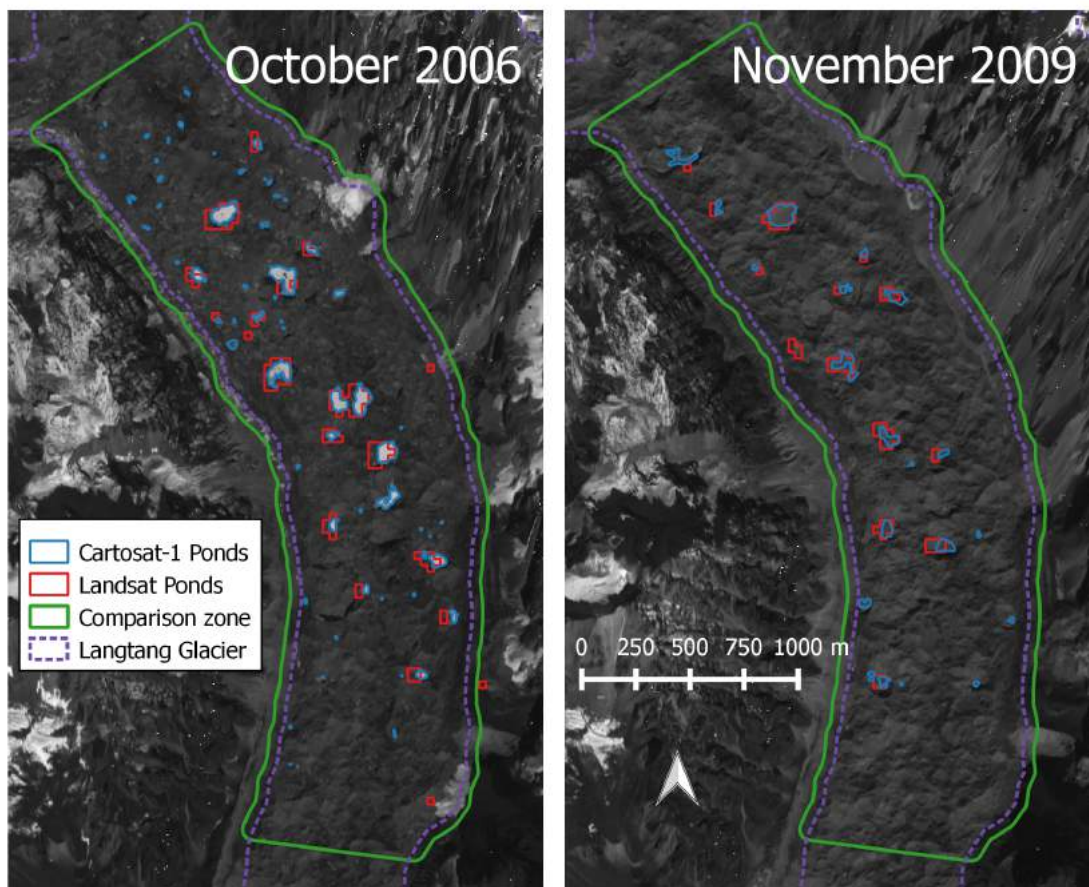


Fig. 3.5 Comparison of features identified by Landsat ETM+ and Cartosat-1 for October 2006 and November 2009, showing strong agreement between the datasets. Landsat misses small ponds and occasionally misidentifies pond features. The 30 m resolution is the dominant source of error for the Landsat routine.

the orthoimages. The combined effects of small pond omission, occasional pond commission, and large-feature overestimation led to a combined error of 35% of pond area for the zone of comparison (Table 3.3). However, given the limited comparison to high-resolution data, it is unclear how transferable these error values are to the rest of the time series as both scenes available for comparison fall in the post-monsoon.

### 3.4.3 Glacier characteristics and pond cover

The debris-covered areas of the study glaciers show significant variability in pond cover, ranging from 0.08% (Ghanna) to 1.69% (Langtang) of the debris-covered area during May-October (Table 3.1). The study glaciers exhibit a wide range of geometric and dynamic conditions. Glaciers in the Langtang Valley range in total area from 1.3 km<sup>2</sup> to 52.8 km<sup>2</sup>,

while the debris-covered portion of the glaciers ranges in size from 0.6 km<sup>2</sup> (Ghanna) to 17.8 km<sup>2</sup> (Langtang). Only Shalbachum and Lirung Glaciers extend below 4400 m.a.s.l., while only Lirung Glacier has a mean elevation for the debris-covered area below 4600 m.a.s.l. The glaciers smallest by area also have the smallest moraine-to-moraine widths (295 m to 970 m). The glaciers have downwasted to different degrees, with mean DGM measurements for the glaciers ranging from 30 m for Shalbachum Glacier to 125 m for Langshisa Glacier.

The study glaciers' debris-covered areas all have mean surface gradients below 10°, a threshold identified by Reynolds (2000) as being conducive to the formation of dispersed ponds. Only Langtang and Langshisa Glaciers exhibit a mean surface gradient below 6°, but none of the glaciers has an average surface gradient below 2°. Langshisa, Shalbachum, and Langtang have the highest mean surface velocities (7.9, 5.3, and 4.8 m a<sup>-1</sup>, respectively), while Ghanna and Lirung have very low average values, suggesting that portions of their debris-covered tongue are nearly stagnant.

Of the ten glacier characteristics tested at the whole-glacier scale, mean pond cover (% debris area) exhibited the strongest linear correlations to glacier area ( $R^2 = 0.93$ ,  $p < 0.01$ ), debris area ( $R^2 = 0.86$ ,  $p < 0.05$ ), width ( $R^2 = 0.85$ ,  $p < 0.05$ ), and mean slope (inverse relationship,  $R^2 = 0.75$ ,  $p < 0.1$ ). A moderate non-significant correlation was detected for DRAA ( $R^2 = 0.56$ ,  $p > 0.1$ ), and a weak correlation existed for mean velocity ( $R^2 = 0.26$ ,  $p > 0.1$ ). Little relationship was evident for glacier minimum or mean elevation, AAR, or DGM ( $R^2 < 0.1$ ). For the study glaciers, pond cover is greater for the larger glaciers, those with low surface gradient, and those with a larger portion of debris-free terrain below the ELA. These relationships are tentative results based on a small sample size that should be tested with a larger set of glaciers across the region and in other regions to better constrain controls on supraglacial ponding.

Reynolds (2000) proposed a basic classification of glaciers based on their surface gradient. Glaciers with gradients in the range 2-6° are expected to experience widespread dispersed ponding, with those in the range 6-10° expected to exhibit isolated small ponds. These categories fit the study glaciers fairly well, with Langshisa (0.88% pond cover) and Langtang (1.69%) in the first category, and Ghanna (0.06%) clearly in the second category. In contrast to the categories of Reynolds (2000), Lirung and Shalbachum have high mean surface gradients (10.2° and 7.1°) and exhibit significant pond cover (0.57% and 0.73%). For both of these glaciers, the standard deviation of velocity over the debris-covered area is nearly equal to the mean, suggesting a relatively strong decay down-glacier, and potentially a zone of compression where conduits and crevasses are forced closed.

If progressive thinning increases pond density as the glacier surface approaches the base level, as may be expected immediately prior to formation of a terminal lake (Benn et al.,

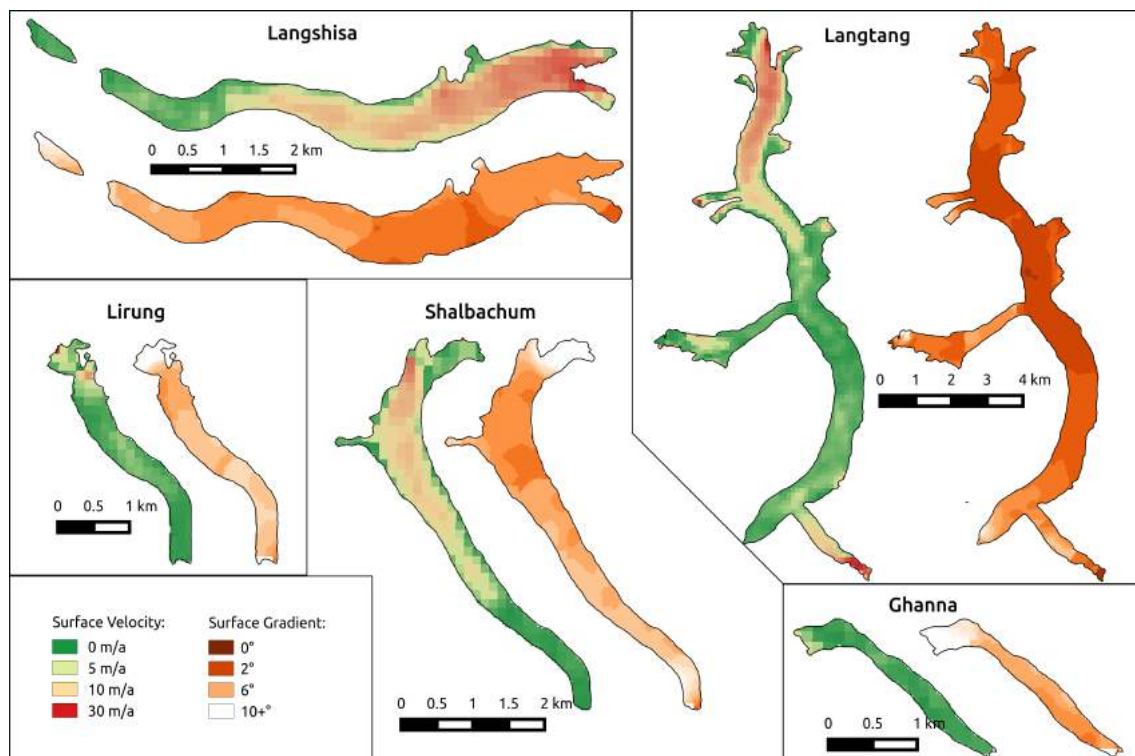


Fig. 3.6 Annual velocity and surface gradient for the debris-covered areas of the study glaciers. Annual velocity was derived using the method of Dehecq et al. (2015) but with Landsat 8 panchromatic data. Surface gradient was derived by a method similar to Quincey et al. (2007) and shows the full range of data.

2012), DGM would show a relationship with ponding. In the results, however, DGM explains very little of the variability in ponding between glaciers. First, apparent ponding may not increase dramatically until the base level is nearly reached, so cumulative thinning may not exhibit a clear relationship with pond formation. Second, Sakai and Fujita (2010) found that large terminal lakes were more likely to form if DGM exceeds 50 m and the terminus surface gradient is below  $2^\circ$ . Although high DGM values were obtained for Langshisa, Lirung, and Langtang Glaciers, the surface gradient condition is not met for any of the study glaciers, and none of the study glaciers exhibits a terminal lake or shows signs of increased water storage near the terminus. Rather, it appears that all ponds identified in the study are ‘perched’ above the hydrological base level. Consequently, DGM may be a useful metric to monitor as glaciers across the region continue to thin in response to climate, but is only meaningful with respect to surface hydrology when glacier thickness is also known.

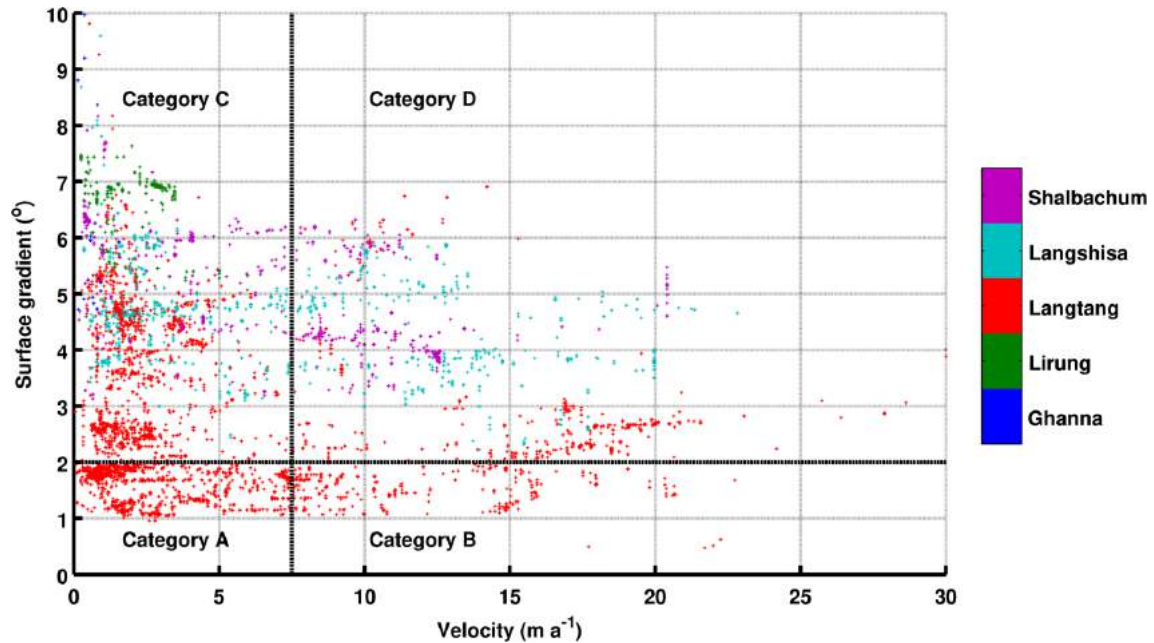


Fig. 3.7 Distribution of local surface gradient and velocity for all observed ponds, with marker size indicating the number of pixels for each pond. Categories A-D correspond to Table 3.4 and Quincey et al. (2007).

### 3.4.4 Pond spatial distributions and controls

Surface velocities and gradients derived for the five debris-covered tongues are shown in Figure 3.6. The five glaciers show distinct patterns of surface velocity, with widespread near-stagnant areas. Langshisa, Langtang, and Shalbachum all show a pattern of strong velocity decay through their debris-covered tongues (i.e. longitudinal compression), but show very low surface velocities for the terminal 1.5 km, 8 km, and 2 km, respectively. Lirung and Ghanna Glaciers have very little area moving  $> 5 \text{ m a}^{-1}$ , although Lirung Glacier is known to show seasonal fluctuations in surface velocity (Kraaijenbrink et al., 2016).

The debris-covered tongues of the five glaciers also show differing patterns of surface gradient. Langshisa Glacier has a surface gradient almost entirely in the  $2^\circ - 6^\circ$  range, only exceeding  $6^\circ$  at its terminus. Of the five study glaciers, only Langtang Glacier shows any area with a surface gradient below  $2^\circ$ , which occurs for a large central portion of the glacier's trunk. Langtang also shows very little area with a surface gradient higher than  $6^\circ$ . Most of the surface of Lirung Glacier has a gradient above  $6^\circ$ , while a few small portions of the glacier exhibit gradients between  $2^\circ$  and  $6^\circ$ . Most of Shalbachum Glacier is in the  $2^\circ - 6^\circ$  surface gradient range, although the lower 3 km and the upper 1 km both show surface gradients above  $6^\circ$ . Ghanna Glacier shows nearly the opposite pattern: a steeper upper portion ( $> 6^\circ$ ), with most of the tongue falling in the  $2^\circ - 6^\circ$  range.

Table 3.4 Distribution of debris area, observed pond area, and count of ponds within each gradient and slope category with (-) denoting no area. The table encompasses the full period of record, so total ponded area is greater than the debris-covered glacier area in category A. Mean density in each terrain category is given for May-October.

	A: low gradient, low velocity			B: low gradient, high velocity			C: high gradient, low velocity			D: high gradient, high velocity		
	Area (km <sup>2</sup> )		N ponds	Area (km <sup>2</sup> )		N ponds	Area (km <sup>2</sup> )		N ponds	Area (km <sup>2</sup> )		N ponds
	Debris	Pond		Debris	Pond		Debris	Pond		Debris	Pond	
Shalbachum	-	-	0	-	-	0	1.53	1.29	385	0.91	1.02	331
Ghanna	-	-	0	-	-	0	0.48	0.03	24	-	-	0
Lirung	-	-	0	-	-	0	1.02	1.26	335	0.01	-	0
Langtang	4.64	9.16	1819	1.40	1.31	458	7.84	6.97	1762	2.23	1.28	506
Langshisa	-	-	0	-	-	0	1.69	1.74	580	1.97	1.40	365
All glaciers	4.64	9.16	1819	1.40	1.31	458	12.55	11.29	3086	5.12	3.70	1202
Portion of total	19.6%	36.0%	27.7%	5.9%	5.2%	7.0%	52.9%	44.3%	47.0%	21.6%	14.5%	18.3%
Mean density	-	2.9%	-	-	1.4%	-	-	1.3%	-	-	1.1%	-

Ponds are present in all four categories identified by Quincey et al. (2007), but appear to be more frequent in zones of lower velocity and lower surface gradient (category A, Figure 3.7). Langtang Glacier dominates the overall distribution of ponds (68% of ponds) as it has the largest area and highest pond density. It is also the only glacier to exhibit all four of the categories, as none of the other four glaciers have surface gradients below  $2^\circ$  anywhere on their debris-covered tongues.

Comparing the total portion of debris-covered area and ponded area within each category produces an estimate of the density of ponds in each zone (Table 3.4). Here, it becomes clear that although only 19.6% of the Langtang Valley's debris-covered glacier area is classified as Category A (low gradient, low velocity), this zone accounts for 36% of the observed supraglacial pond area over the period of record; this category has the highest density of ponds. Category B (low gradient, high velocity) encompasses the smallest portion of the debris-covered area (5.9%) and pond area (5.2%), the second-highest density of ponds. Third highest in terms of pond density is Category C (high gradient, low velocity), which describes the majority of the debris-covered area (52.9%) but just under half of the observed pond area (44.3%). For Category C, there is moderate variability in the pond density between glaciers but no glacier approaches the relative density of Category A. Finally, Category D (high gradient, high velocity) shows the lowest density of ponds, encompassing 21.6% of debris-covered area but only 18.3% of pond area. The variability between glaciers within Category D is also moderate but density values are lower than for all other categories.

The average size of ponds in each category is also apparent from this approach. In Category A, ponds average  $0.0050 \text{ km}^2$  in area (5.6 pixels). For Category B, the average pond size is  $0.0029 \text{ km}^2$  (3.2 pixels). Ponds in Category C average  $0.0037 \text{ km}^2$  (4.1 pixels), while those in Category D average  $0.0031 \text{ km}^2$  (3.4 pixels). The average pond sizes for each category are very consistent between glaciers.

According to these results, pond density seems to increase with lower surface gradients and lower glacier velocities, with surface gradient showing the stronger control. Pond size, though, seems to increase only with lower velocities, showing a mixed interaction with surface gradient. The results are in general agreement with the findings of Quincey et al. (2007), but in contrast to that study, I find numerous smaller ponds in Category B, instead of the potential for a few large ponds. Also, in Category C and D I find a greater portion of ponds than expected, nearly on par with Category B relative to the respective debris areas.

In synthesis, these results are in agreement with the framework of Reynolds (2000) and Quincey et al. (2007) that surface gradient exerts a primary control on pond formation by determining the likelihood of surface accumulation. The results suggest that surface velocity exerts a secondary control on pond formation, because the zones that experience heightened velocity also show a strong velocity decay (Figure 3.6), and this compressive flow may discourage drainage via englacial conduits, rerouting meltwater onto the glacier surface. However, surface velocity exerts a strong control on pond persistence by encouraging connectivity between the supraglacial and englacial hydrologic systems. Thus, when ponds do form in zones of moderate velocity they are typically smaller, because the higher local velocity provides more opportunity for drainage.

### 3.4.5 Pond seasonality

The seasonality of thawed ponds in the Langtang Valley was assessed according to the seasonal definitions of Immerzeel et al. (2014b) to determine the period and magnitude of surface ponding as relevant to the glaciers' surface energy balance and ablation (Figure 3.8a). The frozen surface of ponds in winter is often difficult to distinguish from snow drifts which also accumulate in the surface depressions, a spectral separation that is especially challenging with the spatial resolution of Landsat data. Ponds with a frozen surface layer were therefore not a target of observations and are discounted from the analysis presented here, but would be important to observe from a hydrologic perspective.

Considering thawed ponds only, supraglacial pond cover in the Langtang Valley shows an increase during the pre-monsoon, rises to a peak in the early monsoon, drops during the post-monsoon, and decreases to negligible during the winter months (Figure 3.8a). The seasonal pattern is highlighted by aggregate maps of the pond frequency for each season for Langtang Glacier (Figure 3.8b). During the pre-monsoon, ponds are more frequent on the lowest portions of the debris-covered tongue. Ponds are very common in the monsoon (Figure 3.8b) and distributed across all elevations. Fewer ponds are apparent during the post-monsoon, and very few ponds were observed in winter, as the water surface freezes for a large portion of the year (Figure 3.8b).

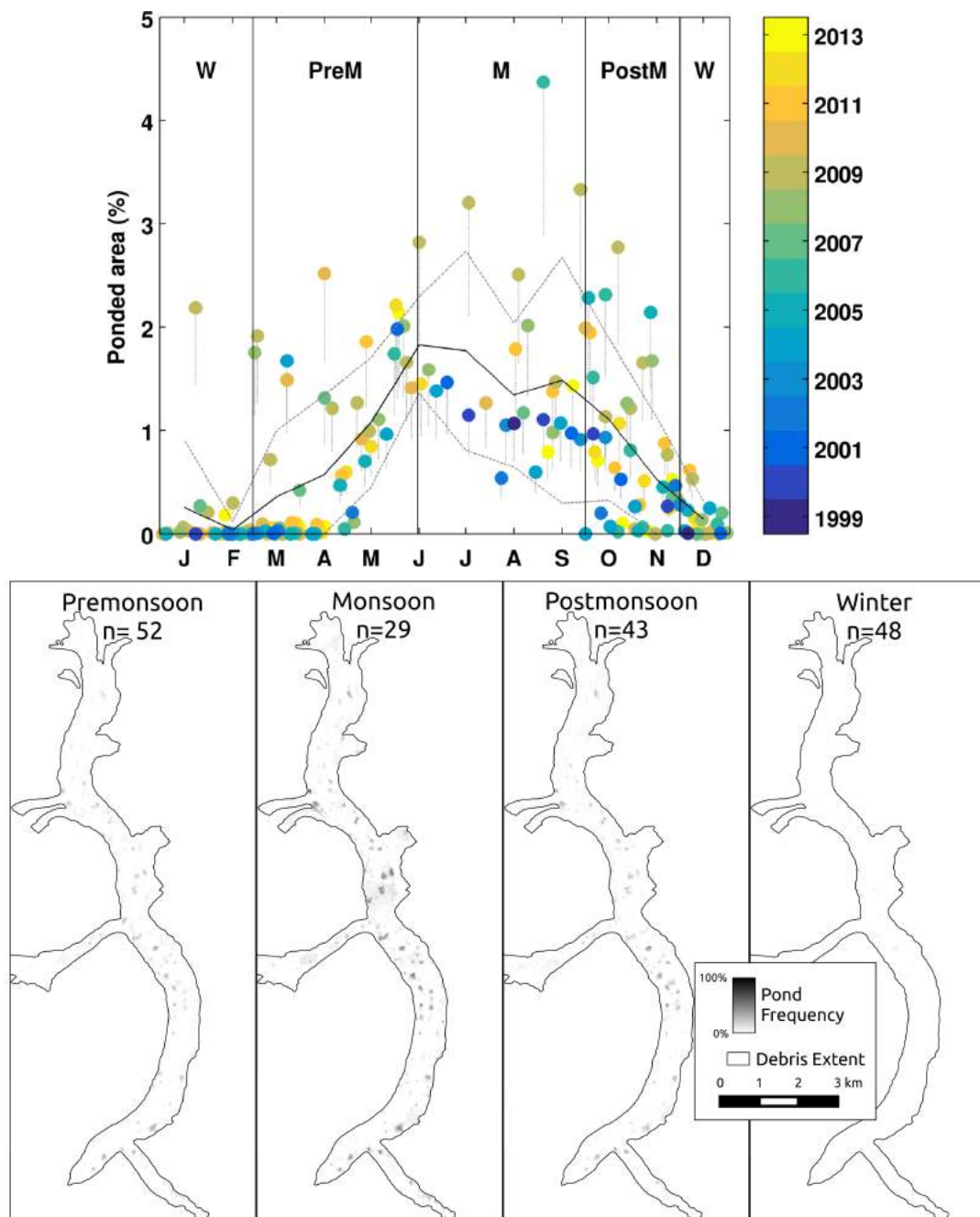


Fig. 3.8 Seasonal pattern of thawed pond cover as percent of observable debris-covered glacier area (top), with individual scenes coloured by year of observation ( $n=172$ ) and dot tails highlighting the effect of a 34% overestimation of pond area. The solid black line is the monthly mean, with the dashed lines showing the standard deviation spread. The seasonal pattern is demonstrated by seasonal pond frequency maps from all data for each season (bottom), highlighting the widespread prevalence of ponds during the monsoon. In the lower panel, only Langtang Glacier is shown for space considerations.

Several authors have suggested a strong seasonality of pond cover (Takeuchi et al., 2012; Liu et al., 2013) due to the seasonal peak in the ablation process and its controls on englacial conduit opening and closure (Reynolds, 2000; Sakai et al., 2000). This study's observations generally support these earlier ideas. There is a reduction in snow cover in the pre-monsoon as temperatures rise, leading to the uncovering and thawing of ponds frozen over winter, and the filling of surface depressions without an englacial drainage outlet. During this period, thawed ponds increase in areal cover to peak at 2% of the glaciers' debris-covered area at the onset of the monsoon. The greatest hydrologic flux occurs during the monsoon due to the combination of high melt rates and rainfall, with snowmelt providing the greatest source of water (Ragettli et al., 2015). During this period, pond cover declines slightly to 1-1.5% of debris-covered area. Fewer ponds remain in the post-monsoon, and thawed pond cover rapidly diminishes due to decreasing temperatures and declining water supply. Very cold temperatures and occasional snowfall occur in the winter, and any remaining ponds freeze and may be obscured by snow.

This analysis was hampered by the 16-day return interval of the Landsat TM and ETM+ observations, which occasionally led to several-month gaps in observations (Figure 3.2). The return period also prevented observation of dynamic hydrologic processes operating on short timescales. Field observations in May 2013 indicated widespread hydrologic activity on the surface of Langtang Glacier (Figure 3.9), with depressions suddenly filling and connecting via surface and englacial flow. Unfortunately, the Landsat record did not contain a cloud-free observation of the site during this period, missing the peak annual supraglacial ponding altogether.

### 3.4.6 Pond persistence, recurrence, and evolution

Changes in pond cover on the multiannual (Liu et al., 2015) and decadal (Gardelle et al., 2011) timescale are a key point of interest, as a potential indicator and feedback for glacier response to climate warming (Benn et al., 2012) and as an early warning for the formation of proglacial lakes (Bolch et al., 2008). Here I present observations of the dynamics of individual pond features and the interannual variability of ponding for the study glaciers.

Supraglacial ponds often persist for several years before an englacial connection develops, or may refill the same basins after drainage points become blocked (Benn et al., 2001; Immerzeel et al., 2014a). Unfortunately, due to the sporadic temporal coverage of the Landsat record it is difficult to distinguish between pond persistence and recurrence. Both are important, and for different reasons: pond persistence (i.e. duration) controls the local effects that water at the glacier's surface may have (e.g. calving, subaqueous melt, sedimentation, debris reorganisation), while pond recurrence directly relates to a pond's effects in the

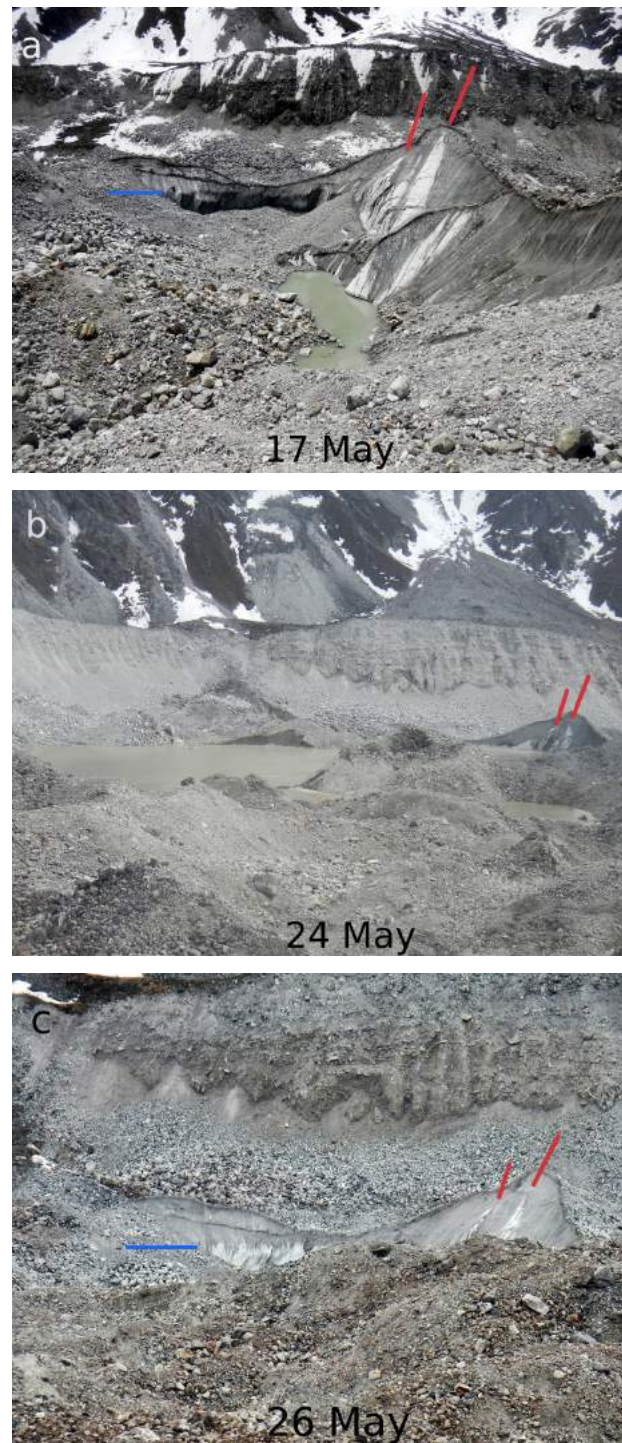


Fig. 3.9 Observations of rapid pond filling and draining during the late pre-monsoon of 2013. Observations on 17 May (a) showed a nearly empty depression ringed with ice cliffs. By 24 May (b), in the absence of any precipitation, the depression had filled substantially via supraglacial meltwater sources, which also filled adjacent depressions. Two days later (c), following a 14-hour rainfall event, the pond had drained, leaving the subaqueous portion of the ice cliff clean. Blue lines indicate the approximate filled water level as seen in the 24 May photo (b), with red markers identifying recognisable clean patches on the ice cliff.

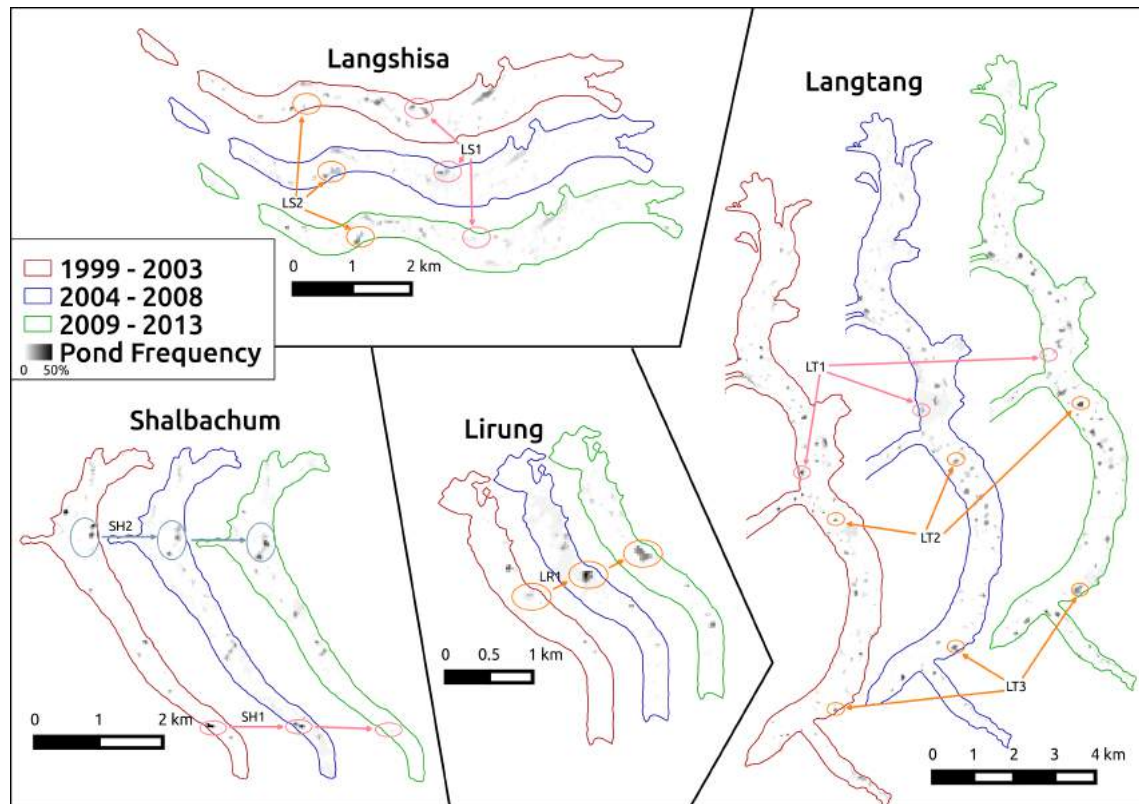


Fig. 3.10 Distribution of supraglacial ponds as percent of cloud-free scenes for the debris-covered glacier area for five-year subsets, highlighting the increase in overall ponded area and the persistence of individual ponds. Ghanna Glacier is not shown due to its lack of pond-cover.

glacier's interior (the frequency that it conveys atmospheric energy via drainage). Here I analyse the repeated pond occurrences, which could indicate either persistence or recurrence.

To highlight the persistence and recurrence of ponds, I examine pond frequency maps (Figures 3.4 and 3.8). Langtang and Lirung glaciers have very persistent or recurring pond locations even over the 15-year study period (identifiable as dark spots), while ponds on the faster-flowing Shalbachum and Langshisa Glaciers tend to be shorter-lived (showing as smears). To highlight persistence and recurrence over shorter periods, pond-frequency maps were computed for three 5-year windows within the study period: 1999 to 2003, 2004 to 2008, and 2009 to 2013 (Figure 3.10). Here, individual ponds can be readily identified as features with a frequency of up to 50% of the scenes within the study period, and lake emergence, expansion, and disappearance processes are evident over the 15-year period. The 5-year pond frequency plots are useful for examining longer-term patterns in pond-cover in a discrete manner, and show that the general distribution of ponds has not changed substantially, although the persistence or recurrence of ponds may change over time as outlined below.

In some cases, a location showing persistent or recurrent ponding for the early period decays slowly, displaying a decreased area and frequency for the middle period before disappearing entirely (see LS1, SH1, and LT1). In other cases, areas of ponding expand or emerge and are very frequently observed for the later period (see LT2 and LT3). More complex cases are also apparent: on Lirung Glacier, a pond system (LR1) becomes much more frequent during the middle period and then both expands and becomes less frequent for the latter period. This pond has also been observed to fill and drain semi-regularly in field observations (e.g. Kraaijenbrink et al., 2016). Pond system SH2 shows even more complex behaviour. In the early period, two individual persistent ponds are very apparent high in the debris-covered area. For the middle period, the same ponds are evident but are less frequent, and another pond is evident nearby. By the third period, all three locations have been slightly advected down-glacier and the uppermost location rarely shows ponding, while the lower two locations show frequent ponding and are occasionally connected.

Over the entire study period, 29.4% of the debris-covered glacier area shows ponding in at least one scene, with 45% of this area observed in 2 or more scenes, suggesting that nearly half of the ponded area shows persistence and recurrence. Furthermore, 40.5% of the ponded area was identified as a pond in 2 or more years, while 8.9% of the ponded area was identified as a pond in at least 5 years. Similarly, persistent and recurrent ponds accounted for 25-50% of all supraglacial ponds in consecutive years in the Khan Tengri mountains (Liu et al., 2015).

### 3.4.7 Interannual variability

Changes in pond cover on the multiannual (Liu et al., 2015) and decadal (Gardelle et al., 2011) timescale are a key point of interest, as a potential indicator and feedback for glacier response to climate warming (Benn et al., 2012) and as an early warning for the formation of proglacial lakes (Bolch et al., 2008). A key objective of the study was therefore to determine whether an increase in supraglacial ponded area has occurred over the study period. However, satellite observations of supraglacial ponds are severely limited by sporadic cloud cover and seasonal snow cover, as well as the failure of the Landsat 7 Scan Line Corrector in 2003. Furthermore there is a marked variable seasonality of pond cover, with peak pond cover occurring during the monsoon when cloud cover is very common, and minimum pond cover occurring in winter when cloud free images are numerous, but many lakes are obscured by snow. A multi-year investigation of ponding must account for these effects before a pattern can be assessed.

To remove biases of cloud and snow cover, I selected all scenes for each glacier where more than 80% of the debris-covered area was observable and where less than 10% of that

observable area was covered by snow. I then assess 3-month periods characterising the seasonal pond behaviour: April-June for the pre-monsoon emergence and filling of ponds, June-August for the peak monsoon pond cover, and August-October for the decline in pond cover associated with pond drainage (Figure 3.8a). For each period, I computed mean pond cover for each debris-covered glacier and scene.

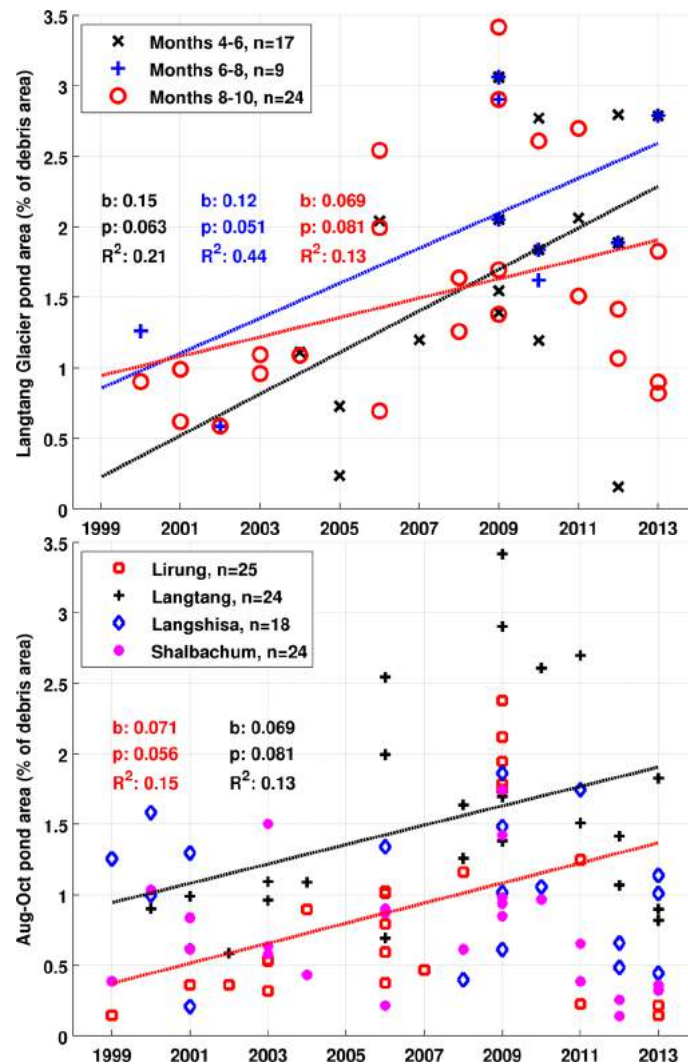


Fig. 3.11 (top) Interannual pattern of supraglacial ponding for Langtang Glacier, expressed as percent of observable debris-covered glacier area. Linear regressions show increasing pond cover for Langtang Glacier for all portions of the ablation season. Data points shown have at least 80% of the debris area visible and less than 10% covered by snow. (bottom) All study glaciers show a pronounced decline in August-October pond cover after 2009, while Lirung and Langtang glaciers still show an overall increase over the study period as indicated by the linear regressions.

After applying the data quality filters, Langtang is the only glacier where debris-covered area is observable in a moderate number of scenes for all three periods. This glacier shows an overall increase in pond cover ( $p < 0.1$ ) for all three subperiods, with the steepest increase in the pre-monsoon (Figure 3.11, top). However, all three trends provide a relatively poor explanation of the variability ( $R^2 < 0.5$ ) and are affected by the higher density of observations after 2007. In particular, more complex behaviour is apparent for the August-October period, where pond cover seems to decline after 2009. This period has the highest density of scenes during the portion of the year when ponds are thawed (Figure 3.2) and is comparable to the periods of analysis of Gardelle et al. (2011) and Liu et al. (2015).

Due to the better scene coverage during August-October, the interannual variability of Lirung, Langshisa, and Shalbachum Glaciers could also be investigated for this season (Figure 3.11, bottom). The mean ponded areas for these four glaciers showed marked variability in ponded area over the study period, with pond cover varying between 0.2% and 4% of debris-covered area. Langshisa and Shalbachum Glaciers show no consistent pattern of ponding over the study period, showing multiple peaks and falls (Figure 3.11). Lirung and Langtang Glaciers exhibit a strong rise in pond cover up to 2009, followed by a fall, but the net effect is an increase in pond cover through this period for these two glaciers ( $p < 0.1$ ).

The variability in pond cover for each glacier could be related to interannual variability in key meteorological conditions controlling the timing and supply of water to fill the surface depressions. Considerable interannual variability in ponded area was also observed by Liu et al. (2015) in the Tian Shan Mountains, and was related to total ablation season precipitation and preceding temperatures. For the Langtang Valley study site, analyses of seasonal temperatures, seasonal precipitation, preceding annual positive degree days, and preceding annual cumulative precipitation did not reveal clear patterns of links between pond cover and meteorology (not shown). Conversely, Gardelle et al. (2011) noted a substantial increase in supraglacial lake area for the Everest region over their 29 year study period, but relied on only three Landsat scenes, all from the post-monsoon.

Notably, the glaciers and years with multiple observations do not show close agreement, suggesting that important changes in surface ponding occur at the glacier scale even within a short time window. This is a challenge for a multi-year analysis: it is not clear whether the observations of Gardelle et al. (2011) and Liu et al. (2015) were affected by the seasonality and rapid variability of pond cover demonstrated by this study, and a better understanding of the temporal variability of supraglacial ponds is needed.

One avenue of research into supraglacial ponding stems from glacier hazards and the possibility of formation of large moraine-dammed lakes. Lirung, Shalbachum, and Langshisa Glaciers are known to have been retreating since 1974 at least (Pellicciotti et al., 2015;

Ragettli et al., 2016), with Lirung Glacier having formed and retreated from a small moraine-dammed lake prior to this study period. This leaves Langtang Glacier as a potential site for terminal lake formation, and it already exhibits advanced downwasting with a DGM of 50 m. However, the intermediate gradient near the terminus ( $2^\circ - 6^\circ$ ), low terminus pond density, and interannual variability in ponding suggest that formation of a terminal lake is still many years away, if indeed it occurs at all.

### 3.5 Summary

My analysis of the spatial and temporal variability of supraglacial ponds in the Langtang Valley, Nepal, substantiates the current understanding of the distribution of these features with a robust radiometric correction and pond identification methodology applied to five debris-covered glaciers and spanning 15 years of observation. This study uses many more observations than previous efforts but generally supports inferences that were drawn by Reynolds (2000); Quincey et al. (2007); Salerno et al. (2012) and Liu et al. (2015) that pond incidence is strongly controlled by local glacier velocity and surface gradient. Surface gradient controls water accumulation (i.e. pond formation) while velocity controls pond drainage, and therefore pond size and persistence. Ponds are thus most concentrated and largest in zones of low surface gradient ( $< 2^\circ$ ) and low velocity ( $< 7.5 \text{ m a}^{-1}$ ), where water is likely to accumulate and ponds are unlikely to drain. Ponds are nearly as common but smallest in zones of low gradient but higher velocity, as they are more likely to drain. Ponds are less common but larger in zones of moderate gradient and low velocity, as they may persist longer and have the opportunity to expand. Finally, ponds are least common and remain very small for zones of moderate gradient and velocity.

In addition the study makes several novel contributions to understanding of supraglacial ponds:

- The study makes the first systematic observations of the seasonality of supraglacial ponds on debris-covered glaciers, finding that thawed ponds cover 1-2% of the basin's debris-covered area for May-October. Pond cover rises rapidly in the pre-monsoon as ponds thaw and seasonal snow melts, peaking at about 2% of the basin's debris-covered area at the onset of the monsoon. Pond cover then gradually declines through the monsoon as ponds drain by establishing connectivity with the englacial hydrologic system, and ponds continue to drain and many freeze over during the post-monsoon. The seasonal patterns of pond cover have important implications for assessments of glacier mass balance and hydrology (e.g. Ragettli et al., 2015) as these features absorb atmospheric and radiative energy at a high rate (Sakai et al., 2000; Miles et al., 2016).

As climate warms in High Mountain Asia, the seasonal timing of supraglacial ponds may change, driven by earlier or stronger meltwater supply.

- Seasonal pond dynamics reveal potential biases in basic assessments of ponded area change, such as those relying on only a few observations. After controlling for seasonal biases, I find an increase in pond-cover for Langtang Glacier spanning the full April-October period when ponds are important for glacier ablation. However, it is also apparent that the glaciers exhibit marked interannual variability, with two exhibiting peak pond density in 2009 followed by a gradual decline and two showing no clear pattern. Use of fewer scenes could lead to strongly differing conclusions concerning pond growth, stability, or decline.
- Supraglacial ponding varies sharply between glaciers in the relatively small Langtang basin, ranging from 0.06%-1.69% of debris-covered area for May-October mean values. The magnitude of ponding is most related to glacier size and surface gradient. Pond cover is also correlated with the standard deviation of surface velocity, but shows no relationship with cumulative glacier thinning. A similar inter-glacier comparison of pond cover is recommended for an expanded set of glaciers to evaluate the consistency of these relationships between basic glacier characteristics and surface ponding in this and other regions.
- Persistent and recurrent ponds are commonplace on the four larger glaciers, with 40.5% of all pond locations observed in multiple years. Notably, many locations appear to persist or recur for the entire analysis, suggesting that individual pond features may have a prolonged effect on the debris-covered surface and englacial conduits.

Our findings suggest several avenues of research to better understand supraglacial ponding for the debris-covered glaciers of High Mountain Asia. First, repeat observations capturing the timing of pond filling or drainage for a large area, especially during the monsoon would greatly advance understanding of the glaciers' hydrologic system. The recent launch of Landsat 8 enables continued long-term analysis of pond cover, and the high data quality and alternating overpass schedule relative to Landsat 7 may reduce some of the spectral and temporal limitations of this study, although the limitations of 30 m spatial resolution pose a challenge for the smallest ponds. Studies of pond distributions leveraging higher-resolution orthoimagery (as in Watson et al., 2016) would constrain the moderate commission error of this study, but would need to take the seasonal variability of ponds into consideration. Finally, pond persistence and recurrence are difficult to distinguish but are useful concepts for understanding the superficial and englacial effects of supraglacial ponds, and should

be investigated further through detailed field studies encompassing a moderate domain to quantify the dynamic effects of supraglacial ponds.



# Chapter 4

## Field observations of Lirung Glacier ponds, 2013 and 2014

### 4.1 Executive Summary

Field observations of supraglacial perched ponds on Lirung Glacier were made for four seasons in 2013 and 2014 (May and October of each year) including basic surveys, installation of instrumentation to monitor ponds' water level and temperature, and measurements of near-surface meteorology. These periods also coincided with aerial, satellite, and terrestrial orthomosaic images, which provide snapshots of the areal coverage of ponds representing each season. Pond density for the glacier is higher in the pre-monsoon than post-monsoon, with individual ponds filling and draining seasonally. The majority of ponds are smaller than a single Landsat pixel; these small ponds account for 32% of total ponded area. Records of pond-related temperature and wind speed show strong diurnal variability. Pond albedo is stable at each observation site, with  $\alpha = 0.08$  or  $0.12$ . Four ponds were monitored with water-level loggers in addition to the repeat orthoimages and DEMs. These ponds exhibit different patterns of pond filling, stability, gradual surface lowering, and drainage, and each pond shows a net surface lowering due to basin expansion. Small ponds do not appear to play a role in the whole-glacier energy balance during winter months. Based on the field observations, numerical modelling of supraglacial pond energy balance will require trade-offs between temporal period, spatial coverage, and model complexity.

## 4.2 Specific Objectives

The chapter seeks to document the supraglacial ponds of Lirung Glacier with a summary of the field observations that were collected in 2013 and 2014 to present. The chapter will specifically document and analyse:

1. Pond area changes based on pre-monsoon and post-monsoon orthomosaic images
2. Water-level fluctuations of instrumented ponds during the pre-monsoon and monsoon
3. Instrumental records of pond temperatures and albedo
4. Wind speed observations in the vicinity of a ponded surface depression
5. Winter pond temperatures

The datasets enable assessment of the patterns of behaviour (drainage, stability, or growth) of individual ponds over the two-year period. The chapter also seeks to briefly evaluate the challenges associated with coarse-resolution orthoimagery based on the observed ponds, and to assess seasonal ponded area fluctuations. The chapter documents pond-related phenomena and determines the annual period over which ponds are important for glacier energy balance considerations.

The pond observations are focused on Lirung Glacier, although the material makes reference to work conducted throughout the whole valley by myself and by colleagues. The data used in this chapter were collected by a large collaborative team of which I am a part, also including scientists from ETH Zürich, the University of Utrecht, and ICIMOD. All analyses and charts presented here are my own, but depend heavily on data collected and processed by colleagues, and in some cases overlap with or build on preliminary analyses carried out by others.

## 4.3 Methods of pond observation

To extend previous analyses of supraglacial pond energy balance (Sakai et al., 2000; Röhl, 2006, 2008), perched ponds on the debris-covered surface of Lirung Glacier were studied during 2013 and 2014 (Figure 4.1). As described in Section 2.4, the debris-covered tongue of Lirung Glacier covers 17% of the glacier's area and ranges from 4000-4350 m.a.s.l. The tongue is dynamically-disconnected from the clean-ice portion of the glacier and is nearly stagnant (Kraaijenbrink et al., 2016), but experiences significant deposition of mass via ice and debris avalanches (Ragettli et al., 2015, 2016; Kargel et al., 2016).

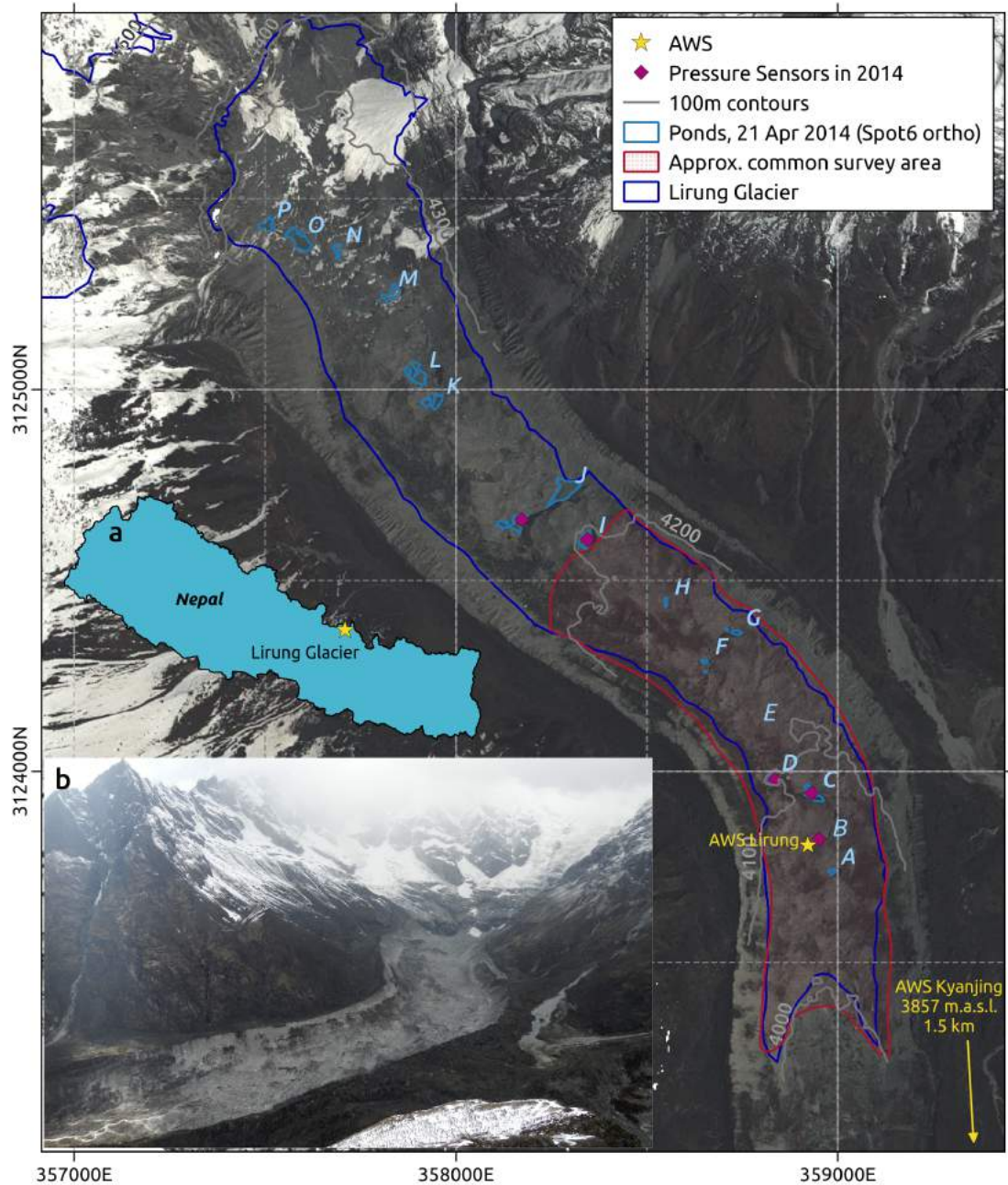


Fig. 4.1 Location of ponds observed in the 2014 Spot6 orthophoto (backdrop). Pond location *B* contained a small pond in 2013, but no pond was observed in 2014. Location *E* had two small ponds in May 2014, but no pond was evident in the April Spot6 orthophoto. UAV and terrestrial orthomosaics encompassed approximately the same coverage. Insets show (a) the location of Lirung Glacier in Nepal and (b) an oblique photo of the debris-covered tongue.

### 4.3.1 Instrumentation

Since 2012, an extensive network of meteorological stations has been established in the Langtang Valley monitoring surface temperature (for ground, debris, and ice surfaces), near-surface air temperature (2 m height), and precipitation quantity and phase (Immerzeel et al., 2014a; Shea et al., 2015b; Heynen et al., 2016; Steiner and Pellicciotti, 2016). For this study, I focus specifically on Lirung Glacier for 2013-2014 and use data from two automated weather stations (AWSs), including one on-glacier and one in the nearby village of Kyanjing Gompa (Table 4.1, Figure 4.1). These two stations each provide observations of downwelling shortwave radiation ( $I_{in}$ ) relative humidity ( $rH$ ), and wind speed ( $u_a$ ), while the Kyajing AWS also measures downwelling longwave radiation ( $L_{in}$ ), atmospheric pressure ( $P_0$ ) and hourly rainfall ( $q_r$ ). The on-glacier Lirung AWS is co-located with a sensor measuring the temperature of the debris surface ( $T_{lb}$ ).

Four ponds on Lirung Glacier (C,D,I,J in Figure 4.1 and Table 4.1) were instrumented with HOBO Water Level Loggers, which measure ambient pressure and temperature. Two of these ponds (C and J) have continuous records extending back to October 2013 and were also instrumented for part of the 2013 monsoon (Table 4.1). A Keller DCX-22 pressure transducer was installed in a dry depression that previously contained a pond, where it measured ambient pressure and temperature for much of the 2014 monsoon. While submerged, each of these sensors recorded water pressure ( $P_{lb}$ ) and pond-bottom temperature ( $T_{lb}$ ). For these records, the observed pond-bottom pressure ( $P_{lb}$ ) was corrected for atmospheric pressure ( $P_0$ ) measured at Kyanjing AWS and adjusted to the pond altitude using the ideal gas law and ambient temperature, producing time series of hydrostatic pressure. These data were then converted to at-sensor water depth based on the water density at the observed pond-bottom temperature. When exposed subaerially, the sensors provide supporting records of atmospheric pressure  $P_0$ .

Two ponds (C,D) were additionally instrumented with a float and string of HOBO Tidbit v2 temperature sensors, attached directly to the corresponding pressure transducer anchor cable. The setup sampled water temperature at the pond surface, at 0.5 m depth, and at 2 m depth. Along with the pond-bottom temperature sensor, these data enabled investigation into the variability of pond temperature along a water column.

Ponds A and D were also monitored by Kipp and Zonen CM7B albedometers for part of May 2014, collecting downwelling and upwelling shortwave radiation ( $I_{in}$  and  $I_{out}$ ). Those data were used to evaluate the two albedo models.

Finally, two anemometers were temporarily installed in the vicinity of pond D to assess the Lirung AWS wind record's applicability for a sheltered pond location. One sensor was

Table 4.1 Instrumentation installed at Lirung Glacier during 2014 used for monitoring and modelling supraglacial ponds.  $D_{Lir}$  is the horizontal distance from the sensor to the Lirung AWS. End date for pressure transducers indicates the point at which the sensor was exposed to atmospheric pressure. Pond locations and elevations are reported based on Spot6 data. Pressure transducers for 2013 are not used for modelling, only for pond process observations. Thermistor and albedometer locations correspond very closely (within 2 m) to pressure transducers for ponds C and D. Anemometers at pond D were installed beside the pond shore and at the top edge of of the ice cliff adjacent to the pond. Locations are given relative to the WGS84 datum.

Data source	Lat. (°)	Long. (°)	Elev.	$D_{Lir}$	Date Start	Date End	Observed variables
Lirung AWS	28.2326	85.5621	4063 m	0	4 May 2014	3 Nov 2014	$I_{in}, rH, u_a$
Lirung T-Logger	–	–	–	0	6 May 2013	24 Oct 2014	$T_a, T_{deb}$
Kyanjing AWS	28.2110	85.5673	3857 m	2440 m	16 Apr 2014	9 Oct 2014	$P_0, I_{in}, L_{in}, q_r, rH, u_a$
Pressure Trans., Pond B	28.2338	85.5622	4059 m	34 m	24 Aug 2014	4 Nov 2014	$P_0$
Pressure Trans., Pond C	28.2338	85.5622	4077 m	137 m	25 Oct 2013	27 Jul 2014	$P_{lb}, T_{lb}, P_0$
Pressure Trans., Pond C	–	–	–	–	9 May 2013	14 Jul 2013	$P_{lb}, T_{lb}, P_0$
Pressure Trans., Pond D	28.2341	85.5612	4096 m	192 m	5 May 2014	2 Sep 2014	$P_{lb}, T_{lb}, P_0$
Pressure Trans., Pond I	28.2380	85.5562	4190 m	987 m	8 May 2014	16 Aug 2014	$P_{lb}, T_{lb}, P_0$
Pressure Trans., Pond J	28.2402	85.5621	4207 m	1135 m	25 Oct 2013	6 Aug 2014	$P_{lb}, T_{lb}, P_0$
Pressure Trans., Pond J	–	–	–	–	11 May 2013	23 Jun 2013	$P_{lb}, T_{lb}, P_0$
Thermistors, Pond C	–	–	–	–	25 Oct 2013	20 Jun 2014	$T_{ws}, T_{50cm}, T_{2m}$
Thermistors, Pond D	–	–	–	–	5 May 2014	2 Sep 2014	$T_{ws}, T_{50cm}, T_{2m}$
Albedometer, Pond A	–	–	–	–	11 May 2014	15 May 2014	$I_{in}, I_{out}$
Albedometer, Pond D	–	–	–	–	9 May 2014	16 May 2014	$I_{in}, I_{out}$
Anemometer, above D	–	–	–	–	9 May 2014	16 May 2014	$u_a$
Anemometer, beside D	–	–	–	–	9 May 2014	16 May 2014	$u_a$

installed above pond D's depression, while a second sensor measured wind from the pond's shore. Both sensors measured wind at 1 m height.

For this thesis all times are reported in Nepal Standard Time (NPT; UTC +5:45), which is a fixed approximation of the local mean solar time in Kathmandu. Local mean solar time for the study site is very slightly different (+5:42:29), with minimal influence in the observation of diurnal fluxes at the site.

### 4.3.2 Orthoimages and DEMs

In addition to the *in-situ* observations of pond water level and temperature, results from aerial and satellite remote sensing campaigns were used to provide repeat observations of pond area and to provide input data for the numerical modelling (Table 4.2). Ponds were manually digitised from each orthoimage.

In 2013 and 2014, three repeat-visit aerial surveys were completed by colleagues using an unmanned aerial vehicle (UAV) to produce ultra-high-resolution orthomosaics and associated DEMs (Kraaijenbrink et al., 2016). These observations extend over approximately half of the

Table 4.2 Data sources for seasonal observations of pond area changes. A DEM is available from each data source at reduced resolution. \*Ponds H and I are covered in the 2013 orthomosaics, but not the associated DEM.

Data Source	Date	Resolution	Ponds covered	Method	Source
UAV orthomosaic	18 May 2013	0.2 m	A-I*	Aerial SfM (Agisoft)	Immerzeel et al. (2014a)
UAV orthomosaic	22 Oct 2013	0.2 m	A-I*	Aerial SfM (Agisoft)	Immerzeel et al. (2014a)
Spot6 orthophoto	21 Apr 2014	1.5 m	All	Satellite stereo photogrammetry	Ragetli et al. (2016)
UAV orthomosaic	1 May 2014	0.2 m	A-G	Aerial SfM (Agisoft)	Kraaijenbrink et al. (2016)
Terrestrial orthomosaic	2-3 Nov 2014	0.25 m	A-I	Terrestrial SfM (Agisoft)	Brun (2015)

Lirung debris-covered tongue (Figure 4.1), as the UAV was unable to operate in the complex conditions in close proximity to Lirung's headwall.

Additionally, a Spot6 stereo image pair was acquired on 21 April 2014, slightly preceding the 2014 UAV flights. Through stereo-photogrammetry and using ground control points measured for the UAV campaigns, the Spot6 data were processed by Silvan Ragetli into an orthophoto and a high-resolution DEM (Ragetli et al., 2016). Unlike the UAV data, the Spot6 acquisition provides a complete coverage of the debris-covered tongue.

Finally, in November 2014, a field campaign collected 682 photos of Lirung Glacier from its lateral moraines and from prominent positions on-glacier. These terrestrial images were analysed in collaboration with colleagues using a Structure-from-Motion process chain (Agisoft Photoscan Professional) and validated with 21 on-glacier GCPs to derive an orthomosaic and DEM (Brun, 2015; Brun et al., 2016). The surveyed area and resolution of these products was roughly comparable to that of the UAV data.

## 4.4 Results

This section will summarise the primary observations of supraglacial ponds determined from field instrumentation and from analysis of the orthoimages. The section will separately present variations in pond area, water-level fluctuations, pond-surface and pond-bottom temperature measurements, albedo, and wind records.

### 4.4.1 Observed pond areas

During 2013 and 2014, ponds were observed to occur in 16 different locations on Lirung Glacier (Figure 4.1, Table 4.3). Some ponds (B,E) were very small and did not persist for much of the record, while others (C,D,I) were more moderate in size and seemed to persist very stably across the observations. Pond J, the largest pond with repeat observations, fluctuated dramatically in size season-to-season, between 7287.8 m<sup>2</sup> and 449.4 m<sup>2</sup> in 2013

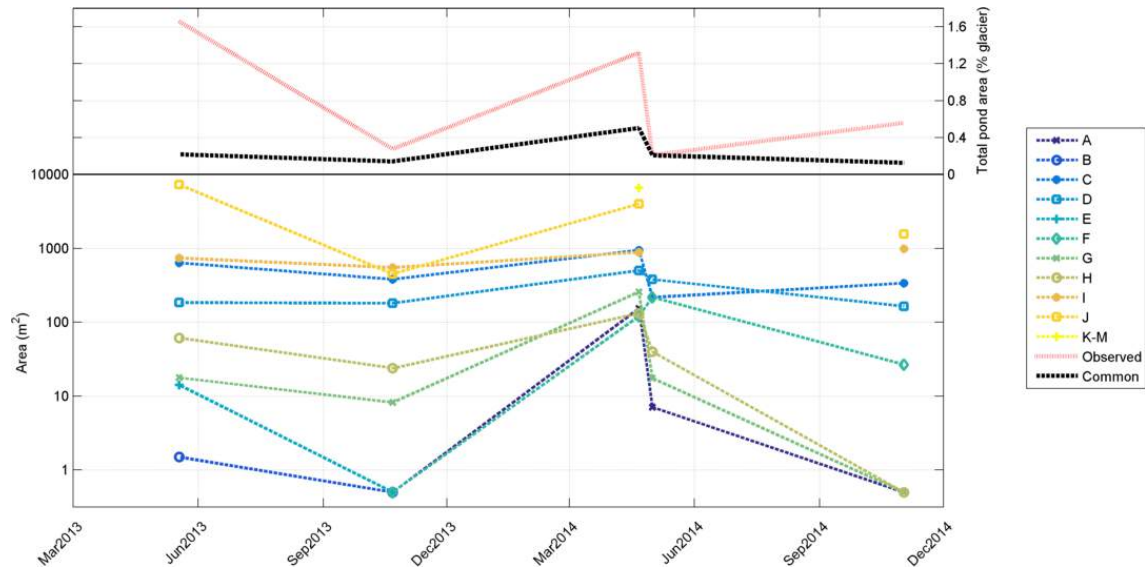


Fig. 4.2 Seasonal changes in ponded area are apparent from the five orthoimages. (top) The percent of debris-covered area covered by ponds, accounting for the full area ‘Observed’ in each image or the ‘Common’ area between all images. (bottom) Area changes observed at each study pond over 2013 and 2014, expressed on a logarithmic scale.

(Figures 4.2 and 4.13). This pond alone made up over one-quarter of total ponded area for Lirung Glacier in April 2014, the only occasion when the entire debris-covered tongue was observed, but was more than twice as large in May 2013, and may have been even larger in May 2014.

In both 2013 and 2014, pond cover was higher early in the pre-monsoon than in the post-monsoon. Unfortunately, other than in April 2014, pond observations were restricted to the lower elevations due to difficult UAV flying conditions near the cirque headwall (see Immerzeel et al., 2014a) and avalanche hazards for terrestrial observations. Here, ponds were typically smaller in area than at the upper portion of the glacier (Figure 4.1, Table 4.3). Controlling for the common area of observation for all orthophotos, which encompasses ponds A-H, a seasonal fluctuation is apparent, with ponds appearing by April (0.5% of the common area), partially draining by May (0.21-0.22%), then declining during the monsoon and post-monsoon to cover 0.13-0.14% of the common area (Table 4.3, Figure 4.2, ‘% Com Deb Area’ series). Most ponds show some shrinkage between April and May 2014 (excepting only pond F), and additional area decrease between May and October/November (except pond C and I in 2014). Including ponds I and J, which were not observed in May 2014, the ponded area of Lirung Glacier declined from 1.66% to 0.27% in May-October 2013, and 1.32% to 0.56% in April-November 2014.

Table 4.3 Measured pond areas for Lirung Glacier in 2013 and 2014. % refers to the pond density in the observed (Obs) or common (Com) debris-covered area ( $A_d$ ). A '-' indicates no pond observed in this location. All other values are pond areas in  $m^2$ . NS indicates that the survey did not include this location. Ponds with \* clearly bordered an ice cliff for part of the period.

Survey	% Obs $A_d$	% Com $A_d$	A*	B*	C*	D*	E*	F	G*	H	I*	J*	K-P
May 2013	1.66	0.22	-	1.5	637.1	184.0	14.2	-	17.8	61.1	738.7	7287.8	NS
Oct 2013	0.27	0.14	-	-	381.0	181.6	-	-	8.2	23.8	550.8	449.4	NS
Apr 2014	1.32	0.50	153.8	-	945.3	501.2	-	120.5	257.4	132.0	884.8	3982.4	6598.7
May 2014	0.21	0.21	7.1	-	217.0	379.0	-	218.0	17.5	40.1	NS	NS	NS
Nov 2014	0.56	0.13	-	-	338.2	164.5	-	26.7	-	-	988.0	1568.7	NS

#### 4.4.2 Changes at individual ponds

Here I present a summary of the observations at each of the primary study ponds (C, D, I, and J), which have the most comprehensive data records (Table 4.1). The position of each pond is visible in Figure 4.1).

##### Pond C

Pond C was the most comprehensively-observed pond on Lirung Glacier through instrumentation and field surveys. This small pond (up to  $637.1 m^2$ ) was heavily shaded by a large bare-ice exposure (hereafter, ice cliff) of 20 m vertical relief during all four field visits (Figures 4.3 and 4.5). The ice cliff presented an overhanging, scalloped face directly above the ice-water contact, which remained fairly similar in geometry over the study period as the cliff backwasted (Figure 4.3). The ice cliff has been thoroughly investigated by the collaborative team through stake measurements, photogrammetric surface reconstruction, and near-surface meteorology (Steiner et al., 2015; Buri et al., 2016b; Brun et al., 2016; Buri et al., 2016a). The pond itself was occasionally covered with a thin layer of slushy ice and snow (e.g. October 2014, Figure 4.3) and contained small icebergs in May 2013.

The pond's water level generally declined in both 2013 and 2014 monsoons, with a prolonged drainage during the 2013 monsoon, but a faster event in the 2014 pre-monsoon (Figure 4.4). In 2013, pond C only showed a gradual water-level lowering, dropping 2.32 m over 44 days (sensor exposed to the air on 14 July). In 2014, pond C began to fill 15 March, and the water level rose 1.77 m to peak on 21 April (38 days filling), then rapidly lowered 2.23 m by 1 May (10 days draining), then lowered very gradually for the remainder of the ablation season.

During the field visit in May 2014 (just after the April 2014 drainage), a very small surface outlet was identified meandering to an englacial conduit opening (position indicated



Fig. 4.3 Pond C in (a) May 2013, (b) October 2013, (c) May 2014, and (d) October 2014, showing ice-cliff retreat during the monsoon in each year. Drainage occurred prior to the field visit in May 2014 (c). A snowstorm immediately preceded the field visit in October 2014, blanketing the ice cliff and forming a depositing a thick layer of wetted snow on the pond surface. Approximate photograph position indicated on Figure 4.5.

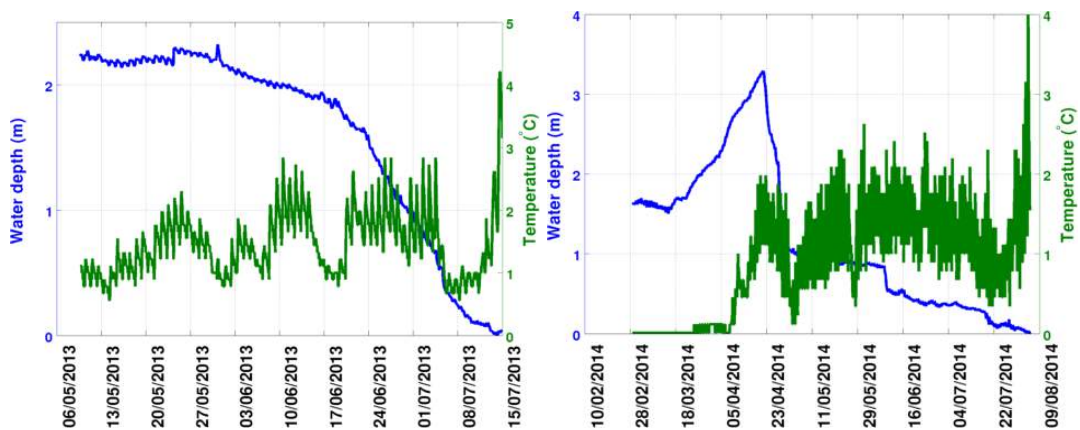


Fig. 4.4 Records of pond water level (relative to pressure transducer elevation) and temperature for pond C in 2013 (left) and 2014 (right).

on Figure 4.5). This position must have been an englacial void during 2013, but had been exposed subaerially due to surface thinning and ice-cliff backwasting. The conduit could have been associated with the faster drainage in late April, but in 2013 this passage may not have been directly or efficiently connected, leading to the slow drainage observed for that year.

A summary of changes for the pond C surface depression is presented in Figure 4.5. While the DEMs are of good quality for all three UAV datasets and the terrestrial product (Kraaijenbrink et al., 2016; Brun et al., 2016), the Spot6 DEM does not represent the surface topography as well, but is included in Figure 4.5 and similar figures for completeness.

The translation of ponded area over the study period, shown in Figure 4.5a is dependent upon the backwasting of its bounding ice cliff, expressed in panels (b) and (c). Glacier surface velocity in this area is  $< 1 \text{ m a}^{-1}$  (Immerzeel et al., 2014b; Brun et al., 2016). After each monsoon season, the perched pond primarily occupies the area of very high surface-elevation change (Figure 4.5d-e), corresponding to the prior position of the ice cliff. In both years, a substantial deposition of debris occurred at about the position of the overhanging ice cliff's lip, the point of debris supply as the ice-cliff backwasted, fundamentally changing the depression geometry and bounding the ponded area (Figure 4.5b-c).

The pond water-level fluctuations and basin elevation profiles demonstrate a continuous overall decline in the altitude of the water surface as the nearby ice-cliff backwasted (Figure 4.5). The magnitude of this decline ( $\sim 8 \text{ m}$ ) was greater than local surface change (0-3 m) and greater in each year than the water-level decline observed by pressure transducers, but those records do not encompass the entire monsoon due to subaerial exposure.

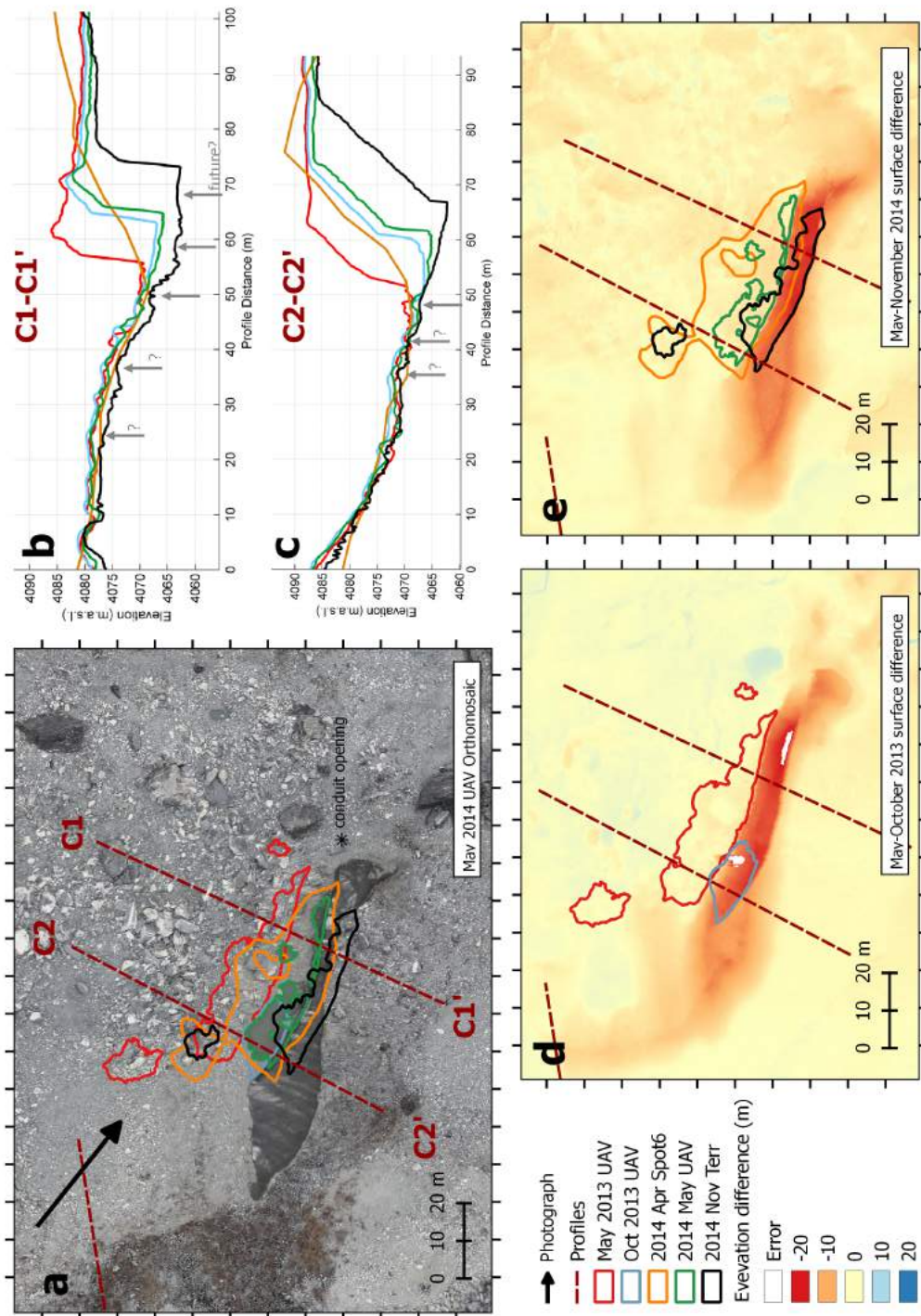


Fig. 4.5 Summary of pond depression surface change over 2013 and 2014. Pond outlines for the five orthomosaics are draped over the May 2014 UAV orthomosaic (a), also indicating profiles C1 and C2, conduit opening position in May 2014, and the perspective of repeat photos in Figure 4.3. Profiles C1 (b) and C2 (c) are shown indicating the position of debris mounds deposited by ice-cliff backwasting. Monsoon surface-elevation changes are shown for 2013 (d) and 2014 (e).

## Pond D

Pond D appeared to be only a small, stagnant perched pond in 2013 and was not investigated in detail. By May 2014, however, the pond had expanded to 206% of its May 2013 area (Table 4.3) and exposed several small ice cliffs at all sides with a very thin veneer of debris (Figure 4.6), suggesting major surface change was underway.

Between May and October 2014, pond D filled slightly and drained (Figure 4.7). The water level rose 1.07 m in the 44 days after pressure transducer installation (5 May) to peak on 18 June. The water level then lowered 2.25 m over the next 70 days (logger exposed 28 August). Water level fluctuated erratically over the entire period, with sharp drops or rises of up to 0.51 m.

Throughout this process, the surface depression expanded rapidly (Figure 4.8). A single large bare-ice cliff emerged on the pond's southern margin, while the other sections of ice exposed in May 2014 had been reburied by debris (Figure 4.6c). Significant amounts of debris had been relocated to the depression's center, dividing the pond into three distinct subaerial water bodies, although it is probable that they were hydraulically-connected through saturated debris. The large ice cliff developed a distinct thermo-erosional notch at about the May 2014 water level. Beneath one section of this cliff flowing water could be heard, suggesting connection at this level to the englacial drainage system (approximate position indicated on Figure 4.8a,c).

A summary of changes for the pond D surface depression is presented in Figure 4.8. This clearly shows the slight expansion of the depression in 2013 (panel d) contrasted with the significant changes in 2014 (panel e). Profile D1 (panel b) indicates the presence of the reburied ice cliff, which has a shallower slope than the remaining cliff face. The two profiles also highlight the stability of the ponded water level for May 2013-May 2014, followed by a decline in water level of 4 m. This is much greater than the net surface lowering of 1 m observed by the pressure transducer (Figure 4.7). This sensor was exposed subaerially on 2 September, and the water level was declining about 1 m per month, suggesting a net water-level decline of 3 m by the 1 November observations, relative to the May orthophoto. It is possible that water-surface lowering accelerated in the late monsoon, or that the glacier surface depression further subsided during this period related to the collapse of englacial voids.

## Pond I

Pond I was not observed in detail in May 2013, but appears in the UAV orthophoto as a pond of moderate size (738.7 m<sup>2</sup>) with an adjacent ice cliff with no evidence of notching and no



Fig. 4.6 Pond D in (a) May 2013, (b) May 2014, and (c) October 2014, showing sudden expansion of the depression and water-level decline in 2014. No suitable photograph was available for comparison from October 2013.

vertical or overhanging face (also see Immerzeel et al., 2014a; Brun et al., 2016). The pond had shrunk slightly in area by October 2013.

During this period, the ice cliff adjacent to pond I grew dramatically, revealing a band of ice cliff extending E-W (toward the photographer in Figure 4.9). This new band of ice cliff is characterised by a lower vertical portion, and has a parallel debris-covered mound with apex near the prior slope. Subsequent visits in 2014 captured the progressive exposure of segments of an englacial conduit at the lowest point of this band of ice cliff (Figure 4.26c). Although the course of the conduit could not be explored, it appears that this feature may be the result of a conduit roof collapse as described by Gulley and Benn (2007) and other studies. As this

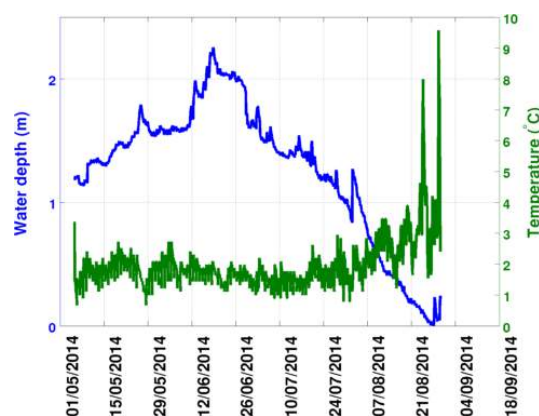


Fig. 4.7 Record of pond water level (relative to pressure transducer elevation) and temperature for pond D in 2014.

feature is immediately down-glacier and at a slightly lower elevation than pond J, it could have been associated with that pond's observed drainage in July 2013 (Figure 4.12, left).

Pond I was monitored with a pressure transducer during the 2014 monsoon (Figure 4.10). The pond surface continuously lowered for the entire period of record (103 days), a total change of 3.58 m between installation (8 May) and exposure (19 August). In spite of the continuous water-level decline, the pond had its largest observed area in November 2014 (Table 4.3). This apparent contradiction is resolved by the density difference between glacier ice and water, as the ice occupies a decreased volume after melting, and therefore the water-level declines although pond area may increase.

The pond depression's changes are summarised in Figure 4.11, and generally follow the themes identified for pond C. The ponded area remained fairly consistent over the study period, but was translated as the bounding ice-cliff backwasted (Figure 4.11a). Glacier surface velocity in this area is  $2 \text{ m a}^{-1}$  (Kraaijenbrink et al., 2016; Brun et al., 2016). The pond water-level fluctuations (Figure 4.10) and basin elevation profiles (Figure 4.11b-c) demonstrate a continuous overall decline in the altitude of the water surface as the nearby ice-cliff backwasted. The surface-elevation differences (Figure 4.11d-e) highlight the position of the englacial conduit exposure. For the 2013 monsoon, this location appears as a band of enhanced elevation change ( $\sim 7 \text{ m}$  difference), while subsequent elevation change in this band is suppressed due to the debris cover.

## Pond J

Pond J was the largest single pond-cliff system on Lirung Glacier during the study period, extending across the full width of Lirung Glacier. Pond J also showed the largest fluctuations in area: observed areas ranged from just  $449 \text{ m}^2$  to nearly  $7300 \text{ m}^2$ , with much larger areas

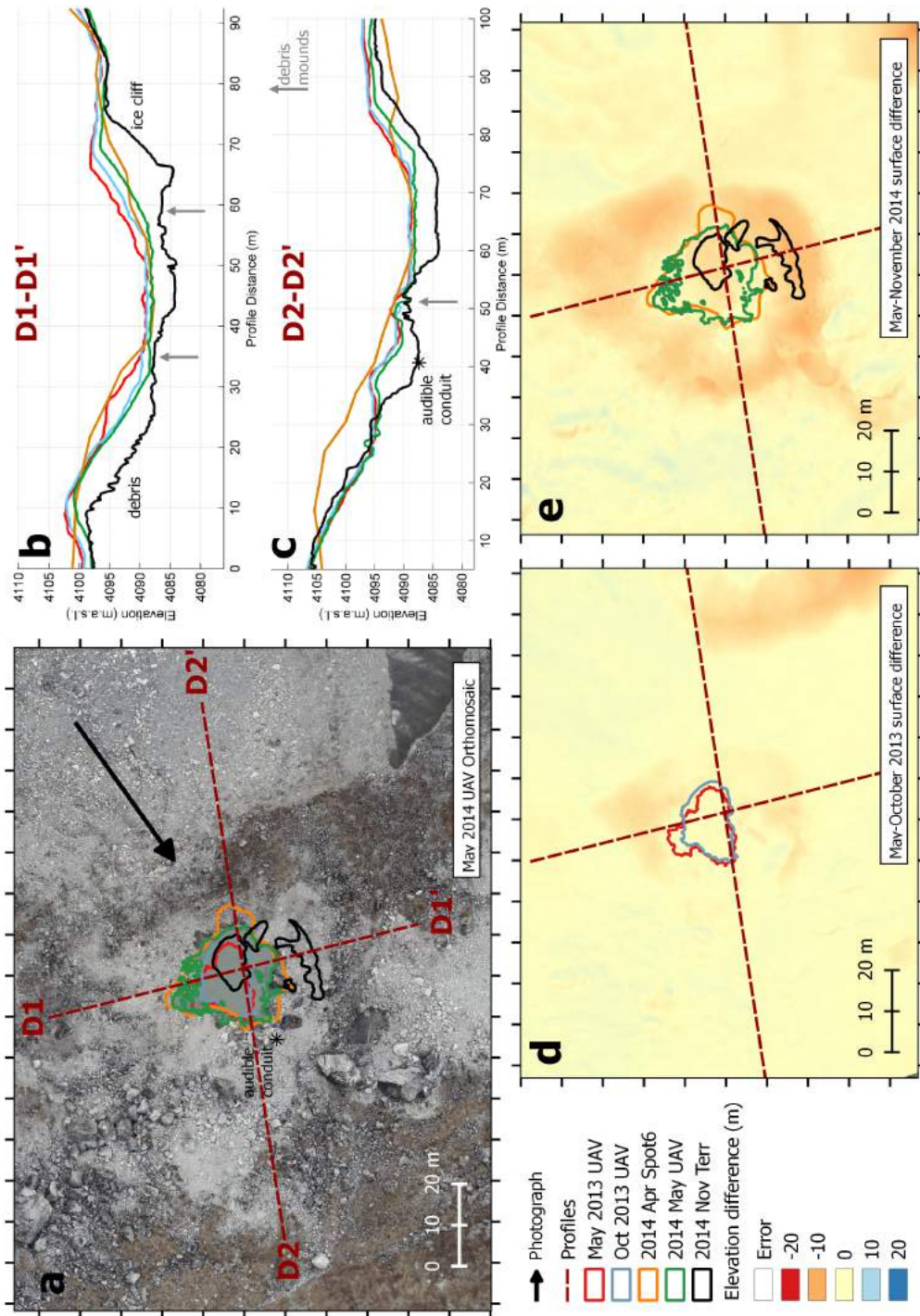


Fig. 4.8 Summary of pond depression surface change over 2013 and 2014. Pond outlines for the five orthomosaics are draped over the May 2014 UAV orthomosaic (a), also indicating profiles D1 and D2, conduit opening position in May 2014, and the perspective of repeat photos in Figure 4.6. Profiles D1 (b) and D2 (c) are shown indicating the position of debris mounds deposited by ice-cliff backwasting. Monsoon surface-elevation changes are shown for 2013 (d) and 2014 (e).



Fig. 4.9 Pond I in (a) October 2013, (b) May 2014, and (c) October 2014. The cliff-pond relative geometry was very stable for this pond, although the whole system has shifted position through melt and glacier flow. No suitable photograph was available for comparison from May 2013.

in the pre-monsoon for both years. The pond has two sections, which were initially divided in May 2013 by an ice dam, enabling different drainage behaviour during the two monsoons. During 2013, pond J's water level gradually rose 1.2 m over 28 days before lowering 2.8 m over 13 days, with the sensor exposed subaerially 23 June (Figure 4.12left). Both sections of the pond drained, but when the water level reached the ice dam, further drainage was prevented for the western portion (Figure 4.14c,d).

In 2014 pond J continually filled: a sudden rise of 1.23 m on 21-22 April, followed by a gradual, uninterrupted rise of at least 4.9 m (Figure 4.12right), connecting the two sections. In April 2014, pond J accounted for over one quarter of the ponded area for Lirung Glacier (16 ponds observed in the Spot6 image, 21 April). The high water level prevented access to the water-level logger for data download and reinitialisation in May 2014. As a result, the data-logger ran out of memory on 8 June. By October 2014, the pond had drained, but unlike 2013 the eastern portion of the pond remained at the ice-dam level, while the western portion drained fully (Figure 4.14).

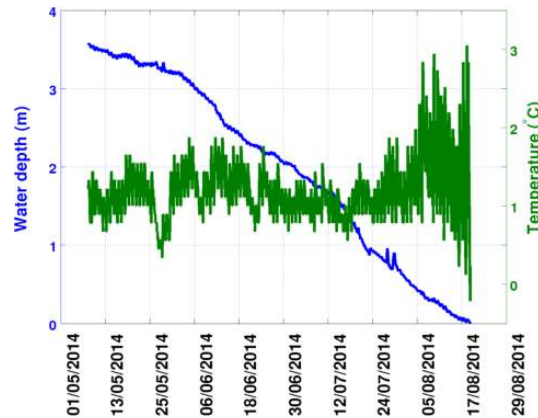


Fig. 4.10 Record of pond water level (relative to pressure transducer elevation) and temperature for pond I in 2014.

The drainage of the eastern half of pond J by October 2013 revealed a well-preserved englacial conduit floor at the base of the large ice cliff with false floors and multiple lateral thermo-erosional incisions at the outer margin of conduit meanders. Emerging from the debris surface within the depression, the conduit was 2 m wide and extended for 40 m along the cliff's base before entering a zone of active rockfall from the ice cliff's backwasting. The heavily-sheltered position of this conduit is the only explanation for its preserved subaerial condition late in the post-monsoon; the adjacent north-facing ice cliff towers 30 m directly above the location.

The drainage of sections of pond J in the monsoons of 2013 and 2014 revealed sets of relict englacial conduits extending farther up-glacier within the former pond depression, but without a large ice cliff for shelter, these segments were rapidly disintegrating (example in Figure 4.26d). In both cases, the conduits took a winding path that did not directly follow the glacier flow direction. The relict conduits had usually experienced roof collapse, although some sections presented weak natural arches. Most notably, the two conduit sections were located in distinct sections of the debris-covered surface, suggesting that the subglacial hydrological network may form a complex network even for a small glacier such as Lirung.

The difference in drainage behaviour between the two years could have several plausible explanations. It could indicate connectivity to separate englacial flowpaths for the two portions of the pond, which are roughly divided in the glacier's center (Figure 4.13) and could have merged from distinct pond-cliff systems. Alternatively, the subaqueous melt beneath the ice cliff may have exposed a different section of the same conduit system, encouraging drainage from a different point. A possible third explanation is the removal of the small ice dam retaining the western portion of the pond during 2014, enabling hydraulic equilibrium with the eastern portion of the pond before and during drainage that year.

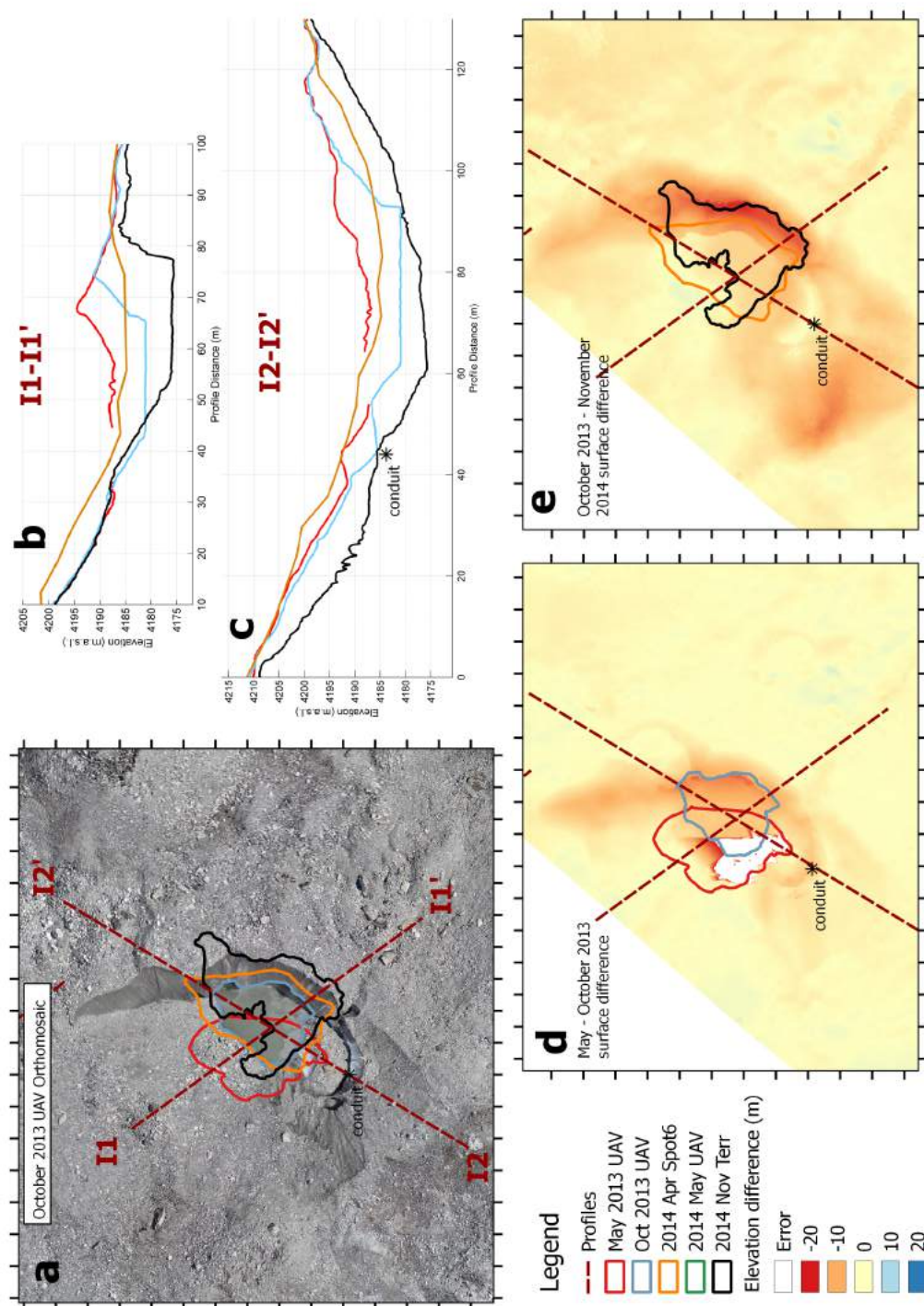


Fig. 4.11 Summary of pond depression surface change over 2013 and 2014. Pond outlines for the five orthomosaics are draped over the October 2013 UAV orthomosaic (a), also indicating profiles I1 and I2, conduit position in October 2013, and the perspective of repeat photos in Figure 4.9. Profiles I1 (b) and I2 (c) are shown also indicating the conduit position. Surface-elevation changes are shown for May - October 2013 (d) and for October 2013 - October 2014 (e). The May 2014 UAV data did not encompass pond I.

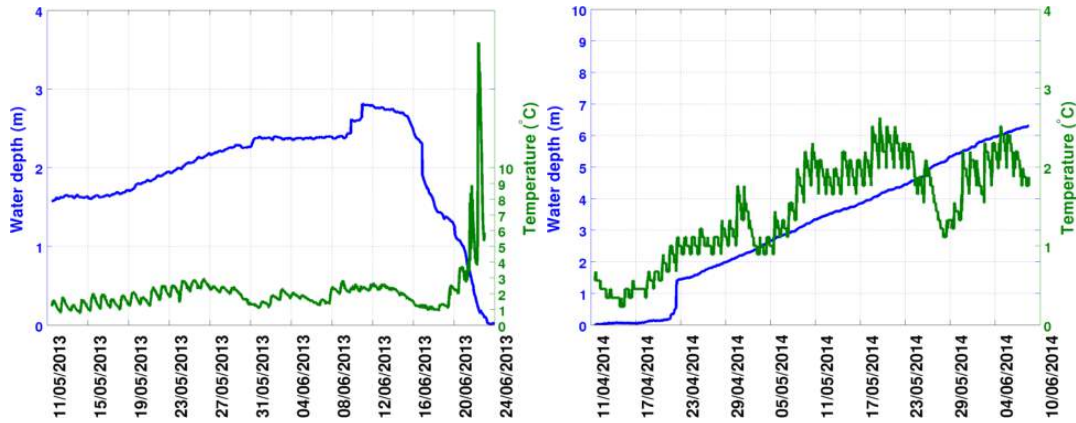


Fig. 4.12 Records of pond water level (relative to pressure transducer elevation) and temperature for pond J in 2013 (left) and 2014 (right).

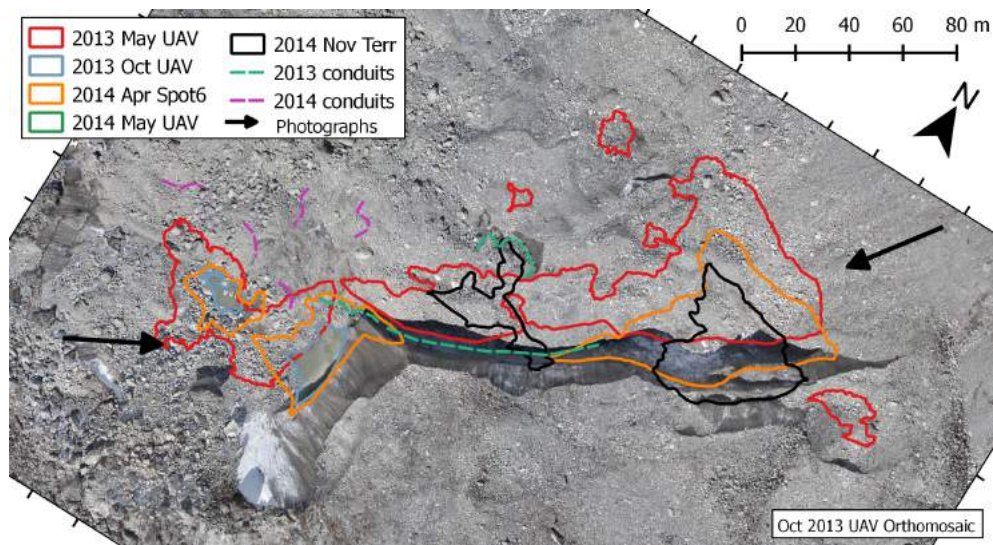


Fig. 4.13 Pond J outlines for May and October 2013, and April and November 2014, indicating approximate perspective of photographs shown in Figure 4.14, and identifying exposed segments of relict englacial conduits observed in October 2013 and 2014. Pond outlines have not been adjusted for glacier flow ( $\sim 2.5 \text{ m a}^{-1}$  per Immerzeel et al., 2014b)), but the majority of outline shift is due to ice-cliff backwasting.



Fig. 4.14 Pond J in (a) May 2013, (b-c) October 2013, (d-e) May 2014, and (f-g) October 2014, highlighting the large seasonal fluctuations in pond size. Panel (a) shows the pond system from the southwest, and panels (c), (e), and (g) provide subsequent views of the western half of the system from the southwest. Panels (b), (d), and (f) provide views of the eastern half of the system from the northeast.

### 4.4.3 Pond temperatures

Temperature records for ponds C and D in 2014 (Figure 4.15) showed strong diurnal fluctuations in surface and bottom temperature driven by variability in nearby air temperature (with 47 and 98 days of observations, respectively, at 15-minute intervals). 2 m air temperatures over the debris surface fluctuated strongly through the season between  $-3^{\circ}\text{C}$  and  $16^{\circ}\text{C}$ , with a consistent diurnal signal ranging from  $6^{\circ}\text{C}$  at 4am to  $12^{\circ}\text{C}$  at midday.

Pond C surface temperatures varied between the freezing point and  $2.5^{\circ}\text{C}$  over the season, and correlated strongly with air temperature. Mean daily water-surface temperatures fluctuated between  $0.2^{\circ}\text{C}$  at 5am and  $1.5^{\circ}\text{C}$  at midday. Pond C bottom temperatures varied between  $0.35$ - $2.5^{\circ}\text{C}$  over the season, with diurnal peaks at  $1.6^{\circ}\text{C}$  just after midday, and median daily lows of just below  $1^{\circ}\text{C}$  near 7am, overall showing a lag behind the air temperature and water-surface temperature fluctuations. Due to the temperature-dependence of water density, which peaks at  $4^{\circ}\text{C}$ , a strong inversion occurred during most of the day, with pond-surface temperatures only greater than pond-bottom temperatures during the late morning, driving natural convection during this time.

Pond D temperatures were similar in pattern to those observed at pond C, with slightly higher values for both pond-surface and pond-bottom temperatures. However, the surface temperature diurnal variations were much stronger, with median hourly  $T_{ws}$  values ranging between  $0.75^{\circ}\text{C}$  and  $2.5^{\circ}\text{C}$ , and with observations up to  $4^{\circ}\text{C}$  overall. The pond-bottom temperatures were higher for pond C than for pond D and showed a slightly larger lag in response to warming air temperature, with lowest daily temperatures observed at 8am and peak temperatures at 2pm. Due to these two differences, the period when  $T_{ws} > T_b$ , driving the strongest natural convection, was much longer for pond D.

The temperature sensors installed in both ponds recorded strong temperature fluctuations at the pond's surface and the frequent occurrence of an inversion layer (Figure 4.16). Mean hourly gradients between the water surface and pond bottom were determined for two periods of the 2014 pre-monsoon for pond C and show distinct behaviour for the two periods (Figure 4.16). The early pre-monsoon record (15-29 April) is bounded temporally by the pond surface thawing and subaerial exposure of the sensors by pond drainage. The second period begins with the thermistor string reinstallation on 7 May, and lasts until 20 June when all the sensors were again exposed subaerially. Unfortunately, it is not clear how transferable these data are to other ponds or to other glaciers or regions.

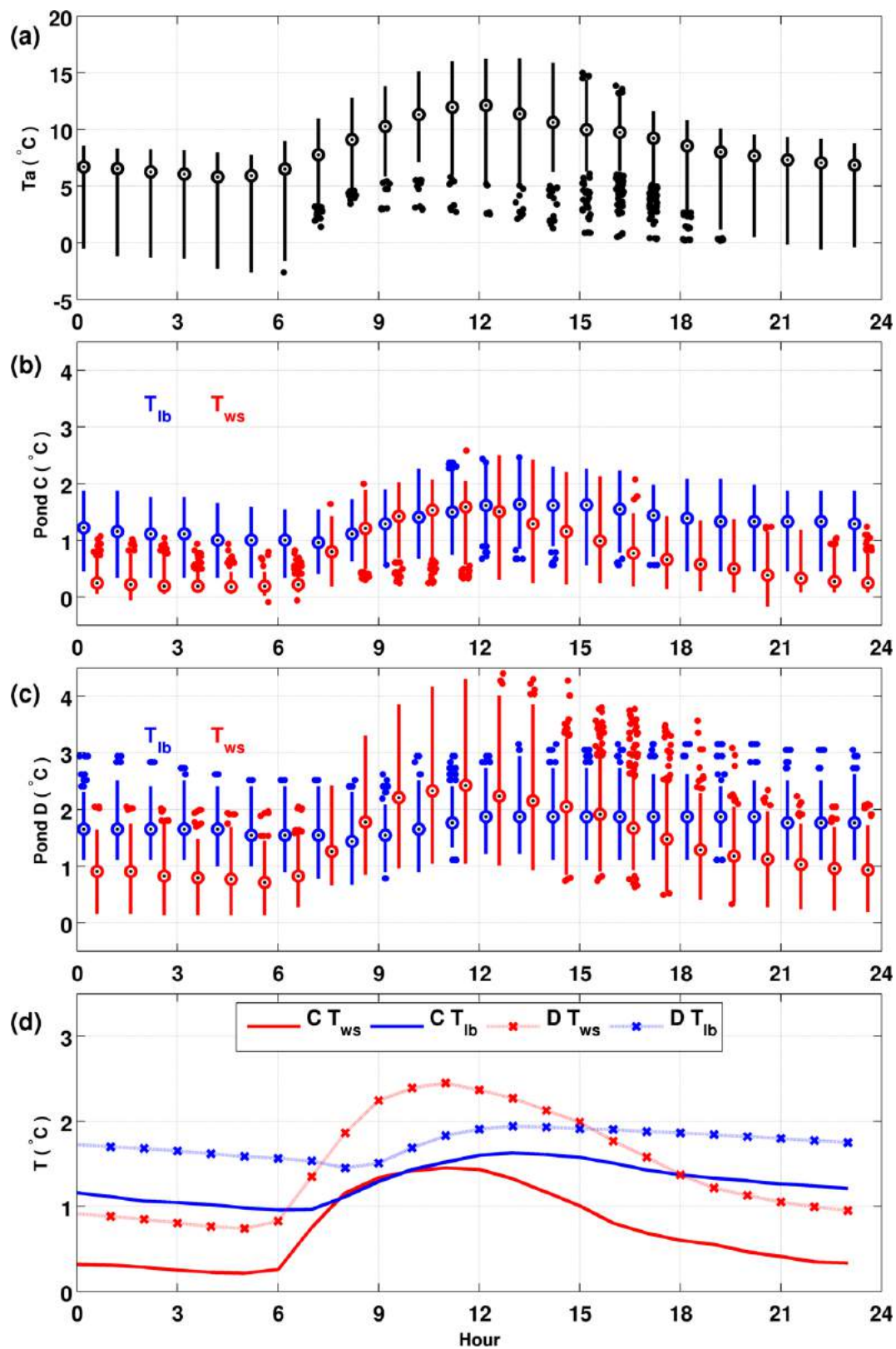


Fig. 4.15 Hourly boxplots of (a) air temperature ( $T_a$ ), (b-c) hourly boxplots of temperature at the water surface ( $T_{ws}$ ) and pond bottom ( $T_{lb}$ ) for ponds C and D, and (d) a comparison of hourly water temperatures at the two ponds.

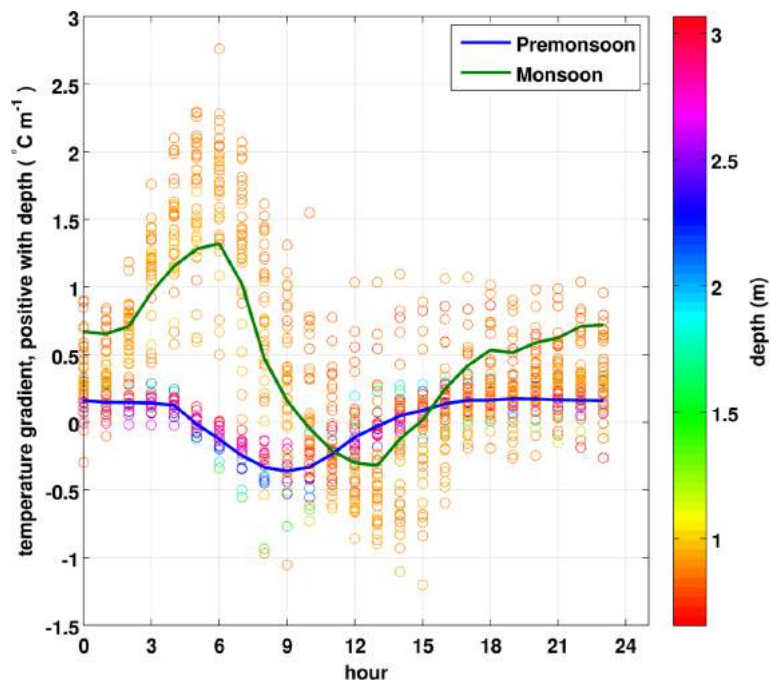


Fig. 4.16 Observed hourly water-column temperature gradients (positive downward) coloured by depth (m) at time of measurement for 15-29 April and 7 May-20 June, 2014, at pond C, highlighting the distinct diurnal signal of temperature fluctuations for the early and late pre-monsoon. The mean hourly gradient is shown for each period. Depth is according to the pressure transducer at the time of the joint surface and pond bottom temperature measurements.

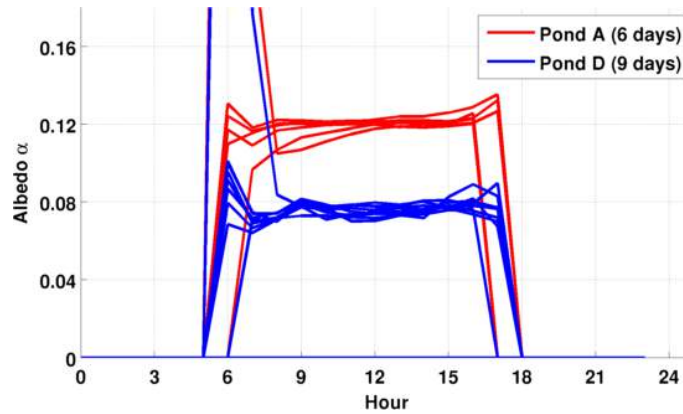


Fig. 4.17 Albedo observations for ponds A and D during May 2014.

#### 4.4.4 Pond albedo

The Kipp and Zonen CM7B albedometers installed in ponds A and D recorded incoming and outgoing shortwave radiation, producing hourly estimates of pond albedo. Data were trimmed to the periods of the day when incoming shortwave radiation was over  $200 \text{ W m}^{-2}$  to reduce signal-to-noise errors. Observations encompassed 6 days for pond A and 9 days for pond D. Albedo for both ponds varied only slightly during the day, increasing slightly in the morning and occasionally again in the late afternoon (Figure 4.17). The early morning and late evening recorded unsteady albedo values due to the decreasing solar elevation angle and declining incoming radiation. Generally, however, the ponds' albedo fluctuated around values of  $\alpha_A = 0.12$  and  $\alpha_D = 0.08$ .

#### 4.4.5 Wind speed

Hourly wind speeds recorded at AWS Lirung and AWS Kyanjing in 2014 over 158 days show similar diurnal patterns (Figure 4.18). At both AWS locations, wind speeds are low at night, then begin to rise sharply by about 9:00, reaching peak values between 11:00 and 13:00, then declining slowly to reach night-time values at 20:00. Although exhibiting similar diurnal signals, the sites differ in terms of wind magnitude. Median night-time winds are  $0.2\text{-}0.5 \text{ m s}^{-1}$  at AWS Lirung, but  $1\text{-}1.3 \text{ m s}^{-1}$  at AWS Kyanjing. The peak hourly median value of wind speed at AWS Lirung is  $1.1 \text{ m s}^{-1}$  and occurs at 11:00, whereas the peak hourly median value at AWS Kyanjing is  $6.1 \text{ m s}^{-1}$  at 13:00. The two locations also show different hourly wind speed variability: the interquartile range at AWS Lirung is  $0.2\text{-}0.4 \text{ m s}^{-1}$  at all hours of the day, whereas AWS Kyanjing has an interquartile range of about  $1.0 \text{ m s}^{-1}$  for the night and early morning, but the interquartile range increases to  $3.0 \text{ m s}^{-1}$  for the late morning and afternoon.

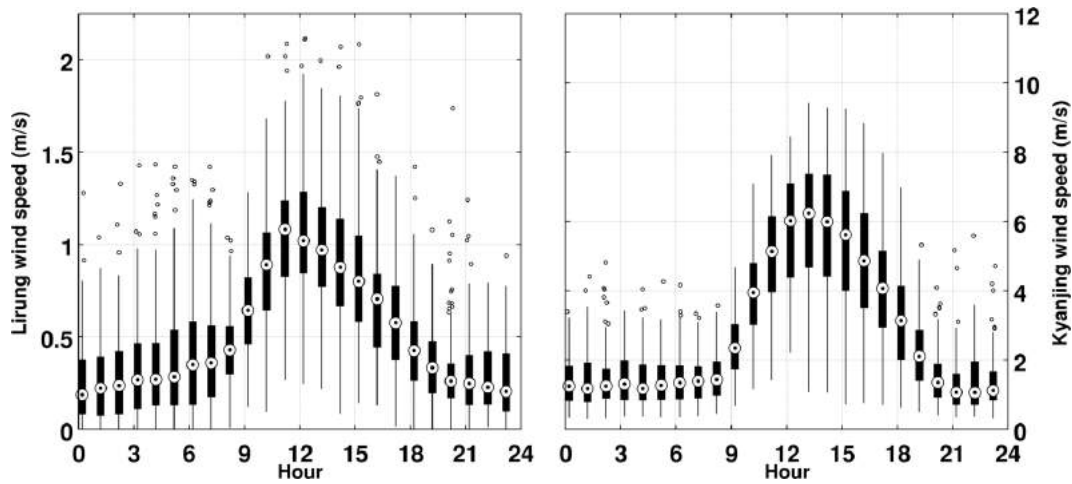


Fig. 4.18 Box plots of hourly wind speeds at AWS Lirung and AWS Kyanjing highlight a similar diurnal pattern, but differing magnitudes (158 days of 15-minute observations).

The wind speeds measured at AWS Lirung were of a comparable magnitude ( $0\text{--}3\text{ m s}^{-1}$ ) to the wind speed observations near pond D for the 6 days of concurrent observation (Figure 4.19). Due to the short record, the box plots highlight variability for some hours, but the diurnal pattern is very similar for the three sensors, with night-time hourly wind speeds of  $0\text{--}1\text{ m s}^{-1}$  and day-time wind speeds of  $1\text{--}3\text{ m s}^{-1}$ . The median hourly observations at the crest above pond D are very similar to observations at AWS Lirung during the night, but are much higher than either of the other sites during the day. Wind speeds within the pond D depression were lower than at the other sites during the night ( $< 0.2\text{ m s}^{-1}$ ), but are very similar to observations at AWS Lirung during the day,

## 4.5 Discussion

### 4.5.1 Ponded area seasonality

The orthoimage pond observations provide basic documentation of pond seasonality, but are limited in coverage of the debris-covered area. The seasonality of ponding evident in Figure 4.2 and Table 4.3, does not precisely replicate the pattern observed in Landsat imagery from 1999-2013. This is due to both spatial and temporal differences in observation: the Landsat imagery does not precisely delineate each pond due to the 30 m ground resolution, but is able to provide observations for much of the year.

When controlling for a common observed area, the orthoimage observed pond density values are nearly identical for 2013 and 2014, with 0.21% relative pond area in May and 0.14% in October-November. This ‘Common’ area experienced significantly more pond-

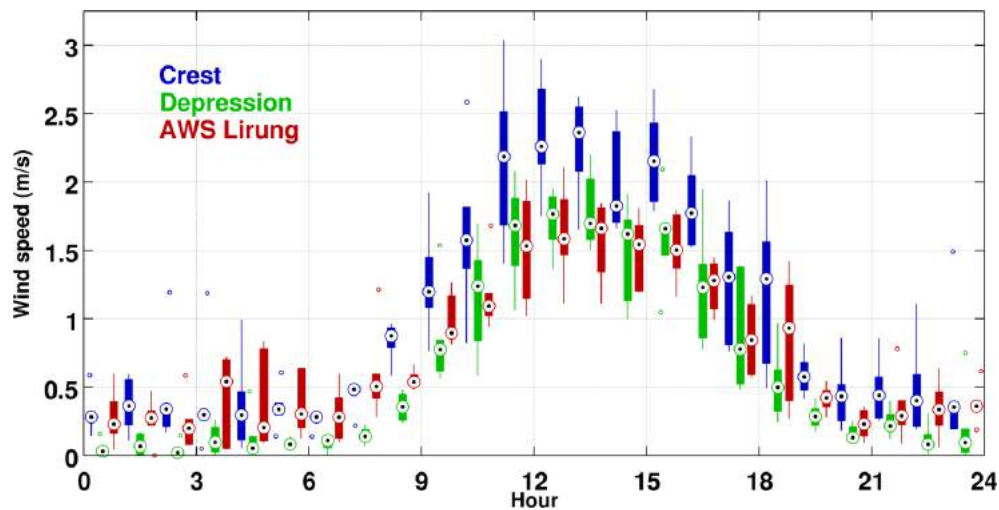


Fig. 4.19 Box plots of hourly wind speeds near pond D and at the AWS Lirung during pre-monsoon 2014 (6 days of observation).

cover in April 2014 (0.5%) than in May. The basin-wide Landsat-derived pond seasonality indicates that ponds are still thawing and growing until the beginning of June, suggesting that pond-cover may peak earlier for Lirung Glacier than the basin as a whole. If true, an earlier pond emergence at Lirung Glacier could be due to its lower altitudinal position than the rest of the valley's debris-covered glaciers, or it could also be a meteorological coincidence in 2014. However, this conjecture is based on very limited data; seasonality of supraglacial ponds is a new subject of investigation and requires targeted observation strategies. Specifically, future research should focus on observations with high spatial and temporal resolution encompassing March–November to clearly describe changes in surface water storage.

#### 4.5.2 Pond size and Landsat observations

Unfortunately, the high-resolution orthomosaic images do not temporally correspond to the Landsat observations presented in Chapter 3, so a direct comparison is not possible. Instead, investigation of pond sizes allows a rough assessment of the coarse-resolution pond observation errors.

46 individual pond observations were made from the five orthoimages, with a mean pond area of 610.5 m<sup>2</sup> and a total observed pond area of 28,081 m<sup>2</sup>. The size of a Landsat pixel (900 m<sup>2</sup>) is the 83rd percentile of pond size, and ponds larger than this threshold accounted for 68.5% of the total pond area. Considering that Landsat may identify pixels with a majority of the pixel covered by ponded water, 450 m<sup>2</sup> is the 67th percentile of pond size, and larger

ponds account for 86.4% of the total observed area. On the other hand, ponds covering 3600 m<sup>2</sup> (the area of 4 Landsat pixels and the threshold considered by Gardelle et al., 2011; Wessels et al., 2002; Liu et al., 2015), are above the 97th percentile of pond size from these observations, and account for only 40.1% of total pond area at Lirung Glacier.

The study of supraglacial ponds by Sakai et al. (2000) also investigated Lirung Glacier, though the glacier's rapid retreat had only just begun at the time of the study and the glacier has lost a substantial portion of its debris-covered area in the interim. In total, 53 ponds were found on the glacier surface but area is only provided for the 7 ponds studied in detail. Those included one pond of 5805 m<sup>2</sup> and six smaller ponds of up to 400 m<sup>2</sup>. A single large pond accounted for a significant portion of the observed pond area, as in 2014.

These pond size-distributions may be biased to the small end due to Lirung Glacier's relatively small size, but indicate that even in the presence of very large ponds (such as pond J), numerous small ponds account for a respectable portion of total ponded area that should not be neglected. On the other hand, the majority of ponds are smaller than a single Landsat pixel, and subpixel effects may result in substantial overestimation of total ponded area if Landsat identifies these pond-containing pixels.

### 4.5.3 Behaviour and interaction of ponds

The water-level variations and pond area changes characterise a variety of behaviours typical of supraglacial ponds. It is first important to distinguish between water-level changes and pond drainage or filling. A perched pond with no input should remain at the same level unless its bounding geometry changes or connectivity is established with the englacial conduit network. This was the case for pond D in 2013, which exhibited minimal changes in pond area or geometry, and showed a static water level from the May 2013 to May 2014 as observed by the DEMs. For ponds with a subaqueous bare-ice interface, melt induced by pond circulation leads to a significant change in bounding geometry, and as a consequence of the density difference between water and ice, the pond water surface lowers even though pond drainage has not occurred. This was clearly the case for pond I in 2014, where basin expansion and steady water-level lowering were evident, although the pond and surface depression maintained nearly static geometry. Thus, the pond's drainage would be characterised as a marked deviation from this background water-level lowering. Similarly, small increases in water level could be due to debris deposition within the pond (another geometric change). Steady water-level increases, on the other hand, can only be attributed to significant water inputs.

### Individual ponds

Based on this framework, the observed changes in the four study ponds can be classified into types of behaviour (Table 4.4).

In 2013, pond C initially showed a stable water level (with diurnal fluctuations), then a gradual water-level decline began 25 May, which accelerated around 20 June. These dates are interpreted to bound the changes in the pond's dynamics: first the transition to significant subaqueous melt (outpacing water inputs) when the pond temperature increases around 25 May, then a slight increase in drainage efficiency around 20 June, leading to a slow, steady water-level decline, and a significant decrease in ponded area by October 2013. In 2014, pond C's rapid spike in water level is clearly a significant input of water, and interrupts a steady water-level decline. The steady decline is resumed after the temporarily backed-up water leaves the system, and without a change in slope or level, as might be expected given the englacial discharge of water. Thus, in 2013 pond C shows water-level lowering associated with subaqueous melt followed by slow drainage, while in 2014 the pond shows the lowering effect of subaqueous melt, interrupted by a brief filling and drainage event.

In 2013, pond D underwent very few changes, and appeared to have been entirely disconnected from the rest of the glacier's hydrological network; it fit the definition of a 'perched' pond. In 2014, though, pond D exhibited an overall water-level rise followed by a decline, encompassing a period when the pond experienced significant basin expansion and shrinkage. The unsteady water-level rise is interpreted to be due to net water influx until 15 June, when a change in the water balance or increased basin expansion led to a general decline in water level. This decline has a steady underlying slope, suggesting subaqueous melt or basin expansion rather than drainage, but is interrupted by sudden changes in water level. These occasional sudden water-level increases may be due to the capture of very large boulders during basin expansion, which would displace a significant volume for the small pond. Some pond drainage is probable, as the pond audibly established a connection to a flowing englacial conduit and significantly declined in surface area during 2014, but such drainage must have been inefficient.

Pond I experienced moderate changes in basin geometry in 2013, associated with a strong net water-level lowering, ponded area decrease, a change in the subaerial ice cliff's appearance, and the emergence of a relict conduit segment through roof collapse. The changes are interpreted to indicate pond-filling prior to the May 2013 visit, submerging any thermo-erosional notches, followed by additional water inputs during the monsoon associated with the conduit roof collapse. Eventual drainage during 2013 lowered the water level and decreased the pond's surface area, exposing vertical segments of the ice cliff and thermo-erosional notches. In 2014, pond I maintained its area but the water level gradually

Table 4.4 Summary of observed pond changes and inferred behaviour for 2013 and 2014. The column ‘Ice cliff’ indicates whether the pond was observed to be in direct contact with a subaerial ice cliff.

Year	Pond	Water level changes	Area changes	Ice cliff	Other	Interpretation
2013	C	Slow water-level decline, change in slope mid-June	50% area decline	Y	–	Subaqueous melt, followed by drainage
2013	D	No change (DEM)	<2% change	N	–	Minimal change
2013	I	6 m lowering (DEM)	25% area decline	Y	Conduit collapse	Subaqueous melt, possible filling, drainage
2013	J	Steady slow increase, then steady decrease	94% area decline	Y	Conduits revealed	Drainage
2014	C	Spike in late April, steady slow lowering	77% area decline, then 36% increase	Y	–	Filling, drainage, then subaqueous melt
2014	D	Unsteady rise and lowering	24% area decline, then 57% decline	Y	–	Slight filling, basin expansion
2014	I	Continuous lowering	11% increase	Y	–	Subaqueous melt
2014	J	Continuous increase to June	60% decrease Apr-Nov	Y	Conduits revealed	Filling and drainage, some subaqueous melt

declined. This slow rate of water-level lowering is certainly due to subaqueous melt and the difference in density between water and ice rather than drainage.

Finally, pond J expressed clear filling and drainage in each of the years. The steady water-level increases are certainly pond-filling, and in both years the pond drained during the monsoon. For 2014, the water-level record only indicates a steady rise of 6 m. In 2013, though, pond J’s behaviour is nuanced: a gradual water-level increase until 31 May is followed by stability until 10 June, two sudden increases in water level, then a gradual decrease until 15 June, when a 10-day drainage occurs. This is interpreted as water inputs outpacing subaqueous melt until 31 May, when a balance is reached. The sudden rises in water level on 9 and 10 June represent significant volume inputs given the pond’s size, most likely associated with either boulder capture or calving. The gradual decline in water level (11-15 June) suggests that subaqueous basin expansion is outpacing water inputs. Pond drainage then begins on 15 June when an efficient connection is established with englacial conduits.

### Behavioural themes

A few common themes are evident from the inferred pond behaviours. First, it is apparent that slow water-level lowering occurs as a background signal at nearly all locations due to basin expansion, commonly associated with subaqueous bare-ice melt. The pond drainage events also appear to occur slowly, spanning several days or weeks, in contrast to a sudden pronounced drainage. On the other hand, moderate water-level increases can occur both rapidly or over the course of several weeks. Diurnal variations of several centimetres occur for all ponds, which were associated with the timing of water supply and evaporation, while

irregular increases in water level due to sudden mass input can occur for both small and large ponds.

Seasonal variability is observed for the whole glacier's ponded area from the orthoimages and from Landsat (Chapter 3), but it is notable that some individual ponds may experience repeated seasonal filling and drainage. In both years, ponds C and J exhibited higher pond area in the premonsoon, followed by a drainage prior to the post-monsoon observations. Pond D also fits this characterisation in 2014, and pond I in 2013. Seasonal fluctuations of individual ponds could be driven by variations in ablation and water delivery, but a structural mechanism is required to enable water to back up. It is possible that conduits return to inefficient configurations after a drainage event due to englacial structural collapse, snowfall, or debris deposition and freeze-on. Alternatively, distinct drainage paths may be utilised in subsequent years, as the water-level lowering renders the previous efficient drainage path inaccessible.

The four pond systems observed in detail persisted over both monsoon seasons, while the small perched ponds on the lower glacier tongue (A,B,E,F,G,H) were only observed to persist for one monsoon season. The striking difference is pond area: ponds that persisted all had mean surface areas  $> 200 \text{ m}^2$ , while those that did not all had mean surface areas  $< 200 \text{ m}^2$ .

Other common attributes of the persisting ponds is that 1) they were adjacent to ice cliffs or developed them, and 2) the water level experienced an overall decline year to year. These attributes may be closely linked, as a continuous water-level decline is only possible with rapid basin expansion and lowering, while a persisting pond is likely to absorb excess energy and warm, leading to eventual subaqueous subdebris ablation and surface lowering.

### **Pond interaction**

The longer records of water level for ponds C and J in 2014 captured an interesting set of events in the early pre-monsoon of 2014. The peak of pond C's water level in the afternoon of 21 April is closely tied to the sudden rise in water level at pond J (estimated volume increase of  $6000 \text{ m}^3$  over the following day). Subsequently, the pond C water level drops over ten days (estimated pond volume change of  $1600 \text{ m}^3$ ) before switching into a gradual decline, while pond J sustains an increase in water level until at least June. I interpret this behaviour as a reconfiguration in the englacial hydrological network on 21 April, which initiated the backup of water in pond J. This change must have simultaneously cut off the supply of water to pond C, allowing it to discharge until its return to a local hydraulic table. Unfortunately, no water-level records were available for other ponds at this time to determine if this event had any other effects on the glacier.

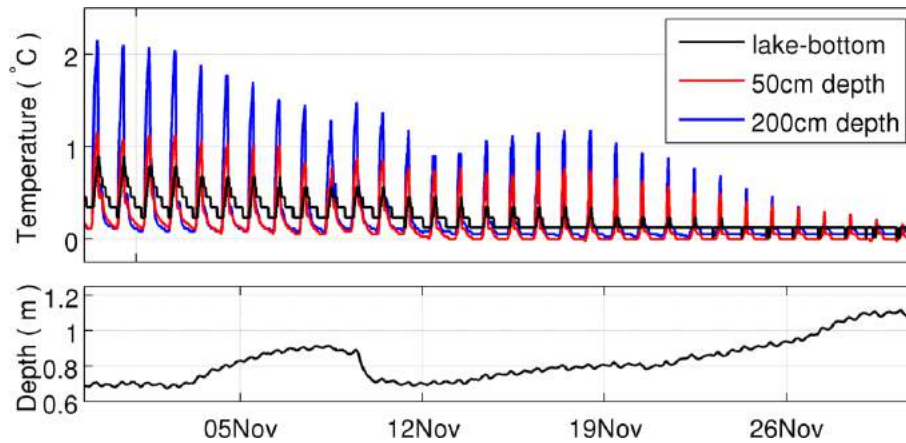


Fig. 4.20 Decline in pond diurnal temperature fluctuations as  $T_a$  declines leading into winter.

### Winter behaviour

As pond C was equipped with a thermistor string (measuring temperature at 50 cm depth, 2 m depth, and the pond-bottom) during the 2013-2014 winter, observations encompassed the freeze-over and thaw-out process ponds undergo annually. The initial period of observation in the late post-monsoon shows a strong diurnal pattern in each of the records (Figure 4.20). During this period, all sensors record a damped response to the diurnal forcing by the air temperature, which is above zero during the day and below zero at night (not shown). The pond-bottom temperature is slower to respond to decreasing air temperatures and the pond-bottom retains heat during the night, resulting in a decreased diurnal amplitude.

Following the post-monsoon decline in diurnal temperature peaks, a distinct regime emerges for the period December-March, characterised by sub-zero temperatures for the 50 cm and 200 cm temperature sensors and freezing-point temperatures for the pond-bottom sensor (Figure 4.21). This period corresponds to ice formation and growth on the pond surface, allowing temperatures to decline below  $0^\circ\text{C}$ . The two profile sensors record similar patterns, while the pond-bottom temperature remains constant for the entire season. In early April, the pond's surface thaws and the 50 cm and 200 cm temperature sensors both resume a diurnal cycle, with peak temperatures to  $2^\circ\text{C}$  and daily minima above freezing (Figure 4.22). Soon thereafter, the pond-bottom temperatures also rise above  $0^\circ\text{C}$ . The diurnal pattern in all three temperature sensors becomes more prominent into late April.

The freezing-in period of the sensors at the surface takes about a month, with the surface frozen about 1 December. The ice-cover temperatures significantly deviate from zero over winter, suggesting development of a moderately-thick insulating layer. This conveniently aligns with an increase in observed water pressure of 0.25 m.w.e., which I interpret as snow overburden. Assuming  $\rho_s = 250 \text{ kg m}^{-3}$  as for settled snow, this would equate to about 1 m

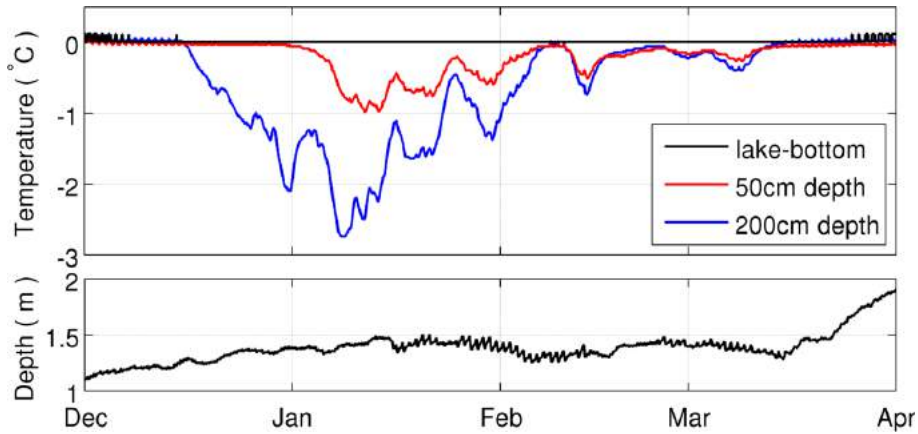


Fig. 4.21 Sub-freezing winter temperatures recorded at depth as a layer of ice forms on the pond's surface. The pond is liquid beneath, as pond-bottom temperature is held constant at the freezing point.

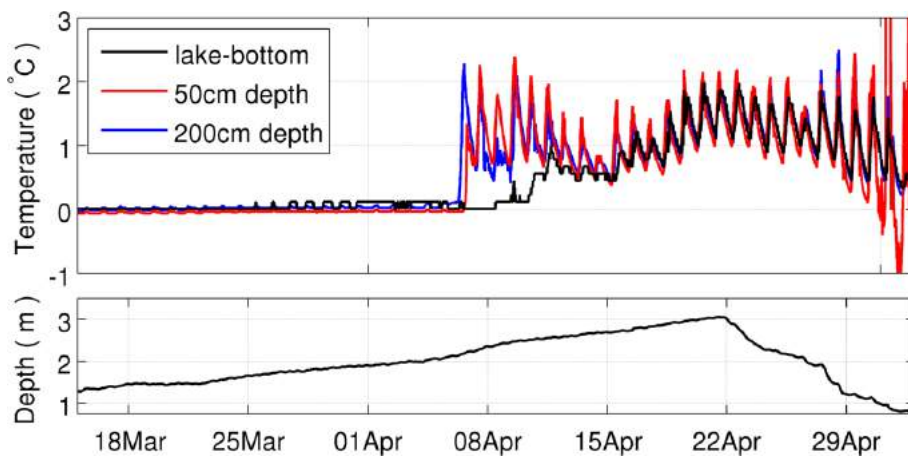


Fig. 4.22 Emergence of diurnal temperature fluctuations in early April, coupled with increasing pond levels, then drainage and subaerial temperature records.

snow accumulation on the iced surface of the pond for much of January 2014, and the lowest portion of this snow surface would have formed a thicker ice crust, such as the remains of ice layers observed at many ponds in the study area (e.g. Figure 4.23). These over-winter observations clearly indicate that the ponded water has little effect as a heat reservoir in winter, and that the pond surface does not directly interact with the atmosphere for this period. Therefore, the pond does not act as an energy source for melt until the surface ice and snow layer diminishes.



Fig. 4.23 (a) Floating ice observed in pond C in May 2013 was the remains of a pond-surface ice layer of moderate thickness, rather than due to supraglacial calving. (b) The collapsed remains of a pond's winter ice surface from Langtang Glacier in May 2014, where the water level lowered sometime after freeze-over. In both cases, the ice fragments have a flat, plate-like appearance.

#### 4.5.4 Pond-related phenomena

This thesis is focused on the analysis of pond energy balance, but repeat field visits to Lirung Glacier enabled observation of pond-related phenomena that have been reported by other authors. Although rigorous measurements were not made by this study (see Benn et al., 2001; Röhl, 2008), these phenomena offer basic evidence of the mechanisms by which supraglacial ponds affect the debris-covered surface, and in turn, shape the development of appropriate numerical models. For this reason, several feature types will be individually summarised, then the implications for glacier mass balance and numerical model development will be briefly discussed.

##### Thermo-erosional notches



Fig. 4.24 Waterline melting resulted in the formation of thermo-erosional notches at many ponds during the study. Here are examples from (a) pond C in October 2013, (b) pond D in October 2014, (c) pond J in October 2013, and (d) a pond on Langtang Glacier in May 2013.

Thermo-erosional notches were observed at most ponds with marginal ice cliffs in the study area, regardless of pond area or depression depth (Figure 4.24). Measurement of

thermo-erosional notches was not conducted systematically during the study, but subaerially-exposed notches (such as Figure 4.24b) extended a few metres, similar to the observations of Röhl (2006). Notches have been observed to extend remarkable distances in other locations (Xin et al., 2011).

Two types of notch were observed. First, a series of horizontal waterline scars was observed on pond C (Figure 4.24a). This appearance was only observed at pond C, and was subaerially modified over the next few days. Based on the pressure transducer data, these features seem to align with brief stable periods in the lowering water level. Thus, this set of features is interpreted as evidence of the peak diurnal melt rates during the pond's slow drainage (Section 5.5.3), when the subaqueous melt rate exceeds the subaerial melt rate.

The second, more common notch type exhibited a single lip with a horizontal roof near the waterline, extending under the ice cliff an unknown distance. These notches are most apparent when the water level is below the notch (Figure 4.24b), but notches are also often identifiable very close to waterlines (Figure 4.24c-d). These notches are interpreted to form over longer periods of a stable water level.

### **Supraglacial calving and subaerial ice-cliff collapse**

Of the four ponds observed in detail, only pond J exhibited signs of calving, evidenced by opening crevasses at its margin and floating ice in the pond (Figure 4.25a). This portion of the ice cliff showed sustained crevasse opening during the study period (Figure 4.14), although the only evidence of supraglacial calving was observed in May 2013. Notably, thermo-erosional notches were not visible at this location at this time, although the pond water level subsequently rose several metres before drainage (Figure 4.12), so it is possible that continued notch development at the time of observation was obscured by a rising waterline, or that evidence of the notch did not remain after calving.

Another interesting case of ice cliff crevasse opening was observed on Langtang Glacier in May 2013 (Figure 4.25b). Here, part of a large ice cliff (>40 m prominence) took the shape of an overhanging cave with a scalloped ice surface. The roof of the cave showed crevasse sutures, some of which were reopening; rocks were observed to fall directly through the opened crevasses to the cave floor below. The crevasses are likely to have opened due to enhanced ice deformation as the ice structure lacked support. However, debris is also likely to have played some role in the crevasse opening: the closed crevasse scars show a slightly darker appearance, and reduced albedo could lead to differential ablation and the local flattening of the vicinity of the crevasse scar. Subsequent deposition of debris would then increase overburden for the cave roof structure, and would also greatly increase longwave radiation receipts, causing local ice melt.

### **Ponds and englacial conduits**

Relict englacial conduits were revealed subaerially in several locations by the drainage of ponds or the backwasting of pond-associated ice cliffs during the study (Figure 4.26). Exposed conduits were in varying states of preservation: some presented a circular opening at surface with a complete roof, while some conduits presented an ice wall on one side of the flow-path with occasional ice arches spanning the channel. The relict conduits were always located with an ice cliff and in association with a supraglacial pond, whether drained or filled.

Relict conduits were exposed through at least three mechanisms. First, a decline in pond water level exposed segments of relict conduits at pond J in both years. In form, these segments were always characterised by a single wall, rather than a complete conduit tunnel structure. The structures sometimes occurred leading into the pond depression from up-glacier, and sometimes along the base of the ice cliff confining the depression. It is possible that these segments were exposed subaerially by subdebris ablation after the pond's drainage, but it is likely that the conduits were exposed within the pond prior to drainage due to the very low rates of subdebris ablation for this debris at the site (Ragettli et al., 2015).

Second, on several occasions relict conduits were exposed by ice-cliff backwasting. Without exception, these conduits had a complete tunnel structure, presenting a single circular opening. They appeared in inconsistent locations across the ice cliffs, sometimes opening at the base or sometimes elevated off the pond floor, occasionally intersecting the cliff in multiple locations. I interpret the shape of these conduit openings to be the result of the intersection between a planar ice face and a sinuous conduit passage, and I consider the location to be semi-random based on the distribution of englacial conduits. When located at the depression base, however, these features are likely to have enabled pond drainage, while other positions on the ice cliff may have led to partial drainage or filling of the pond based on the hydraulic head difference.

Third, in at least one case, structural collapse led to the exposure of a conduit segment. The clearest case of this process occurred near pond I between May and October 2013, although a similar process may have occurred for pond D between May and October 2014. In both cases, a surface depression expanded dramatically, higher than nearby rates of ice-cliff backwasting. Importantly, neither feature exhibited a large ice cliff prior to the change, but the area of change was bounded by a large continuous ice cliff on one side and a debris hummock parallel to it within the depression.

### **Implications for glacier mass balance and modelling**

Based on these observations and in agreement with others' work, supraglacial ponds can have pronounced local and distal effects on the shape and evolution of a debris-covered glacier's surface. Some of these effects are direct, such as pond-associated ablation, while others are indirect.

First, the presence of thermo-erosional notches implies that subaqueous melt rates are higher than subaerial melt rates on average, suggesting that pond-associated ablation may be significant. For ice cliffs adjacent to supraglacial ponds, a continuously-high subaqueous melt rate will also enable the ice cliff to persist for a longer duration. In the case of pond drainage, the thermo-erosional notch results in an overhanging ice cliff, which may slowly adjust to planar geometry before reburial. In both cases, the prolonged ice-cliff presence results in a sustained high meltwater production (Buri et al., 2016b). As notches were observed at all ponds with a bare-ice cliff, this indirect effect is probably widespread.

Second, high notch incision rates can lead to calving, but evidence of calving was only observed at one pond location, the largest at the study site (pond J). Most of the ponds and associated surface depressions were fairly small (< 100 m across) and the work of Sakai et al. (2009) suggests that high thermo-erosional rates, sufficient to lead to calving, probably require a larger fetch to develop strong surface currents. Larger, deeper ponds are more likely to develop an internal thermocline and significantly warmer pond water temperatures than observed on Lirung Glacier (Chikita and Joshi, 2000; Xin et al., 2011).

Third, the association of perched ponds and englacial conduit exposure suggests that some ponds may be an integral component of a discontinuous surface and englacial coupled hydrological network, rather than isolated perched features in an enclosed basin simply waiting to establish connectivity with the englacial system in order to drain. Relict conduit structures were found leading into ponded surface depressions in addition to the classic scenario of a conduit outlet. The water-level records support this possibility, with very irregular water-level rises and declines and no evidence of a sudden drainage for any instrumented pond.



Fig. 4.25 (a) Floating ice observed in pond J in May 2013 was likely sourced from supraglacial calving associated with the major crevasse opening due to the lack of backstress. The ice floating at the surface is similar in composition to the exposed glacier ice. (b) Similar opening crevasses were observed on other very prominent, overhanging ice cliffs, such as this cliff on Langtang Glacier in May 2013, where rocks were observed to fall directly through the crevasses to the cave below. The lack of support for the overhanging ice leads to locally-enhanced ice deformation.

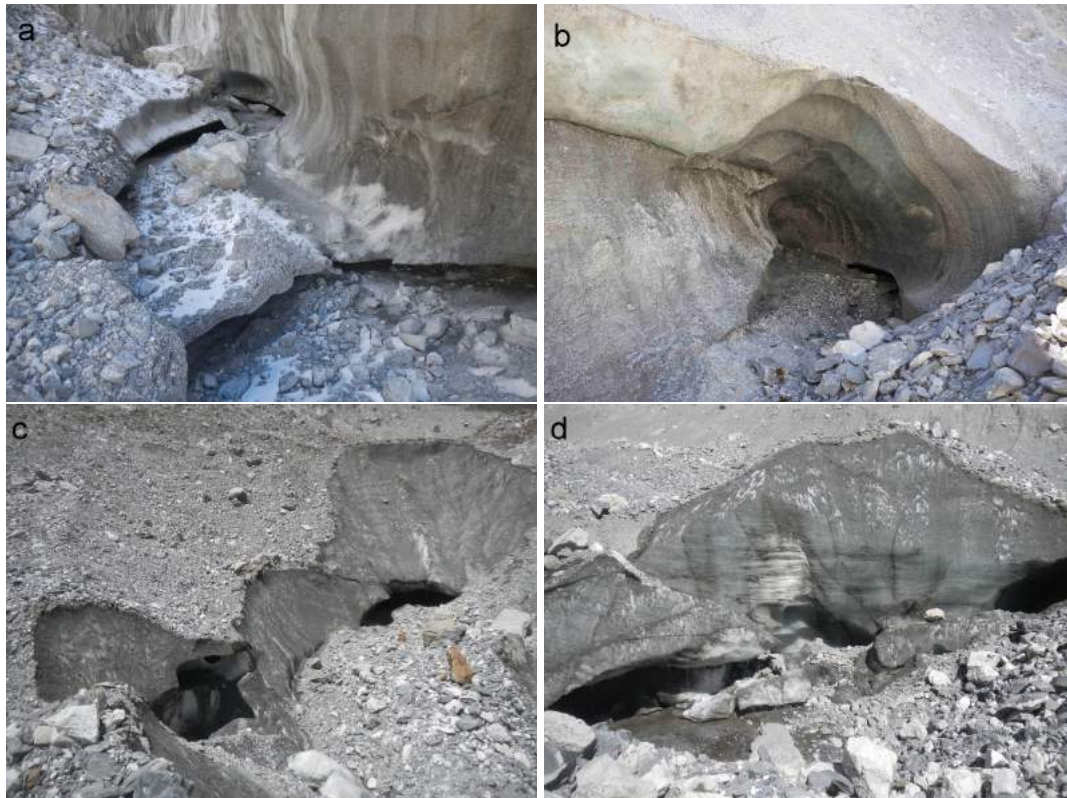


Fig. 4.26 Examples of englaciated conduits exposed in the vicinity of a supraglacial pond: (a) the drainage of pond J exposed a complex of conduits at the ice cliff base in October 2013, (b) a prototypical conduit was exposed near former pond A in May 2014 [photo by Jakob Steiner], (c) ice-cliff backwasting near pond I revealed conduit segments in May 2014, and (d) by October 2014, the drainage of the western portion of pond J revealed conduit segments which may have connected to the conduit in (a).

## 4.6 Summary

Based on field surveys, instrumental records, and high-resolution orthoimages, I have provided a basic characterisation of the supraglacial ponds of Lirung Glacier in May and October of 2013-2014. Overall ponded area is higher in the pre-monsoon (May) than post-monsoon (October), and pond area for Lirung Glacier may be even higher in April than May. Monsoon pond-area observations were not possible although this may be the period of highest overall pond density (Chapter 3). However, water-level records at the four study ponds generally show surface lowering in the early monsoon, and it is possible that Lirung Glacier experiences an earlier seasonal transition due to its low elevation, which may result in earlier meltwater delivery to ponds as compared to the other glaciers of the Langtang Valley.

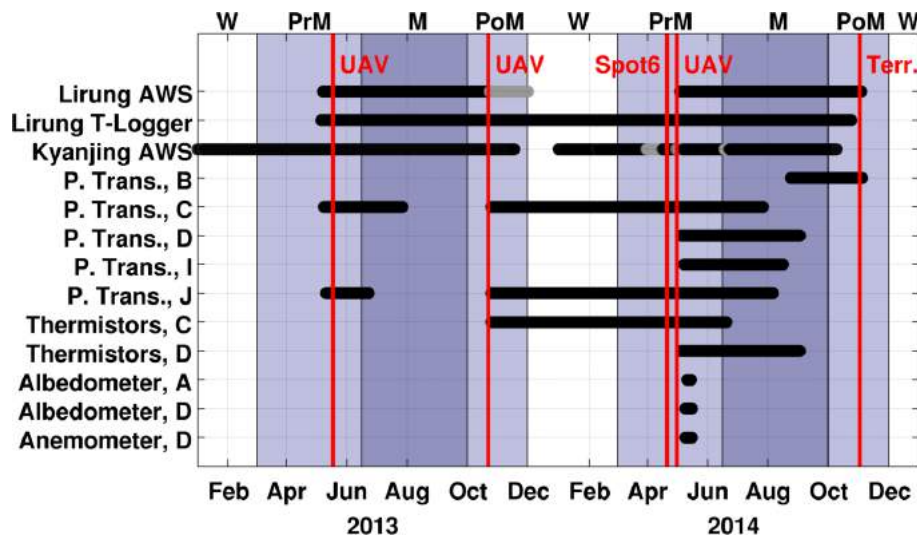


Fig. 4.27 Temporal summary of pond and meteorological data available for this study in 2013 and 2014, with solid black lines indicating data availability and grey indicating incomplete data. Datasets: AWS indicates ‘automated weather station’; P. Trans. indicates ‘pressure transducer’; letters A, B, C, D, I, and J are the pond location of the sensor. Vertical red lines identify orthomosaic acquisition dates from Table 4.2. Seasons are differentiated by background shading and identified above the chart: W for winter, PrM for pre-monsoon, M for monsoon, and PoM for post-monsoon.

Using seasonal orthoimages and instrumental records of pond water level, I assessed the behaviour of four ponds in detail, finding different patterns of pond filling, stability, gradual surface lowering, and drainage. Seasonal refilling of pond depressions was observed at two ponds, but an overall water-level decline over the study period suggests distinct outlets for each year’s drainage. Two of the perched ponds appear to have been englacially connected during March 2014. The freeze-over and thaw-out of a supraglacial pond was documented over winter 2013-2014, and suggests that ponds play little role in the glacier’s

energy balance during that period. I also note interesting pond-related processes observed at the site, including thermo-erosional notch development, subaerial ice structure collapses, and the close association of ponds and englacial conduits.

The observations and field data presented in this chapter provide the basis for energy-balance modelling of Lirung Glacier's supraglacial ponds, but the data have inconsistent spatial and temporal coverage (Figure 4.27). To determine pond energy balance across the entire glacier, a model will first need to be developed to take advantage of the extensive observations available for some ponds (C, D, I, and J). This must be reduced in complexity to represent the ponds without pressure transducer observations. Challenges also remain for source data selection, including both AWS and DEM sources. For the period of model evaluation, the increased spatial and temporal coverage of observations in 2014 make it the logical choice.

# Chapter 5

## Modelling the energy balance of a supraglacial pond

### 5.1 Executive Summary

Supraglacial ponds on debris-covered glaciers present a mechanism of atmosphere-glacier energy transfer that is poorly-studied, and only conceptually included in mass-balance studies of debris-covered glaciers. This research advances previous efforts to develop a model of mass and energy balance for supraglacial ponds by applying a free-convection approach to account for energy exchanges at the subaqueous bare-ice surfaces. The model is developed using field data from a pond on Lirung Glacier, Nepal, that was monitored during the 2013 and 2014 monsoon periods. Sensitivity testing is performed for several key parameters, and alternative melt algorithms are compared with the model. The pond acts as a significant recipient of energy for the glacier system, and actively participates in the glacier's hydrologic system during the monsoon. Melt rates are  $2\text{-}4\text{ cm d}^{-1}$  (total of  $98.5\text{ m}^3$  over the study period) for bare ice in contact with the pond, and  $< 1\text{ mm d}^{-1}$  (total of  $10.6\text{ m}^3$ ) for the saturated debris zone. The majority of absorbed atmospheric energy leaves the pond system through englacial conduits, delivering sufficient energy to melt  $2612\text{ m}^3$  additional ice over the study period ( $38.4\text{ m}^3\text{ d}^{-1}$ ). Such melting might be expected to lead to subsidence of the glacier surface. Supraglacial ponds efficiently convey atmospheric energy to the glacier's interior and rapidly promote the downwasting process.

## 5.2 Specific Objectives

This chapter seeks to develop and test a model representing the energy and mass balance of a supraglacial (perched) pond based on the field observations on Lirung Glacier (Chapter 4). Few studies have attempted to quantify the energy exchanges associated with supraglacial ponds, or their effects on glacier ablation. Xin et al. (2011) identified two kinetic types of melt: i) winds may force currents to drive thermo-erosion and notch development near the lake surface; and ii) free convection, due to the density-temperature relationship of water, may drive pond circulation and therefore promote melt along the entire water-ice interface. Sakai et al. (2000) and Röhl (2008) each adapted empirical relationships from iceberg melt observations to examine subaqueous and waterline melting of ice cliffs, while Luthje and Pedersen (2006) adapted a method based on free convection to study basal melting of ponds on the Greenland ice sheet. To date, no effort has been made to compare these algorithms or to apply a melt model based on physical principles to supraglacial ponds on debris-covered glaciers. These are therefore objectives for the chapter.

## 5.3 Methods

Here I first present the framework and calculations of the model, then describe the source data and configurations for testing the model.

### 5.3.1 Model setup

Supraglacial lakes on debris-covered glaciers are complex systems with multiple boundary exchanges of energy and mass. This study closely follows the analytical framework of Sakai et al. (2000), although improvements have been made to nearly all computations. The approach treats the whole lake as a single control volume that can change in mass and energy (Figure 5.1). Changes in mass are expressed in practice by a change in volume ( $\Delta V$ ), and indicated by water-level changes ( $\Delta h$ ). This can be due to adjacent ice-cliff melt or catchment runoff ( $\dot{V}_i$ ), discharge ( $\dot{V}_d$ ), rainfall ( $\dot{V}_R$ ), or latent fluxes of water ( $\dot{V}_{LE}$ ), all in  $\text{m}^3 \text{s}^{-1}$ . Three distributed energy fluxes [ $\text{W m}^{-2}$ ] need to be modelled for energy-balance calculations: 1) at the air-atmosphere surface of the pond's water ( $Q_n$ ); 2) at the saturated debris surface at the pond's base ( $Q_d$ ); and 3) at the subaqueous bare-ice surface ( $Q_i$ ), and all need to be scaled by their respective areas. Additionally, energy can be advected into or out of the system via mass transfer across the control boundary volume. Combined with the energy fluxes, the rates of energy input ( $I$ ) and discharged ( $D$ ) lead to a rate of change in stored energy ( $\Delta S$ ), all in [W].

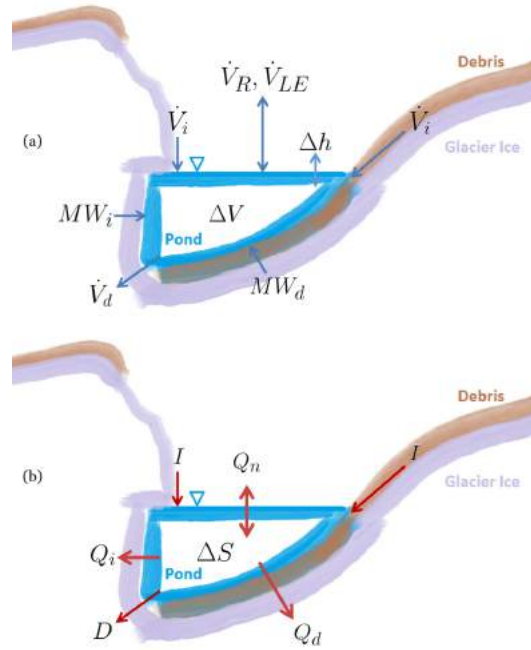


Fig. 5.1 Conceptual mass (a) and energy (b) exchanges for the pond control volume.

### Stored mass and energy

Considering the control volume as a reservoir of mass and energy, the internal energy of the pond  $S$  [J] that is available for melt can be calculated using Equation 5.1, where  $c_w$  [ $\text{J kg}^{-1} \text{K}^{-1}$ ] is the specific heat of water,  $\rho_w$  [ $\text{kg m}^{-3}$ ] is the density of the water,  $T_p$  [K] is the mean pond temperature, and  $V_p$  [ $\text{m}^3$ ] is the current volume of the pond. Changes in this stored energy must be compensated by energy transfer at the control volume boundaries, expressed in Equation 5.2. Here  $Q_n$  is the net surface flux from the atmosphere,  $Q_i$  is the energy exchange at subaqueous bare-ice surfaces,  $Q_d$  is the energy exchange through subaqueous debris,  $I$  [W] is the rate of energy advected into the pond by runoff inputs, and  $D$  [W] is the rate of energy removed from the pond by discharge.  $A_p$ ,  $A_i$ , and  $A_d$  [ $\text{m}^2$ ] are the areas of the atmosphere, ice, and debris boundaries.

$$S = c_w \rho_w V_p (T_p - 273.15 \text{ K}) \quad (5.1)$$

$$\Delta S = Q_n A_p + Q_i A_i + Q_d A_d + I + D \quad (5.2)$$

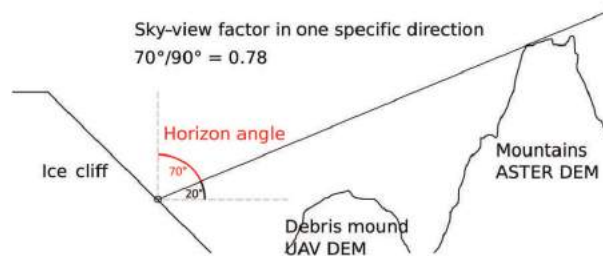


Fig. 5.2 Geometry for determining hemispheric sky and terrain view-factors ( $V_sI$  and  $V_d$ ), reproduced from Figure 7a in Steiner et al. (2015).

### Surface energy balance

At the water surface (Equation 5.3), energy exchanges between the pond and atmosphere include net shortwave ( $I_n$ ) and longwave ( $L_n$ ) radiative fluxes, sensible ( $H$ ) and latent ( $LE$ ) turbulent fluxes, and advected energy due to rainfall ( $Q_r$ ), all in [ $\text{W m}^{-2}$ ]. Most terms are calculated as described by Steiner et al. (2015) and so here I provide only a brief description of the terms, highlighting the differences between my equations and those of the earlier study. Note that  $I$  is the rate of energy advected into the pond by inputs of water, with units of [ $\text{W}$ ], while  $I_n$  is the net shortwave flux of energy at the pond's surface, with units of [ $\text{W m}^{-2}$ ].

$$Q_n = I_n + L_n + H + LE + Q_r \quad (5.3)$$

Incoming shortwave radiation is determined based on individually-modelled direct ( $I_s$ ), diffuse ( $D_s$ ), and debris-reflected ( $D_t$ ) radiation components (see Figure 5.2 and Steiner et al., 2015, Section 3.1.1), incorporating view factors determined using the pond's position. The sky view-factors are the hemispherically-integrated horizon angles determined for near  $V_{sL}$  and far  $V_{sI}$  terrain, and range from 0 to 1. The debris-view-factor  $V_d$  is the complement of  $V_{sL}$ , to express exposure to the debris surface, which usually has a high-temperature relative to the majority of topography. The view factors are determined using the lake's position and a high-resolution DEM.

The pond's albedo is estimated using the empirical relation previously applied by Sakai et al. (2000), itself determined from Tsho Rolpa Lake, where  $\alpha$  is albedo and  $\theta_s$  is solar elevation (Equation 5.4). The net shortwave flux  $I_n$  [ $\text{W m}^{-2}$ ] is then calculated as in Equation 5.5.

$$\alpha = 0.78 \theta_s^{-0.45} \quad (5.4)$$

$$I_n = (I_s + D_s + D_t)(1 - \alpha) \quad (5.5)$$

The net longwave radiation  $L_n$  [ $\text{W m}^{-2}$ ] is calculated (Equation 5.6) as a combination of atmospheric ( $L_{in}$ ) and debris ( $L_d$ ) sources, scaled by view factors  $V_sL$  and  $V_d$  (Steiner et al., 2015, Section 3.1.2), and radiation emitted by the pond surface ( $L_o$ ).  $L_o$  is calculated using the Stefan-Boltzmann law (Equation 5.7) with the pond's surface temperature  $T_{ws}$  [K] and emissivity  $\epsilon_w = 0.95$  (Sakai et al., 2000). The modelling of shortwave and longwave radiation inputs at the pond surface was carried out by Pascal Buri.

$$L_n = L_{in} + L_d - L_o \quad (5.6)$$

$$L_o = \epsilon_w \sigma T_{ws}^4 \quad (5.7)$$

Turbulent fluxes are determined using the bulk aerodynamic method with atmospheric stability correction as implemented by Han et al. (2010), Reid and Brock (2014), and Steiner et al. (2015). The only changes made are associated with the application to a water surface rather than debris, resulting in a saturated film of air at the water temperature and the use of an appropriate surface roughness value for a water surface ( $z_0 = 5 \times 10^{-4}$  m from literature values ranging between  $2.7 \times 10^{-5}$  m and  $1 \times 10^{-3}$  m). The specific energy flux associated with rainfall is estimated using the rainfall rate  $q_r$  [ $\text{m s}^{-1}$ ], and the air temperature  $T_a$  [ $^{\circ}\text{C}$ ] (Equation 5.8).

$$Q_r = c_w \rho_w T_a q_r \quad (5.8)$$

### Subaqueous melt

Energy transfer through the saturated debris zone at the pond bottom is assumed to occur only via conduction, as in Sakai et al. (2000) and Röhl (2008). As in Röhl (2008), the bulk thermal conductivity  $k_{eff}$  [ $\text{W m}^{-1} \text{K}^{-1}$ ] is calculated in Equation 5.9 as a combination of the values for rock ( $k_r$ ) and water ( $k_w$ ), scaled by porosity  $\phi$ . The energy flux through this layer  $Q_d$  [ $\text{W m}^{-2}$ ] can then be calculated based on the pond bottom water temperature  $T_{wb}$  [ $^{\circ}\text{C}$ ], the ice temperature  $T_i$  (assumed to be at the freezing point  $0^{\circ}\text{C}$ ), and the thickness of the saturated debris zone  $d_d$  [m] (Equation 5.10). The melt rate  $v_d$  [ $\text{m s}^{-1}$ ] is the energy flux divided by the latent heat of fusion for water,  $L_f$  [ $\text{J kg}^{-1}$ ] (Equation 5.11).

$$k_{eff} = k_r(1 - \phi) + k_w\phi \quad (5.9)$$

$$Q_d = \frac{k_{eff}(T_{wb} - T_i)}{d_d} \quad (5.10)$$

$$v_d = \frac{Q_d}{L_f \rho_w} \quad (5.11)$$

Several different methods have been applied to model subaqueous melt rates  $v_i$  [ $\text{m s}^{-1}$ ]. Sakai et al. (2000) applied an empirical relation determined from iceberg melt observations (Weeks and Campbell, 1973). This method assumed a strong forced-convection scenario based on average pond temperatures  $T_p$  [ $^{\circ}\text{C}$ ] and a contact length  $x_i$  [m], but the pond's vertical velocity at the bare-ice contact was fixed at  $u_w = 0.02 \text{ m s}^{-1}$  (Equation 5.12). Röhl (2008) implemented a different empirical relation, which depended entirely on water temperature (Equation 5.13, here converted to  $\text{m s}^{-1}$ ). However, the equation was initially formulated based on the freezing point of seawater at  $-1.8^{\circ}\text{C}$  (Russell-Head, 1980), so a more appropriate equation would implement the  $0^{\circ}\text{C}$  freezing point of freshwater instead. Luthje and Pedersen (2006) applied free-convection algorithms optimised for horizontal plates (Linden, 2002; Taylor and Feltham, 2004), to estimate subaqueous melt rates on the Greenland Ice Sheet. For this approach (Equation 5.14), dimensionless constant  $r = 0.1$ ,  $g$  is the standard acceleration due to gravity,  $\nu$  is the kinematic viscosity of water, and  $\kappa_l$  is the thermal diffusivity of water).

$$v_i = 7.14 \times 10^{-10} \frac{u_w^{0.8}}{x_i^{0.2}} (T_p - T_i) \quad (5.12)$$

$$v_i = \frac{1.8 \times 10^{-2} (T_p + 1.8)^{1.5}}{24 \times 60 \times 60} \quad (5.13)$$

$$v_i = \frac{rc_w}{L_f} \left( \frac{\beta g \kappa_l^2}{\nu} \right)^{1/3} (T_p - T_i)^{4/3} \quad (5.14)$$

Our approach takes a step back to the driving causes of melt at the ice-water interface. While wind-driven water currents leading to forced convection can develop for ponds with sufficient fetch (Sakai, 2012), many ponds are much smaller and vertical water velocities are negligible (Xin et al., 2011). Instead, natural convection can occur, where temperature-dependent density differences drive a convective current. Freshwater density peaks at  $4^{\circ}\text{C}$ , so for temperatures below this point, colder parcels will tend to rise, driving circulation. For this analysis, suspended sediment concentrations (SSC) are assumed to be near-constant (i.e. the pond is well-mixed), so only thermal differences drive circulation. Observed SSC values for similar ponds are  $10 - 400 \text{ mg L}^{-1}$  (Bhatt et al., 2007; Takeuchi et al., 2012), and SSC variations of more than  $100 \text{ mg L}^{-1}$  have a sufficiently strong effect on density to drive stratification for much larger ponds (Chikita and Joshi, 2000). The case of natural convection

along a vertical plate was examined and linearised by Churchill and Chu (1975), whose approach is applied here to the case of water near the freezing point.

This first requires evaluation of the Grashof number (Gr), representing the ratio between buoyancy and viscosity (Equation 5.15). Here  $g$  is gravitational acceleration,  $D_l$  [m] is the mean vertical subaqueous ice-water contact length (characteristic length for this geometry),  $\rho_{ws}$  and  $\rho_0$  are the water density [ $\text{kg m}^{-3}$ ] at the lake surface and freezing point, which together drive convection, and  $\rho_f$  and  $\nu_f$  are the density and kinematic viscosity evaluated at  $T_f$ , the mean of the surface and freezing-point temperatures [ $^{\circ}\text{C}$ ]. The Prandtl number ( $\text{Pr}_f$ , the ratio between kinematic viscosity and thermal diffusivity) is evaluated at  $T_f$  to determine the Rayleigh number (Ra), which is used to evaluate if the flow is turbulent and to calculate the Nusselt (Nu) number (Equations 5.16 and 5.17). Finally, the mean coefficient of heat transfer  $h_i$  can be evaluated and applied to determine the heat flux  $Q_i$  [ $\text{W m}^{-2}$ ] and melt rate  $v_i$  [ $\text{m s}^{-1}$ ] due to free convection (Equations 5.18, 5.19, and 5.20).

$$\text{Gr} = \frac{gD_l^3(\rho_{ws} - \rho_0)}{\rho_f \nu_f^2} \quad (5.15)$$

$$\text{Ra} = \text{Gr Pr} \quad (5.16)$$

$$\text{Nu} = \begin{cases} 0.68 + \frac{0.67 \text{Ra}^{1/4}}{\left[1 + \left(\frac{0.492}{\text{Pr}}\right)^{9/16}\right]^{4/9}} & : 10^5 \leq \text{Ra} < 10^9 \\ \left(0.825 + \frac{0.387 \text{Ra}^{1/6}}{\left[1 + \left(\frac{0.492}{\text{Pr}}\right)^{9/16}\right]^{8/27}}\right)^2 & : \text{Ra} \geq 10^9 \end{cases} \quad (5.17)$$

$$h_i = \frac{\text{Nu } k_w}{D_l^3} \quad (5.18)$$

$$Q_i = h_i(T_p - T_i) \quad (5.19)$$

$$v_i = \frac{Q_i}{L_f} \quad (5.20)$$

It is worth noting that the method of Sakai et al. (2002) and the free-convection approach applied here both use a characteristic length ( $X_i$  in Equation 5.12 and  $D_l$  in Equations 5.15 and 5.18, respectively). These two are related concepts defining the characteristic length regulating the transfer of energy in the distinct kinetic modes (advected and natural convection). However, the characteristic lengths are perpendicular due to the geometric difference between buoyancy-driven free convection and wind-driven forced convection. The ice-contact length

for Equation 5.12( $X_i$ ) has to do with the flow of currents across the ice at the water surface, so this is effectively the width of the ice cliff at the waterline. For Equation 5.15, however, the characteristic length ( $D_l$ ) is the mean vertical contact length, which determines the total interface for natural convection. This corresponds to the mean depth of the pond at the ice interface.

### Fluxes of mass and energy

The mass balance of the pond according to Figure 5.1a is given by Equation 5.21. Observed changes in volume ( $\Delta V$ ) must be accounted for by inflows ( $\dot{V}_i$ ), generated melt ( $MW_i$ ,  $MW_d$ ), exchanges of vapour ( $\dot{V}_{LE}$ ) or rain ( $\dot{V}_r$ ) at the pond's surface, or outflows ( $\dot{V}_d$ ). The volumetric rate of evaporation or condensation can be calculated directly from the magnitude of the latent energy flux ( $Q_{LE}$ ) from Equation 5.22. The rain input is simply the precipitation rate scaled by pond area  $A_p$  (Equation 5.23).

$$\Delta V = \dot{V}_i + \dot{V}_{LE} + \dot{V}_r + MW_i + MW_d - \dot{V}_d \quad (5.21)$$

$$\dot{V}_{LE} = \frac{Q_{LE}A_p}{c_w \rho_{ws} T_{ws}} \quad (5.22)$$

$$\dot{V}_R = q_r A_p \quad (5.23)$$

$$\dot{V}_d = \frac{D}{c_w \rho_{ws} T_p} \quad (5.24)$$

Two fluxes remain unspecified at the control volume boundaries (Figure 5.1): mass and energy brought into the system by inflows ( $\dot{V}_i$  and  $I$ ), and mass and energy removed from the system by discharge ( $\dot{V}_d$  and  $D$ ). Field measurements indicate surface water temperatures of  $< 0.1^\circ\text{C}$  for all surveyed flows emerging at the glacier surface or at the terminus, suggesting that negligible energy is added to the system by inflows ( $Q_i = 0 \text{ W}$ ). This enables the simultaneous solution of the mass and energy equations, as the outflow discharge energy ( $D$ ) may be calculated directly from Equation 5.2, and assuming that this discharge removes water at the average pond temperature ( $T_p$ ), the volumetric discharge ( $\dot{V}_d$ ) can be estimated by Equation 5.24. Finally, the flow of water into the pond ( $\dot{V}_i$ ) can be inferred from Equation 5.21.

### 5.3.2 Model evaluation

The above framework has substantial data requirements and has many physically-meaningful parameters that are difficult to constrain, and cannot be calibrated. As a result, I adopt a diagnostic modelling approach to identify the importance of different lake processes. This section describes the data collected and physical parameter selections for driving the standard model configuration.

#### Field data

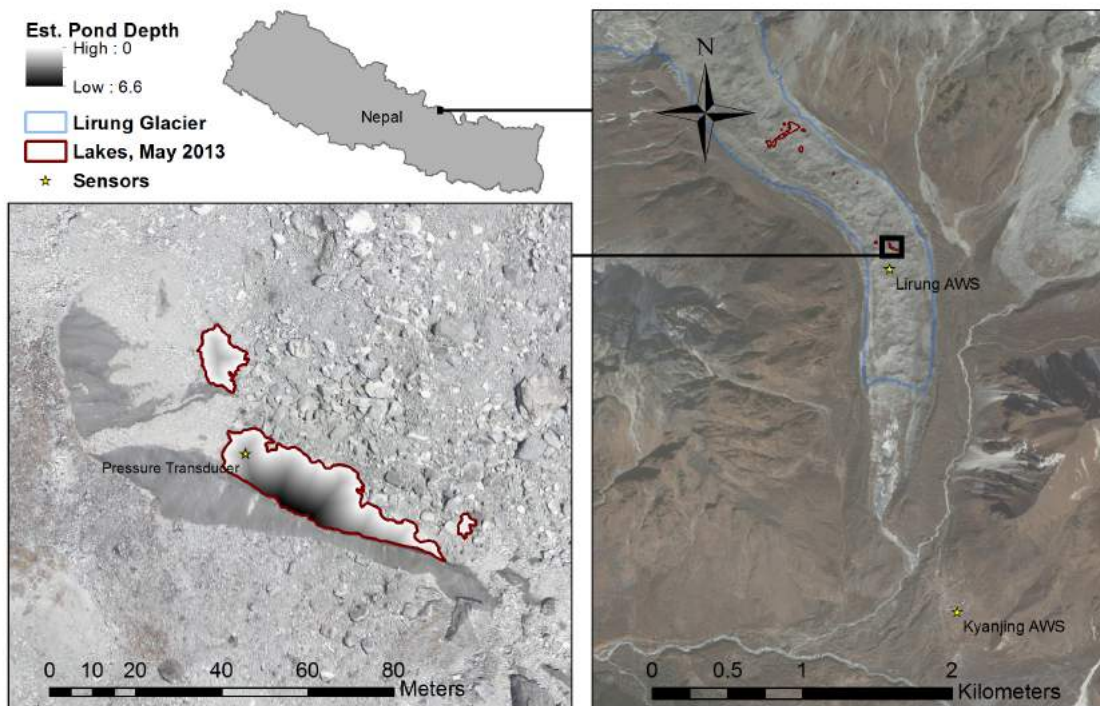


Fig. 5.3 Study site on Lirung glacier and station locations used in this study, with estimated pond depths indicated for the study pond (Pond C). The three bodies of water are hydraulically connected through the thick debris cover, and are modelled jointly.

To develop and test the model, I use the 2013 instrumental records and observations of pond C on Lirung Glacier in the Langtang Valley ( $28^{\circ}13'57''$  N,  $85^{\circ}33'43''$  E WGS84; Figure 5.3). The study pond at 4070 m.a.s.l. was monitored beginning on 8 May 2013, equipped with a HOBO Water Level Logger to measure water pressure and pond bottom water temperature (just above the saturated debris zone). The sensor was cast into the pond, approximately equidistant from the shore and ice cliff (Figure 5.3). The pond's drainage led to the subaerial exposure of the instrument on 15 July 2013 (Figure 5.4), so the study period

is day-of-year (DOY) 130-197, encompassing the late pre-monsoon and the early monsoon of 2013. For May-October 2014 a float was installed with a surface temperature sensor and tethered to the pressure transducer cable to investigate temperature variability within the pond. An automated weather station (AWS Lirung, 4076 m.a.s.l.) was installed 80 m to the south of the pond to monitor atmospheric conditions at the site, recording incoming shortwave radiation ( $I_s$ ), 2 m air temperature ( $T_a$ , shielded and vented), relative humidity ( $rH$ ), and wind speed ( $u_a$ ) and direction. All variables were measured at 5-minute intervals and aggregated to 1-hour values. The barometric sensor from an off-glacier automatic weather station 2.3 km from the study pond at Kyanjing Village (AWS Kyanjing; Figure 5.3) was adjusted to the pond altitude using the ideal gas law, then applied to correct the HOBO pressure signal for conversion to at-sensor depth according to the hydrostatic equation. Precipitation data were taken from the tipping bucket gauge at AWS Kyanjing. Lirung Glacier was observed in May and October 2013 using an unmanned aerial vehicle (UAV), from which a detailed DEM and orthophoto were developed (Immerzeel et al., 2014b) covering the study pond.

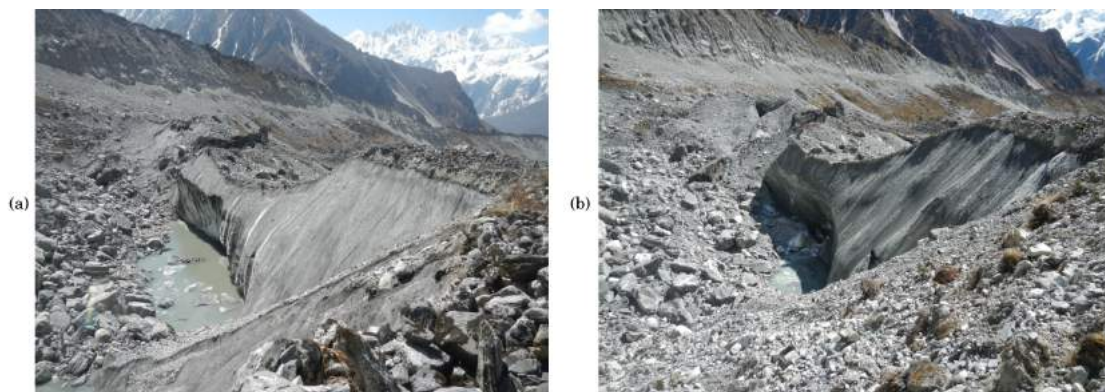


Fig. 5.4 The study pond in (a) May and (b) October 2013, showing ice-cliff retreat and a decreased water level after the monsoon.

### Geometric assumptions

Converting the pressure records to lake volume requires a depth-area-volume relationship. Basic observations with a sonar transducer were limited due to the hazard of rockfall from the small pond's ice cliff, but measurements of pond depths increased linearly approaching the ice cliffs. This suggests a vertical or undercut subaqueous ice cliff, in agreement with observations of notch formation and overhangs at the base of ice cliffs on other debris-covered glaciers (Benn et al., 2001; Röhl, 2008). Considering that a pond in a supraglacial depression likely once filled the entire depression, the current exposed terrain may be similar to the pond basal topography. The slope of Lirung Glacier's surface depressions was investigated

by identifying all closed depressions more than 50 m<sup>2</sup> in the UAV DEM and collecting the slope statistics for each depression and the glacier as a whole. The glacier-wide mean slope for such depressions was 53.2% (28°), while the mean value for the study pond's depression was 67.8% (34°).

The depth beneath water surface at the time of DEM acquisition was then extrapolated from the pond shore (excluding the ice-cliff edge) using the 53.2% slope to produce an estimate of pond depth at the time of DEM acquisition (Figure 5.3), which was added to the pond elevation to produce a grid of subaqueous surface altitudes. Finally, to develop a depth-area-volume curve, the minimum altitude of the pond bottom was determined and incremented by 0.01 m, determining at each step the submerged debris area, pond volume, ice-cliff contact length and mean ice-cliff depth. A time series of water-level altitudes was determined using the hydrostatic equation and the pond's surface elevation at the time of UAV acquisition, and time series of geometric properties were determined from the depth-area-volume curve.

### Temperature assumptions

To apply the model, several measures of water temperature are needed. The pond bottom temperature ( $T_b$ ) is measured directly and assumed to be uniform, and I prescribe an ice temperature ( $T_i$ ) at the ice-water interface of 0°C for the subaqueous ice cliff and the saturated debris zone. The mean water temperature for the pond ( $T_p$ ), the water surface temperature ( $T_{ws}$ ), and film temperature ( $T_f$ ) are all necessary for the energy-balance calculations.

Field observations in this study and by prior investigators (Sakai et al., 2000; Röhl, 2008) indicated very small water surface horizontal velocities for small ponds, suggesting that pond overturning is minimal other than at the ice interface and near inlet and discharge mass exchanges. This limited evidence of widespread convection suggests that the pond's average temperature and surface temperature could be estimated from the temperature gradient within the pond. The thermistors showed strong temperature fluctuations at the pond's surface and the frequent occurrence of an inversion layer (Figure 5.5) similar to that observed by Xin et al. (2011) in timing and gradient magnitude, although the pond was much shallower during the 2014 observation period than the 2013 model period here. Mean observed hourly gradients between the water surface and pond bottom were applied with the 2013 monsoon-observed pond bottom temperatures and pond depths to generate surface and average temperatures for the study period (Figure 5.5). The film temperature ( $T_f$ ) is derived according to Churchill and Chu (1975) as the mean of the surface and freezing-point temperatures.

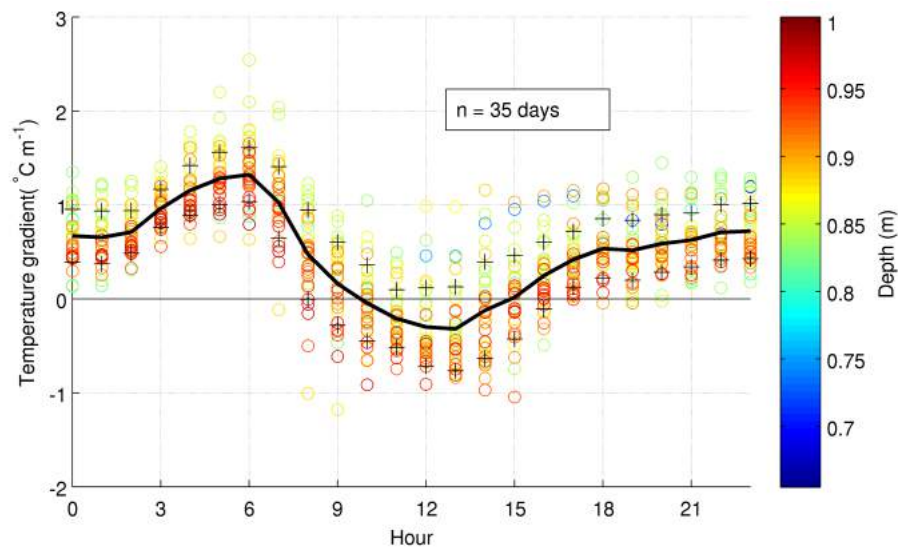


Fig. 5.5 Observed hourly water-column temperature gradients (positive downward) coloured by depth at time of measurement (m) for May-October 2014. The mean hourly gradient is shown as the solid black line, while the  $\pm 1$  standard deviation cases are denoted by +. Depth is according to the pressure transducer at the time of the joint surface and pond bottom temperature measurements. Night-time temperatures exhibit a strong inversion which switches due to diurnal heating at the surface.

### Configuration testing

Due to a paucity of calibration and validation data for this study, several sensitivity tests are performed to consider the effects of key assumptions and parameter choices. For each test, the resulting subaqueous melt and estimated discharge were determined. The test run titles are in *italic*, and model outcomes are summarised in Table 5.1.

This study attempts to represent pond geometry in a more realistic manner than previous analyses, but is limited by the assumption of a constant subaqueous slope of 53.2%. Subaqueous slope is therefore varied between 40% (21.8°) and 80% (38.7°) to consider maximum subaqueous melt quantities based on reasonable subaqueous geometries.

The observed temperature gradients in the pond exhibit hourly clustering over the 2014 monsoon season, but these measurements were made across a narrow range of pond depths. The pond temperature is a critical variable for most components of the model, so four distinct temperature distributions were used to consider a range of possible outcomes: the mean temperature gradient based on the 2014 observations, the mean gradient plus (minus) one standard deviation, and a uniform pond temperature as measured at the pressure transducer ( $T_p = T_{lb} = T_{ws}$ ).

In addition to the free-convection approach presented in this chapter (Equations 5.15-5.20), three other subaqueous bare-ice melt algorithms were evaluated (Sakai et al., 2000; Luthje and Pedersen, 2006; Röhl, 2008), as in Equations 5.12-5.14. The Sakai algorithm (Equation 5.12) was tested with three assumed vertical pond velocities (runs *sakai*, *sakai0.01*, and *sakai0.04*), and the Röhl algorithm (Equation 5.13) was tested with freezing points based on seawater (*rohl*) or freshwater (*rohl0C*), while the Luthje algorithm (*luthje*; Equation 5.14) is independent of parameter assumptions, though all three algorithms would also be strongly affected by assumed temperature gradients.

The discharge is assumed to be at the mean pond temperature, but drainage points could occur at the surface or base of the pond. Using these temperature estimates will bound the estimated discharge flow required to balance the energy equation (Equation 5.2). Inputs to the pond are modelled to be at the freezing point, and therefore do not add melt-available energy to the pond system. Field measurements indicated supraglacial runoff commonly  $< 0.1^\circ\text{C}$ , but the potential effect of this assumption is tested by assuming inlet temperatures of  $0.1^\circ\text{C}$  and  $0.25^\circ\text{C}$ , encompassing the range of values observed by Takeuchi et al. (2012).

Key parameters affecting the energy exchanges were varied within a range of literature values. Table 5.1 indicates the parameter values used in the standard model run and the alternative values used for the sensitivity tests. The conductivity of the saturated debris layer  $k_{eff}$  is varied between the values for water ( $k_w = 0.565 \text{ W m}^{-1} \text{ K}^{-1}$ ) and rock ( $k_r = 2.0 \text{ W m}^{-1} \text{ K}^{-1}$ ) given by Röhl (2008), while the value for permafrost used by Sakai et al. (2000) is also tested ( $k_{eff} = 0.4 \text{ W m}^{-1} \text{ K}^{-1}$ ). The assumed subaqueous debris thickness  $d_d$  is also adjusted to 0.5 m and 3.0 m, the limits of debris thickness observed at ice-cliff exposures near the study site. For the surface energy balance, emissivity  $\epsilon_w$  and surface roughness  $z_0$  [m] are varied among common literature values for water. The albedo model used by Sakai et al. (2000), normally evaluated for the date and hour and based on the pond's geographic location, is instead replaced by fixed values at the extremes of on-site observations ( $\alpha = 0.08, 0.12$ ).

## 5.4 Results

### 5.4.1 Standard run results

Based on the subsurface geometry estimate and the pressure transducer data, the pond contained  $1250 \text{ m}^3$  of water and had a surface area of  $650 \text{ m}^2$  at the beginning of the study period. The water level was initially stable then drained slowly, lowering approximately 2.3 m in 50 days before the sensor was exposed subaerially. At this time, the pond's volume was

estimated to be  $200 \text{ m}^3$  with a surface area of  $400 \text{ m}^2$ . Observed pond bottom temperatures fluctuated between  $0.8^\circ\text{C}$  and  $3.0^\circ\text{C}$  with peaks at midday, while calculated pond surface temperatures varied between  $3.5^\circ\text{C}$  at midday and freezing at night. Consequently, the melt-available energy stored within the pond rises dramatically from baseline values around  $4 \times 10^9 \text{ J}$  at night to peak values around  $10 \times 10^9 \text{ J}$  at midday (Figure 5.6b,g).

The diurnal peaks in stored energy are supplied by the residual of the pond surface energy balance (Equation 5.3), which often peaks above  $1000 \text{ W m}^{-2}$  (Figure 5.6a,f). The peak shortwave balance is commonly  $> 800 \text{ W m}^{-2}$ , with the longwave balance fluctuating between  $50$  and  $-50 \text{ W m}^{-2}$ . While sensible and rain energy fluxes have a minimal effect (peaks of  $40$  and  $10 \text{ W m}^{-2}$ , respectively), the latent surface flux commonly peaks at  $200 \text{ W m}^{-2}$ . The latent flux also switches roles: in the dry pre-monsoon (Figure 5.6a), it is an energy sink as the pond surface evaporates, but condensation is prevalent in the wet monsoon, when it is an energy source (Figure 5.6f).

Modelled subaqueous subdebris melt rates (Equations 5.9-5.10) were very low, between  $2 \times 10^{-4}$  and  $6 \times 10^{-4} \text{ m d}^{-1}$  (Figure 5.6c,h), while melt rates for subaqueous bare ice (Equations 5.15-5.19) were considerably higher, between  $0.01$  and  $0.06 \text{ m d}^{-1}$  (Figure 5.6d,i). Scaled by the areas of these surfaces, the cumulative subaqueous melt over the period of record was  $8.3 \text{ m}^3$  ( $0.12 \text{ m}^3 \text{ d}^{-1}$ ) for saturated debris and  $98.5 \text{ m}^3$  ( $1.4 \text{ m}^3 \text{ d}^{-1}$ ) for bare ice (*standard* in Table 5.1). Both quantities peak around midday, when both the pond bottom and water surface temperatures are highest.

The sum of all surface energy fluxes (Equation 5.2) has peak values up to  $8 \times 10^5 \text{ W}$ . This is dominated by the surface energy balance, which is an order of magnitude higher than the rate of change in stored energy. The excess energy (Figure 5.6e,j) is accounted for by the pond's discharge, which has an average value of  $0.029 \text{ m}^3 \text{ s}^{-1}$ . The calculated discharge peaks at  $0.1$  to  $0.3 \text{ m}^3 \text{ s}^{-1}$  in the late morning, then slowly decreases through the afternoon. The calculated influx nearly matches the discharge, as mass changes from melt, evaporation/condensation, and rain are all much smaller.

## 5.4.2 Configuration tests

A summary of the results of the *standard* model run and sensitivity analyses is presented in Table 5.1, with italic font in the text below referring to the run name in this table.

### Geometry

The application of different slope values resulted in a linear change in the pond's calculated initial and final volumes, ranging between  $950 \text{ m}^3$  and  $160 \text{ m}^3$  (run *slope040*, 40% slope)

Table 5.1 Principal results of model runs. – indicates a result no different to the standard run.  $MW_i$  refers to the cumulative subaqueous bare-ice melt volume,  $MW_d$  refers to the cumulative subaqueous subdebris melt volume,  $\bar{V}_d$  is the mean pond discharge,  $\bar{v}_i$  and  $\bar{v}_d$  and the subaqueous ice and debris mean melt rates, and  $\dot{V}_{dmax}$  is the peak pond discharge.

Run title	Parameter	Run value	Standard value	$MW_i$ ( $m^3$ )	$\bar{v}_i$ ( $m d^{-1}$ )	$MW_d$ ( $m^3$ )	$\bar{v}_d$ ( $m d^{-1}$ )	$\bar{V}_d$ ( $m^3 s^{-1}$ )	$\dot{V}_{dmax}$ ( $m^3 s^{-1}$ )
<b>Standard</b>	–	–	–	<b>98.5</b>	<b>0.029</b>	<b>10.6</b>	<b><math>3.4 \times 10^{-4}</math></b>	<b>0.028</b>	<b>0.24</b>
slope040	basal slope	40%	53.2%	78.8	–	9.9	–	0.026	0.24
slope0678	basal slope	67.8%	53.2%	117.1	–	11.2	–	0.030	0.25
slope080	basal slope	80%	53.2%	131.9	–	11.6	–	0.031	0.25
Tminus1sig	$\nabla T$	obs $\mu - \sigma$	obs $\mu$	97.6	0.029	–	–	–	0.32
Tplus1sig	$\nabla T$	obs $\mu + \sigma$	obs $\mu$	107.6	0.032	–	–	0.03	0.27
Tlb	$\nabla T$	0; $T = T_{lb}$	obs $\mu$	94.1	0.028	–	–	0.023	0.16
sakai	Sakai algorithm	–	–	79.3	0.024	–	–	–	0.24
sakai0.01	Sakai, $u_w$	0.01 $m s^{-1}$	0.02 $m s^{-1}$	45.5	0.014	–	–	–	0.24
sakai0.04	Sakai, $u_w$	0.04 $m s^{-1}$	0.02 $m s^{-1}$	138.1	0.042	–	–	0.029	0.24
rohl	Röhl algorithm	–	–	329.3	0.098	–	–	0.023	0.23
rohl0C	Röhl, $T_{melt}$	0°C	–1.8°C	92.1	0.028	–	–	0.026	0.24
luthje	Lüthje algorithm	–	–	97.9	0.03	–	–	0.026	0.24
TdTlb	$T_d$	$T_{lb}$	$T_p$	–	–	–	–	0.024	0.15
TdTws	$T_d$	$T_{ws}$	$T_p$	–	–	–	–	0.076	2.00
Ti0.1	$T_i$	0.1°C	0°C	–	–	–	–	0.032	0.35
Ti0.25	$T_i$	0.5°C	0°C	–	–	–	–	0.039	0.99
dd0.5	$d_d$	0.5 m	1.5 m	–	–	31.9	$1.00 \times 10^{-3}$	0.029	–
dd3	$d_d$	3 m	1.5 m	–	–	5.3	$1.67 \times 10^{-4}$	–	–
keffSakai	$k_{eff}$	0.4 $W(mK)^{-1}$	1.28 $W(mK)^{-1}$	–	–	3.3	$1.04 \times 10^{-4}$	–	–
keff0.565	$k_{eff}$	0.565 $W(mK)^{-1}$	1.28 $W(mK)^{-1}$	–	–	4.7	$1.47 \times 10^{-4}$	–	–
keff2	$k_{eff}$	2 $W(mK)^{-1}$	1.28 $W(mK)^{-1}$	–	–	16.6	$5.22 \times 10^{-4}$	–	–
epshigh	$\epsilon_w$	0.97	0.95	–	–	–	–	0.027	–
epslow	$\epsilon_w$	0.92	0.95	–	–	–	–	0.030	0.25
z0low	$z_0$	$2.70 \times 10^{-5} m$	0.0005 m	–	–	–	–	0.024	0.25
z0high	$z_0$	0.001 m	0.0005 m	–	–	–	–	0.029	–
alphaflow	$\alpha$	0.08	modelled	–	–	–	–	0.029	0.25
alphahigh	$\alpha$	0.12	modelled	–	–	–	–	–	–

and  $1800\text{ m}^3$  and  $800\text{ m}^3$  (run *slope080*, 80% slope). The slope is particularly important as it determines the pond's subaqueous surface areas, directly controlling the cumulative melt. It also determines the ice-face depth, which is the critical length for free convection, so it affects the melt rate at the ice face ( $\overline{v_i}$ ). This removes more or less energy from the pond, which has a small effect on mean discharge ( $\overline{V_d}$ ). Of the four configurations, *slope080* produced the highest average and peak discharges ( $0.031\text{ m}^3\text{ s}^{-1}$  and  $0.25\text{ m}^3\text{ s}^{-1}$ , respectively). Run *slope040* produced the lowest average and peak discharges ( $0.026\text{ m}^3\text{ s}^{-1}$  and  $0.24\text{ m}^3\text{ s}^{-1}$ , respectively). Slope has a small effect on the surface energy balance by altering  $T_{ws}$  (Table 5.1).

### Pond temperature

The different pond temperature scenarios had no effect on subaqueous subdebris melt, which is calculated based on the pond bottom temperature. They had a minor effect on the subaqueous bare-ice melt, as this depends on the pond's maximum temperature. Of the three scenarios, run *Tlb* produced the lowest estimate of cumulative melt ( $94.1\text{ m}^3$ ) and melt rate ( $0.028\text{ m d}^{-1}$ ), and run *Tplus1sig* produced the highest cumulative melt ( $107.6\text{ m}^3$ ) and melt rate ( $0.032\text{ m d}^{-1}$ ). The temperature scenarios had a substantial effect on the calculated energy stored within the pond, resulting in high estimated discharges to accommodate the high rates of change within the energy reservoir for the high gradient case, and a very low average discharge for the no-gradient case (Table 5.1).

### Melt models

The Sakai algorithm was evaluated for  $u_w = 0.01, 0.02,$  and  $0.04\text{ m s}^{-1}$ , giving  $45.5, 79.3$  and  $138.1\text{ m}^3$  of meltwater, respectively (Table 5.1). The Röhl algorithm estimates  $329.3\text{ m}^3$  of meltwater, but adapting the equation to freshwater's  $0^\circ\text{C}$  freezing point, gives  $92.1\text{ m}^3$  meltwater. The algorithm of Luthje and Pedersen (2006) generates  $97.9\text{ m}^3$  of meltwater. The different algorithms produce different average discharge values based on the amount of energy removed from the pond by the melt process. Excluding the Röhl algorithm as applied to saltwater, the Luthje algorithm produces the lowest average ( $0.026\text{ m}^3\text{ s}^{-1}$ ) and peak ( $0.24\text{ m}^3\text{ s}^{-1}$ ) discharge estimates. The Sakai algorithm with  $u_w = 0.04\text{ m s}^{-1}$  generates the highest average ( $0.029\text{ m}^3\text{ s}^{-1}$ ) and peak ( $0.24\text{ m}^3\text{ s}^{-1}$ ) discharge estimates, closely followed by the standard run (Table 5.1).

### Inflow and discharge temperature

Two alternative assumptions were considered for the temperature of the pond's discharge, compared to  $T_d = T_p$  for the *standard* run. For  $T_d = T_{lb}$  (run *TdTlb*), the average pond discharge is slightly reduced at  $0.024 \text{ m}^3 \text{ s}^{-1}$ , but the peak discharge estimate is halved to  $0.15 \text{ m}^3 \text{ s}^{-1}$ . The opposite is true for  $T_d = T_{ws}$  (run *TdTws*), which estimates a high average discharge of  $0.076 \text{ m}^3 \text{ s}^{-1}$  and peak discharge of  $2.00 \text{ m}^3 \text{ s}^{-1}$ . These assumptions do not have an effect on the melt calculations.

Two distinct scenarios were assessed for the temperature of inflows, set to  $0^\circ\text{C}$  for the *standard* run. For  $T_i = 0.1^\circ\text{C}$  (run *Ti0.1*), the slight increase in pond energy must be accommodated by a moderate increase in pond discharge to an average value of  $0.032 \text{ m}^3 \text{ s}^{-1}$  and maximum value of  $0.35 \text{ m}^3 \text{ s}^{-1}$ . For  $T_i = 0.25^\circ\text{C}$  (run *Ti0.25*), the increase is substantial, to an average value of  $0.039 \text{ m}^3 \text{ s}^{-1}$  and maximum value of  $0.99 \text{ m}^3 \text{ s}^{-1}$ . Beyond  $T_i = 0.25^\circ\text{C}$ ,  $T_i$  approaches  $T_d$  and the model cannot shunt stored heat with the discharge, producing unrealistic estimates.

### Parameters

The subaqueous subdebris melt is determined from two unconstrained variables, the debris thickness  $d_d$  and the effective saturated debris thermal conductivity  $k_{eff}$ . Changing these parameters resulted in subdebris melt estimates ranging from 44% to 300% of the *standard* results (runs *dd0.5* to *keff2* in Table 5.1), while  $k_{eff} = 0.4 \text{ J K}^{-1} \text{ m}^{-1} \text{ s}^{-1}$  as in Sakai et al. (2000) gives only 31.2% of the standard result (run *keffSakai*). However, varying these parameters had almost no effect on discharge calculations because the subdebris melt accounts for a very small portion of the pond's energy budget. Three parameters controlling the pond surface energy balance were also varied: the water emissivity  $\epsilon_w$  (affects  $L_o$ ), roughness height  $z_0$  (affects  $H$  and  $E$ ), and albedo  $\alpha$  (affects  $I_n$ ). However, none of these parameters can affect the subaqueous melt rates in the model, and literature values altered discharge results by  $< 5\%$ .

## 5.5 Discussion

### 5.5.1 Pond geometry

Modelled melt rates are dependent on the geometry assumed (see runs *slope040*, *slope040*, and *slope080* in Table 5.1), but pond geometry is difficult to constrain. Few systematic pond-depth readings exist; notable exceptions occur in Benn et al. (2000, 2001), Röhl (2008),

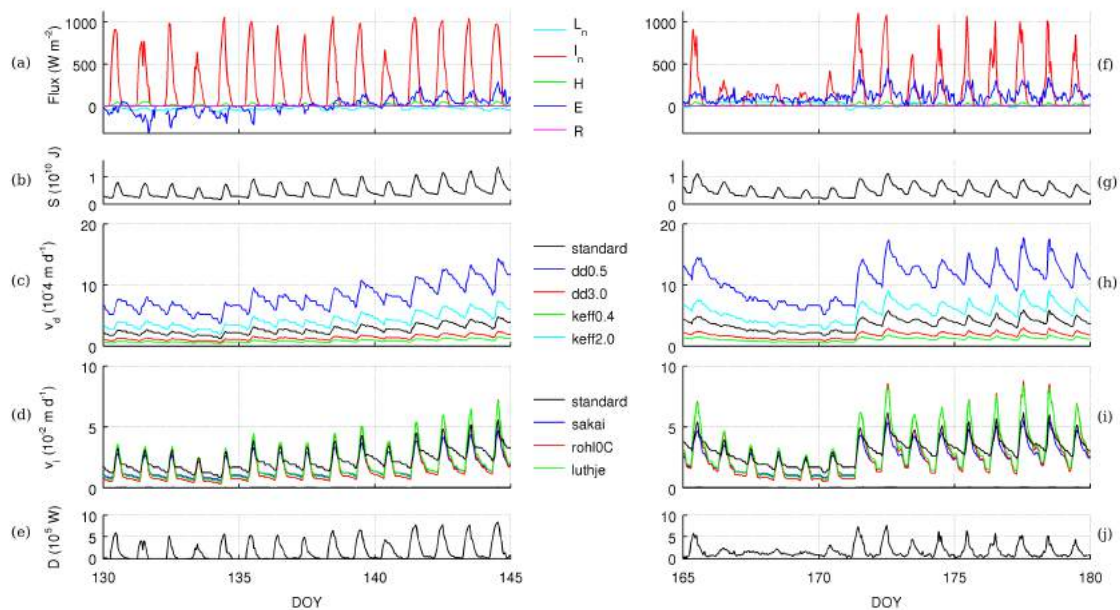


Fig. 5.6 Subsets of modelled time series for the 2013 pre-monsoon (a-e) and monsoon (f-g). The surface energy balance is the key exchange of energy, dominated by net shortwave  $I_n$  and latent  $E$  fluxes (a,f). Stored energy  $S$  diurnally fluctuates by 300% of its base value (b,g). Subaqueous subdebris melt  $v_d$  is low, depending entirely on parameter selection and pond temperature (c,h). Timing of subaqueous bare-ice melt  $v_i$  varies greatly based on algorithm choice and pond temperature (d,i). Discharged energy  $D$  balances the energy budget for the pond (e,j). Heavily overcast conditions prevailed during DOY 166-169, resulting in continuously positive net longwave  $L_n$  but a reduction in net surface energy inputs (f), leading directly to a decrease in modelled discharge  $D$  (j). During this period, pond temperatures declined, resulting in lower modelled  $v_d$  and  $v_i$  (h,i).

and Thompson et al. (2012), where bathymetric surveys for much larger ponds are reported. Basic surveys of several ponds were also reported by Sakai et al. (2000), but pond depths were estimated. Sakai (2012) established empirical estimates of volume and maximum depth for terminal lakes in the Himalaya, all of which were much larger than this study pond. Their empirical relations produce smaller volumes and depths than the model run *slope040*. More work is needed to understand the geometry of supraglacial ponds, which has a strong influence on melt rates.

The study pond appears in Figure 7B of Immerzeel et al. (2014b), who observed the surface downwasting and velocity for Lirung Glacier for the 2013 monsoon. As the pressure transducer was exposed subaerially before the second UAV flight, the later DEM and lake extent ( $145.6\text{ m}^2$ ) cannot be used directly for calibration. Since the lake drained partially between May and October 2013, formerly-subaqueous topography was exposed with a mean

slope of 41%. The October 2013 DEM was analyzed to develop a rating curve, which was directly compared to the 53.2% slope-derived rating curve, with topography truncated at the October 2013 pond altitude for comparability. For the relevant range of altitudes, the 53.2% slope assumption produces pond volume, surface area, and debris area estimates in close correspondence with the revealed terrain in October 2013.

### 5.5.2 Pond temperature

Modelled subaqueous bare-ice melt rates are also dependent on the assumed temperature distribution in the pond (model runs *Tmins1sig*, *Tplus1sig*, and *Tlb* in Table 5.1). Note that *Tlb* is measured, so these model runs calculate identical subdebris melt rates. The temperature profile influences the energy reservoir calculations (Equation 5.1), and consequently has a strong effect on the discharge estimate. Using the observed 2014 monsoon gradients produced night-time pond surface temperatures at the freezing point during the 2013 monsoon for model runs *standard* and *Tplus1sig*, which was not observed in the 2014 monsoon. This is due to the different pond depths during the monsoon periods of 2013 (~2 m) and 2014 (~1 m). A more realistic approach would take the variable air and pond temperature into account, while a computational fluid dynamics approach would provide the most accurate assessment of temperature distributions and energy exchanges, but at significant computational cost. This study pond showed similar mean daily surface and pond bottom temperatures to observations by Sakai et al. (2000), who ran their model with observed pond bottom temperatures. This approach (model run *Tlb*) only slightly reduces the calculated melt rates. Few distributed observations of supraglacial pond temperatures have been made (Röhl, 2008), and the melt models are very sensitive to estimated mean temperatures, so additional data is needed to constrain melt estimates and understand pond circulation patterns.

### 5.5.3 Subaqueous melt

The subaqueous melt values calculated in this study are lower than those observed on other lakes on debris-covered glaciers, likely due to the small size and particular location of the lake. Benn et al. (2001) reported wind-generated currents driving thermo-erosional melt rates between  $0.7 - 2.7 \text{ cm h}^{-1}$ , with a strong diurnal fluctuation over the four hours of observation. If the mean observed value ( $2.7 \text{ cm h}^{-1}$ ) is representative of the daily mean, this would equate to a rate of  $0.504 \text{ m d}^{-1}$ , but for a supraglacial lake of  $52,500 \text{ m}^2$  compared to  $600 \text{ m}^2$  for this pond. Röhl (2006) identified high rates of thermo-erosion at the water level, although the subaqueous ice cliff was not affected substantially. Sakai et al. (2009) identified lake fetch as a key feature in determining wind-driven thermo-erosional melt, which is identified as

a criterion for calving in supraglacial lakes. The pond had average water temperatures of  $1 - 1.5^{\circ}\text{C}$ , and a fetch of 20 m in the direction of the dominant up-glacier winds. Following their Figures 5-7, Sakai et al. (2009) estimated a melt rate of  $< 0.08 \text{ m d}^{-1}$  during the monsoon. This study's modelled melt rates are even lower, but the pond is hidden from up-glacier winds by an overhanging ice cliff (Figure 5.4), making the site suitable for free convection. Most ponds previously studied have had higher temperatures between  $2 - 7^{\circ}\text{C}$  (Sakai et al., 2009; Xin et al., 2011), which would produce much higher melt rates for all the model runs, and Röhl (2008) suggests a relationship between size and pond temperature. The combined effects of small pond size, shading from the sun, and low wind exposure result in lower temperatures and lower thermo-erosional rates for the study pond.

Following the 2013 monsoon period and the associated pond drainage, evidence was revealed of waterline melting that had occurred during the pond drawdown (Figure 5.7). These step cuts were measured to be several centimetres deep (actual measurements made by Jakob Steiner and Pascal Buri), and occasionally exhibited a lower sill as observed by Röhl (2006), but were only apparent for 1.85 m above the observed water level in October, which was 3.0 m lower than in May. Lowering during the earlier monsoon period may have cut similar notches, and if so these must have melted subaerially since. It appears that these formed during periods of relative water-level stability concurrent with peak melt rates (Figure 5.7), melting up to 3 cm in 12-hour periods according to the *standard* run, twice the mean melt rate over the study period.

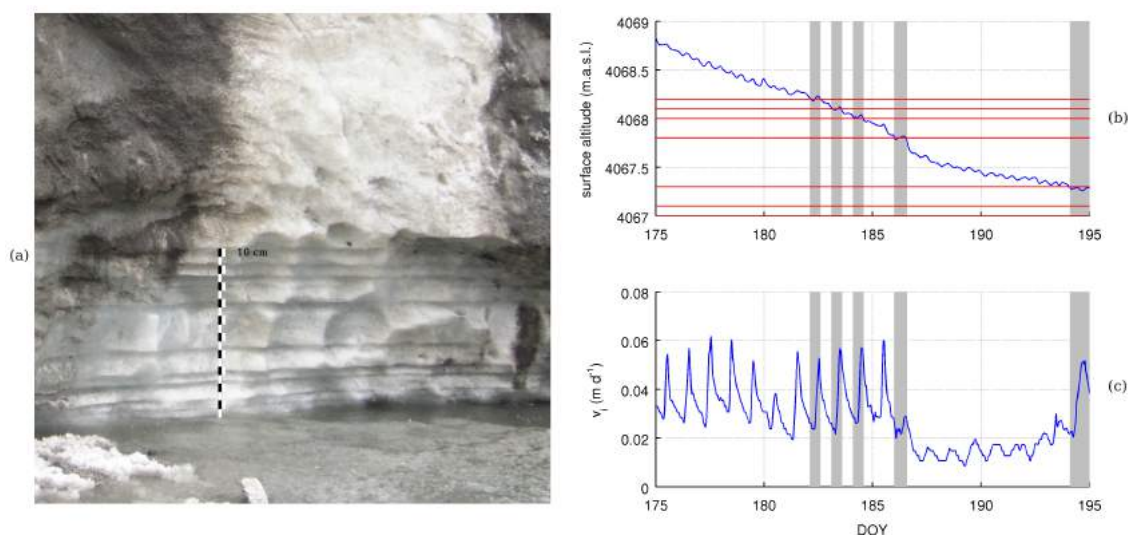


Fig. 5.7 (a) Observed notching at the study site during monsoon 2013. (b) Water-level decline over the study period, noting the water level at the time of notch development. (c) Melt rates corresponding to notch development.

The results summarised in Table 5.1 show estimated melt in close agreement between melt algorithms, with approximately 98.5 m<sup>3</sup> subaqueous ice melted during the study period. As shown in Figure 5.6d, the timing of melt differs greatly among the models. The free-convection model (*standard* run) predicts a strong diurnal cycle in the melt rate, but a gradual decline as overturning weakens. The other melt models predict much higher peak melt rates during the day but lower melt rates at night. Consequently, the distinct parametrisations for subaqueous ice-melt are suited for different scenarios. The model developed in this study is reliable for the free-convection case, where a pond has minimal currents and a monitored temperature gradient, but is likely to underestimate melt if significant currents are present. Performance of the forced convection algorithm applied in Sakai et al. (2000) depends entirely on the selected value of  $u_w$ . This study shows that  $u_w \leq 0.02 \text{ m s}^{-1}$  estimates less energy transfer than a simple free-convection model. However, the same algorithm shows great promise for water bodies with longer fetch (Sakai et al., 2009).

The empirical algorithm applied by Röhl (2008) was determined for seawater and likely overestimates melt values significantly. When corrected for freshwater, the algorithm produces melt estimates in close agreement with the free-convection model. As it depends solely on an estimated average pond temperature, it is ideal for scaling or for estimating localised melt rates, such as for studying thermo-erosional notch development.

Similarly, the Luthje and Pedersen (2006) algorithm is driven solely by average water temperature, but was developed for natural convection over a horizontal clean-ice surface. Critically, the algorithm assumes a well-mixed water column, which does not hold for this pond or others with thorough temperature measurements (Xin et al., 2011). However, it exhibited good agreement with the free-convection model for the study pond's geometry, but is likely to be inaccurate for ponds affected by wind. There is need for a unifying model that performs well under both kinetic settings, estimating wind-induced thermo-erosional melting while also calculating theoretical-minimum melt rates based on free convection.

#### 5.5.4 Hydrologic activity

The results for pond discharge and influx indicate that even with a fairly stable water level, the study pond plays an active role in the hydrologic system, in agreement with results from Sakai et al. (2000) and Benn et al. (2001). The pond is a significant recipient of atmospheric energy, does not seem to increase substantially in temperature, and can only use a small proportion of excess heat to drive local subaqueous bare-ice or subdebris melt. The calculated discharge values may be high based on geometry, temperature, and parameter assumptions, but the sensitivity analysis indicates only a small change in mean discharge for most of these variables, so the high discharges are likely to be realistic.

The excess energy is advected from the pond by discharge averaging  $0.028 \text{ m}^3 \text{ s}^{-1}$  (*standard* run), suggesting a low residence time in the pond of 9.2 hours. Field observations in 2014 identified a very small surface outlet meandering to an englacial channel opening that had been exposed due to surface thinning and ice-cliff backwasting, but in 2013 this passage must have been blocked. Assuming discharge occurs at the surface temperature (run *TdTws*), the low estimated surface temperatures at night produce discharge estimates of up to  $2.00 \text{ m}^3 \text{ s}^{-1}$ . This scenario is unlikely considering that the daily peak flow at the Lirung Glacier outlet for this and prior periods was  $2.5 - 3 \text{ m}^3 \text{ s}^{-1}$  (Bhatt et al., 2007; Ragetti et al., 2015). Instead, the discharge most likely exits in an inefficient manner, accounting for the slow drainage rates, in contrast to the fast lake drainage mechanism envisaged by Gulley and Benn (2007). Inefficient, slow drainage may be associated with flow through accumulated debris blocking a cut-and-closure conduit, which has backed up water to a temporarily-stable higher level (Gulley, 2009).

Furthermore, the influx water is not sourced locally. The pond's catchment area of  $14800 \text{ m}^2$  would have to downwaste 11.2 m on average to supply adequate inflows. The adjacent ice cliff was studied by Buri et al. (2016b), but modelled melt from this source only accounts for 1 – 4% of the inflows estimated by this study, while this ice cliff certainly provides the greatest melt signal within the pond's basin (Immerzeel et al., 2014b). These clues point to the importance of interactions between englacial conduits and the glacier's surface in determining the development, role, and eventual drainage of supraglacial ponds.

### 5.5.5 Cliff/lake system propagation

For an ice-cliff in a combined lake system to stably backwaste, the lake's subaqueous backwasting rate must exceed the subaerial horizontal melt rate, whether via melt or calving (Sakai, 2012). The study pond demonstrated thermo-erosional notching at the waterline (Figure 5.7) in spite of limited pond fetch and low temperature, supporting the assertion by Röhl (2006) that subaqueous cliff melting is controlled additionally by geometry, water fluctuations, and debris supply. In this study, subaqueous ice is estimated to have backwasted at an average rate of  $2.91 \text{ cm d}^{-1}$ , comparable to the  $3.25 - 5.65 \text{ cm d}^{-1}$  (May) and  $0.18 - 0.23 \text{ cm d}^{-1}$  (October) observed at the adjacent  $40^\circ - 51^\circ$  cliffs (Steiner et al., 2015).

As suggested by several studies (Sakai et al., 2000; Benn et al., 2001), a significant role of the ponds is to convey atmospheric energy to the glacier's interior. For this study, most energy inputs to the pond are accounted for by the pond's discharge to the glacier's englacial and subglacial conduits, where it is likely to cause rapid melting (Gulley and Benn, 2007; Röhl, 2008). Observations of near-freezing water temperatures at the glacier's terminus outlet and at englacial conduit emergence points indicate that all of the discharge thermal energy is

lost to melting. If this is true, this study estimates a total of 2612 m<sup>3</sup> of melting in the interior of the glacier solely due to this small pond (over 68 days for a rate of 38.4 m<sup>3</sup> d<sup>-1</sup>), far outweighing the locally-caused melt. With an average area of 496 m<sup>2</sup> across the study period, this is the equivalent of 5.3 m ablation attributable to the lake's area. As noted by Sakai et al. (2000) and by Benn et al. (2001), this contributes to the formation of new cliff-lake systems by causing down-glacier conduit collapse and blockage.

### 5.5.6 Limitations

Although promising for understanding pond-related energy exchanges, there are limitations to this diagnostic approach. Temperature gradients have been assigned based on limited observations, and no attempt has been made to model energy dynamics within the pond itself. Pond edge effects are not thoroughly treated in the model. Pond-induced calving is neglected by the model. Although not observed at the field site, this is generally the mechanism of fastest pond expansion (Benn et al., 2001). Rockfall is neglected by the model, but was shown to be a minimal energy input by Sakai et al. (2000), and it also displaces volume. Due to a lack of observations, a limited representation of the pond's saturated debris base is used, requiring improved understanding in terms of composition and energy fluxes. In this implementation the model is also dependent on source data and empirical relationships developed outside the study pond.

### 5.5.7 Differences to prior efforts

Although supraglacial pond energy balance and pond-associated ablation has been assessed previously to some degree (Sakai et al., 2000; Röhl, 2008), this analysis makes several key advances over the methods of prior efforts.

First, ponds are represented much more accurately in the model, both in terms of geometry and thermal structure. The prior effort by Sakai et al. (2000) approximated ponds with a simple cylinder, whereas this analysis uses information from nearby topography to represent the subaqueous debris and bare-ice surfaces. Consequently the water-level variations observed by the pressure transducer is converted into changes in pond volume with a depression rating curve, a representation that is more realistic than a cylinder for large changes in water level. In terms of thermal structure, the model reconstructs pond temperature distributions based on hourly temperature gradient observations, while the implementation of Sakai et al. (2000) only used pond-bottom temperature measurements.

The model also uses an improved prescription of meteorological forcing relative to the Sakai et al. (2000) model. Advanced radiation modelling is carried out to transfer

the measurements at the Lirung AWS to the location of the pond, accounting for shading, reflection, and emission of individual radiation sources by the terrain. Further improvements to the surface energy balance include a stability correction for turbulent fluxes and the incorporation of rain as a flux of both heat and mass.

The calculation of pond-proximal melt driven by natural (Rayleigh-Bénard) convection is physically-based and appropriate for cold, sheltered ponds such as those observed on Lirung Glacier. For ponds with a larger fetch-length, the parametrisations used by Sakai et al. (2000); Röhl (2006) may be more appropriate, although a physically-based approach to those situations is lacking and desirable. The analysis of Sakai et al. (2009) investigates the interaction between water surface fetch and thermo-erosional melt, but even in those situations, natural convection should operate as a theoretical minimum of heat transfer, and is therefore a meaningful calculation.

Finally, as compared to the other calculations of pond-associated melt, this effort involved rigorous testing of the model's sensitivity to all principal parameters. The study also tested the melt equations of Sakai et al. (2000); Röhl (2006); Luthje and Pedersen (2006) to determine the melt estimates from each approach, finding that they were of comparable magnitude.

## 5.6 Summary

This study advances energy-balance modelling efforts for supraglacial ponds on debris-covered glaciers, then applies many model configurations for a small pond on Lirung Glacier during May-October 2013 to understand the importance of unconstrained properties and the likely range of melt values. Notably, the pond-atmosphere surface inputs large amounts of energy, with exceptionally high latent fluxes. The net surface energy balance dominates the pond's energy fluxes by an order of magnitude for a variety of parameter choices. The excess energy can only be accounted for by the pond's discharge, and is likely to contribute to substantial amounts of englacial or subglacial melt, the equivalent of 5.3 m local ablation for the ponded area. Therefore, ponds seem to be able to convey a large amount of energy into the glacier interior, demonstrated by this study for a relatively small pond. This distal melt may lead to conduit collapse and the formation of additional cliff-lake systems (Benn et al., 2012).

The study tested several model configurations to calculate subaqueous melt. Subaqueous bare-ice melt was estimated to occur at an average rate of  $2.91 \text{ cm d}^{-1}$  for a total volume of  $98.5 \text{ m}^3$ , in the correct range of values to match the adjacent cliff's backwasting. This result is in close agreement with algorithms used by Sakai et al. (2000) and Luthje and Pedersen (2006), and an adaptation of the algorithm used by (Röhl, 2008). Moreover, the result is

also in good agreement with modelled and observed backwasting of the adjacent ice-cliff (Steiner et al., 2015), a precondition for the two systems to occur together (Sakai, 2012). The subaqueous melt algorithms are expected to be suitable for distinct applications based on the dominant kinetic regime driving pond-associated melting (Xin et al., 2011). Subaqueous subdebris melt is unconstrained in the model, but a sensitivity analysis indicates that it plays a minor role at this site in terms of energy loss and melt production (10.6 m<sup>3</sup> total) unless the debris is very thin, pond basal temperatures are higher than those observed, or convection occurs in the saturated debris layer.

A combination of field measurements and physically-based modelling has enabled me to identify several important processes associated with a small supraglacial pond on a debris-covered glacier that are likely to be relevant to other ponds in similar settings. First, water inflow to the pond is not only sourced within the pond's immediate catchment area but involves a significant supraglacial or englacial input from up-glacier. Second, outflow discharge occurs slowly, suggesting an inefficient outflow channel, perhaps one blocked by debris. Third, the pond is an active component of the entire glacier's hydrologic system, with up to 10% of the glacier's total discharge passing through it, and resulting in a high overturn rate. Taken together, the results support those of others suggesting that supraglacial ponds are both an important indicator of, and provide a key feedback mechanism for, a debris-covered glacier's response to climate change (Benn et al., 2001; Sakai and Fujita, 2010; Benn et al., 2012). Recent pronounced thinning on Lirung Glacier means that the surface is frequently intersecting former englacial conduits, supplying water to locations where it may be impounded. The surface ponds then absorb atmospheric energy and convey it to the interior of the glacier, leading to englacial conduit enlargement and collapse, further basin formation, and the creation of new ponds.



# Chapter 6

## Supraglacial pond associated ablation for Lirung Glacier

### 6.1 Executive Summary

Building on the supraglacial pond observations at Lirung Glacier for 2013 and 2014 presented in Chapter 4 and the supraglacial pond energy-balance model developed and tested in Chapter 5, this chapter determines the energy balance of each of Lirung Glacier's supraglacial ponds, and the total pond-associated ablation for the glacier.

The instrumental records of pond thermal regime and near-surface meteorological conditions enable the determination of empirical relationships for pond surface temperature and near-surface wind speed. Additionally, analyses of pond albedo observations suggest that sophisticated albedo models do not accurately represent shortwave radiation at the ponds observed, but that fixed albedo values are more reasonable representations.

The model introduced in Chapter 5 is reduced in complexity to adapt to the varying data availability for each of the 14 ponds observed on Lirung Glacier in 2014. The four primary study ponds (C,D,I,J) are represented with the full energy-balance approach (Chapter 4). Model complexity and source data are progressively reduced to eventually apply a surface energy-balance model to fixed pond area from Spot6 observations in April 2014.

All ponds are modelled with the most sophisticated framework that is possible given the data availability, as well as all simpler models, enabling the progressive evaluation of model error through all reductions in model complexity. The results from different model complexity levels are compared and extrapolated (if necessary) to whole-glacier estimates of pond energy absorption. Energy exchange at the pond surface is an accurate representative for total pond-associated ablation, but the partition of absorbed energy between pond-proximal

and englacial melt varies by pond ( $70 \pm 25\%$ ). The models exhibit low sensitivity to pond albedo, very low sensitivity to DEM resolution, and higher sensitivity to meteorological data. The greatest errors associated with reduced model complexity are due to inadequate representations of pond areal change that result from pond drainage or filling. Model results suggest that ponds absorbed sufficient energy to account for  $\sim 10\%$  of Lirung Glacier's ablation in 2014.

## 6.2 Specific Objectives

This chapter first presents basic analyses of the meteorological and physical observations in order to determine suitable environmental forcing conditions for the pond energy-balance model. However, only four ponds can be modelled with the energy-balance model presented in Chapter 5. The rest (total 14 ponds in 2014) do not satisfy that model's data requirements (e.g. a high-resolution DEM and water-level time series). The chapter therefore progressively degrades model complexity and source data requirements to represent each pond with the most complete data possible, while also assessing the relative error as the model is degraded. The chapter's specific goals are therefore to:

1. Develop empirical relationships to project environmental conditions to each pond location, including: near-surface air temperature  $T_a$ , pond water surface temperature  $T_{ws}$ , pond albedo  $\alpha$ , and wind speed at the pond surface  $u_a$ .
2. Model the energy balance of ponds C, D, I, and J with a variety of configurations of the energy-balance model presented in Chapter 5. This will use a stepwise degradation of input data, including meteorological station choice, topographic data source and resolution, quality of temporal documentation, and model complexity.
3. Determine the surface energy balance for each of the 14 ponds observed on Lirung Glacier in 2014, using the highest model complexity possible for each pond as well as the lowest common denominator of model complexity possible for all ponds.
4. Estimate the whole-glacier potential ablation associated with supraglacial ponds for Lirung Glacier in 2014.

## 6.3 Methods and Approach

### 6.3.1 Data: empirical relationships of environmental conditions

Based on the pond and meteorological observations presented in Chapter 4, this section focuses on the determination of appropriate algorithms to estimate the energy balance at supraglacial ponds without *in-situ* instrumentation. Specifically, I present air temperature lapse rates observed for Lirung Glacier and the non-glacier terrain of the Langtang valley, develop empirical models for pond surface temperature estimation, evaluate models of pond albedo, and develop hourly empirical regressions to transfer observed wind speeds from Kyanjing AWS to the glacier surface.

Further numerical-modelling exercises use these datasets and methods to analyse pond energy balance for all Lirung Glacier supraglacial ponds (this chapter) and for all debris-covered glacier surface ponds across the catchment as observed by the Landsat instruments (Chapter 7).

#### Air temperature on Lirung Glacier

The pond energy-balance model testing in Chapter 5 used the observed air temperature at the Lirung AWS for determination of pond C's surface energy balance. The elevation difference between these two locations was 14 m, so temperature differences between the two sites were minimal. However, for extension of the energy-balance model to other ponds at a wider range of elevations, appropriate lapse rates are necessary.

To estimate air temperature at pond locations, I modify air temperature observations from the Lirung AWS (Table 4.1) using the on-glacier lapse rates in Table 6.1 according to Equation 6.1, where  $T_j$  [°C] is the temperature at elevation  $Z_j$  [m.a.s.l.] and LR [°C m<sup>-1</sup>] is the lapse rate. When observations are not available from the Lirung AWS, a two-stage adjustment is made to temperature data from the Kyanjing AWS: first, lapsing using the environmental lapse rate to the glacier terminus elevation (4029 m.a.s.l. for Lirung Glacier during the study period), then using the on-glacier lapse rate to the pond elevation.

$$T_2 = T_1 + \text{LR} \times (Z_2 - Z_1) \quad (6.1)$$

#### Pond temperature estimation

The pond energy-balance model testing in Chapter 5 used the vertical temperature gradients and observed pond-bottom temperatures to represent the pond surface temperature. Seeking to develop a method to estimate  $T_{ws}$  for ponds without  $T_{lb}$  records, I investigate several linear

Table 6.1 Seasonal lapse rates measured by a network of temperature loggers on Lirung Glacier and throughout Langtang Valley.

Lapse Rate ( $^{\circ}\text{C m}^{-1}$ )	Pre-monsoon	Monsoon	Post-monsoon	Source
Environmental	-0.0061	-0.0044	-0.0049	Heynen et al. (2016)
On-glacier	-0.005	-0.0066	-0.0078	Steiner and Pellicciotti (2016)
Start Date	1 Mar	15 Jun	1 Oct	
End Date	14 Jun	30 Sep	31 Dec	

and more complex relationships between  $T_{ws}$ ,  $T_{lb}$ ,  $T_a$ , and the time of day. A relationship with pond depth is not investigated, as pond depth (like  $T_{lb}$ ) requires in-situ observation. Pond surface temperature shows a linear relationship with  $T_{lb}$ , but the relationship with  $T_a$  is better represented by an exponent of 2, while the interaction with  $\sin(\pi \times \text{Time})$  is improved with an exponent of 4 (Figure 6.1). For use in the equations, Time is expressed as the fraction of a day in decimal form (e.g. 18:00 = 0.75). Based on these observations, four regression models were constructed with linear or non-linear variable dependencies, and including or excluding  $T_{lb}$  (Equations 6.2 to 6.5). These four regression models were applied to ponds C and D individually, and to their combined data. Table 6.2 summarises the performance of the regression models and provides  $\beta$  coefficients for each term.

$$\text{M1} : T_{ws} = a_0 + a_1 \times T_a + a_2 \times T_{lb} \quad (6.2)$$

$$\text{M2} : T_{ws} = a_0 + a_1 \times T_a \quad (6.3)$$

$$\text{M3} : T_{ws} = a_0 + a_1 \times T_a^2 + a_2 \times T_{lb} + a_3 \times (\sin(\pi \times \text{Time}))^4 \quad (6.4)$$

$$\text{M4} : T_{ws} = a_0 + a_1 \times T_a^2 + a_3 \times (\sin(\pi \times \text{Time}))^4 \quad (6.5)$$

$$\beta_i = \frac{a_i}{\sigma_i} \quad (6.6)$$

All models perform reasonably well, with  $R^2$  values above 0.5 and  $d$  (index of agreement) values above 0.8. The non-linear regression models (M3,M4) perform better than the linear models (M1,M2). However, the performance is not much better than simple use of a mean hourly observed surface temperature, which produces  $R^2$  values of 0.67 (pond C only), 0.64 (pond D only), and 0.50 (both ponds) and corresponding  $d$  values of 0.892, 0.877, and 0.795. However, the empirical models are likely to be more reasonable for application to other ponds.

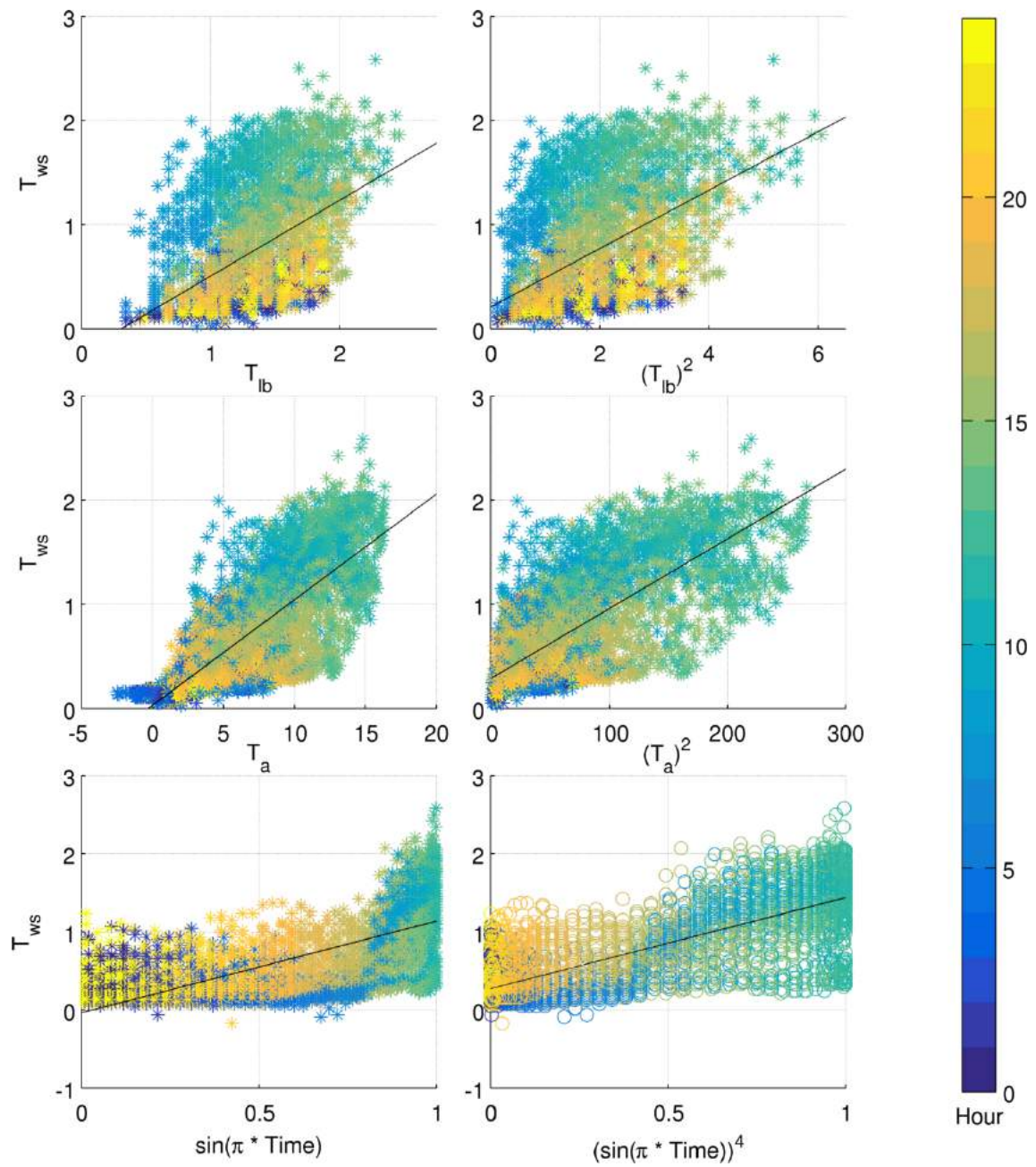


Fig. 6.1 Linear and non-linear relationships of  $T_{ws}$  to  $T_{lb}$ ,  $T_a$ , and time of day for pond C. All points are coloured by time of day. a)  $T_{lb}$  b)  $T_{lb}^2$  c)  $T_a$  d)  $T_a^2$  e)  $\sin(\pi \text{Time})$  f)  $(\sin(\pi \text{Time}))^4$

Table 6.2 Coefficients and model performance for models M1-M4 as applied to each pond individually and to both ponds' observations together.  $R^2$  is the coefficient of determination, and  $d$  is the index of agreement.  $\beta_1$ ,  $\beta_2$ , and  $\beta_3$  are the coefficients for the  $T_{lb}$ ,  $T_a$ , and time of day terms in Equations 6.2-6.5, normalised by the term's standard deviation as in Equation 6.6.

Setup	Model	$\beta_1$	$\beta_2$	$\beta_3$	p-val	$R^2$	$d$
'Pond C'	'M1'	0.823	-0.066		< 0.001	0.605	0.341
'Pond C'	'M2'	0.776			< 0.001	0.603	0.342
'Pond D'	'M1'	0.708	0.204		< 0.001	0.606	0.473
'Pond D'	'M2'	0.753			< 0.001	0.566	0.496
'Both'	'M1'	0.594	0.290		< 0.001	0.577	0.503
'Both'	'M2'	0.712			< 0.001	0.507	0.543
'Pond C'	'M3'	0.236	0.165	0.536	< 0.001	0.684	0.305
'Pond C'	'M4'	0.393		0.472	< 0.001	0.669	0.333
'Pond D'	'M3'	0.346	0.229	0.487	< 0.001	0.716	0.401
'Pond D'	'M4'	0.447		0.432	< 0.001	0.669	0.433
'Both'	'M3'	0.193	0.387	0.475	< 0.001	0.662	0.450
'Both'	'M4'	0.434		0.352	< 0.001	0.541	0.524

In particular, M3 and M4 appear to be best suited for estimating pond surface temperature at ponds with and without pressure transducer records, although both records still present significant scatter from the 13,890 15-minute observations (Figure 6.2).

### Albedo of the pond surface

In this section, I evaluate several models of pond albedo using the the field observations at ponds A and D (presented in Chapter 4) to determine the most suitable for pond surface energy-balance modelling.

Chapter 5 applied a simple empirical relation (Equation 5.4) based on measurements at Tsho Rolpa (Yamada, 1998), and also used two fixed albedo values [ $\alpha = 0.08, 0.12$ ]. I test these albedo representations and the broadband parametrisation of albedo developed by Jin et al. (2011), which individually models the reflection and volume scattering of diffuse and direct shortwave radiation. This model was developed for oceanic applications and presents a validated functional form depending on wavelength, but the broadband parametrisation depends only on refractive index ( $v_0 = 1.34$ ) and wind speed ( $u_a$ ). I ignore the foam adjustment calculation and chlorophyll content for this application, and use the observed wind speed at Lirung AWS. For the fixed albedo configurations, I set  $\alpha = 0$  when the sun dips below the horizon.

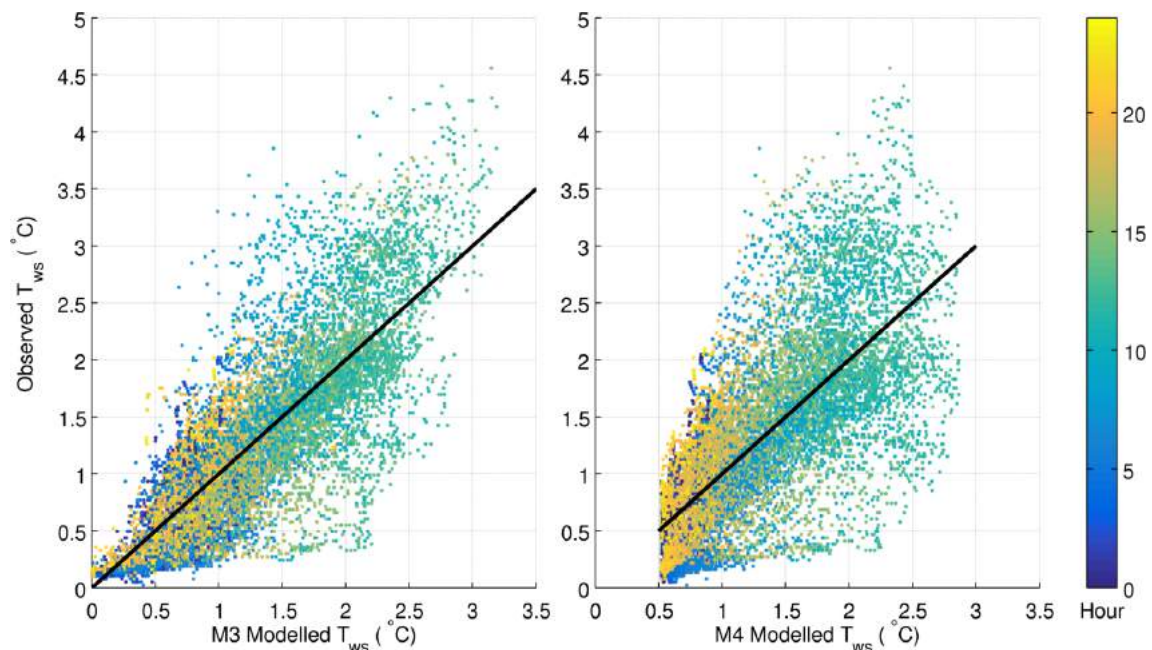


Fig. 6.2 Plots of modelled and observed surface temperature at ponds C and D (observations for both ponds, combined) for regression models M3 (left) and M4 (right).

I evaluate each albedo model for the periods of record for the albedometers at Ponds A and D in May 2014 (Table 4.1) and compare the modelled and measured albedo values. The magnitude and pattern of albedo could not be reproduced by either the Yamada (1998) or Jin et al. (2011) models. The Yamada (1998) model produces a stronger diurnal variability than observed and since it relies only on a single parameter (solar zenith) it fails to predict any difference between the ponds. The Jin et al. (2011) model is more sophisticated, and reproduces some of the diurnal variability of albedo, but estimated albedo magnitudes are 50% too low. This is most likely due to the high turbidity of the ponds, which leads to low penetration depth and a higher broadband albedo.

I assessed the performance of each of the four albedo models at both study sites using the coefficient of determination  $R^2$ , the index of agreement  $d$ , and the root-mean-square-error  $RMSE$  for both  $\alpha$  and  $I_{out}$  (Table 6.3). The Yamada (1998) model is a poor predictor of the diurnal pattern of pond albedo at both ponds ( $R^2 = 0.31$ ) but the magnitude is about right during peak sunshine hours, so the produced pattern for  $I_{out}$  is accurate for both ponds ( $R^2 = 0.94, 0.95$ ). Still, the Yamada (1998)  $\alpha$   $RMSE$  is the worst of all models. The Jin et al. (2011) model performs the worst in terms of  $R^2$  and  $d$  for both  $I_{out}$ , but reproduces the daily pattern of  $\alpha$  better than the Yamada (1998) model. Although a simplistic approximation, the fixed albedo values perform best for all metrics, minimising the error in both  $I_{out}$  and  $\alpha$ .

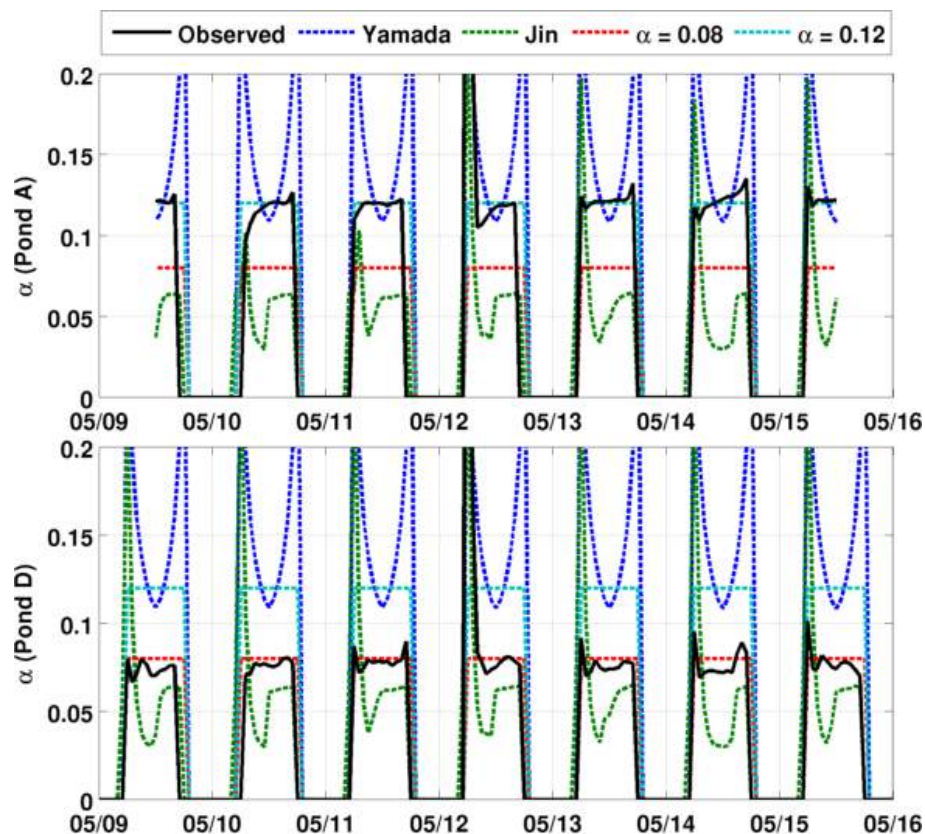


Fig. 6.3 Albedo observed and modelled for ponds A and D during May 2014, showing a generally poor performance for sophisticated methods, but reasonable agreement for fixed-value approximations. The pond D record extends 3 additional days.

Based on these results and for modelling simplicity, the chapter uses  $\alpha = 0.08$ , and a sensitivity analysis will use  $\alpha = 0.12$  to assess the potential range of shortwave input and its effect on the ponds' energy balance.

### Wind in a pond depression

In this section I analyse the wind speed observations collected at Kyanjing AWS, at Lirung AWS, and in the pond D surface depression with two goals. First, I analyse the three on-glacier wind speed records (Lirung AWS, above pond D depression, inside pond D depression) to evaluate the applicability of wind speed observed at Lirung AWS to the pond surface. Second, I develop hourly empirical relationships between wind speeds observed at Kyanjing AWS and Lirung AWS. Together, these goals establish the representation of wind speeds within a pond surface depression from meteorological sensors.

For the first goal, I compare the two wind speed records near pond D to each other and to the on-glacier Lirung AWS record (Figure 6.4). The wind sensor above the pond

Table 6.3 Performance of albedo models at ponds A and D in terms of  $\alpha$  and  $I_{out}$ .  $d$  is the index of agreement. All metrics are dimensionless except  $I_{out} RMSE$ , which is in  $W m^{-2}$ .

Albedo model: Pond:	Yamada		Jin		$\alpha = 0.08$		$\alpha = 0.12$	
	A	D	A	D	A	D	A	D
$\alpha R^2$	0.31	0.31	0.52	0.39	0.47	0.43	0.47	0.43
$\alpha d$	0.73	0.62	0.72	0.78	0.69	0.77	0.80	0.77
$\alpha RMSE$	0.088	0.093	0.065	0.048	0.064	0.043	0.060	0.054
$I_{out} R^2$	0.95	0.94	0.82	0.76	0.99	0.98	0.99	0.98
$I_{out} d$	0.98	0.88	0.69	0.86	0.94	0.99	1.00	0.92
$I_{out} RMSE$	12.24	32.56	39.09	20.55	20.81	5.18	5.48	25.67

D depression experienced higher wind speeds than the sensor inside the depression at all times of the day. Both sites experience the same basic diurnal signal as the Lirung AWS and are highly correlated with the Lirung AWS for the hourly variations. The Lirung AWS and the sensor above the depression correlate particularly well ( $R^2 = 0.90$ ), although with a correlation slope greater than 1, leading to an RMSE of  $0.44 m s^{-1}$ . The Lirung AWS does not reproduce the in-pond wind speed variations quite as well ( $R^2 = 0.82$ ), but the magnitudes of the datasets are also very comparable, so the correlation slope is very close to 1 and the RMSE is  $0.31 m s^{-1}$ . This basic analysis of wind speeds at supraglacial ponds suggests that the Lirung AWS, itself in a shallow depression, is slightly sheltered from the Lirung surface boundary layer. More prominent locations may experience 40% higher wind speeds, an important consideration for distributed energy-balance modelling. However, for the purposes of this study, the data suggest that the Lirung AWS record is appropriate for a sheltered location removed from the glacier surface boundary layer, such as the ponds identified in this study.

For the second goal, analyses were conducted to relate the Kyanjing AWS and Lirung AWS wind observations. The Kyanjing AWS is very exposed to wind compared to Lirung AWS (Figure 6.5a). Wind speeds are often 4-7 times higher than at the Lirung AWS, but show similar diurnal fluctuations. Hourly wind data for the comparable period of the two stations were regressed to develop a diurnal correction for Kyanjing wind observations.  $p < 0.001$  for all hourly regressions except 4am, 5am, and 8am data (Figure 6.5d). The final model reproduces wind speed observed at Lirung AWS with an overall  $R^2$  of 0.61 and an index of agreement of 0.87, even though it fails to reproduce some of the scatter observed at Lirung AWS, especially at night (Figure 6.5b). This model has  $RMSE = 0.24 m s^{-1}$  and a mean absolute error of  $0.19 m s^{-1}$  for the period of record, and is used to represent on-glacier wind speeds when Lirung AWS observations are not available.

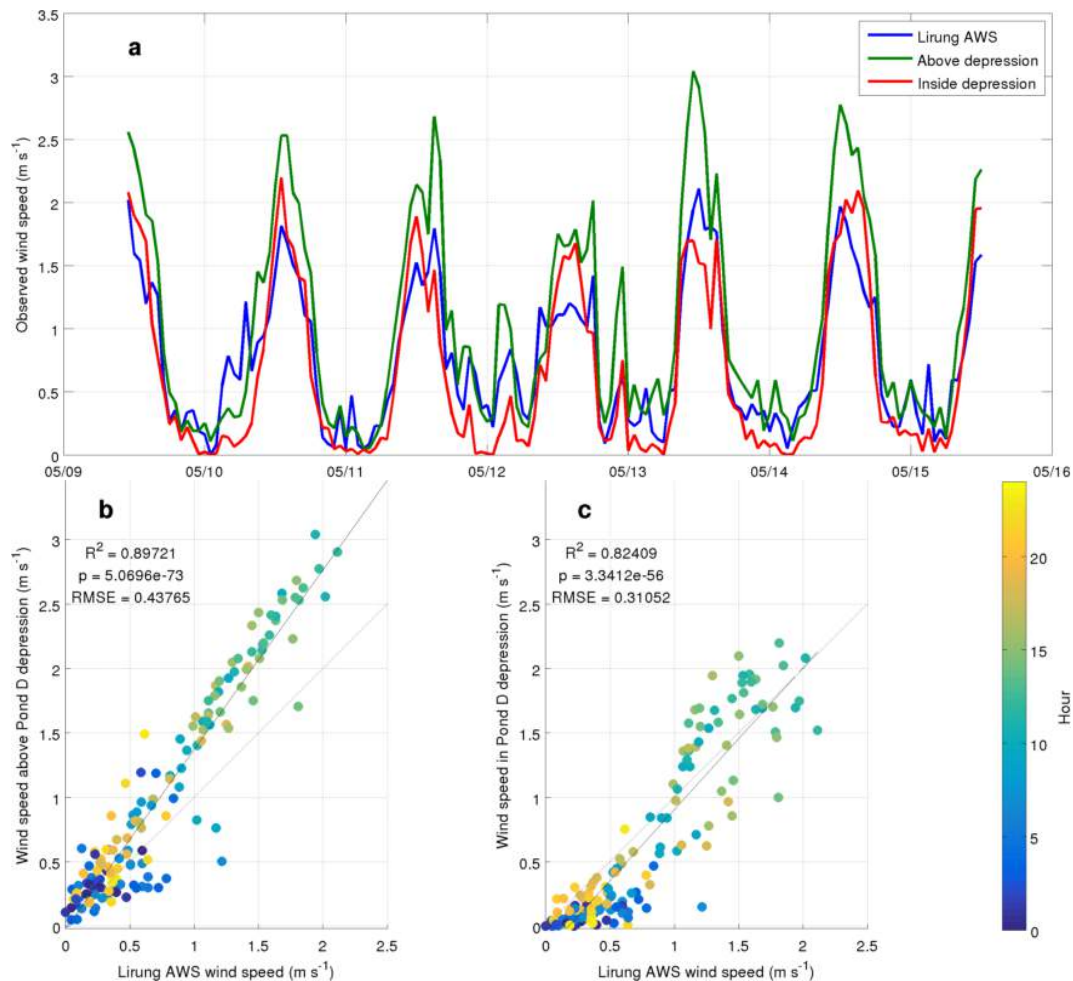


Fig. 6.4 (a) The observed wind speed at Lirung AWS and at the two anemometers near Pond D show similar diurnal fluctuations. A direct comparison shows that the Lirung AWS underpredicts wind speed at prominent locations but with a strong correlation (b), while the correlation is slightly weaker but of correct overall magnitude when compared to wind speeds in the pond depression. For (b) and (c) the black line is a best-fit through the data and the grey line is 1:1.

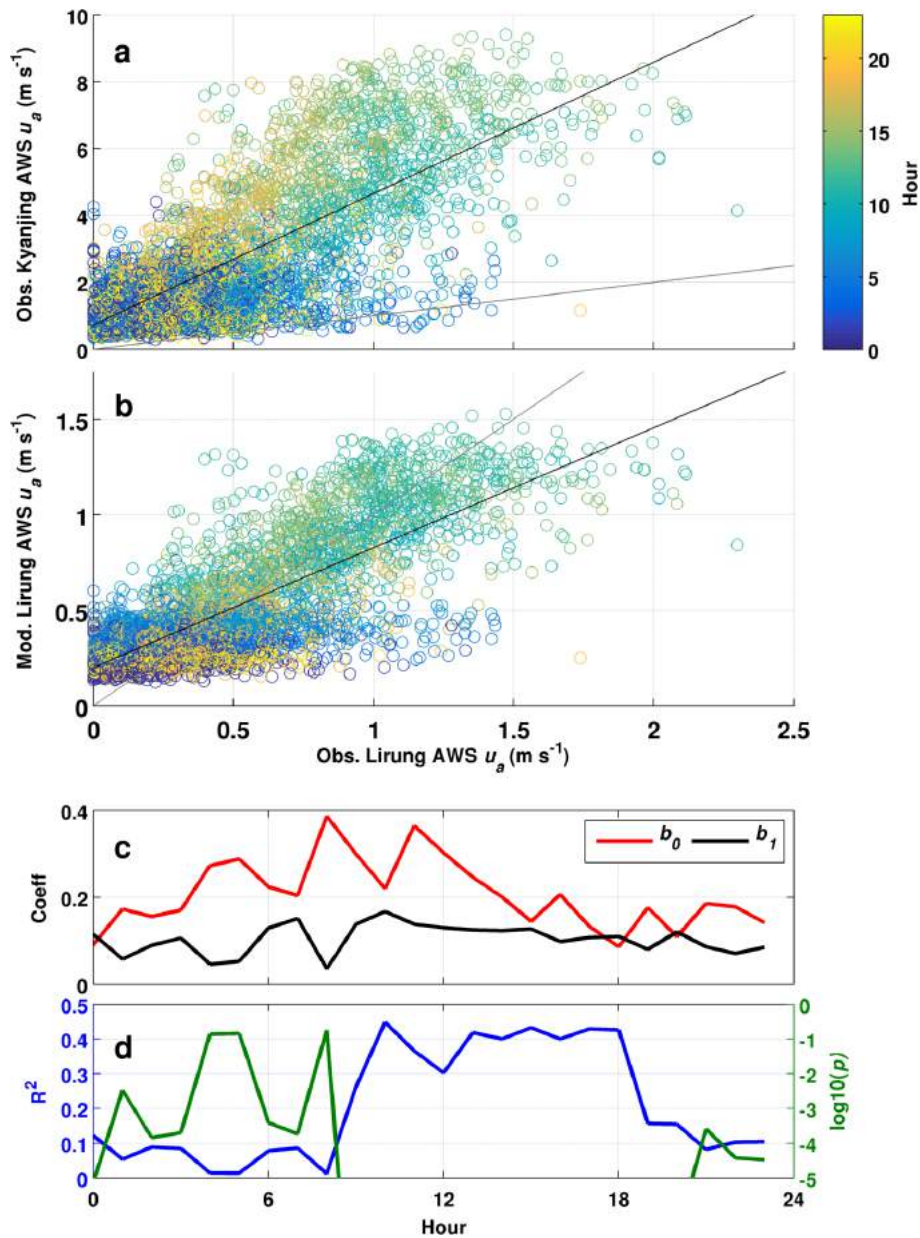


Fig. 6.5 a) Concurrent wind speeds observed at the Kyanjing and Lirung AWS locations based on 159 days of hourly observations from 2014 show strong correlation, but incorrect magnitude. b) An hourly regression model produces the correct magnitudes, but misses some variability at Lirung AWS. The hourly linear regression parameters (c) and model fits (d) are also shown, with a log scale for  $p$ . For (a,b), the black line is a best-fit through the data and the grey line is 1:1.

### 6.3.2 Reducing model complexity

To achieve the goals outlined above, model complexity was progressively reduced through five levels A-E, beginning at the full complexity of the model described in Chapter 5. This section describes the complexity structure and the configuration of input data for each level.

Numerical model development must balance model complexity and applicability. More complicated models require more complete forcing data that is available for fewer sites (Figure 6.6). In the case of supraglacial ponds, the combined limitations of orthophoto spatial coverage (Table 4.2), AWS temporal coverage (Table 4.1), and few pressure transducer units (Table 4.1) mean that only four ponds (C,D,I,J) can be evaluated with the full energy-balance model presented in Chapter 5. At the other end of the spectrum, 14 ponds on Lirung Glacier were observed by the Spot6 orthophoto and associated DEM, which is within the time period of observations available from Kyanjing AWS. A range of model simplifications between these two end points allows a more thorough investigation of modelling errors for the simplest setup. Thus, I progressively degrade the pond energy-balance model through four levels of complexity (A-D), varying the geometric and meteorological sources of data and the evaluation period (Table 6.4).

The level A of model complexity is the full energy-balance model presented in Chapter 5, including water level and area fluctuations, computation of subaqueous bare-ice and saturated debris melt, and the complete mass and energy budget for the pond as a control volume. This model requires pressure transducer observations of water-level fluctuations, so it can only be evaluated for a few ponds (C, D, I, J). The model is run under five configurations under level A. For run A1 I use the May 2014 UAV DEM and outlines. For A2 I use a degraded version of the May 2014 UAV DEM. A3 also uses the degraded UAV DEM, but with off-glacier Kyanjing AWS records combined with a simple on-glacier logger recording air and debris temperature. Run A4 instead uses this meteorological setup with the Spot6 DEM. Finally, A5 uses the Spot6 DEM and off-glacier meteorological records. All level A runs were evaluated with  $\alpha = 0.08$  and  $0.12$  to determine the model sensitivity to pond albedo.

The B level of model complexity calculates the surface energy balance of the ponds, accounting for variations in water level and pond area (B1-B5). The surface energy balance is determined exactly as in runs A1-A5, but is considered separately for comparison to further reductions in model complexity.

The C level of model complexity also accounts for the surface energy balance of the ponds. Unlike level B, level C represents pond geometry with linearly-changing pond area based on initial and final area observations. Thus, C-level runs do not need pressure transducer data and can be applied to ponds A-H, for which at least two area observations are available in 2014. Two configurations are tested: C1 uses the Lirung AWS meteorological data and pond

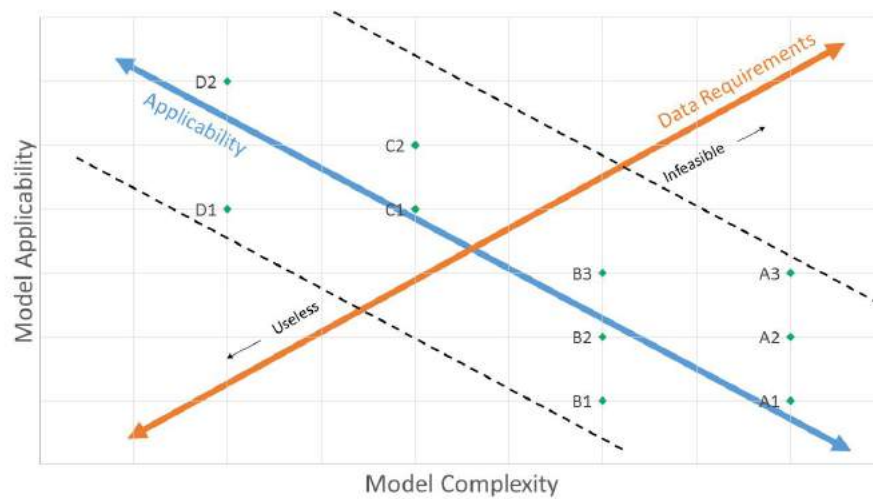


Fig. 6.6 Conceptual diagram of useful numerical modelling trade-offs, showing relative locations of the model configurations used in this study. More complicated models can be applied to few locations due to increasing data requirements, while reduced complexity models are useful if they enable application to a wider area.

area observations from the May 2014 UAV and Nov 2014 terrestrial orthoimages. C2 uses the April 2014 Spot6 orthoimage as a third observation of pond area, and uses the Kyanjing AWS meteorological data, which has an extended period of observation.

The D level model runs follow the C runs, but use a static pond area. D1 uses the Lirung AWS data and the May UAV pond area observations, and can be evaluated for ponds A-H. D2 uses the Kyanjing AWS meteorological data and the April 2014 Spot6 pond observations, and is evaluated for all ponds on the glacier.

The structured model degradation enables application of the best data and model possible for each pond in order to determine its energy balance. It also enables assessment of the performance of simpler model configurations by comparing results for the overlapping period of input data for all ponds (4 May to 8 June). The effects of the topographic coarsening (A1 vs A2) and meteorological source data simplification (A2 vs A3, A4 vs A5) can also be determined. Finally, I can make a detailed assessment of the portion of the surface energy flux that is advected to the glacier's interior (A vs B runs), and determine the model accuracy when applied to the entire glacier with progressively simpler models (B-D runs).

### 6.3.3 Input meteorological data

Model runs use meteorological data from the Kyanjing AWS and Lirung AWS (Table 4.1). The Lirung AWS lacks a barometric pressure sensor, so pressure observations from Kyanjing

Table 6.4 Formulation of model and source data progressive degradation, and portion of pond area that is observed and can be modelled by each approach. Runs B1-B5 exactly follow the specification of runs A1-A5, but using only the surface energy balance output from the full model, and are not explicitly included in the table. %Obs is the percentage of observed pond area represented in the model, while %Tot is the percentage of the total pond area observed in April 2014, when all ponds could be delineated.

Run	Model Complexity	Meteorological forcing	Geometry (DEM res)	Model Start	Ponds (#)	Pond Area	
						% Obs.	% Tot.
A1	Full EB	AWS Lirung	May UAV (1 m)	4 May 2014	C, D (2)	67.8	14.2
A2	Full EB	AWS Lirung	May UAV (3m)	4 May 2014	C, D (2)	67.8	14.2
A3	Full EB	AWS Kyanjing + surface T-logger	May UAV (3m)	16 Apr 2015	C, D (2)	67.8	14.2
A4	Full EB	AWS Kyanjing + surface T-logger	Apr Spot6 (3m)	16 Apr 2015	C, D, I, J (4)	46.5	46.5
A5	Full EB	AWS Kyanjing	Apr Spot6 (3m)	16 Apr 2015	C, D, I, J (4)	46.5	46.5
B1-B5	Surface EB	Same configuration as A1-A5	–	–	–	–	–
C1	Surface EB, linear change	AWS Lirung	May & Nov (3m)	4 May 2014	A-H (6)	100.0	20.9
C2	Surface EB, linear change	AWS Kyanjing + surface T-logger	Apr, May, & Nov (3m)	4 May 2014	A-H (6)	100.0	20.9
D1	Surface EB, fixed geometry	AWS Lirung	May UAV (3m)	4 May 2014	A-H (6)	100.0	20.9
D2	Surface EB, fixed geometry	AWS Kyanjing + surface T-logger	Apr Spot6 (3m)	16 Apr 2015	All ponds (13)	100.0	100.0

AWS are used for all analyses to remove the atmospheric component of observed pond-bottom pressure. Due to a small elevation difference, the Kyanjing AWS pressure record is adjusted to the pond altitudes using the ideal gas law and Kyanjing  $T_a$ . This preserves the pattern and amplitude of barometric pressure variability, but provides the correct magnitude of atmospheric pressure.

Air temperature  $T_a$  and debris surface temperature  $T_{deb}$  are necessary inputs for the models.  $T_a$  is used to determine turbulent fluxes at the water surface, while  $T_{deb}$  is required to model longwave radiation emitted by the glacier's debris surface. I use on-glacier measurements of both variables made at the Lirung AWS (Table 4.1). The mean seasonal on-glacier lapse rates reported by Steiner and Pellicciotti (2016) are used to extrapolate temperature from the Lirung AWS location to each pond's altitude. The  $T_a$  calculations are detailed in Section 6.3.1.  $T_{deb}$  varies based on solar exposure and topographic prominence (Steiner and Pellicciotti, 2016), so I use the on-glacier record to represent  $T_{deb}$  across the glacier for the calculation of debris-emitted longwave radiation.

Pond surface temperature  $T_{ws}$  is a necessary variable for all model runs in order to calculate the longwave radiation and turbulent fluxes at the pond surface. I use regression model M3 (Equation 6.4, 'Both' in Table 6.2) to calculate  $T_{ws}$  for ponds with a record of  $T_{lb}$ . For those ponds without a  $T_{lb}$  record, I instead apply regression model M4 (Equation 6.5, 'Both' in Table 6.2) to calculate  $T_{ws}$ .

Wind data is used from the Lirung AWS and applied directly at the pond surface, but Kyanjing wind speeds are adjusted with the hourly coefficients determined from linear regression, which reproduce the timing and overall magnitude of wind speed (Figure 6.5).

Finally, the nearest complete record of precipitation is Kyanjing AWS. This is assumed uniform across the glacier and is used for all model runs directly, with rainfall prescribed at  $T_a$  for energy-balance calculations.

### 6.3.4 Specification of pond geometry

To produce time series of pond water levels for ponds C, D, I, and J for model runs A1-B5, the pressure transducer records were converted to hydrostatic pressure by subtracting the adjusted Kyanjing AWS barometric pressure record. Hydrostatic pressure values were converted to water depth using  $\rho_w$  based on the pond temperature. The pond depth values were converted to water-level altitudes by determining the mean observed depth on the DEM survey date and adjusting the full dataset.

The model runs that account for fluctuations in water level (A1-B5) require altitude-area-volume relationships for each pond. First, all closed depressions showing evidence of ponding over the study period were identified in the Spot6 DEM, and the mean slope of these depressions excluding ice cliffs ( $20^\circ$ , or 36.5%) was applied to the non-cliff pond shores to estimate pond depth. This slope value is slightly lower than values tested in Chapter 5, but the slope had only a minor effect on the surface energy balance. For each pond, the altitude-area-volume relationship was then determined by the approach outlined in Chapter 5, which also produces estimates of the subaqueous bare-ice and saturated debris areas for each altitude (Section 5.5.1).

## 6.4 Results and Discussion

This section initially summarises the pond energy-balance results for the highest-complexity level A runs. The section then considers all model results for the period common to all model levels and ponds, 4 May to 8 June 2014 (35 days). This relatively short period allows direct evaluation of the effects of different model configurations (Table 6.4) by eliminating seasonal biases for the different study ponds. Individual ponds' results are then compared to highlight the effect of pond area representation from the distinct model setups. Finally, the section extrapolates the different model results based on spatial and temporal coverage to estimate the total energy absorbed by supraglacial ponds for the whole glacier in 2014.

### 6.4.1 Summary of energy-balance results, A1-A5

To summarise the principal results from model level A, this subsection notes seasonal patterns in the surface energy fluxes, calculates the total melt-available energy absorbed by each pond,

and reports the required discharge for each pond to remove excess energy (Table 6.5). Due to the seasonal bias introduced by the variable model evaluation period, the section is brief before discussion focuses on a common period for more thorough comparison.

### Pond surface energy balance

The same general breakdown of surface energy flux magnitude and seasonality was apparent for all ponds. Values given for the surface energy balance apply to pond D, run A1 (Figure 6.7), to highlight the seasonal differences exhibited by all ponds. Mean values for individual ponds are discussed in Section 6.4.2 with a common period of analysis to eliminate seasonal bias.

The net shortwave flux  $I_n$  is a major source of energy for the ponds, with diurnal peaks at midday up to  $1000 \text{ W m}^{-2}$ . Daily mean values of  $I_n$  are about  $170 \text{ W m}^{-2}$  for most ponds and model configurations, and are higher in the pre-monsoon ( $\sim 225 \text{ W m}^{-2}$ ) than in the monsoon ( $\sim 125 \text{ W m}^{-2}$ ).

The net longwave flux  $L_n$  varies both diurnally and seasonally, and ranges from  $-80 \text{ W m}^{-2}$  to  $80 \text{ W m}^{-2}$  for the study ponds. Diurnal peak-to-peak ranges are higher in the pre-monsoon ( $\sim 80 \text{ W m}^{-2}$ ) than during the monsoon ( $\sim 40 \text{ W m}^{-2}$ ), with daily peak values around midday. Daily means vary from slightly negative ( $-30$  to  $10 \text{ W m}^{-2}$ ) during the pre-monsoon to strongly positive ( $\sim 40 \text{ W m}^{-2}$ ) during the monsoon.

Sensible turbulent fluxes ( $H$ ) also fluctuate diurnally, but are of low magnitude for the entire period ( $< 60 \text{ W m}^{-2}$ ), with daily mean values of  $0$ - $25 \text{ W m}^{-2}$ .

Latent turbulent fluxes ( $E$ ) also show strong diurnal peaks, but switch from strongly negative values in the pre-monsoon (peaks to  $-500 \text{ W m}^{-2}$ , daily means of  $-150$  to  $50 \text{ W m}^{-2}$ ) to strongly positive values throughout the monsoon (peaks to  $500 \text{ W m}^{-2}$ , daily means of  $\sim 100 \text{ W m}^{-2}$ ).

Energy advected by rainfall ( $Q_r$ ) was a very small component of the surface energy balance, with daily means  $< 60 \text{ W m}^{-2}$ .

As the sum of the individual energy fluxes, the net surface energy balance ( $Q_n$ ) also expresses diurnal and seasonal patterns. Diurnal variability of  $Q_n$  is pronounced, with midday high values of  $500$  to  $1500 \text{ W m}^{-2}$ , and night-time low values of  $-200$  to  $100 \text{ W m}^{-2}$ . Daily mean values are  $\sim 220 \text{ W m}^{-2}$  during the pre-monsoon and  $\sim 290 \text{ W m}^{-2}$ , as the monsoon decrease in  $I_n$  is offset by the increases in  $L_n$  and  $E$ .

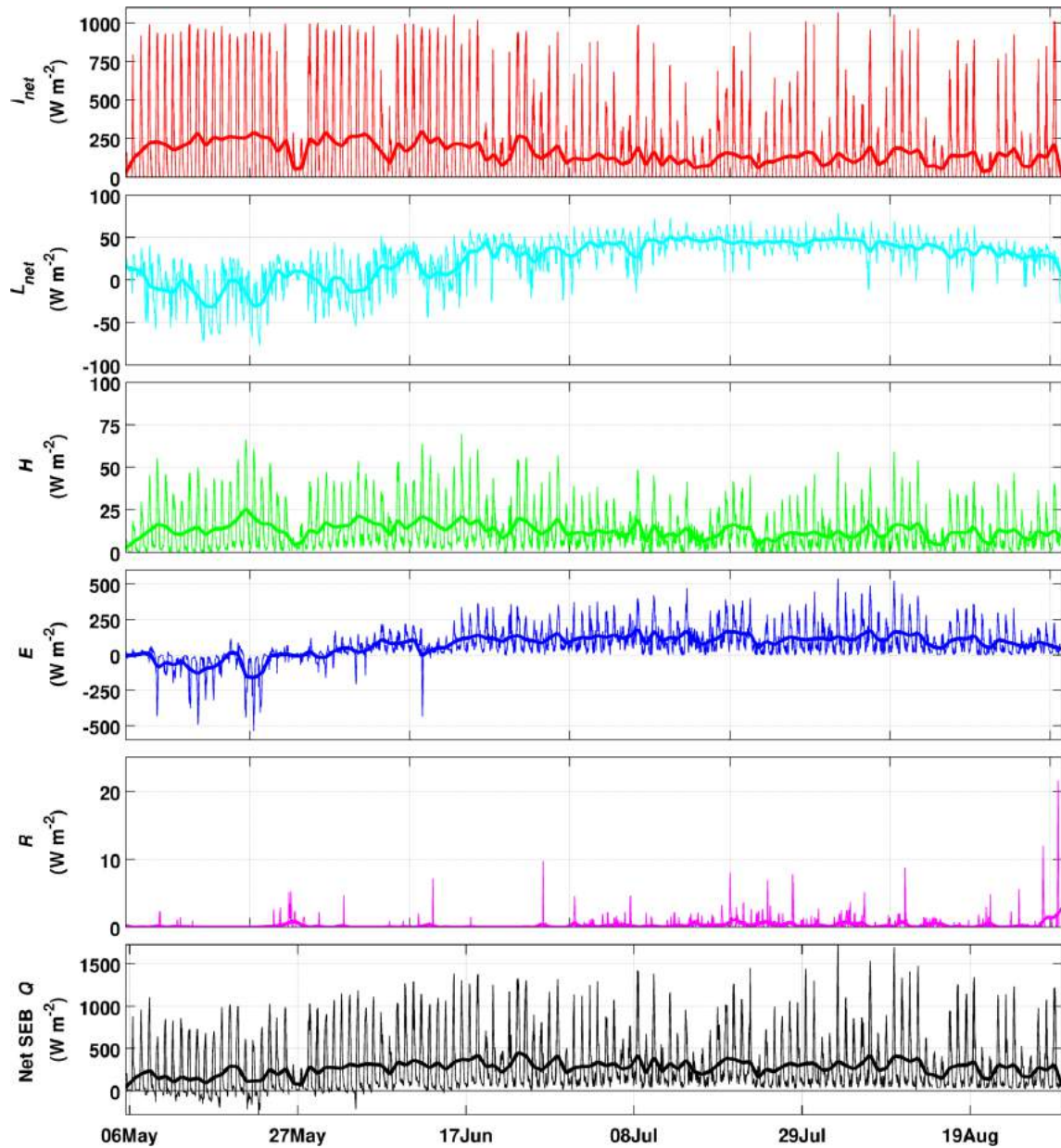


Fig. 6.7 Example pond surface energy-balance results from pond D, run A1, for  $\alpha = 0.08$ . All surface energy fluxes show different magnitude in the monsoon relative to the pre-monsoon. The largest changes are less-consistent  $I_n$ , increased  $L_n$  baseline, and positive  $H$ , which result in always-positive  $Q_n$  during the monsoon. For this study, the monsoon period begins on 15 June.

### Modelled melt and pond energy partition

The ponds' energy inputs are partitioned into the reservoir of stored energy ( $S$ ), discharge energy  $\frac{\bar{D}}{A_p}$ , subaqueous bare-ice melt  $\frac{Q_i A_i}{A_p}$ , and subdebris melt  $\frac{Q_d A_d}{A_p}$  (Chapter 5).

Table 6.5 Summary of model results for the level A runs, including model configuration, pond, run time  $\Delta t$ , net surface energy balance  $\Sigma(Q_n A_p)$ , cumulative subaqueous bare-ice ( $MW_i$ ) and subdebris melt ( $MW_d$ ), and total discharged energy  $\Sigma D$ , all expressed in  $m^3$  ice melt equivalent. Also shown are the total ( $\Sigma Ex$ ) and mean specific ( $\frac{\Sigma Ex}{A_p \Delta t}$ ) ablation related to the pond. Local Melt is the portion (%) of absorbed energy accounted for by subaqueous and subdebris melt, and Englacial Melt is the portion discharged internally.

Units			$m^2$	$m^3$	$m^3$	$m^3$	$m^3$	$m^3$	$m\ d^{-1}$	%	%	$m^3\ s^{-1}$	$m^3\ s^{-1}$
Run	Pond	$\Delta t$	$\bar{A}_p$	$\Sigma(Q_n A_p)$	$MW_i$	$MW_d$	$\Sigma D$	$\Sigma Ex$	$\frac{\Sigma Ex}{A_p \Delta t}$	Local Melt	Englacial Melt	$\bar{V}_d$	$V_{dmax}$
A1	C	90	122	717	60.8	2.5	647	710	0.065	9%	91%	0.0046	0.044
A2	C	90	122	702	60.8	2.5	632	696	0.063	9%	91%	0.0045	0.042
A3	C	108	394	891	239	4.5	606	850	0.038	29%	71%	0.0071	0.157
A4	C	108	394	948	239	4.5	657	900	0.040	27%	73%	0.0068	0.157
A5	C	108	122	830	235	4.5	546	785	0.035	30%	70%	0.0064	0.152
A1	D	116	122	3548	2357	5.2	942	3304	0.072	71%	29%	0.0073	0.077
A2	D	116	394	3597	2357	5.2	991	3353	0.073	70%	30%	0.0075	0.079
A3	D	116	394	3944	2357	5.2	1464	3826	0.084	62%	38%	0.0091	0.087
A4	D	116	207	4209	2357	5.2	1586	3948	0.086	60%	40%	0.0093	0.087
A5	D	116	207	3795	2311	5.2	1222	3538	0.077	65%	35%	0.0084	0.084
A4	I	99	394	4013	1586	3.8	2248	3838	0.086	41%	59%	0.0170	0.207
A5	I	99	394	3607	1530	3.8	1905	3438	0.077	45%	55%	0.0159	0.215
A4	J	52	207	31395	20552	96.1	8532	29180	0.051	71%	29%	0.2308	2.339
A5	J	52	207	26696	20106	96.1	4333	24535	0.043	82%	18%	0.2063	2.115

The total melt and energy attribution for level A model runs is reported in Table 6.5. Total surface energy inputs  $\Sigma(Q_n A_p)$  ranged from 702.1  $m^3$  of ice-melt-equivalent to 31,394.5  $m^3$ , while modelled subaqueous bare-ice melt totals  $MW_i$  ranged from 60.8  $m^3$  to 20,551.8  $m^3$ . The modelled subaqueous subdebris melt  $MW_d$  was very low for all configurations and ponds, accounting for 2.5 - 96.1  $m^3$  ice melt. The discharged excess energy  $\Sigma D$  was considerable, ranging from 546.1  $m^3$  to 8,531.6  $m^3$ .

The four study ponds range in mean surface area from 122.2  $m^2$  (pond C) to 10,939.9  $m^2$  (pond J). Ponds D (393.8  $m^2$ ) and I (451.6  $m^2$ ) also have low mean surface areas. The mean areas control the total surface flux of energy, but also control the areas of subaqueous bare ice and saturated debris, and therefore the total energy attributed to melt at those interfaces.

To represent the total melt associated with the ponds, I sum up the pond's proximal and distal ablation to produce  $\Sigma Ex$ :

$$\Sigma Ex = MW_i + MW_d + \Sigma D \quad (6.7)$$

$\Sigma Ex$  varies significantly based on pond area, with the largest pond (J) accounting for significantly more melt than all other ponds. Normalising by pond area and period of model evaluation, the metric  $\frac{\Sigma Ex}{A_p \Delta t}$  appears relatively stable for all ponds, varying primarily with the model evaluation period (Table 6.5). Records for ponds C and J are primarily limited to the pre-monsoon and early monsoon, when  $Q_n$  is much lower, while D and I extend much

farther into the monsoon. Across all ponds and model configurations, this mean surface melt-equivalent has a mean value of  $6.3 \text{ cm d}^{-1}$  and a standard deviation of  $1.8 \text{ cm d}^{-1}$ . This metric is later assessed for a comparable period of evaluation between model runs in Section 6.4.2.

The partition of pond-associated ablation energy between local and englacial locations can only be determined for the level A runs, which have in-situ temperature observations (Table 6.5). Subaqueous subdebris melt accounts for a very small portion of the surface energy exchange for any model configuration or pond (0.1-0.6%). The portion of melt energy accounted for by subaqueous bare-ice melt and discharged energy varies dramatically based on pond size and shape, and on the period of record. Larger ponds and those bordered by extensive ice cliffs have a high subaqueous exposed ice area, permitting enhanced local melt ( $MW_i$ , Ponds D and J) and accounting for up to 82% of the surface energy exchange (Pond J, A5). Conversely, as little as 9% of the surface energy balance goes to subaqueous ice melt for the smaller pond C (runs A1 and A2). Averaging this partition across runs for each pond, local melt accounted for 22% of  $E_x$  at pond C, 65% at pond D, 43% at pond I, and 76% at pond J. Averaging across the A4 model results for all ponds, the partition of pond-associated ablation potential energy is 50% to local melt and 50% to englacial discharge. However, based on total energy modelled for all A4 runs, 66% of the total melt energy leads to local melt and 34% drains englacially.

### Inferred englacial discharge

Pond discharge is calculated by the model based on the excess energy from the whole-pond energy balance, which must be removed from the control volume (Section 5.3.1), and is assumed to enter the englacial conduit network. Inferred discharge values vary based on pond size and behaviour during the study period (Table 6.5).

For 2014, mean modelled discharge at pond C was  $0.0045\text{-}0.0071 \text{ m}^3 \text{ s}^{-1}$ , with peak values of  $0.04\text{-}0.16 \text{ m}^3 \text{ s}^{-1}$ . For pond D, the model calculates a mean discharge of  $0.0073 \text{ m}^3 \text{ s}^{-1}$  to  $0.0093 \text{ m}^3 \text{ s}^{-1}$ , with peak values of  $0.077\text{-}0.087 \text{ m}^3 \text{ s}^{-1}$ . The mean modelled discharge of pond I was  $0.016\text{-}0.017 \text{ m}^3 \text{ s}^{-1}$ , and peak modelled discharge was  $0.21\text{-}0.22 \text{ m}^3 \text{ s}^{-1}$ . For pond J, mean modelled discharge values were  $0.21\text{-}0.23 \text{ m}^3 \text{ s}^{-1}$ , with peak values of  $2.1\text{-}2.3 \text{ m}^3 \text{ s}^{-1}$ .

As with the other basic energy-balance results, these values differ based on pond changes (filling or drainage) and the seasonal timing of the model evaluation period. For pond C, runs A1 and A2 miss the filling and drainage in April 2014 (Section 4.4.2), and estimate much lower discharge values. Unlike the pond C model runs, all pond D runs have the same evaluation period, and are closely clustered.

Higher discharge estimates were produced for pond I, which was similar to pond C in 2013 in terms of size (400-500 m<sup>2</sup>) and behaviour (gradual continuous water-level decline), when pond C accounted for up to 10% of the whole glacier's discharge (Section 5.5.4). The largest pond, J, accounted for an even larger portion of the daily peak flow reported for the glacier's outlet (2.5 – 3 m<sup>3</sup> s<sup>-1</sup> per Bhatt et al., 2007; Ragettli et al., 2015). Pond J continually filled during the period of analysis; its final volume was 78,490 m<sup>3</sup>.

It is important to note that these estimates, as in Chapter 5, are the minimum discharge flux required to account for the excess energy. Additional inputs of water may be possible at a variety of temperatures, and would simply add to the discharge flux depending on the excess energy brought into the system. Thus, considering the possible scenario that pond J discharge flows directly into pond I with minimal loss of energy by englacial melt, the addition of advected energy will simply increase the calculated discharge of pond I. These relationships were explored in Chapter 5, but the values presented here reflect the discharge required to account for the excess energy of each pond itself.

## 6.4.2 Comparisons for common period

To remove seasonal biases from the comparison between models and ponds, this section focuses on a period common to all model setups, 4 May to 8 June 2014. The complete model results for this period are included in Tables A.5 and A.6, but this section compares subsets of the results to evaluate the effects of model configuration.

The section first compares the energy-balance results for the four ponds using model run A4. The effects of DEM resolution and choice are assessed by comparing outputs from models A1-A2 (1 m and 3 m resolution UAV DEMs) and A3-A4 (UAV and Spot6 3 m DEMs), holding other inputs constant. Meteorological data source effects are assessed by comparing runs driven with on-glacier or off-glacier AWS (A2 vs A3) and off-glacier AWS with or without on-glacier air temperature records (A4 vs A5). The results for increased albedo ( $\alpha = 0.12$ ) are also presented for this period. The section concludes by comparing the full energy-balance model results to the results from simpler surface energy-balance configurations (level A vs levels B-D).

### Differences between ponds, run A4

After limiting the model results to a common period, differences in modelled pond energy balance are apparent (Tables A.5 and A.6). Here, results are presented for run A4 for the common period, which could be evaluated for all four study ponds (Table 6.6).

$\bar{I}_n$  is above  $200 \text{ W m}^{-2}$  for all four ponds due to the pre-monsoon conditions during the common period. However, higher values are calculated for ponds D and I ( $\sim 233 \text{ W m}^{-2}$ ) than for ponds C and J ( $\sim 205 \text{ W m}^{-2}$ ).  $\bar{L}_n$  varies slightly among the four ponds, ranging from  $-13$  to  $-6 \text{ W m}^{-2}$ . The mean sensible heat flux  $H$  was  $12$ - $13 \text{ W m}^{-2}$  for all four ponds, showing little variability. However, the mean latent heat flux  $E$  varied from  $-8$  to  $12 \text{ W m}^{-2}$  between ponds for the common period, with values close to zero based on the late pre-monsoon common period (Figure 6.7). The mean heat flux due to rain ( $Q_r$ ) during the common period was  $< 1 \text{ W m}^{-2}$  and is not included in Table 6.6. The mean net surface energy balance  $\bar{Q}_n$  ranges from  $205 \text{ W m}^{-2}$  (pond J) to  $246 \text{ W m}^{-2}$  (pond I) for the common period. Intermediate values of  $Q_n$  were calculated for ponds C and D ( $223 \text{ W m}^{-2}$  and  $239 \text{ W m}^{-2}$ , respectively).

The variability in surface fluxes is the result of differences in topographic shading, pond altitude and modelled surface temperature, while variability in subaqueous melt rates and discharge is due to differences in pond area and mean temperature. Ponds C and J are shaded by the steep, prominent ice cliffs on their southern margins (Section 4.4.2), while ponds D and I are less shaded by their marginal ice cliffs, which are both less steep and less prominent. This leads to reduced sky-view factors for ponds C and J, and consequently lower receipts of shortwave radiation.

The four study ponds range in altitude from  $4074 \text{ m.a.s.l.}$  to  $4207 \text{ m.a.s.l.}$  The  $133 \text{ m}$  pond-surface elevation difference between ponds C and J leads to a  $0.67$ - $1.04^\circ\text{C}$  difference in  $T_a$  based on the on-glacier lapse rates (Table 6.1). Pond surface temperatures, though, are not wholly dependent on altitude, leading to differences in  $I_n$  and  $E$ .

Mean subaqueous melt rates ( $\bar{v}_i$  and  $\bar{v}_d$ ) range by a factor of two between ponds (Table 6.6).  $\bar{v}_i$  was  $0.018 \text{ m d}^{-1}$  for pond C,  $0.022 \text{ m d}^{-1}$  for pond I, and  $0.036 \text{ m d}^{-1}$  for both ponds D and J.  $\bar{v}_d$  results have nearly the same pattern of magnitudes, although the melt rates are 100 times lower. The mean pond surface temperatures for ponds C, D, I, and J were  $0.88^\circ\text{C}$ ,  $1.34^\circ\text{C}$ ,  $0.84^\circ\text{C}$ , and  $1.35^\circ\text{C}$ , respectively, highlighting the strong sensitivity of melt rates to water temperatures.

Pond discharge, as reflected by mean  $\bar{V}_d$  and maximum values  $\dot{V}_{dmax}$ , varied by two orders of magnitude between ponds. There is a clear dependence of modelled discharge on pond area, as larger ponds absorb significantly more energy at the water surface, but may not have adequate marginal bare-ice areas to dissipate excess energy. The mean modelled discharge thus ranges from the moderate value of  $0.0063 \text{ m}^3 \text{ s}^{-1}$  for pond C (equal to  $6.3 \text{ L s}^{-1}$ ) to the considerable value of  $0.27 \text{ m}^3 \text{ s}^{-1}$  for pond J. Peak discharge estimates during the common period were about ten times higher than mean values, and ranged from  $0.035 \text{ m}^3 \text{ s}^{-1}$  for pond

Table 6.6 Pond energy-balance model results for the level A runs, including pond altitude, pond area  $A_p$ , mean shortwave energy flux  $\overline{SW_{net}}$ , mean longwave energy flux  $\overline{LW_{net}}$ , mean sensible heat flux  $\overline{H}$ , mean latent heat flux  $\overline{E}$ , mean net surface energy balance  $\overline{Q}$ , mean subaqueous bare-ice and subdebris ( $\overline{v_i}$  and  $\overline{v_d}$ ) melt rates, and mean and peak pond discharge ( $\overline{V_d}$  and  $\dot{V}_{dmax}$ ). All values are for the 35-day common period of 4 May to 8 June, 2014.

Pond	m.a.s.l.	$m^2$	$W m^{-2}$	$m d^{-1}$	$m d^{-1}$	$m^3 s^{-1}$	$m^3 s^{-1}$				
	Altitude	$A_p$	$I_n$	$L_n$	$H$	$E$	$Q_n$	$\overline{v_i}$	$\overline{v_d}$	$\overline{V_d}$	$\dot{V}_{dmax}$
C	4074	170	202	-6	13	12	223	0.018	0.00025	0.0063	0.035
D	4095	419	233	-13	13	6	239	0.036	0.00040	0.0090	0.080
I	4190	554	234	-11	12	10	246	0.022	0.00024	0.020	0.21
J	4207	13113	207	-8	12	-8	205	0.036	0.00041	0.27	2.2

C to  $2.2 m^3 s^{-1}$  for pond J, still below the peak daily discharge reported for the glacier's outlet (Bhatt et al., 2007; Ragettli et al., 2015).

The total energy absorbed by each pond at the water surface ( $\Sigma Q_n A_p$ ) is controlled by pond area, which also controls the subaqueous bare-ice and debris areas. Mean pond areas for the common period range from 170-13,113  $m^2$ , so the magnitudes of modelled melt ( $MW_i$ ,  $MW_d$ , and  $\Sigma D$ , expressed in  $m^3$  of icemelt equivalent) vary greatly between the four ponds (Table 6.7). The total melt energy  $Ex$  for the common period accounts for 370  $m^3$  of glacier melt for pond C, but 26,081  $m^3$  for pond J. The size-dependence is clarified by the specific melt rate  $\frac{\Sigma Ex}{A_p \Delta t}$ , which varies between 0.057-0.062  $m d^{-1}$ , decreasing with increased pond altitude.

In all cases,  $MW_d$  is a very small portion of  $Ex$  ( $< 1\%$ ), but  $MW_i$  and  $\Sigma D$  account for varying portions of  $\Sigma Ex$ : 'Local' melt accounts for only 9% of  $\Sigma Ex$  at pond C, but 78% of  $\Sigma Ex$  at pond I. Based on the total modelled  $\Sigma Ex$  for all ponds in the common period, 68% of  $\Sigma Ex$  is accounted for by 'Local' melt at the subaqueous surfaces, while 32% occurs englacially. These values are in close agreement with Section 6.4.1, but without seasonal biases in surface energy balance.

#### DEM effects: A1 vs A2, A3 vs A4

Minor changes were modelled for the difference in DEM resolution between model runs A1 (1 m) and A2 (3 m), and for the change in 3 m DEM source between model runs A3 (UAV) and A4 (Spot6). Runs A1-A3 were not possible for ponds I and J, limiting these comparisons to ponds C and D (Table 6.8).

Considering results for A2 relative to A1, the difference in DEM resolutions led to minor changes in the mean fluxes at the pond surface (all  $< 10 W m^{-2}$  difference), resulting in -3.6% decrease in  $Q$  for pond C ( $-6.7 W m^{-2}$ ), but a 2.0% increase for pond D ( $+4.1 W m^{-2}$ ).

Table 6.7 Modelled melt for the level A4 runs, including pond, pond area  $A_p$ , cumulative surface energy balance  $\Sigma(Q_n A_p)$ , subaqueous bare-ice and subdebris melt ( $MW_i$  and  $MW_d$ ), cumulative discharge energy  $\Sigma D$ , total melt energy  $\Sigma Ex$ , specific melt rate  $\frac{\Sigma Ex}{A_p \Delta t}$ , and local and englacial portions of melt energy. All values are for the 35-day common period of 4 May to 8 June, 2014.

Pond	m <sup>2</sup> $A_p$	m <sup>3</sup> $\Sigma Q_n A_p$	m <sup>3</sup> $MW_i$	m <sup>3</sup> $MW_d$	m <sup>3</sup> $\Sigma D$	m <sup>3</sup> $\Sigma Ex$	m d <sup>-1</sup> $\frac{\Sigma Ex}{A_p \Delta t}$	% Local	% Englacial
C	170	373	31	1.3	338	370	0.062	9%	91%
D	419	959	685	1.5	196	882	0.060	78%	22%
I	554	1193	577	1.1	551	1129	0.058	51%	49%
J	13113	28036	17889	85.0	8107	26081	0.057	69%	31%

Table 6.8 Summary of % differences between runs to test the effects of DEM resolution and choice. The ‘Local’ and ‘Englacial’ values refer to the magnitude of change, while all other values express the results of runs A2 or A4 as % deviation from the values of runs A1 or A3.

Run compare	Pond	% $Q$	% $\Sigma(Q_n A_p)$	% $\Sigma D$	% $\Sigma Ex$	% Local	% Englacial
A2 vs A1	C	-3.6%	-3.7%	-4.3%	-3.8%	0.47%	-0.47%
A2 vs A1	D	2.0%	2.0%	34%	2.2%	-2.0%	2.0%
A4 vs A3	C	-4.5%	2.7%	2.6%	2.4%	-0.20%	0.20%
A4 vs A3	D	-2.8%	0.95%	-3.3%	-0.75%	0.58%	-0.58%

Similar differences were calculated for the cumulative surface energy flux ( $\Sigma(Q_n A_p)$ ). The cumulative discharged energy  $\Sigma D$  shows a larger response to the DEM resolution change, registering differences of -4.3% and +34% for ponds C and D, respectively. In the case of pond D, little energy was modelled to be discharged englacially (Tables 6.7 and A.6) so a slight increase in surplus energy leads to a large magnitude of change. Closely following differences in  $Q$ , the total melt energy  $\Sigma Ex$  shows differences of -3.8% and +2.2% for ponds C and D. The partition between local and englacial melt changes slightly, 0.47% at pond C and 2.0% at pond D, for run A2 relative to run A1.

Considering results for A4 relative to A3, the difference in DEM source (both with 3 m resolution) produces changes in energy-balance of a similar magnitude to the resolution coarsening (Table 6.8). For both tests, total modelled melt ( $Ex$ ) varied less than 5% over the common period. The partition between local and englacial melt does not appear to be sensitive to changes in the local representation of topography.

### Source meteorology effects: A2 vs A3, A4 vs A5

Three distinct meteorological data configurations were used: on-glacier AWS, off-glacier AWS with on-glacier temperature records, and off-glacier AWS without supplemental tem-

Table 6.9 Summary of % important differences between model runs to test the effects of different meteorological data sources. The ‘Local’ and ‘Englacial’ values refer to the magnitude of change, while all other values express the results of runs A2 or A4 as % deviation from the values of runs A1 or A3.

Run	Pond	$W \text{ m}^{-2}$ $I_n$	$W \text{ m}^{-2}$ $E$	$W \text{ m}^{-2}$ $Q$	% $Q$	% $\Sigma(Q_n A_p)$	% $\Sigma D$	% $\Sigma Ex$	% Local	% Englacial
A3 vs A2	C	27	29	54	30%	6%	11%	6%	-4%	4%
A3 vs A2	D	14	31	39	19%	16%	216%	18%	-14%	14%
A5 vs A4	C	0	-29	-31	-14%	-14%	-15%	-14%	1%	-1%
A5 vs A4	D	0	-29	-31	-13%	-13%	-55%	-14%	11%	-11%
A5 vs A4	I	0	-29	-31	-13%	-13%	-23%	-13%	5%	-5%
A5 vs A4	J	0	-28	-30	-15%	-15%	-46%	-16%	11%	-11%

perature records. A comparison of runs A3 vs A2 and A5 vs A4 enables consideration of the effect of these setups in isolation, and highlights moderate model response to differing meteorological data source (Table 6.9).

At ponds C and D, it is possible to compare the model results determined from an on-glacier AWS (run A2) to those from an off-glacier AWS with on-glacier temperature records (run A3). The change in meteorological station leads to differences in the pond C and D surface energy balance (Table 6.9), with notable differences in  $I_n$  and  $E$ , both higher with the off-glacier AWS. The result is a 20-30% higher average  $Q$  for run A3 than A2, but the cumulative surface energy  $\Sigma(Q_n A_p)$  only increases by 6-16% as a result of changing pond areas. The relative change in discharged energy  $D$  at pond D is very high (216%) and leads to a change in the partition of local and englacial melt, but the change in total melt energy  $Ex$  closely follows the cumulative surface energy exchange.

All four ponds were modelled with configurations A4 and A5, which used off-glacier meteorological data with (A4) and without (A5) an on-glacier temperature sensor. The effect of the on-glacier temperature record is pronounced and uniform across the ponds (Table 6.9). Latent heat fluxes at the ponds ( $E$ ) are diminished by  $\sim 30 \text{ W m}^{-2}$  without the on-glacier sensor, while other surface energy fluxes are affected only slightly. This leads to a 13-15% decrease in mean and total surface energy fluxes ( $Q$  and  $\Sigma(Q_n A_p)$ ), and a 13-16% reduction in total melt energy  $Ex$ . Changes in  $\Sigma D$  are inconsistent between the ponds (15-55% change), and the partition of local and englacial melt changed variably (1-11% change).

### Albedo effects: 0.08 vs 0.12

The tests of  $\alpha = 0.12$  produced results that were only slightly different from those for  $\alpha = 0.08$  for any model level and pond. To summarise results from the 14 level A model

Table 6.10 Comparison of cumulative surface energy balance  $\Sigma(Q_n A_p)$  and total melt energy  $\Sigma Ex$  for the common period and full period of analysis for all A and B level runs.  $\Sigma(Q_n A_p)$  and  $\Sigma Ex$  are expressed as  $\text{m}^3$  of glacier melt equivalent energy.

Run	Pond	Common Period				Full Period			
		nDays	$\Sigma Ex$ [ $\text{m}^3$ ]	$\Sigma(Q_n A_p)$ [ $\text{m}^3$ ]	$\frac{\Sigma Ex}{\Sigma(Q_n A_p)}$	nDays	$\Sigma Ex$ [ $\text{m}^3$ ]	$\Sigma(Q_n A_p)$ [ $\text{m}^3$ ]	$\frac{\Sigma Ex}{\Sigma(Q_n A_p)}$
A1	C	35	353	357	99%	90	710	716	99%
A2	C	35	340	344	99%	90	696	702	99%
A3	C	35	361	363	99%	108	850	891	95%
A4	C	35	370	373	99%	108	900	948	95%
A5	C	35	318	321	99%	108	785	830	95%
A1	D	35	734	802	92%	116	3304	3548	93%
A2	D	35	750	818	92%	116	3353	3597	93%
A3	D	35	889	950	94%	116	3826	3944	97%
A4	D	35	882	959	92%	116	3948	4209	94%
A5	D	35	759	834	91%	116	3538	3795	93%
A4	I	35	1129	1193	95%	99	3838	4013	96%
A5	I	35	980	1041	94%	99	3438	3607	95%
A4	J	35	26081	28036	93%	52	29180	31394	93%
A5	J	35	21958	23875	92%	52	24535	26696	92%

runs, values of change relative to runs with  $\alpha = 0.08$  are reported as  $\mu \pm 1\sigma$ . Full results are given in Tables A.7 and A.8.

The 4% increase in  $\alpha$  leads to a 4.4% decrease in  $I_n$  for all ponds and model runs, and a  $-4.4 \pm 0.37\%$  change in  $Q$  and  $\Sigma(Q_n A_p)$  for the common period.  $\Sigma D$  exhibits a varied response ( $-22 \pm 23\%$ ) due to the subaqueous melt independently modelled at each pond. Since the modelled subaqueous melt does not change, the partition of melt changes slightly with the albedo increase, and local melt accounts for  $2.7 \pm 1.9\%$  more of the total melt. On the whole,  $Ex$  decreases  $4.7 \pm 0.5\%$  in response to the 4% albedo increase.

Additional pond albedo observations are needed to develop better understanding of the reflectivity of turbid supraglacial pond water, which does not seem to conform to simple parametrisations based on solar elevation angle (Section 6.3.1). Albedo of ponds may plausibly vary between 0.06-0.16, accounting for variable turbidity and elevation angles. Based on the modelling tests, the results based on  $\alpha = 0.08$  would overestimate  $Ex$  for  $\alpha = 0.16$  by 10%, and underestimate  $Ex$  for the case of  $\alpha = 0.06$  by 2.3%.

### EB-SEB comparison: Level A vs B

The ratio  $\frac{\Sigma Ex}{\Sigma(Q_n A_p)}$  represents the portion of the surface energy balance that is accounted for by local ablation and englacial discharge. The difference between the surface energy balance and pond-associated ablation energy is primarily due to the change in stored energy for the pond control volume between modelling start and end dates. Thus, ponds with more extreme

Table 6.11 Summary of results for model levels B-D for the common period and full period including the number of ponds modelled  $n$  by each model. Shown for the common period are model evaluation period  $\Delta t$  (days), total mean pond area  $\overline{\Sigma A_p}$  ( $\text{m}^2$ ), total excess surface energy balance  $\Sigma(Q_n A_p)$  ( $\text{m}^3$  ice melt), mean surface energy balance  $Q$  ( $\text{W m}^{-2}$ ), mean shortwave energy balance  $I_n$  ( $\text{W m}^{-2}$ ), and mean sensible  $H$  and latent  $E$  heat fluxes ( $\text{W m}^{-2}$ ). Shown for the full period are model evaluation period  $\Delta t$  (days), total mean pond area  $\overline{\Sigma A_p}$  ( $\text{m}^2$ ), and total excess surface energy balance  $\Sigma(Q_n A_p)$  ( $\text{m}^3$  ice melt).

Run	$n$	Common Period								Full Period		
		$\Delta t$	$A_p$	$\Sigma(Q_n A_p)$	$Q_n$	$I_n$	$L_n$	$H$	$E$	$\Delta t$	$A_p$	$\Sigma(Q_n A_p)$
B1	2	35	616	1159	195	195	-1	14	-16	103	516	4265
B2	2	35	616	1162	193	198	-5	14	-16	103	516	4299
B3	2	35	589	1313	240	218	-9	13	14	112	601	4835
B4	4	35	14255	30561	228	219	-9	12	5	93.75	11992	40564
B5	4	35	14255	26071	197	219	-9	10	-24	93.75	11992	34928
C1	6	35	840	1529	184	206	-6	12	-31	182	701	7901
C2	6	35	841	1930	229	220	-11	13	5	171	771	10209
D1	6	35	879	1613	184	206	-6	12	-31	182	879	9750
D2	14	35	13575	28333	216	215	-10	12	-3	171	13575	175430

water-level differences (and therefore greater changes in volume) have lower values. Across all ponds and model levels for the common period,  $\frac{\Sigma Ex}{\Sigma(Q_n A_p)}$  has a mean value of 94.9%, with a standard deviation of 3.3%. Over the common period, the models are consistent for individual ponds, which have mean ratios of 99%, 92%, 94%, and 93% for ponds C, D, I, and J, respectively (Table 6.10). Considering the full period, values change for some ponds and the results have a mean value of 95.0% with a standard deviation of 2.2%.

Overall, the utility of the cumulative surface energy balance  $\Sigma(Q_n A_p)$  as a proxy for pond-associated melt  $\Sigma Ex$  is limited by initial and final model conditions. However, the study ponds indicate that  $\Sigma(Q_n A_p)$  overestimates  $\Sigma Ex$  by  $5 \pm 5\%$  for both the common period and the full period of analysis.

### SEB comparison: Levels B-D

The common period is also useful to compare the surface energy balance results for model levels B-D (Table 6.11). Full results for each pond are displayed in Table A.9.

As the cumulative surface energy balance  $\Sigma(Q_n A_p)$  and total pond-associated melt  $\Sigma Ex$  differ by  $5 \pm 5\%$ , the metric  $\frac{\Sigma(Q_n A_p)}{A_p \Delta t}$  is used as a proxy for  $\frac{\Sigma Ex}{A_p \Delta t}$ , the total specific ice melt rate in  $\text{m d}^{-1}$  for the ponded area. Values of  $\frac{\Sigma(Q_n A_p)}{A_p \Delta t}$  for runs B1-D2 are displayed in Figure 6.8, and range from 0.043-0.68  $\text{m d}^{-1}$ . Considering all runs together, the mean value

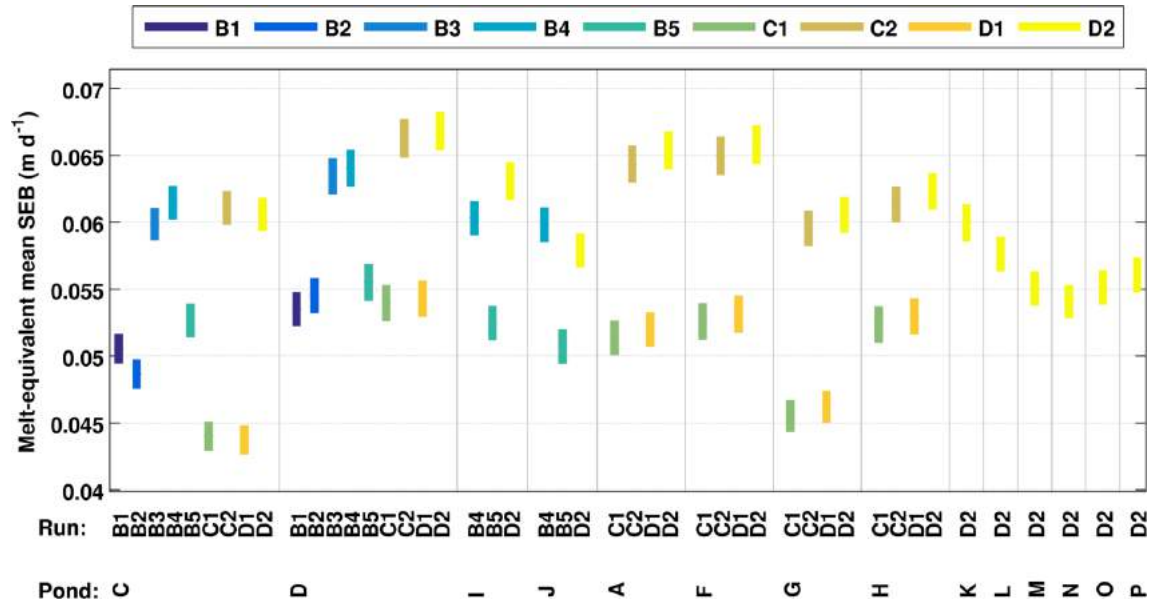


Fig. 6.8 Comparison of surface energy-balance results for all ponds for the common period. Box end-points are for  $\alpha = 0.08$  and  $\alpha = 0.12$  cases.

is  $0.057 \text{ m d}^{-1}$ , with a standard deviation of  $0.0062 \text{ m d}^{-1}$ , but each model has a narrower spread of results.  $\frac{\Sigma(Q_n A_p)}{A_p \Delta t}$  has a total range of about  $0.02 \text{ m d}^{-1}$  for each pond.

The effect of meteorological data source is evident (Figure 6.8), with very close results across all ponds for runs B1, B2, C1, and D1 (mean  $0.052 \text{ m d}^{-1}$ , standard deviation  $0.0038 \text{ m d}^{-1}$ ), all of which use the Lirung AWS data. Runs A3, A4, C2, and D2 all use the Kyanjing AWS data with an on-glacier temperature record, and are closely clustered (mean  $0.062 \text{ m d}^{-1}$ , standard deviation  $0.0037 \text{ m d}^{-1}$ ). As discussed in Section 6.4.2, the B5 results are similar to B1 and B2 (mean  $0.054 \text{ m d}^{-1}$ , standard deviation  $0.002 \text{ m d}^{-1}$ ).

### 6.4.3 Effects of pond geometry: Levels B-D

For the common period, the representation of pond geometry has a minimal effect on the specific energy flux  $\frac{\Sigma(Q_n A_p)}{A_p \Delta t}$ . For example, the differences between results from C1 and C2 or D1 and D2, where meteorology varies, are much greater than the differences between C1 and D1 or C2 and D2, where geometry varies (Figure 6.8). However, pond area is a clear determinant of the total energy absorbed by the ponds (Tables 6.6 and 6.11). Thus, a significant difference between the runs occurs as a result of the representation of pond area throughout the evaluation period. Here ponds C, D, and J are examined to highlight these differences, while results for the other ponds are displayed in Appendix A.

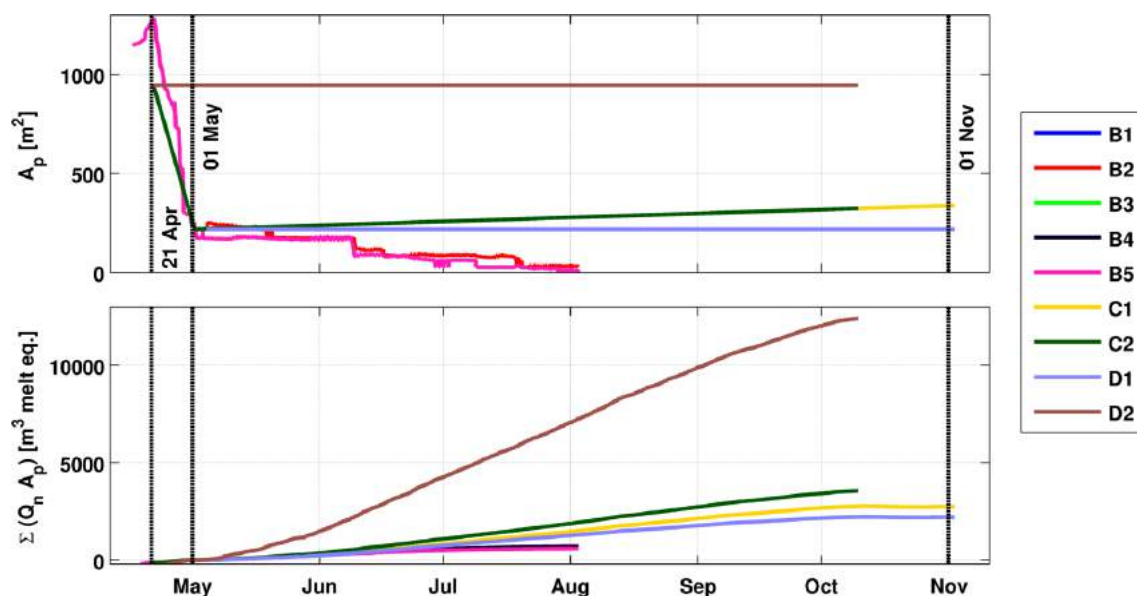


Fig. 6.9 Comparison of pond area (top) and cumulative surface energy balance (bottom) for pond C across all model runs, showing that different approximations of area control cumulative energy balance, and can be a strong source of error. For pond area, run B1 plots beneath B2, B3 and B4 beneath B5, and C1 beneath C2. For cumulative SEB, runs B1-B5 are nearly indistinguishable, and all line series begin with 0 on May 1, the date of UAV observation. Vertical dashed lines are the orthoimage dates, and all shown model runs are for  $\alpha = 0.08$ .

### Pond C results

Pond C experienced a sharp decline in pond area between the 21 April and 1 May orthoimages, then pond area increased slightly by 1 November (Table 4.3). The change in pond area is represented to differing degrees by the model runs (Figure 6.9). Runs B1 and B2 begin after the pond's major drainage in late April, and show a gradual decline in pond area associated with the water-level lowering over the study period, while B3-B5 also show the peak pond area and its rapid decline in late April.

Runs C1 and C2 use a linear interpolation of area through the entire model period, and show a slight increase in Pond C area between May and November. Although this appears to present an error for the surface energy balance, runs C1 and C2 may portray areal changes more accurately during this period than B level runs due to water-level lowering associated with basin expansion and subaqueous melt (Section 4.5.3). This highlights a key limitation of the B level model runs, which rely on a static relationship between pond water surface elevation, area, and volume. Since continuous ice-cliff backwasting during the study period slowly reveals additional area, the November pond area is larger than that observed in May although the water level has continuously declined.

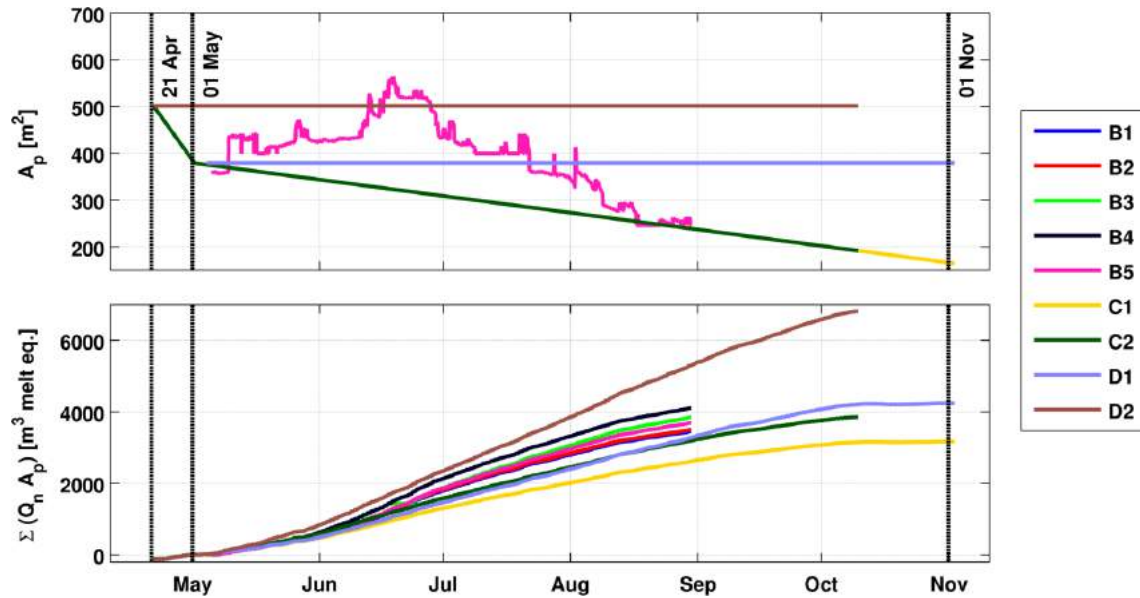


Fig. 6.10 Comparison of pond area (top) and cumulative surface energy balance (bottom) for pond D across all model runs, showing a case where basic representations of area reproduce the general pond behaviour. For pond area, run B1 plots beneath B2, B3 and B4 beneath B5, and C1 beneath C2. For cumulative SEB, all line-series begin with 0 on May 1, the date of UAV observation. Vertical dashed lines are the orthoimage dates, and all shown model runs are for  $\alpha = 0.08$ .

The D level runs use a fixed area estimate, ignoring any changes in pond geometry over the study period. Consequently, run D1 slightly underestimates cumulative SEB by using the 1 May observed pond area, while D2 greatly overestimates cumulative SEB by applying the 21 April pond area, which was approximately the peak area.

Of the model configurations applied to pond C, run C2 appears to present the most complete and accurate set of changes for 2014, and estimates the transfer of enough energy at the pond surface to melt  $3,688 m^3$  of ice by 9 October (when the Kyanjing AWS experiences data errors), after which runs C1 and D1 expect very little additional ablation. This estimate is in general agreement with model runs C1 and D1, which calculate  $2,739 m^3$  and  $2,197 m^3$ , respectively, and all three are slightly higher than runs B1-B5 (about 50% difference) and much lower than run D2 (500% difference) for the comparable periods.

### Pond D results

The model runs were in much closer agreement for pond D, although it too showed moderate water-level fluctuations during 2014 (Figure 6.10, Section 4.5.3). Like pond C, pond D decreased in area between 21 April and 1 May, and further decreased in area by 1 November.

The pressure transducer captured an increase in water level until mid-June, followed by water-level decline until subaerial exposure at the end of August. Consequently, B level model runs clearly reproduce the areal fluctuations during the monsoon, but because these fluctuations encompass both the 21 April and 1 May observed areas, the C and D level runs are in close agreement for cumulative SEB. As with Pond C, the D2 run is higher than other estimates because the pond's peak area was possibly on 21 April, although the discrepancy is not so strong for pond D.

For pond D, the C2 model run accurately reproduces the overall area fluctuations, and calculates a cumulative surface energy balance sufficient to melt 4,088 m<sup>3</sup> during 2014. However, this model misses an extra boost in cumulative SEB from the higher pond area during the monsoon as captured by the pressure transducers; this increase in area absorbed enough energy to melt up to 350 m<sup>3</sup> more ice.

Notably, the short period of peak pond area in late April makes only a small difference to the results for both ponds C and D. For pond C, energy transfer during this period could total 200-240 m<sup>3</sup> of ice melt (6-10% of the whole season total), while for pond D, only enough energy is absorbed for 115-133 m<sup>3</sup> of ice melt (2.5-3% of the total). While this period may be very important from a hydrological perspective, relatively little energy is absorbed by the ponds due to the pre-monsoon conditions.

### **Pond J results**

Pond J represents a different set of challenges for the models. Since the pond was just outside the UAV survey area, the surface energy balance could only be modelled with runs B4, B5, and D2. The pond continually filled after the 21 April orthophoto, so D2 greatly underestimates pond area for the common period. However, it is clear that the pond's surface absorbed at least 23,900-28,000 m<sup>3</sup> ice-melt-equivalent energy during the common period (runs B4-B5) as compared to 8,250 m<sup>3</sup> estimated by D2 for the same period.

Another complication is that the pond's drainage was not observed by the pressure transducer, so it is unclear how to extend the runs of B4 and B5 to the full period. When the drainage occurs, the SEB will be greatly reduced, although the 1 November pond area of 1,569 m<sup>2</sup> was still larger than any other pond with repeat observations. Assuming that models B4 and B5 are correct and the pond's drainage occurred sometime after 1 July, the pond would have a cumulative SEB equivalent to  $5 \times 10^4$  to  $6 \times 10^4$  m<sup>3</sup> of icemelt by 1 July. and pond L's constant area of 1404 m<sup>2</sup> (as represented in run D2) had a cumulative SEB of  $1.1 \times 10^4$  m<sup>3</sup> between 1 July and 1 November, suggesting that a cumulative SEB for pond J of  $6.1 \times 10^4$  to  $7.1 \times 10^4$  m<sup>3</sup> is reasonable when accounting for actual pond behaviour. The

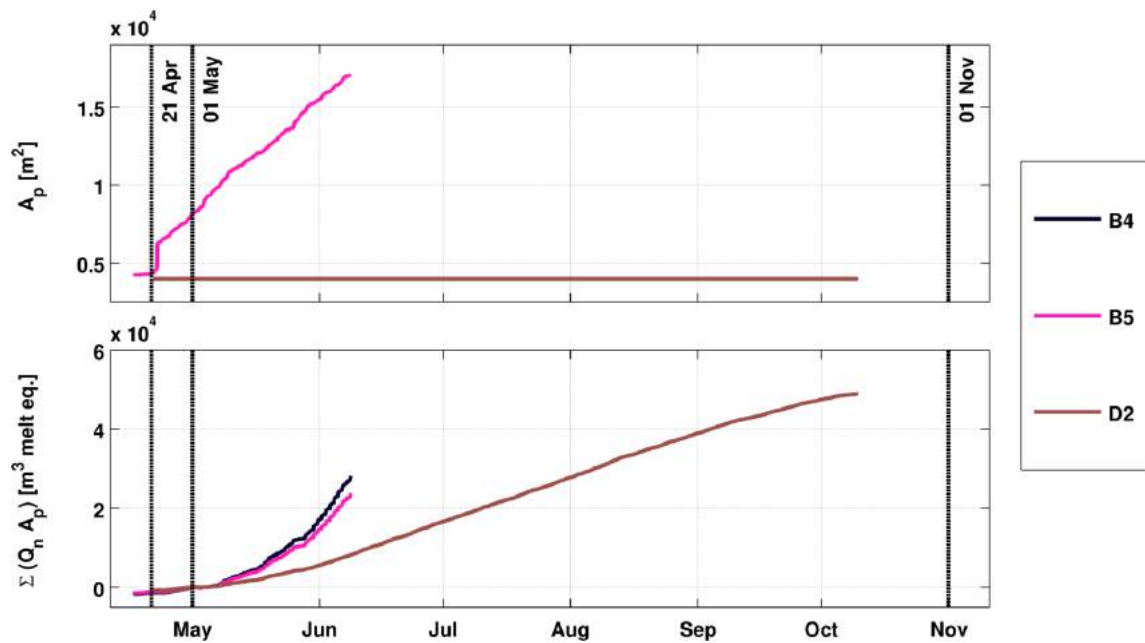


Fig. 6.11 Comparison of pond area (top) and cumulative surface energy balance (bottom) for pond J across all model runs, highlighting the severe underestimation of area and cumulative SEB. The unknown timing of the pond's drainage presents a challenge for total melt estimation. For pond area, run B4 plots beneath B5. For cumulative SEB, all line-series begin with 0 on May 1, the date of UAV observation. Vertical dashed lines are the orthoimage dates, and all shown model runs are for  $\alpha = 0.08$ .

fixed-area representation of run D2 neglects all pond behaviour, but the run's estimate of  $5.0 \times 10^4 \text{ m}^3$  for pond J cumulative SEB appears reasonable.

#### 6.4.4 Glacier-scale estimates of pond-absorbed energy

Several methods may be used to calculate the pond-absorbed energy across Lirung Glacier in 2014. Two approaches are applied here: results from model D2 are used directly to develop an upper-bound estimate, and a combined spatial and temporal scaling to generalise the results of the other runs to the whole glacier and full model period.

Only model run D2 can be evaluated for the whole glacier and full model period. The results of this configuration suggest that surface ponds absorbed enough energy to melt  $1.75 \times 10^5 \text{ m}^3$  of glacier ice between 21 April and 9 October, 2014. Considering the glacier's debris-covered area of  $1.03 \text{ km}^2$ , the energy absorbed by these ponds could account for the equivalent of 0.17 m of downwasting for the entire debris-covered area, 20% of the 0.87 m mean surface lowering for April 2014 to April 2015 (Ragetti et al., 2016). This value is probably an upper bound of pond-absorbed energy. Model configuration D2 uses constant area for each pond, although ponds were documented to subsequently decrease in area (Chapter 4).

A better approach is to scale the results from each model based on the duration, portion of total pond area modelled, and portion of total debris-covered area modelled. Basic statistics were determined for each model configuration, including the April pond area represented by the model  $\Sigma A_{mod}$ , the modelled portion of the total April 2014 observed ponded area, the temporal duration of the model run  $\Delta t$ , the portion of the full 16 April to 1 November 2014 evaluation period encompassed by the model, and the cumulative modelled surface energy balance from all ponds for the model period  $\Sigma(Q_n A_p)$  (Table 6.12). The trade-off between model complexity and applicability is very clear. Runs B1-B3 only cover a small portion of the pond area observed in April, and could only be evaluated for a small portion of the 16 April - 1 November study period, but have the most detailed representation of processes. On the other extreme, run D2 sacrifices model complexity for near-complete coverage of the ponds and evaluation period. Runs B4-D1 strike a balance of temporal coverage and model complexity.

Using this approach, whole-glacier pond cumulative SEB estimates vary between model configurations from  $5.56 \times 10^4 \text{ m}^3$  (C1) to  $1.92 \times 10^5 \text{ m}^3$  (D2), corresponding to 6.2% to 21% of the whole glacier's observed thinning during this period. The highest results were for run D2, which overestimates area for most ponds. Although the model runs vary by more than a factor of three, the mean value is  $1.08 \times 10^5 \text{ m}^3$  of ice-melt-equivalent energy. This

Table 6.12 Scaling of surface energy-balance model results to whole-glacier estimates, showing results for  $\alpha = 0.08$ .  $\Sigma A_{mod}$  refers to the total area of modelled ponds in April 2014, when all ponds could be observed.  $\Delta t$  is the mean model period for each model run, which is only a portion of the full 16 April to 1 November evaluation period.  $\Sigma(Q_n A_p)$  is given for the actual modelled value as well as the full-period whole-glacier scaled value. Also shown are the equivalent thinning over Lirung Glacier's 1.03 km<sup>2</sup> debris-covered tongue, and the portion of total thinning reported by Ragettli et al. (2016).

Run	Modelled ponds	$\Sigma A_{mod}$ [m <sup>2</sup> ]	% total pond area [%]	$\Delta t$ [days]	% full model period [%]	Modelled $\Sigma(Q_n A_p)$ [m <sup>3</sup> ]	Scaled $\Sigma(Q_n A_p)$ [m <sup>3</sup> ]	DCG Thinning [m a <sup>-1</sup> ]	% Ablation [%]
B1	C,D	1447	11%	103	52%	4265	77329	0.075	8.6%
B2	C,D	1447	11%	103	52%	4299	77960	0.076	8.7%
B3	C,D	1447	11%	112	56%	4835	80627	0.078	9.0%
B4	C,D,I,J	6314	47%	93.8	47%	40564	185147	0.180	21%
B5	C,D,I,J	6314	47%	93.8	47%	34928	159422	0.155	18%
C1	A,C,D,F,G,H	2110	16%	182	91%	7901	55578	0.054	6.2%
C2	A,C,D,F,G,H	2110	16%	171	86%	10209	76433	0.074	8.5%
D1	A,C,D,F,G,H	2110	16%	182	91%	9750	68588	0.067	7.7%
D2	All	13576	100%	182	91%	175430	191817	0.186	21%
Mean:							108100	0.105	12%
Standard Deviation:							54212	0.053	6.0%

would be equivalent to 0.105 m of thinning over the whole debris-covered area, or 12% of the 2014 volume loss observed for the debris-covered area.

A major source of discrepancy between the model runs is the model treatment of pond J, which accounts for as much as one-quarter of the total pond area on Lirung Glacier. Model configurations that relied only on small ponds (B1, B2, B3, C1, C2, D1) all produced significantly lower cumulative SEB estimates (mean  $7.3 \times 10^4$  m<sup>3</sup>) than B4, B5, and D2 (mean  $1.79 \times 10^5$  m<sup>3</sup>), which modelled pond J explicitly. As discussed in Section 6.4.3, this pond by itself may account for  $3 \times 10^4$  to  $7 \times 10^4$  m<sup>3</sup> of melt-equivalent energy, suggesting that scaled results for runs B1, B2, B3, C1, C2, and D1 may underestimate the total energy absorbed by ponds.

The scaled results are probably slightly higher than the actual energy driving subaqueous ice melt or delivered to the englacial system ( $\Sigma Ex$ ), which is  $5 \pm 5\%$  lower than the cumulative surface energy balance ( $\Sigma(Q_n A_p)$ ). Additionally, the drainage of pond J may have carried energy through the entire glacier rather than contributing to englacial melt. Thus, the mean extrapolated value of 12% may be high, and certainly the run D2 value of 21% should be regarded as an upper-bound estimate for the contribution of ponds to debris-covered glacier volume losses. Most model runs estimate pond contributions of 8-9% of total glacier volume loss. Although the partition of this influence varies by pond, about 70% of this ice melt is modelled to occur in direct contact with the pond, while about 30% is delivered by pond discharge to englacial conduits.

## 6.5 Efficiency of ponds and cliffs as vectors of atmospheric energy

It is apparent that although ponds occupy a relatively small portion of the debris-covered glacier surface, they are focal points for atmosphere-ice energy transfer. If they were to occupy just 1.32% of Lirung Glacier's surface (as observed in April 2014, Table 4.3) for the entirety of the ablation period, they would account for over 20% of the glacier's volume losses during this period (run D2 uses the fixed April pond area, Table 6.12). Pond cover varies seasonally, but a mean areal coverage of at least 1% seems to be common for Langtang Valley glaciers during the monsoon (Figure 3.8). Although it is not clear whether these values are transferable to other catchments, with glaciers in more or less advanced states of decay, the implication is that ponds can account for a considerable portion of ablation for the debris-covered area in spite of very low coverage.

The efficiency of ponds as vectors of atmospheric energy can be compared to ice cliffs and the general debris-covered surface indirectly. Immerzeel et al. (2014a) used high-resolution geodetic differencing to develop representative degree-day factors for Lirung Glacier's ice cliffs and debris-covered surface in 2013, with the ice cliffs ablating  $6\text{--}10\text{ mm K}^{-1}\text{ d}^{-1}$ , much higher than the background rate of  $0.7\text{ mm K}^{-1}\text{ d}^{-1}$ . Overall, the study found a mean downwasting of 1.09 m over 156 days, for a mean degree-day factor of  $0.74\text{ mm K}^{-1}\text{ d}^{-1}$ . This study suggests that ponds absorb enough energy to account for  $0.06\text{--}0.09\text{ m d}^{-1}$  of ice melt; the equivalent of 9.4–14.0 m of thinning (for the pond area) over a 156-day period. For the 2014 season, Ragettli et al. (2016) calculated 0.87 m of ablation for Lirung Glacier, so ponds absorb energy at a rate 10–15 times higher than the rest of the glacier combined, perhaps slightly higher than for exposed ice cliffs on an area basis. This is slightly higher than the results of Sakai et al. (2000) for Lirung Glacier in 1996, which calculated that ponds absorbed energy 7 times faster than a debris-covered surface, but part of the difference may be the effects of a slightly warmer contemporary climate and possibly a thicker superficial debris layer.

## 6.6 Summary

The instrumental records of pond thermal regime and near-surface meteorological conditions enabled the establishment of empirical relationships for pond surface temperature and near-surface wind speed based on weather stations located on-glacier or off-glacier. Analyses of albedo observations at two ponds suggest that sophisticated albedo models do not accurately represent shortwave radiation reflection at the ponds observed, but that fixed albedo values are

more reasonable representations, although the ponds show distinct albedo values ( $\alpha = 0.08, 0.12$ ) likely related to suspended sediment concentrations.

The model complexity structure enabled this chapter to model the surface energy receipts of all Lirung Glacier ponds for 2014. Analysis of ponds C, D, I, and J with the full energy-balance approach (Runs A1-A5) revealed the mean pond-associated ablation rates of  $\frac{\sum Ex}{A_p \Delta t} = 6.3 \pm 1.8 \text{ cm d}^{-1}$  for the ponded area, while a strong seasonal cycle was evident in the surface energy balance due to changes in the latent heat flux and the longwave radiation balance. The level A model runs, truncated to the common period, also permitted assessment of model sensitivity to DEM resolution (very low) and source (very low), meteorological data source (high), and albedo (low).

By comparing the full energy-balance model (level A) to the surface energy balance (level B), I determine that energy exchange at the pond surface is an accurate proxy for pond-associated melt energy, but that the partition of absorbed energy between pond-proximal and englacial melt is highly variable. On average 70% of pond-absorbed energy leads to local melt, with the remainder drained englacially. Analyses suggest that the greatest model errors are due to inadequate representations of pond areal change that occurs with both drainage and filling, while other differences between specific model configurations were largely due to differences in source meteorology. Finally, the model results were compared and extrapolated to whole-glacier estimates of pond energy absorption, and suggest that ponds absorbed sufficient energy to account for  $1.08 \times 10^5 \text{ m}^3$  of icemelt over the study period. This equates to ~10% of Lirung Glacier's ablation in 2014 in spite of the ponds covering ~1% of the glacier's debris-covered area. Clearly, ponds induce glacier melt at a much higher rate than the general debris-covered surface of Lirung Glacier, and can play a considerable role in the overall glacier mass balance.



# Chapter 7

## Idealised SEB modelling of ponds, all Langtang Valley glaciers

### 7.1 Executive Summary

This chapter applies a pond surface energy-balance model with meteorological data from Kyanjing AWS and mean monthly hypsometric pond densities in order to model the energy receipts of all supraglacial ponds across all the debris-covered glaciers of the Langtang Valley. The model is used to assess the altitudinal and seasonal variations of the pond surface energy balance, and to estimate the pond contribution to energy balance at the glacier and basin scale. Supraglacial ponds are found to absorb large quantities of atmospheric energy, sufficient to account for 5 – 16% of the glaciers' debris-covered area thinning. This energy accounts for ~0.1 m of glacier thinning on average for the basin's debris-covered area (~12% of the corresponding volume loss measured by Ragettli et al., 2016). Pond energy absorption has strong spatial and seasonal variability based on the glacier-specific spatio-temporal distribution of ponds. The pond energy absorption is also controlled by the seasonal variability in meteorological conditions, with very little energy absorption in the pre-monsoon and post-monsoon, primarily due to decreased latent heat exchange for those periods relative to the monsoon. Altitude is an additional control on pond surface energy balance, but mean pond surface energy balance remains strongly positive even at the basin's ELA (5400 m).

## 7.2 Specific Objectives

The objective of this chapter is to determine the pond energy receipts for all Langtang Valley glaciers for a typical hydrological year. This will integrate the results of Chapters 3 and 6 by using the monthly mean pond distributions observed with Landsat imagery (Chapter 3) as forcing conditions for one of the simplified pond surface energy-balance models applied to the supraglacial ponds of Lirung Glacier (Chapter 6). Although the formulation of the model is simplistic due to data availability, this chapter will nonetheless provide a baseline estimate for the ablation associated to supraglacial ponds for all of the glaciers of Langtang Valley, the first estimate of this type.

## 7.3 Model setup

For this application of the pond energy-balance model, data are not available to constrain pond water-level fluctuations or volumes. Thus, the model cannot account for discharge, inflows of water, or changes in ponded volume. Instead, the analysis focuses only on the energy balance at the pond's water surface to calculate the cumulative energy absorbed based on the ponded area. Therefore the surface energy-balance model (as used in the level C runs in Chapter 6) is evaluated for 50 m elevation bands for the debris-covered area of each of the five glaciers in Langtang Valley, to determine the cumulative surface energy balance for the April-November period of 2013 and 2014, when the pond surfaces are most commonly thawed.

### 7.3.1 Spatial and seasonal pattern of ponds

The glaciers were broken into 50 m elevation bins according to the SRTM DEM (Figure 7.1), and the glaciers' area in each bin was determined. Then, based on the observation of ponds in Landsat data for the 1999-2013 period (Chapter 3), monthly maps of pond frequency were assembled as the ratio of pond observation for each pixel to the total number of observations at that pixel (excluding cloud and shadow-obscured scenes at each pixel), expressed as a percentage. As the ponds are clustered in particular regions of the debris-covered glaciers, the aggregation highlights the variability of pond density across and between glaciers (Figure 7.2).

For each glacier elevation band, the monthly mean pond frequency was computed and multiplied by the debris-covered glacier hypsometry to determine the average monthly ponded area for each glacier and elevation band. Figure 7.3 shows the results for Langtang Glacier.

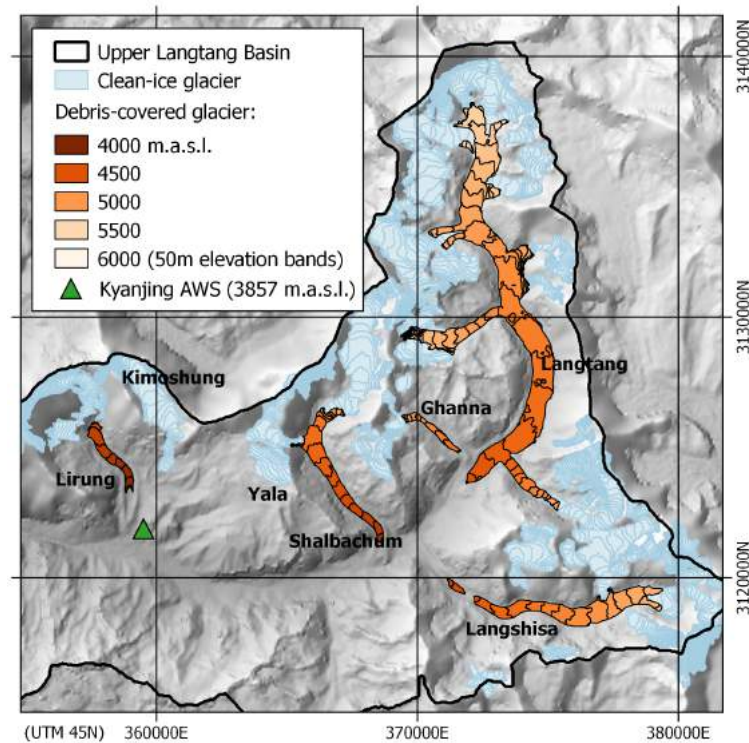


Fig. 7.1 Principal glaciers and debris-covered glacier area of the Langtang Valley, divided into 50 m elevation bands (CGIAR-CSI SRTM4.1 90 m elevation data).

This mean monthly pond area-altitude relationship was assumed to represent conditions at the month midpoint (on or around the 15th of each month) and linearly interpolated to hourly values for the 15 April-15 November study period, producing a time series of pond surface area distributed along each glacier's elevation range.

### 7.3.2 Meteorology

Nearly-continuous meteorological observations were made at the Kyanjing AWS for 2013 and 2014. For this section, the period of analysis is 16 April to 9 October 2014 (176 days), which is immediately preceded and followed by a several-day span of AWS errors. The Kyanjing AWS collected hourly observations of  $Q_r$ , RH,  $T_a$ ,  $w_s$ ,  $P_0$ ,  $I_{in}$ , and  $L_{in}$ .

Observations of  $Q_r$  and RH are directly applied to the elevation band without modification, as R plays only a minor role in the pond surface energy balance by advecting energy and RH's relationship with altitude is poorly documented at present.

To adjust the observations of  $T_a$  for altitude, the two-stage lapse rate described in Chapter 6 is used (Equation 6.1). This involves a shift to the glacier's terminus elevation using the seasonal environmental lapse rates determined by Heynen et al. (2016), followed by a shift

Table 7.1 Characteristics of the five debris-covered glaciers in the study area. Minimum and mean elevation are for the debris-covered area, which is divided into  $N$  50 m elevation bins. Distance is the horizontal distance from the glacier terminus to the Kyanjing AWS, which is located at 3857 m.a.s.l. Mean pond cover is the % of debris-covered area for April-October determined from Chapter 3. Ponds cover 1.04% of the debris-covered glacier area on average for this period.

	Area (km <sup>2</sup> )		Elevation (m.a.s.l.)			Distance (km)	Mean pond cover (%)
	Glacier	Debris	Min	Mean	$N$ bins		
Shalbachum	11.7	2.8	4218	4607	19	9.3	0.49
Ghanna	1.3	0.6	4718	4879	10	12.6	0.03
Lirung	6.1	1.2	4025	4287	15	1.7	0.55
Langtang	52.8	17.8	4468	4944	27	12.7	1.27
Langshisa	21.7	4.4	4526	4884	18	11.9	0.73

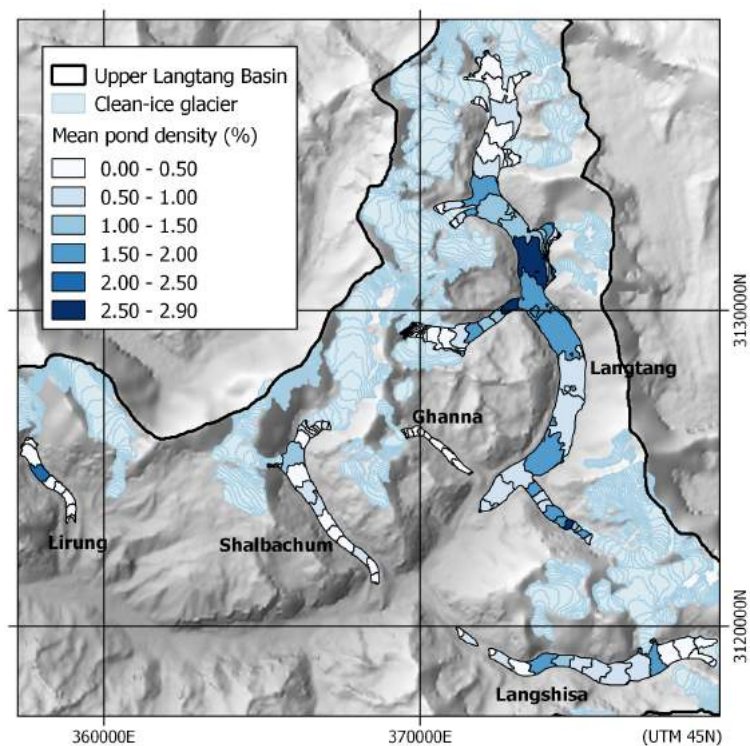


Fig. 7.2 Density of supraglacial ponds on each glacier aggregated to 50 m elevation bins.

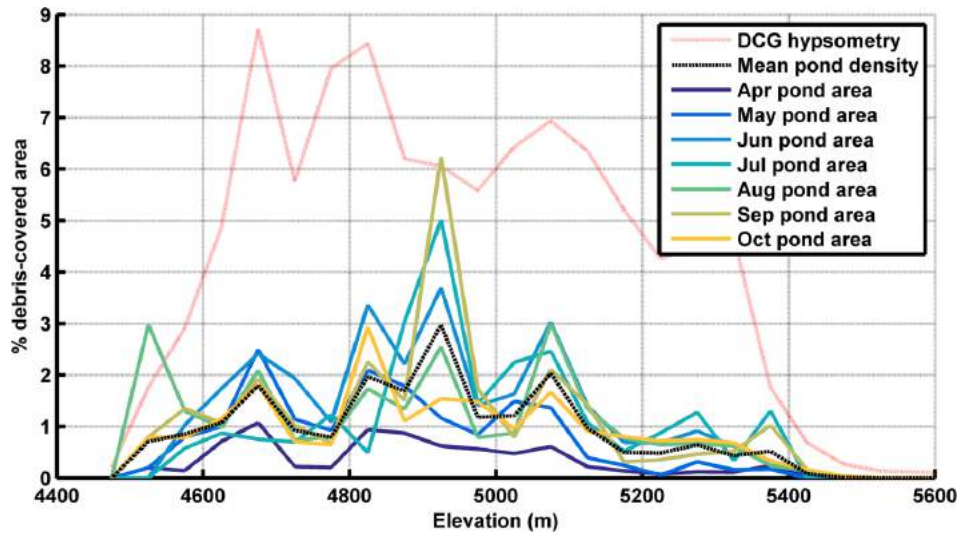


Fig. 7.3 Debris-covered glacier hypsometry (% total DCG area) and altitudinal distribution of supraglacial pond density (% DCG area ponded in 50 m elevation band) for Langtang Glacier.

to the elevation band's central elevation using the seasonal lapse rates observed by Steiner and Pellicciotti (2016) for Lirung Glacier (Table 6.1).  $w_s$  is adjusted from the Kyanjing AWS according to the hourly empirical relationship determined in Chapter 6 to reflect the movement of air within surface depressions on the debris-covered glaciers.  $P_0$  is adjusted from the Kyanjing AWS with the ideal gas law and  $T_a$ .

In order to transfer observed radiation fluxes from Kyanjing AWS to the many pond locations across the five glaciers, pond geometric conditions need to be represented. As in Chapters 4 and 6, incoming shortwave and longwave radiation is determined based on individually-modelled direct ( $I_s$ ), diffuse ( $D_s$ ), and debris-reflected ( $D_t$ ) radiation components (see Chapter 4). The population of view-factors determined for all ponds on Lirung Glacier was assessed, and shows reasonably strong clustering around a central value (Table 7.2), with a low standard deviation for each metric. These calculations are biased to the dataset of heavily-shaded, small ponds of Lirung Glacier, while larger ponds on the other study glaciers may be subject to distinct viewing conditions. The mean values were directly applied to all study ponds (see Steiner et al., 2015, for a description of the implementation of the view-factors). For all runs,  $\alpha = 0.10$  was used for pond albedo.

$T_{deb}$  is used directly from the observations at the AWS location on Lirung Glacier (~4063 m.a.s.l.). Although the debris surface may be cooler at higher-elevation locations, data is not available to prescribe a reasonable decay with altitude. Additionally,  $T_{deb}$  is only used to derive terrain-emitted longwave radiation, which is a small component of the surface energy balance.

Table 7.2 Mean  $\mu$  and standard deviation  $\sigma$  of pond view-factors determined from Chapter 6 level E model runs.

View Factor	$\mu$	$\sigma$
$V_{sI}$	0.6815	0.0460
$V_{sL}$	0.8848	0.0512
$V_d$	0.11522	0.0512

## 7.4 Results and Discussion

I first report on the pond energy-balance model's behaviour with respect to the domain of the study, then consider the quantities of energy absorbed by the ponds over the evaluation period.

### Altitudinal changes in pond energy balance

Although many of the meteorological conditions driving the pond energy-balance model are fixed, the air temperature lapse rates lead to a substantial decrease of  $Q$  with altitude. To assess the response of energy fluxes with altitude, I apply the model to a hypothetical unit area of pond within each 50 m elevation band of each glacier, then average across the full evaluation period. These mean values are displayed in Figure 7.4 and highlight the decrease of  $T_a$  with altitude. The mean  $T_a$  value of  $7.0^\circ\text{C}$  at 4000 m decreases to  $-2.4^\circ\text{C}$  at 5550 m, although diurnal fluctuations are still very strong, with midday temperatures commonly  $\sim 4^\circ\text{C}$ . Since  $T_{ws}$  is a parametrisation of  $T_a$ , this variable also decreases slightly from  $1.0^\circ\text{C}$  to  $0.9^\circ\text{C}$ . Diurnal fluctuations in  $T_{ws}$  remain moderate, but the model does not attempt to reproduce the freezing and thawing of the pond surface, which could account for some of the daily absorbed energy. Wind speed and  $T_{deb}$  are applied uniformly across the range of altitudes, as no data was available to constrain their behaviour with increasing elevation.

Based on these variations in meteorological forcing, the major change in the SEB with altitude is related to the turbulent fluxes  $E$  and  $H$ . The mean sensible heat flux  $H$  shows a moderate change with increasing altitude, varying from  $9.7 \text{ W m}^{-2}$  at 4000 m to  $-1.8 \text{ W m}^{-2}$  at 5550 m. The latent heat flux is much larger at 4000 m, with a mean value of  $67.1 \text{ W m}^{-2}$ , but also shows a very strong sensitivity to the decrease in temperature with altitude, decreasing to  $-73.9 \text{ W m}^{-2}$  at 5550 m. Consequently, the mean surface energy balance for the ponds ( $Q$ ) also declines with altitude from  $285.2 \text{ W m}^{-2}$  at 4000 m to  $135.7 \text{ W m}^{-2}$  at 5550 m.

A few interesting transition points are apparent from these results based on the whole study period. First, considering the whole-period average value, the latent flux transitions from an atmospheric source to a sink of energy at about 4650 m. Second, the surface energy

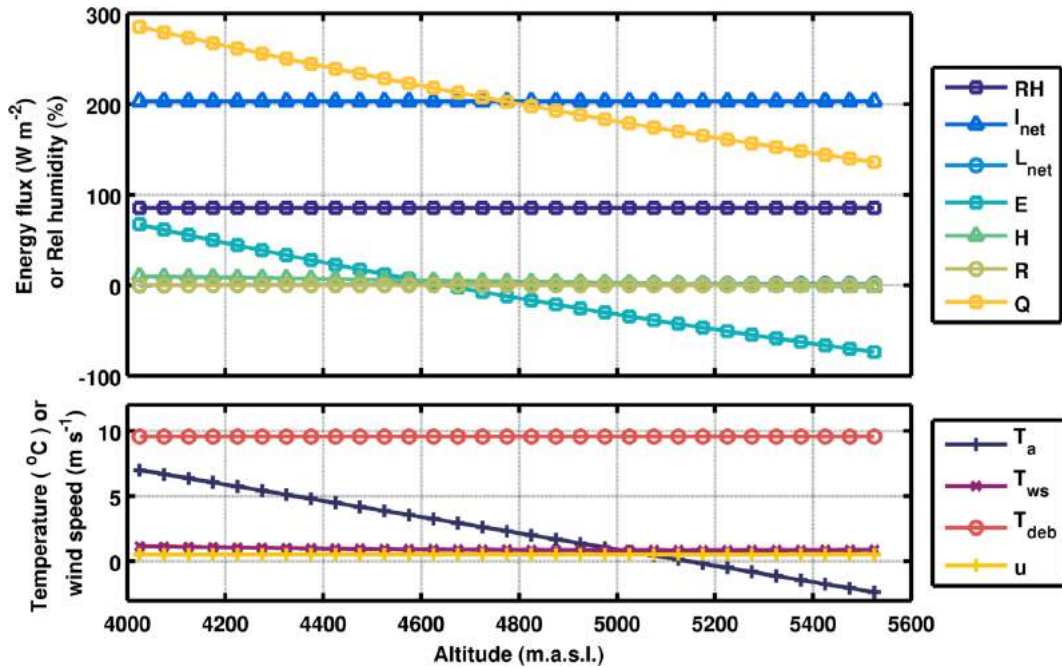


Fig. 7.4 Behaviour of mean meteorological forcing and mean surface energy-balance components for the altitudinal range of the study. Most variables change only slightly over the 1500 m range of elevations, but a strong decrease in  $T_a$  leads to a decline in turbulent fluxes  $E$  and  $H$ , and consequently the net surface energy balance  $Q$ . The mean seasonal values for  $L_{net}$  are all close to zero at all elevations.

balance  $Q$  is equal to the shortwave flux  $I_{net}$  at about 4750 m, assuming the average pond configuration of view-factors. Finally, both of these transitions are below 5000 m, where mean  $T_{ws}$  is equal to mean  $T_a$  and the parametrisation for  $T_{ws}$  is probably no longer accurate. However, a lower value of  $T_{ws}$  at these altitudes would maintain a stronger water vapour deficit and boost  $E$  slightly, leading to an increase in  $Q$  as long as the pond surface remained thawed for some part of the day. Even at 5000 m, the mean surface energy balance is strongly positive, so it may be possible for high-altitude ponds to fully thaw on a daily basis even when mean  $T_a$  is below freezing (5150 m), in which case the ponds can still act as recipients of atmospheric energy. It is important to note that the surface energy balance has a very strong seasonal pattern, so these transition points based on mean seasonal values are representative, but not necessarily valid for any specific point in the year.

### Seasonal pond energy balance

Specifically considering the seasonal variations in surface energy, I find that the seasonal differences in energy fluxes are as important as the altitudinal effects (Figure 7.5). Diurnal

fluctuations are common for all surface energy fluxes in both seasons and at both 4000 m and 5550 m. However, each flux shows a different response to seasonal and altitudinal changes:

- $I_{net}$  is identical at 4000 m and 5550 m within the model, which does not account for reduced atmospheric attenuation. Seasonally, the pre-monsoon has occasional cloud cover, so strong diurnal fluctuations have regular peaks of  $900 \text{ W m}^{-2}$ , while the frequent cloud cover of the monsoon greatly modifies the diurnal shortwave radiation receipts.
- $L_{net}$  is almost always negative in the pre-monsoon and almost always positive in the monsoon. However, the diurnal fluctuations differ for the two seasons, with higher amplitude in the pre-monsoon, which often has warm days and cold, clear nights. The slightly higher values for 5550 m than 4000 m are due to a lower modelled  $T_{ws}$  but identical  $T_{deb}$  for higher elevations.  $L_{net}$  never has a magnitude greater than  $100 \text{ W m}^{-2}$ .
- $H$  shows very little seasonal difference, and is much higher at 4000 m (peaks  $40 \text{ W m}^{-2}$ ) than at 5550 m (peaks  $10 \text{ W m}^{-2}$ ). Monsoon values are slightly higher than pre-monsoon values for both elevations.
- $E$  has the strongest seasonal variability of any surface flux. The latent exchange is strongly negative in the pre-monsoon at both elevations, with prominent daily minima up to  $-450 \text{ W m}^{-2}$ . In the monsoon, however,  $E$  is strongly positive with peaks at midday for 4000 m up to  $400 \text{ W m}^{-2}$ , and near-zero with very little diurnal fluctuation at 5550 m (maximum  $20 \text{ W m}^{-2}$ ).
- The rain-advected energy  $R$  is very small ( $< 5 \text{ W m}^{-2}$ ) for both seasons and sites, but slightly higher at 4000 m due to warmer  $T_a$ .
- The net surface energy balance  $Q_n$  is positive in the day and negative at night for both sites in the pre-monsoon. In the monsoon, the same pattern occurs but now night-time values are zero for 5550 m and positive for 4000 m. Peak pre-monsoon and monsoon values are higher for 4000 m ( $950 \text{ W m}^{-2}$  and  $1300 \text{ W m}^{-2}$ , respectively) than for 5550 m ( $650 \text{ W m}^{-2}$  and  $900 \text{ W m}^{-2}$ ).

#### 7.4.1 Pond energy absorption by glacier

The total supraglacial pond energy absorption varies based on each glacier's debris-covered area altitude distribution and pond density (Table 7.3). Due to the disparity of glacier sizes

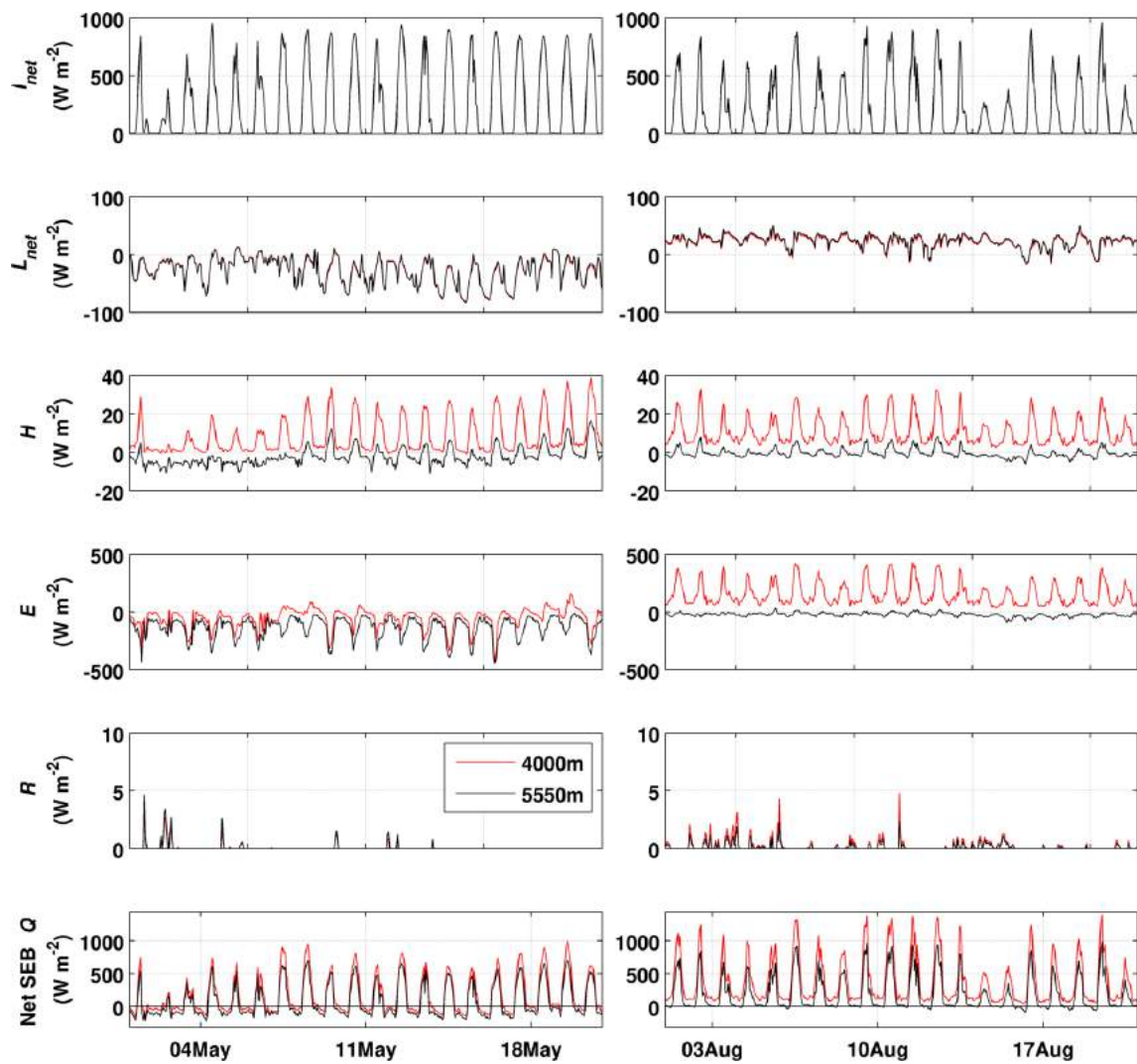


Fig. 7.5 Surface energy-balance components at 4000 m (red) and 5550 m (black) for excerpts from May (left) and August (right), highlighting the difference between the pre-monsoon and monsoon.

Table 7.3 Cumulative surface energy balance for supraglacial ponds of the debris-covered glaciers in the Langtang Valley, 2014. Pond density is the April-October mean pond coverage as a percent of the debris-covered area. Mean ablation rates are from Ragettli et al. (2016) for 2006-2015. The ponds' cumulative surface energy balance is expressed as volume-equivalent of ice melt and a mean thinning rate for the debris-covered area of the glacier. Pond ablation is the portion of mean thinning accounted for by the pond surface energy balance. For all calculations  $\rho_i = 900 \text{ kg m}^{-3}$ .

Glacier	Pond Density [%]	Mean ablation (2006-2015)		Pond cumulative SEB		Pond ablation [%]
		[m a <sup>-1</sup> ]	[m w.eq. a <sup>-1</sup> ]	[m]	[m <sup>3</sup> ]	
Shalbachum	0.73%	1.20	1.08	0.075	$3.28 \times 10^5$	6.23%
Ghanna	0.03%	0.49	0.44	0.0024	$1.41 \times 10^3$	0.49%
Lirung	0.55%	1.49	1.34	0.068	$8.46 \times 10^4$	4.55%
Langtang	1.27%	0.83	0.75	0.136	$2.41 \times 10^6$	16.30%
Langshisa	0.49%	0.99	0.89	0.052	$1.47 \times 10^5$	5.30%
All	1.04%	0.96	0.86	0.111	$2.97 \times 10^6$	11.62%

(Table 7.1), the cumulative pond surface energy-balance values differ by several orders of magnitude (enough to melt between  $1.41 \times 10^3$  and  $2.41 \times 10^6 \text{ m}^3$  of ice). Converting these values to a mean surface lowering distributed across the entire debris-covered area, pond-absorbed energy is sufficient to lead to  $2.4 \times 10^{-3} \text{ m}$  (Ghanna) to 0.13 m (Langtang) of surface lowering. The difference in values is strongly controlled by the difference in pond area observed by Landsat (Chapter 3), where Ghanna Glacier had nearly no supraglacial pond area, while Langtang Glacier's surface has an overall pond density of 1.27% for the model period. The glaciers of intermediate size and pond density also have an intermediate mean thinning attributable to supraglacial pond-absorbed energy.

Ragettli et al. (2016) calculated mean surface lowering and ablation for 2006-2015 based on geodetic differencing from satellite stereo-imagery. Using the mean lowering values for the debris-covered areas from that study, which range from  $0.49 \text{ m a}^{-1}$  (Ghanna) to  $1.49 \text{ m a}^{-1}$  (Lirung), I calculate the portion of the debris-covered area's volumetric loss that can be accounted for by the energy absorbed by supraglacial ponds for each glacier and for the basin as a whole. This calculation assumes that pond coverage in 2014 was similar to a typical year in 1999-2013 (period of Landsat pond observations), and that ablation in 2014 was similar to the mean in the period 2006-2015 (Ragettli et al., 2016). Consequently, these values are representative of the portion of thinning that could be attributable to pond-associated ablation on average, rather than corresponding to a specific year. However, following these assumptions, atmospheric energy absorbed by ponds could be responsible for up to 16.3% of the debris-covered area's total ablation (Langtang Glacier), or as little as 0.49% (Ghanna

Glacier). Ponds account for about 5% of the total ablation for the three other debris-covered glaciers, but since Langtang is by far the largest glacier, the whole-valley average ablation attributable to ponds is 11.62%.

The value for Lirung Glacier determined by this method (4.55% of total glacier volume loss) is lower than was determined for 2014 in Chapter 6 (10%). Part of the difference is due to a different value of surface lowering in 2014 (0.87 m for 2014 in Chapter 6,  $1.49 \text{ m a}^{-1}$  for the 2006-2015 average, both values according to Ragettli et al., 2016). Using  $0.87 \text{ m a}^{-1}$ , the pond cumulative SEB calculated here would account for 7.8% of Lirung Glacier's downwasting, closer to the ~10% estimated in Chapter 6 (Table 6.12).

The difference is also partly due to the discrepancy between pond area observed from Spot6 in April 2014 (1.32% of glacier area) and the Landsat 1999-2013 average for April-October (0.55%). It is unclear which dataset is more appropriate to represent monsoon conditions. Landsat pond observations include errors of commission and omission due to the  $900 \text{ m}^2$  pixels (Chapter 3), but provide a monthly mean pond distribution. The high-resolution Spot6 orthoimage provides a complete picture of ponding for a single point in time, and does not necessarily correspond to pond areal changes through the monsoon (Chapter 4). In spite of large error margins and variability between glaciers, supraglacial ponds appear to be responsible for a considerable portion of the glaciers' ablation.

### 7.4.2 Spatial patterns and energy partition

Variations in pond density are a primary control on the spatial distribution of cumulative energy absorbed by ponds (Figure 7.6), with individual 50 m bands showing highly-variable results. The surface energy balance of ponds also varies spatially across the glaciers based on pond altitude as discussed above. Consequently, bands with high pond densities and relatively lower altitudes are the strongest recipients of energy via ponds.

These bands of high pond energy absorption are not distributed systematically across the glaciers. For Langtang Glacier, several bands absorb melt-equivalent energy greater than 0.15 m and up to 0.3 m, and these are distributed across all elevations. Langshisa Glacier has two prominent bands, one near the head and one near the toe of the debris-covered zone. Both bands exhibited relatively elevated pond densities (Figure 7.2). Lirung Glacier has a single prominent band corresponding to the location of pond J (Chapters 4 and 6), and shows moderate values of pond energy absorption for the upper reaches of the debris-covered area. Shalbachum Glacier has relatively consistent pond energy absorption across all bands, with a slightly higher value (0.1 m) near the head of the debris-covered area. Finally, Ghanna Glacier has very low pond energy absorption values, as it has very low pond density.

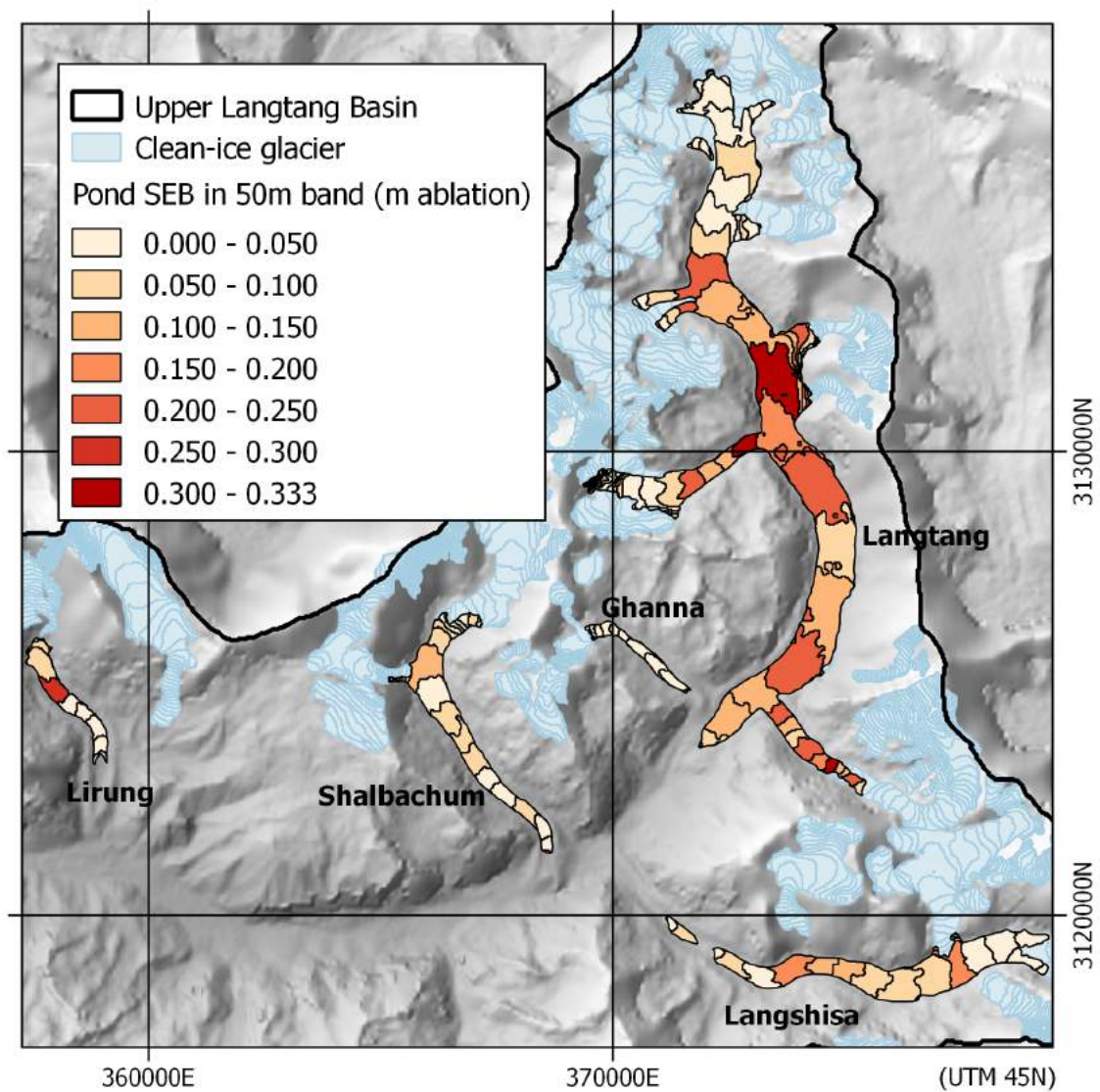


Fig. 7.6 The cumulative surface energy balance of supraglacial ponds in each elevation band, expressed as equivalent metres of surface thinning in that zone (with  $\rho_i = 900 \text{ kg m}^{-3}$ ). Energy absorbed by ponds may occur locally or down-glacier.

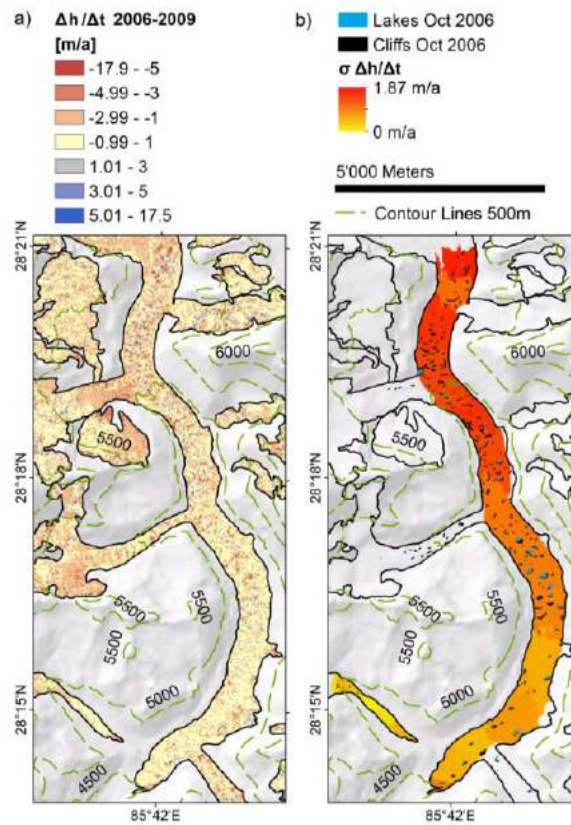


Fig. 7.7 Observed thinning of Langtang Glacier, reproduced from Ragetti et al. (2016): (a)  $\Delta h/\Delta t$  map of Langtang Glacier tongue, Oct 2006 – Nov 2009 (outlier corrected and missing data filled with inverse distance weighting), (b) standard deviation of  $\Delta h/\Delta t$  values calculated per 50 m elevation band. The cliffs and lakes indicated in (b) were delineated manually on the basis of the Oct 2006 orthorectified satellite image.

Overall, bands with high mean pond density values and low altitude show high values of pond cumulative surface energy balance, with supraglacial ponds absorbing sufficient energy to equate to  $\sim 0.3$  m of surface lowering for that band in a single year. Although the partition of proximal and englacial melt appears to differ for each pond, the ponds studied in detail suggest a roughly equal division (Chapter 6). Thus, although moderate pond energy-absorption values can occur up-glacier, these locations may contribute to melt along englacial conduits distributed down-glacier.

This implies surface subsidence at lower altitudes in spite of thick debris cover inhibiting glacier surface ablation. Pond-proximal melt occurs laterally in depressions at the ice-water interface, and conduit collapse events down-glacier lead to the exposure of occasional bare-ice cliffs as a window of enhanced atmosphere-ice energy transfer. The result is a highly-variable and punctuated expression of surface lowering across the debris-covered area of the glacier (Figure 7.7).

### 7.4.3 Seasonal accumulation of energy

The seasonal variability in pond cover (Chapter 3) combines with the seasonal and altitudinal variations in pond surface energy balance to create a non-uniform temporal pattern of atmosphere-pond cumulative energy transmission (Figure 7.8).

Daily mean rates of atmosphere-pond energy transfer  $Q$  are very similar for each glacier (Figure 7.8a). This is in spite of glacier hypsometric differences (Table 7.1). The mean  $Q$  shows a strong increase through May from near-zero in April to sustained high values of about  $300 \text{ W m}^{-2}$  for June, July, and August. This suggests that individual ponds present in any of these months would absorb energy at about the same rate.

The seasonal pond density patterns differ slightly between glaciers, but all show peak values in June-July as a portion of debris-covered area (Figure 7.8b). This may be prior to the development of efficient englacial and subglacial networks, such that seasonal snowmelt delivered to the glacier is inhibited and backs up to the glacier surface. Several glaciers show a slight second peak in September, which could be an expression of conduit closure nearing the end of the ablation season.

Consequently, relative pond-associated energy absorption rates are low for April-May, high for June, and about the average for July-September (Figure 7.8c). Ghanna Glacier is the major exception to this pattern, as supraglacial ponds were only observed in April, May, and September, and at very low densities. Lirung Glacier shows a pronounced dip in pond energy absorption in July due to its low pond density value for this month.

As a result, 40-50% of each glacier's cumulative energy absorption (Figure 7.8d) occurs by the end of July, even though only 10-20% occurs before 1 June. The high portion of

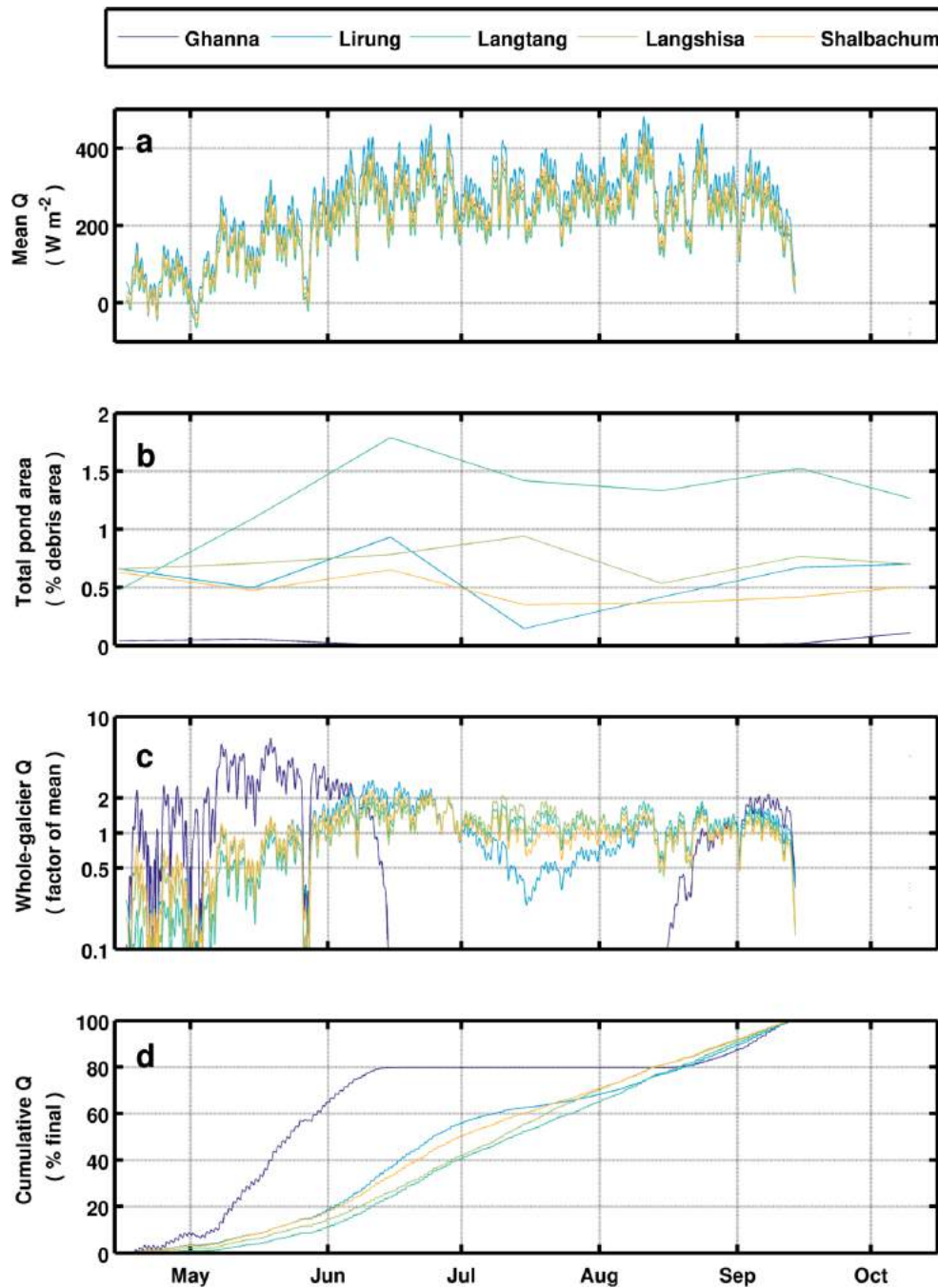


Fig. 7.8 (a) Daily mean rates of atmosphere-pond energy transfer  $Q$  are very similar for each glacier in spite of altitudinal differences, and show a strong increase through May to sustained high values for June, July, and August. (b) The pond density variations differ between glaciers, but all show peak values in June-July, expressed as % debris-covered area. (c) Energy absorption rates are low for April-May, high for June, and about the average for July-September. These values are as a factor of the whole-period mean, with a log scale. (d) 40-50% of each glacier's cumulative energy absorption occurs by the end of July, even though only 10-20% occurs before 1 June. Ghanna Glacier does not follow these patterns due to the extremely low pond density values.

energy absorbed in June (25-30% of the total) is due to the combined high pond density and monsoon meteorological conditions. Although the Kyanjing record terminates abruptly, the September surface energy balance  $Q$  is on a downward trend to mirror that of May leading into the colder post-monsoon, and ponds present during this period would absorb less energy, accounting for an additional 10-20% of the cumulative total to that point.

#### 7.4.4 Comparison with other studies

Results from this chapter indicate that supraglacial ponds absorb enough atmospheric energy to account for 12% of the ablation of the debris-covered glacier area in the Langtang Valley, the equivalent of ~0.1 m of ablation for this area. These values may seem remarkable and the uncertainties deserve some additional discussion. First, the validation of Landsat pond observations in Chapter 3 indicated a net 30% commission error for observed pond area based on two scenes. Second, it is not entirely clear from the Landsat observations, or the high-resolution orthomosaics, entirely how much of the ponded surface water drains in any year. Many ponds persist for multiple years before drainage, although field surveys at Lirung Glacier mostly identified ponds that filled and drained seasonally. Small ponds that do not drain, of course, lose all stored energy over winter (Chapter 4), so not all the energy absorbed at the pond surface necessarily leads to ablation. Finally, there are large uncertainties in meteorological conditions in the upper portions of the glaciers, where no measurements have been made.

Consequently, 10-12% should be regarded as an upper bound for the influence of ponds at the scale of the debris-covered glacier area. Three other estimates of pond-associated ablation are useful as a reference, although the values are not directly comparable. The most similar analysis is that of Sakai et al. (2000), which attributed 3.4% of Lirung Glacier's total ablation to ponds, although they covered only 0.43% of the debris-covered area. Focusing on the terminus area of the Tasman Glacier, (Röhl, 2008) attributed 4% of all ice loss (ice loss at the terminal lake) to supraglacial ponds, but that study could only estimate the effects of ponds at the glacier's surface (it did not estimate internal ablation). Thompson et al. (2016) calculated an upper bound of Ngozumpa Glacier's internal ablation of 9%, with the portion attributable to pond drainage only representing a small portion of this quantity.

However, these values are not irreconcilable: the results of Chapter 6 indicate that, for the studied ponds, ~70% of pond-associated ablation occurs in the pond proximity. This includes all subaqueous melting, and would also account for the melting of subaerially-calved blocks, and equates to a maximum of ~6-8% of total debris-covered area ablation. This value is about double the estimates of Sakai et al. (2000) and Röhl (2008), which is likely due to the higher pond coverage in this study. The other ~30% of the pond-associated ablation energy

leads to englacial ablation, a maximum of ~3-4% of total debris-covered area ablation, which is higher than the assessment of Thompson et al. (2016). As not all ponds will drain in a given year, the englacial component of ablation may vary year-to-year, but is unlikely to achieve the maximum value on any year.

## 7.5 Summary

Using a pond surface energy-balance model, 2014 meteorological data, and 1999-2013 mean monthly hypsometric pond densities, I modelled the energy absorbed by supraglacial ponds of the debris-covered glaciers of the Langtang Valley, providing the first estimate of pond-associated energy absorption at the basin scale.

Pond energy absorption has a very strong spatial and seasonal variability based on the glacier-specific spatio-temporal distribution of ponds. The pond energy absorption is also controlled by the seasonal variability in meteorological conditions, with little energy absorption occurring in the pre-monsoon and post-monsoon, primarily due to differences in the latent heat exchange for those periods. Altitude is an additional control on pond surface energy balance. However, the mean pond surface energy balance remains strongly positive even at the basin's ELA (5400 m), which is near the limit of the glaciers' debris cover.

Supraglacial ponds were found to absorb sufficient energy to account for ~0.1 m of debris-covered area thinning on average across the basin, while in certain elevation bands of high pond density, ponds absorb sufficient energy to account for 0.3 m of thinning. The whole-basin pond energy absorption equates to ~12% of the total debris-covered-area volume loss measured by Ragettli et al. (2016), with ponds accounting for 5 – 16% of individual glaciers' thinning in the debris-covered areas. A large portion of pond-associated energy absorption is modelled to occur in June due to higher pond areal coverage and the onset of monsoon meteorological conditions.



# Chapter 8

## Summary and conclusions

The aim of this thesis was to determine the ablation that may be attributed to supraglacial ponds for debris-covered glaciers, using the Langtang Valley of Nepal as a case study. Quantifying the ablation associated with ponds is important for closing the budget of glaciers' mass balance, but is also essential for understanding the evolution of debris-covered glaciers under continued climate warming. Few such estimates exist (Sakai et al., 2000; Röhl, 2008; Thompson et al., 2016), as they require careful assessment of pond-associated ablation processes, both via mass wastage in ponds' proximity and via englacial delivery of absorbed energy, and an understanding of the spatial coverage of ponds.

### 8.1 Outcomes of Research Objectives

In Chapter 1, five key research objectives were identified to assess the ablation that may be attributed to supraglacial ponds in the Langtang Valley. A summary of the methods and outcomes for each objective is summarised below.

#### 8.1.1 Determine the spatial, seasonal and interannual variability of ponds in the Langtang Valley (Chapter 3)

This study sought to understand the when and where of supraglacial ponding. Thawed supraglacial ponds were targeted as this is when ponds are important from an energy-balance perspective, and because frozen ponds are difficult to distinguish from snow and ice cliffs. To identify thawed supraglacial ponds for the debris-covered tongues of five glaciers in the Langtang Valley of Nepal, I analysed 172 Landsat TM and ETM+ scenes from 1999-2013 (Tables A.1 to A.4). I used an advanced atmospheric correction routine (LandCor/6S) and improved upon previous band-ratio and image morphological techniques to identify ponds,

then characterised the spatial, seasonal, and interannual patterns of ponding. Mean ablation-season pond densities were compared to a suite of glacier morphometric characteristics to assess the differences in ponding between glaciers, and surface gradient and velocity attributes were compiled for each pond location to evaluate the Quincey et al. (2007) framework of glaciological controls. Interannual variability of pond-cover was assessed for each glacier, controlling for pond seasonality, and patterns of coalescence, fragmentation, persistence, and recurrence were identified.

My analysis of the spatial variability of supraglacial ponds in the Langtang Valley quantitatively substantiates the current understanding of the distribution of these features within a glaciological context. This study uses many more observations than previous efforts but supports inferences drawn by Reynolds (2000); Quincey et al. (2007) and Salerno et al. (2012) that pond incidence is strongly controlled by local glacier velocity and surface gradient. Surface gradient controls water accumulation (i.e. pond formation) while velocity controls pond drainage, and therefore pond size and persistence. Ponds are thus most concentrated and largest in zones of low surface gradient ( $< 2^\circ$ ) and low velocity ( $< 7.5 \text{ m a}^{-1}$ ), where water is likely to accumulate and ponds are unlikely to drain. Ponds are nearly as common but smallest in zones of low gradient but higher velocity, as they are more likely to drain. Ponds are less common but larger in zones of moderate gradient and low velocity, as they may persist longer and have the opportunity to expand. Finally, ponds are least common and remain very small for zones of moderate gradient and velocity.

The density of supraglacial ponding varies strongly between glaciers in the relatively small Langtang basin, ranging from 0.06%-1.69% of debris-covered area (May-October mean values). The magnitude of ponding is most clearly related to glacier size and surface gradient, but shows no relationship with cumulative glacier thinning. A similar inter-glacier comparison of pond cover is recommended for an expanded set of glaciers to evaluate the consistency of these relationships between basic glacier characteristics and surface ponding in this and other regions. The distribution of the terrain categories described by Quincey et al. (2007) may also prove a worthwhile avenue of investigation.

The study makes the first systematic observations of the seasonality of supraglacial ponds on debris-covered glaciers, finding that thawed ponds cover 1-2% of the basin's debris-covered area for May-October. Pond cover rises rapidly in the pre-monsoon as ponds thaw and seasonal snow melts, peaking at about 2% of the basin's debris-covered area at the onset of the monsoon. Pond cover then gradually declines through the monsoon as ponds drain by establishing connectivity with the englacial hydrologic system, and ponds continue to drain and many freeze over during the post-monsoon

The seasonality of pond-cover highlights a potential bias in basic assessments of ponded area change, such as those relying on only a few observations over multiple years or decades. After controlling for seasonal biases, I find an increase in pond-cover for Langtang Glacier spanning the full April-October period when ponds are important for glacier ablation. However, pond cover shows strong interannual variability, with two glaciers exhibiting peak pond density in 2009 followed by a gradual decline and two showing no clear pattern over the whole study period. Use of fewer scenes for these analyses could lead to strongly-differing conclusions concerning pond growth, stability, or decline.

Finally, persistent and recurrent ponds are commonplace on the four larger glaciers, with 40.5% of all pond locations observed in multiple years. Notably, many locations appear to persist or recur for the entire analysis, suggesting that individual pond features may have a prolonged effect on the debris-covered surface and englacial conduits.

### **8.1.2 Document Lirung Glacier supraglacial pond physical characteristics, behaviour, and meteorological forcing (Chapter 4)**

This study sought to document the supraglacial ponds of Lirung Glacier and to collect data for use in an energy-balance model. Field observations of supraglacial perched ponds on Lirung Glacier were made for May and October of 2013 and 2014. Basic surveys of the ponds were conducted, water-level loggers were installed to monitor ponds' water level and temperature, and measurements were made of near-surface meteorology. Aerial, satellite, and terrestrial orthomosaic images were collected coinciding with the field seasons to provide snapshots of the areal coverage of ponds representing each season. The diverse datasets were analysed to assess each pond's behaviour and characteristics, as well as to document pond-related natural phenomena.

As with the Landsat data, analysis of the orthomosaic images indicates that pond density for the glacier is higher in the pre-monsoon (0.2%) than post-monsoon (0.13%), with individual ponds filling and draining seasonally. The majority of ponds are smaller than a single Landsat pixel; these small ponds account for 32% of total ponded area. However, the area surveyed by repeat observations has a lower pond density (0.5%) than the whole debris-covered tongue as surveyed in April 2014 (1.3%). Monsoon pond area observations were not possible although this may be the period of highest overall pond density (Chapter 3). However, water-level records at the four study ponds generally show surface lowering in the early monsoon, and it is possible that Lirung Glacier experiences an earlier seasonal transition due to its low elevation, which may result in earlier meltwater delivery to ponds as compared to the other glaciers of the Langtang Valley.

Records of pond-related temperature and wind speed show strong diurnal variability. Pond albedo is stable at each observation site, with  $\alpha = 0.08$  or  $0.12$ . Four ponds were monitored with water-level loggers in addition to the repeat orthoimages and DEMs, and show different patterns of pond filling, stability, gradual surface lowering, and drainage. Seasonal refilling of pond depressions was observed at two ponds, but an overall water-level decline over the study period suggests distinct outlets for each year's drainage. The freeze-over and thaw-out of a supraglacial pond was documented over winter 2013-2014, and suggests that ponds play little role in the glacier's energy balance during that period. I also note interesting pond-related processes including thermo-erosional notch development, subaerial ice structural collapses, and the close association of ponds and englacial conduits.

### **8.1.3 Develop an improved model of energy balance for a supraglacial pond (Chapter 5)**

The objective of this study was to develop and test an energy-balance model for supraglacial ponds which could be used to assess the ablation associated to an individual pond. The research advanced the efforts of Sakai et al. (2000) and Röhl (2008) to develop a control volume model of mass and energy balance for supraglacial ponds, and applied a free-convection approach to account for energy exchanges at the subaqueous bare-ice surfaces. The model was evaluated and tested using 2013 field data from a pond on Lirung Glacier, Nepal (Chapter 4), using many model configurations to understand the importance of unconstrained parameters and the likely range of melt values. The subaqueous melt algorithms used by Sakai et al. (2000), Luthje and Pedersen (2006), and Röhl (2008) were compared with the free-convection approach.

Notably, the pond-atmosphere surface inputs large amounts of energy, with exceptionally high latent fluxes. The net surface energy balance dominates the pond's energy fluxes by an order of magnitude for a variety of parameter choices. The excess energy can only be accounted for by the pond's discharge, and is likely to contribute to substantial amounts of englacial or subglacial melt, the equivalent of 5.3 m of local ablation for the ponded area. Therefore, ponds seem to be able to convey a large amount of energy into the glacier interior, demonstrated by this study for a relatively small pond.

The study tested several model configurations to calculate subaqueous melt. Subaqueous subdebris melt is unconstrained in the model but a sensitivity analysis indicates that it plays a minor role at this site in terms of energy loss and melt production ( $10.6 \text{ m}^3$  total) unless the debris is very thin, pond basal temperatures are higher than those observed, or convection occurs in the saturated debris layer. Subaqueous bare-ice melt was estimated to occur at an

average rate of  $2.91 \text{ cm d}^{-1}$  for a total volume of  $98.5 \text{ m}^3$ , in the correct range of values to match the adjacent cliff's backwasting. This result is in close agreement with algorithms used by Sakai et al. (2000) and Luthje and Pedersen (2006), and an adaptation of the algorithm used by Röhl (2008). Moreover, the result is also in good agreement with modelled and observed backwasting of the adjacent ice-cliff (Steiner et al., 2015), a precondition for the two systems to occur together (Sakai, 2012). The subaqueous melt algorithms are expected to be suitable for distinct applications based on the dominant kinetic regime driving pond-associated melting (Xin et al., 2011), but the natural convection algorithm is the most suitable for this pond's small size.

A key implication of the study was that the input of water to a small pond could not be accounted for by the melt in the pond's local depression, suggesting an input of water from distal sources. Larger ponds with more dynamic water levels most certainly source water from englacial systems, suggesting that a moderate-to-significant portion of the englacial hydrological flux is rerouted to the surface for debris-covered glaciers. Additionally, the pond is an active component of the entire glacier's hydrologic system, with up to 10% of the glacier's total discharge passing through it, and resulting in a high overturn rate.

#### 8.1.4 Model ablation due to ponds at Lirung Glacier (Chapter 6)

The objective of this chapter was to apply the newly-developed model of supraglacial pond energy balance (Chapter 5) to all the observed ponds documented on Lirung Glacier (Chapter 4). First, I used the observations of pond temperature and near-surface conditions to determine empirical relationships for pond surface temperature and near-surface wind speed, as many ponds do not have direct observations of surface conditions. Also, analyses of pond albedo observations indicated that fixed albedo values are reasonable representations for the pond surface, providing the forcing conditions needed for the model. The model introduced in Chapter 5 was reduced in complexity to adapt to the varying data availability for each of the 14 ponds observed on Lirung Glacier in 2014. This varied between the full energy-balance approach (Chapter 4), which could be applied to four ponds, and a surface energy-balance model applied to fixed pond areas, which could be applied at all pond locations. Finally, the results from different model complexity levels were compared and extrapolated to whole-glacier estimates of pond energy absorption.

Analysis of ponds C, D, I, and J with the full energy-balance approach (Runs A1-A5) revealed the mean pond-associated ablation rates of  $\frac{\sum E_x}{A_p \Delta t} = 6.3 \pm 1.8 \text{ cm d}^{-1}$  for the ponded area, while a strong seasonal cycle was evident in the surface energy balance due to changes in the latent heat flux and the longwave radiation balance. The models exhibited low sensitivity to pond albedo, very low sensitivity to DEM resolution, and higher sensitivity to

meteorological data. By comparing the full energy-balance model (level A) to the surface energy balance (level B), I determine that energy exchange at the pond surface is an accurate representation of pond-associated melt energy, but that the partition of absorbed energy between pond-proximal and englacial melt is highly variable. On average, 70% of pond-absorbed energy leads to local melt, with the remainder drained englacially.

Analyses with the lower-complexity models suggested that the greatest model errors are due to inadequate representations of pond areal change that occurs with both drainage and filling, while other differences between specific model configurations were largely due to differences in source meteorology. Comparing and extrapolating the individual results to whole-glacier estimates of pond energy absorption, the models suggest that ponds absorbed sufficient energy to account for  $1.08 \times 10^5 \text{ m}^3$  of icemelt over the study period. This equates to ~10% of Lirung Glacier's ablation in 2014 in spite of the ponds covering ~1% of the glacier's debris-covered area. Clearly, ponds induce glacier melt at a much higher rate than the general debris-covered surface of Lirung Glacier, and can play a considerable role in the overall glacier mass balance.

### **8.1.5 Assess the pond-associated ablation for the entire Langtang catchment (Chapter 7)**

This final chapter sought to assess the surface energy receipts for all supraglacial ponds in the Langtang catchment for a typical year, and, assuming that this energy led to ablation, calculate the portion of total ablation for which ponds could be responsible. To accomplish this, I applied a pond surface energy-balance model with 2014 meteorological data from Kyanjing AWS and mean monthly hypsometric pond densities, combining the pond distributions derived in Chapter 3 with the surface energy-balance model assessed in Chapter 6. With this model, I assessed the altitudinal and seasonal variations of energy absorbed by ponds, and estimated the pond contribution to energy balance for each glacier within the basin.

The absorption of energy by ponds varied spatially and seasonally based on the glacier-specific distribution of ponds. In addition, seasonal variability in meteorological conditions plays a role in controlling pond energy absorption. Little energy absorption was modelled for the pre-monsoon and post-monsoon primarily due to differences in the latent heat exchange for those periods relative to the monsoon. Finally, altitude affects pond surface energy balance by controlling air temperature. The mean pond surface energy balance was modelled to be positive even at the basin's ELA (5400 m), which is near the limit of the glaciers' debris-cover.

Considering the entire basin, supraglacial ponds were found to absorb sufficient energy to account for ~0.1 m of debris-covered-area thinning on average. In certain elevation bands of high pond density, ponds were modelled to absorb sufficient energy to account for 0.3 m of thinning. The whole-basin pond energy absorption equates to ~12% of the total debris-covered-area volume loss measured by Ragetti et al. (2016), with ponds accounting for 5 – 16% of individual glaciers' thinning in the debris-covered areas. A large portion of pond-associated energy absorption is modelled to occur in June due to higher pond areal coverage and the onset of monsoon meteorological conditions.

## 8.2 Synthesis

The overall goal for the study was to determine the portion of debris-covered glaciers' ablation that may be attributed to supraglacial ponds, using the Langtang valley as a case study. To arrive at a result, the thesis has developed systematic observations of Langtang Valley's supraglacial ponds from the Landsat archive, conducted field observations of select ponds and of meteorological conditions, developed and tested a numerical model of pond energy balance, and evaluated the model for numerous individual ponds on Lirung Glacier and with an idealised distribution of ponds across the whole valley. The primary outcome of this thesis is that supraglacial ponds absorb enough atmospheric energy to account for ~12% of the ablation of the debris-covered glacier area in the Langtang Valley, the equivalent of ~0.1 m of ablation for this area.

Importantly, ~70% of this energy (up to 7-8% of the total ablation for the debris-covered area) is accounted for at the glacier surface through subaqueous and waterline melting, as well as the melting of subaerially-calved icebergs. These processes have been documented through rigorous observation of individual features (e.g. Benn et al., 2001; Röhl, 2006) and over larger domains (e.g. Röhl, 2008; Thompson et al., 2016), and lead to high rates of topographic change in otherwise stagnant, low-ablation zones (Immerzeel et al., 2014b). The other ~30% of the absorbed energy (up to 3-4% of the total ablation for the debris-covered area) is delivered englacially and causes internal ablation. In turn, this leads to surface subsidence, conduit collapse, and the formation of new ice cliffs and pond depressions (Sakai et al., 2000; Benn et al., 2012).

Clearly these features are crucial for calculating the whole glacier's melt, a point which is best exemplified by a simple thought exercise. Assume the overall combined pond and ice-cliff coverage of 8% of the debris-covered area of Lirung Glacier (as reported by Immerzeel et al. (2014a)), and assume that ponds and cliffs both absorb energy ten times faster than the rest of the debris-covered surface (Sakai et al., 2000). This is a conservative estimate:

the real ice-cliff area is higher than observed by orthophoto, as the orthophoto could not observe the high portion of the glacier where ponds and cliffs are most dense, and the rate of transfer for ponds and cliffs may be more than ten times higher. Given these conditions, for a unit of downwasting across the background 92% area of the debris-covered surface, 10 units will occur for the 8% occupied by cliffs and ponds. The area-wide average would then be 1.72 units, with ponds and ice-cliffs accounting for 42% of the total melt, a value not dissimilar to that found by Thompson et al. (2016) for the ice cliffs of the terminus area of Ngozumpa Glacier (40%). As that study observed a high association of ponds and cliffs (75% of cliffs were adjacent to ponds in 2010), and the two features' evolution are closely intertwined (Röhl, 2008; Brun et al., 2016), it is often difficult to disentangle the volume losses of the two features.

Regardless, the numerical results of the thesis suggest that ponds are indeed responsible for a considerable portion of mass loss for debris-covered glaciers, bringing these surfaces closer to parity with clean-ice glaciers at equivalent altitudes (Gardelle et al., 2013; Käab et al., 2012; Ragettli et al., 2016). As envisioned by Kirkbride (1993), Sakai et al. (2000), and Benn et al. (2012), ponds are consequences of a debris-covered glacier's response to climate change, but provide a key feedback mechanism to reform the glacier's surface through englacial ablation, leading to continued pond development.

In the case of the debris-covered glaciers in the Langtang Valley, pronounced thinning in recent years (Immerzeel et al., 2014a; Pellicciotti et al., 2015; Ragettli et al., 2016) has led to a fragmented, discontinuous hydrological network exchanging water between surface and efficient englacial segments, and increasing the likelihood of pond-formation. The surface ponds then efficiently absorb atmospheric energy and translate it into ablation. This leads to pronounced topographic evolution at the glacier's surface, while energy conveyed to the interior of the glacier promotes englacial conduit enlargement and collapse, further basin formation and pond development, and renewed hydrological network fragmentation. The surface gradient and velocity of the five debris-covered glaciers do not suggest immediate development of a base-level lake. However, the perched supraglacial ponds throughout the Langtang Valley are playing a remarkable role in enabling enhanced ablation for the Valley's debris-covered glaciers (Pellicciotti et al., 2015), accounting for 5-16% of the observed ablation on the four major glaciers.

## **8.3 Future directions of research**

The analyses of this thesis have highlighted many avenues of potential future research. These directions of future study are focused on pond observations, although there are opportunities for improving calculation of pond-associated ablation.

### **8.3.1 Pond seasonality**

This thesis made the first glacier-wide and catchment-wide observations of seasonal variability of supraglacial ponds (Chapter 3), but pond identification and area assessment was limited by the relatively coarse resolution of Landsat sensors, which led to an overall error of +30% of pond area when validated against two high-resolution orthoimages, and by seasonal variability in cloud cover, which greatly reduced the number of viable scenes during the monsoon. Additionally, the study could only document the seasonal variability of thawed ponds, as combined spatial and spectral limitations prevented distinguishing between frozen ponds and bare glacier ice. Consequently, there is a need for additional studies to assess the seasonality of supraglacial ponding, both to understand the evolution of water storage (Watson et al., 2016) and simply to constrain the annual cycle of ponding. While multispectral platforms such as Landsat, ASTER, and Sentinel-2 can support this goal, and validation with high-resolution satellite orthoimagery is necessary, the ideal dataset would have a high repeat-visit frequency and high spatial resolution, but still be able to clearly distinguish between ponded water and debris. A possible solution might be found with the newer satellite SAR datasets, which can penetrate cloud cover, often have a frequent repeat-visit cycle, and have been already been applied to the Greenland Ice Sheet to monitor supraglacial lakes.

### **8.3.2 Pond persistence, drainage, and recurrence**

Related to the prior topic, this study was not able to constrain the length of ponds' life cycle before drainage (persistence). This is a major opportunity in the field, as the portion of ponds that drain in a given year has significant implications for englacial ablation and glacier hydrology. Reliable, high-frequency observations as outlined for seasonality would provide the opportunity to track individual supraglacial ponds through periods of flooding, basin expansion, and eventual drainage. Similar research has been conducted on the Greenland Ice Sheet (e.g. Liang et al., 2012) and can provide crucial information for hydrological modelling (e.g. Banwell et al., 2012).

### **8.3.3 Pond density for an increased sample of glaciers**

A direct extension of this work is to evaluate the overall density of ponding for a larger set of glaciers. Relatively few values of pond density are available, so although ponds can efficiently enhance ablation, it is difficult to tell how important supraglacial ponds are in the broader region of the HKKH. An extension of the analysis conducted in Chapter 3, but for a larger region, would provide a valuable understanding of the variability of ponding throughout the larger region. Such a dataset could be used in further supporting understanding of the spatial controls of pond cover, and would be useful in understanding how to represent ponds in models of debris-covered glaciers that evolve through time (e.g. Rowan et al., 2015).

### **8.3.4 Internal ablation and conduit collapse**

The delivery of atmospheric energy to englacial conduits is an important consequence of pond drainage, but few efforts have attempted to assess internal ablation, conduit evolution, and conduit collapse. Field investigations (Gulley et al., 2009a), geodetic differencing (Immerzeel et al., 2014a; Thompson et al., 2016), and numerical modelling (Jarosch and Gudmundsson, 2012) all provide tools to evaluate internal ablation and its role in driving surface subsidence and evolution, but this is a topic deserving focused future attention.

### **8.3.5 Pond surface conditions and near-surface meteorology**

The evaluation of a pond surface energy-balance model to represent exchange at the pond surface is relatively straightforward. However, any model is only as good as the data used to drive it, and in the case of supraglacial ponds, few measurements exist of albedo, surface temperature, and wind speed, all of which play important roles in the ponds' absorption of energy (Sakai et al., 2000). Additional observations of pond characteristics will develop a better statistical representation in glacier- or catchment-scale models. At the catchment scale (Chapter 7), it is important to note that the spatial variability in wind speed and air temperature is poorly constrained, even in the heavily-instrumented Langtang Valley (Ragettli et al., 2015), and additional studies of near-surface meteorology at the catchment scale (e.g. Collier and Immerzeel, 2015; Heynen et al., 2016) are needed to better constrain pond surface energy balance.

### **8.3.6 Pond energy-balance modelling**

There are also a few logical extensions of the energy-balance model developed in Chapter 5. Further investigation is needed to represent the switch between the wind-driven and natural

convection kinetic types, which vary based on diurnal meteorological conditions (Xin et al., 2011) and pond size (Sakai et al., 2009). This would improve understanding of the partition between pond-associated ablation at the glacier surface and internal ablation due to drainage, but is only useful for modelling well-documented large ponds that persist over many observations. To investigate this, an advance beyond the simple control volume approach is needed (e.g. Sakai et al., 2009), combined with a variety of idealised pond geometries, orientations, and thermal regimes to represent the range of plausible ponds. However, it is unclear that this would greatly advance understanding or estimation of supraglacial pond-associated ablation, and this avenue would be difficult to implement.

## 8.4 Conclusion

This thesis has conducted a multifaceted analysis of supraglacial perched ponds in the Langtang Valley of Nepal to assess their importance in enhancing ablation for debris-covered glaciers. A sophisticated Landsat remote-sensing analysis was first conducted to determine the magnitude and spatial and temporal distribution of supraglacial ponds on the five debris-covered glaciers for 1999-2013. The remote-sensing observations were supported by field investigations of pond characteristics, water-level changes, and evolution over four campaigns between May 2013 and October 2014, and supporting meteorological data were also collected. Based on these data, a numerical model of pond mass and energy balance was developed that calculates surface energy exchanges, subaqueous melt, and the excess energy delivered to the glacier's interior. The model was then applied in various levels of complexity and meteorological forcing to ponds on Lirung Glacier, enabling calculation of the pond-associated ablation for the entire glacier. Finally, a simplified version of the model representing surface energy exchange only was applied to the five debris-covered glaciers of the Langtang Valley based on the Landsat-derived distributions of supraglacial ponds, enabling calculation of the energy absorbed by ponds for the whole catchment.

The results of this thesis indicate that supraglacial ponds absorb sufficient energy to account for ~12% of observed ablation in the debris-covered area, enough to account for ~0.1 m of surface change on average. Based on the modelling at Lirung Glacier, ~70% of this energy leads to enhanced melt in the vicinity of ponds at the glacier's surface, while the remainder is delivered to englacial conduits and leads to internal ablation. Consequently, although supraglacial ponds typically cover a small portion of the debris-covered surface (1-2%), they play a crucial role in debris-covered glacier surface evolution. Future work is needed to extend these findings through continued and improved methods of pond observation and modelling applied at other sites. The results suggest that supraglacial ponds

are an important factor in determining ablation for debris-covered glaciers, and need to be represented in models of glacier mass balance and evolution.

# References

- Adhikary S., M. Nakawo, K. Seko, B. S. (2000). Dust influence on the melting process of glacier ice: experimental results from Lirung Glacier , Nepal Himalayas. *Debris-Covered Glaciers*, (264):43–52.
- Ageta, Y., Iwata, S., Yabuki, H., Naito, N., Sakai, A., Narama, C., and Karma (2000). Expansion of glacier lakes in recent decades in the Bhutan Himalayas. In *Debris-Covered Glaciers*, volume 264, pages 165–175.
- Anderson, L. S. and Anderson, R. S. (2016). Modeling debris-covered glaciers: extension due to steady debris input. *The Cryosphere*, 10:1105–1124.
- Aoki, T. and Asahi, K. (1998). Topographical map of the ablation area of the Lirung Glacier in the Langtang Valley, Nepal Himalaya. *Bulletin of Glacier Research*, 16:19–31.
- Bajracharya, S. R., Maharjan, S. B., Shrestha, F., Guo, W., Liu, S., Immerzeel, W., and Shrestha, B. (2015). The glaciers of the Hindu Kush Himalayas: current status and observed changes from the 1980s to 2010. *International Journal of Water Resources Development*, 31(2):161–173.
- Bajracharya, S. R. and Mool, P. (2009). Glaciers, glacial lakes and glacial lake outburst floods in the Mount Everest region, Nepal. *Annals of Glaciology*, 50(53):81–86.
- Banwell, A. F., Arnold, N. S., Willis, I. C., Tedesco, M., and Ahlstrøm, A. P. (2012). Modeling supraglacial water routing and lake filling on the Greenland Ice Sheet. *Journal of Geophysical Research*, 117(F4):1–11.
- Basnett, S., Kulkarni, A. V., and Bolch, T. (2013). The influence of debris cover and glacial lakes on the recession of glaciers in Sikkim Himalaya, India. *Journal of Glaciology*, 59(218):1035–1046.
- Benn, D., Bolch, T., Hands, K., Gulley, J., Luckman, a., Nicholson, L., Quincey, D., Thompson, S., Toumi, R., and Wiseman, S. (2012). Response of debris-covered glaciers in the Mount Everest region to recent warming, and implications for outburst flood hazards. *Earth-Science Reviews*, 114(1-2):156–174.
- Benn, D., Gulley, J., Luckman, A., Adamek, A., and Glowacki, P. S. (2009). Englacial drainage systems formed by hydrologically driven crevasse propagation. *Journal of Glaciology*, 55(191):513–523.
- Benn, D., Wiseman, S., and Warren, C. (2000). Rapid growth of a supraglacial lake, Ngozumpa Glacier, Khumbu Himal, Nepal. In *Debris-Covered Glaciers*, volume 264, pages 177–185.

- Benn, D. I., Wiseman, S., and Hands, K. A. (2001). Growth and drainage of supraglacial lakes on debris-mantled Ngozumpa Glacier, Khumbu Himal, Nepal. *Journal of Glaciology*, 47(159):626–638.
- Bhatt, M. P., Masuzawa, T., Yamamoto, M., and Takeuchi, N. (2007). Chemical characteristics of pond waters within the debris area of Lirung Glacier in Nepal Himalaya. *Journal of Limnology*, 66(2):71–80.
- Bolch, T., Buchroithner, M. F., Peters, J., Baessler, M., and Bajracharya, S. (2008). Identification of glacier motion and potentially dangerous glacial lakes in the Mt. Everest region/Nepal using spaceborne imagery. *Natural Hazards and Earth System Science*, 8(6):1329–1340.
- Bolch, T., Fujita, K., Scheel, M., Bajracharya, S., and Stoffel, M. (2012). The State and Fate of Himalayan Glaciers. *Science (New York, N.Y.)*, 306(6079):310–314.
- Bolch, T., Pieczonka, T., and Benn, D. I. (2011). Multi-decadal mass loss of glaciers in the Everest area (Nepal Himalaya) derived from stereo imagery. *The Cryosphere*, 5(2):349–358.
- Bookhagen, B. and Burbank, D. W. (2010). Toward a complete Himalayan hydrological budget: Spatiotemporal distribution of snowmelt and rainfall and their impact on river discharge. *Journal of Geophysical Research: Earth Surface*, 115(3):1–26.
- Boon, S. and Sharp, M. (2003). The role of hydrologically-driven ice fracture in drainage system evolution on an Arctic glacier. *Geophysical Research Letters*, 30(18):3–6.
- Bosson, J.-B. and Lambiel, C. (2016). Internal Structure and Current Evolution of Very Small Debris-Covered Glacier Systems Located in Alpine Permafrost Environments. *Frontiers in Earth Science*, 4(April).
- Bozhinskiy, A., Krass, M., and Popovnin, V. (1986). Role of debris cover in the thermal physics of glaciers. *Journal of Glaciology*, 32(1):255–266.
- Brock, B. W., Mihalcea, C., Kirkbride, M. P., Diolaiuti, G., Cutler, M. E. J., and Smiraglia, C. (2010). Meteorology and surface energy fluxes in the 2005–2007 ablation seasons at the Miage debris-covered glacier, Mont Blanc Massif, Italian Alps. *Journal of Geophysical Research: Atmospheres*, 115(9):1–16.
- Brun, F. (2015). *Monitoring supra-glacial ice-cliffs over debris-covered glaciers using high resolution ground measurements*. Master's thesis, Université Joseph Fourier, Grenoble, France.
- Brun, F., Buri, P., Miles, E. S., Wagnon, P., Steiner, J. F., Berthier, E., Ragettli, S., Kraaijenbrink, P., Immerzeel, W. W., and Pellicciotti, F. (2016). Quantifying volume loss from ice cliffs on debris-covered glaciers using high resolution terrestrial and aerial photogrammetry. *Journal of Glaciology*, 1(May):accepted.
- Buri, P., Miles, E. S., Steiner, J. F., Brun, F., and Pellicciotti, F. (2016a). A physically-based 3D model of ice cliff evolution on a debris-covered glacier. *Journal of Geophysical Research: Earth Surface*, in prep.

- Buri, P., Pellicciotti, F., Steiner, J. F., Evan, S., and Immerzeel, W. W. (2016b). A grid-based model of backwasting of supraglacial ice cliffs on debris-covered glaciers. *Annals of Glaciology*, 57(71):199–211.
- Burns, P. and Nolin, A. (2014). Using atmospherically-corrected Landsat imagery to measure glacier area change in the Cordillera Blanca, Peru from 1987 to 2010. *Remote Sensing of Environment*, 140:165–178.
- Carenzo, M., Pellicciotti, F., Mabillard, J., Reid, T., and Brock, B. W. (2016). An enhanced debris temperature index model accounting for thickness effect. *Advances in Water Resources*, in press.
- Carrivick, J. L. and Tweed, F. S. (2013). Proglacial lakes: character, behaviour and geological importance. *Quaternary Science Reviews*, 78:34–52.
- Chander, G., Markham, B. L., and Helder, D. L. (2009). Summary of current radiometric calibration coefficients for Landsat MSS, TM, ETM+, and EO-1 ALI sensors. *Remote Sensing of Environment*, 113(5):893–903.
- Chen, W., Fukui, H., Doko, T., and Gu, X. (2013). Improvement of glacial lakes detection under shadow environment using ASTER data in Himalayas, Nepal. *Chinese Geographical Science*, 23(2):216–226.
- Chikita, K. and Joshi, S. (2000). Hydrological and thermal regimes in a supra-glacial lake: Imja, Khumbu, Nepal Himalaya. *Hydrological Sciences*, 45(4):507–522.
- Chu, V. W. (2014). Greenland ice sheet hydrology: A review. *Progress in Physical Geography*, 38(1):19–54.
- Churchill, S. W. and Chu, H. H. (1975). Correlating equations for laminar and turbulent free convection from a vertical plate. *International Journal of Heat and Mass Transfer*, 18(11):1323–1329.
- Clarke, G. K. (2005). Subglacial Processes. *Annual Review of Earth and Planetary Sciences*, 33(1):247–276.
- Clarke, G. K. C., Jarosch, A. H., Anslow, F. S., Radić, V., and Menounos, B. (2015). Projected deglaciation of western Canada in the twenty-first century. *Nature Geoscience*, (8):372–377.
- Clayton, L. (1964). Karst Topography on Stagnant Glaciers. *Journal of Glaciology*, 9:107–112.
- Cogley, J. G., Kargel, J. S., Kaser, G., and van der Veen, C. J. (2010). Tracking the source of glacier misinformation. *Science (New York, N.Y.)*, 327(5965):522.
- Collier, E. and Immerzeel, W. W. (2015). High-resolution modeling of atmospheric dynamics in the Nepalese Himalaya. *Journal of Geophysical Research: Atmospheres*, 120:9882–9896.
- Collier, E., Maussion, F., Nicholson, L. I., Mölg, T., Immerzeel, W. W., and Bush, A. B. G. (2015). Impact of debris cover on glacier ablation and atmosphere–glacier feedbacks in the Karakoram. *The Cryosphere*, 9(4):1617–1632.

- Collier, E., Nicholson, L. I., Brock, B. W., Maussion, F., Essery, R., and Bush, A. B. G. (2014). Representing moisture fluxes and phase changes in glacier debris cover using a reservoir approach. *The Cryosphere*, 8(4):1429–1444.
- Conway, H. and Rasmussen, L. (2000). Summer temperature profiles within supraglacial debris on Khunibu Glacier, Nepal. In *Debris-Covered Glaciers*, number 264.
- Cook, S. J. and Quincey, D. J. (2015). Estimating the volume of Alpine glacial lakes. *Earth Surface Dynamics*, 3(4):559–575.
- Crandall, D. R. and Fahnestock, R. K. (1965). Rockfalls and Avalanches from Little Tahoma Peak on Mount Rainier Washington.
- Cuffey, K. M. and Paterson, W. (2010). *The Physics of Glaciers*. Elsevier B.V., 4 edition.
- Das, S. B., Joughin, I., Behn, M. D., Howat, I. M., King, M. A., Lizarralde, D., and Bhatia, M. P. (2008). Fracture Propagation to the Base of the Greenland Ice Sheet During Supraglacial Lake Drainage. *Science*, 1(May):778–781.
- Dehecq, A., Gourmelen, N., and Trouve, E. (2015). Deriving large-scale glacier velocities from a complete satellite archive: Application to the Pamir – Karakoram – Himalaya. *Remote Sensing of Environment*, 162:55–66.
- Deline, P., Hewitt, K., Reznichenko, N., and Shugar, D. (2015). *Rock Avalanches onto Glaciers*. Number January.
- Diolaiuti, G., Citterio, M., Carnielli, T., D’Agata, C., Kirkbride, M., and Smiraglia, C. (2006). Rates, processes and morphology of freshwater calving at Miage Glacier (Italian Alps). *Hydrological Processes*, 20(10):2233–2244.
- Elliott, J. R., Jolivet, R., Gonzalez, P. J., Avouac, J.-P., Hollingsworth, J., Searle, M. P., and Stevens, V. L. (2016). Himalayan megathrust geometry and relation to topography revealed by the Gorkha earthquake. *Nature Geoscience*, (January):1–8.
- Emmer, A., Loarte, E. C., Klimeš, J., and Vilímek, V. (2015). Recent evolution and degradation of the bent jatunraju glacier (cordillera blanca, Peru). *Geomorphology*, 228:345–355.
- Evatt, G. W., Abrahams, I. D., Heil, M., Kingslake, J., Mitchell, S. L., Andrew, C., and Clark, C. D. (2015). Glacial melt under a porous debris layer. *Journal of Glaciology*, 61(229):825–836.
- Flowers, G. E. and Clarke, G. K. C. (2002). A multicomponent coupled model of glacier hydrology 2. Application to Trapridge Glacier, Yukon, Canada. *Journal of Geophysical Research*, 107(B11):2288.
- Foster, L. A., Brock, B. W., Cutler, M. E. J., and Diotri, F. (2012). A physically based method for estimating supraglacial debris thickness from thermal band remote-sensing data. *Journal of Glaciology*, 58(210):677–691.
- Fountain, A. G. and Walder, J. S. (1998). Water flow through temperate glaciers. *Reviews of Geophysics*, 36(97):299.

- Frey, H., Machguth, H., Huss, M., Huggel, C., Bajracharya, S., Bolch, T., Kulkarni, A., Linsbauer, A., Salzmann, N., and Stoffel, M. (2014). Estimating the volume of glaciers in the Himalayan & Karakoram region using different methods. *The Cryosphere*, 8(6):2313–2333.
- Fujii, Y. (1977). Field Experiment on Glacier Ablation under a Layer of Debris Cover: Glaciological Expedition of Nepal, Contribution No. 33. *Journal of the Japanese Society of Snow and Ice*, 39:20–21.
- Fujita, K. and Nuimura, T. (2011). Spatially heterogeneous wastage of Himalayan glaciers. *Proceedings of the National Academy of Sciences of the United States of America*, 108(34):14011–14014.
- Fujita, K. and Sakai, a. (2014). Modelling runoff from a Himalayan debris-covered glacier. *Hydrology and Earth System Sciences*, 18(7):2679–2694.
- Fujita, K., Sakai, A., Nuimura, T., Yamaguchi, S., and Sharma, R. R. (2009). Recent changes in Imja Glacial Lake and its damming moraine in the Nepal Himalaya revealed by in situ surveys and multi-temporal ASTER imagery. *Environmental Research Letters*, 4(4):045205.
- Fujita, K., Sakai, a., Takenaka, S., Nuimura, T., Surazakov, a. B., Sawagaki, T., and Yamanokuchi, T. (2013). Potential flood volume of Himalayan glacial lakes. *Natural Hazards and Earth System Science*, 13(7):1827–1839.
- Fushimi, H., Yoshida, M., Watanabe, O., and Upadhyay, B. P. (1980). Distributions and Grain Sizes of Supraglacial Debris in the Khumbu Glacier, Khumbu Region, East Nepal. *Journal of the Japanese Society of Snow and Ice*, 41:18–25.
- Fyffe, C. L., Brock, B. W., Kirkbride, M. P., Mair, D. W. F., Arnold, N. S., Smiraglia, C., Diolaiuti, G., and Diotri, F. (2015). An investigation of the influence of supraglacial debris on glacier-hydrology. *The Cryosphere Discussions*, 9(5):5373–5411.
- Fyffe, C. L., Reid, T. D., Brock, B. W., Kirkbride, M. P., Diolaiuti, G., Smiraglia, C., and Diotri, F. (2014). A distributed energy-balance melt model of an alpine debris-covered glacier. *Journal of Glaciology*, 60(221):587–602.
- Gades, A., Conway, H., Nereson, N., Naito, N., and Kadota, T. (2000). Radio echo-sounding through supraglacial debris on Lirung and Khumbu Glaciers, Nepal Himalayas. In *Debris-Covered Glaciers*, volume 264, pages 13–22.
- Galewsky, J. (2009). Rain shadow development during the growth of mountain ranges: An atmospheric dynamics perspective. *Journal of Geophysical Research: Earth Surface*, 114(1):1–17.
- Gardelle, J., Arnaud, Y., and Berthier, E. (2011). Contrasted evolution of glacial lakes along the Hindu Kush Himalaya mountain range between 1990 and 2009. *Global and Planetary Change*, 75(1-2):47–55.
- Gardelle, J., Berthier, E., Arnaud, Y., and Käab, a. (2013). Region-wide glacier mass balances over the Pamir-Karakoram-Himalaya during 1999–2011. *The Cryosphere*, 7(4):1263–1286.

- Gardner, A. S., Moholdt, G., Cogley, J. G., Wouters, B., Arendt, A. A., Wahr, J., Berthier, E., Hock, R., Pfeffer, W. T., Kaser, G., Ligtenberg, S. R. M., Bolch, T., Sharp, M. J., Hagen, J. O., van den Broeke, M. R., and Paul, F. (2013). A reconciled estimate of glacier contributions to sea level rise: 2003 to 2009. *Science (New York, N.Y.)*, 340(6134):852–7.
- Grabs, W. E. and Hanisch, J. (1993). Objectives and Prevention Methods for Glacier Lake Outburst Moods (GLOFs). In *Snow and Glacier Hydrology*, number 218, pages 341–352. IAHS Publ. no. 218.
- Gulley, J. (2009). Structural control of englacial conduits in the temperate Matanuska Glacier, Alaska, USA. *Journal of Glaciology*, 55(192):681–690.
- Gulley, J. and Benn, D. (2007). Structural control of englacial drainage systems in Himalayan debris-covered glaciers. *Journal of Glaciology*, 53(182):399–412.
- Gulley, J. D., Benn, D. I., Müller, D., and Luckman, A. (2009a). A cut-and-closure origin for englacial conduits in uncrevassed regions of polythermal glaciers. *Journal of Glaciology*, 55(189):66–80.
- Gulley, J. D., Benn, D. I., Screatton, E., and Martin, J. (2009b). Mechanisms of englacial conduit formation and their implications for subglacial recharge. *Quaternary Science Reviews*, 28(19-20):1984–1999.
- Hagg, W., Mayer, C., Lambrecht, A., and Helm, A. (2008). Sub-debris melt rates on southern Inylchek Glacier, central Tian Shan. *Geografiska Annaler, Series A: Physical Geography*, 90 A(1):55–63.
- Hambrey, M. J., Quincey, D. J., Glasser, N. F., Reynolds, J. M., Richardson, S. J., and Clemmens, S. (2008). Sedimentological, geomorphological and dynamic context of debris-mantled glaciers, Mount Everest (Sagarmatha) region, Nepal. *Quaternary Science Reviews*, 27(25-26):2361–2389.
- Han, H., Ding, Y., and Liu, S. (2006). A simple model to estimate ice ablation under a thick debris layer. *Journal of Glaciology*, 52(179):528–536.
- Han, H., Wang, J., Wei, J., and Liu, S. (2010). Backwasting rate on debris-covered Koxkar glacier, Tuomuer mountain, China. *Journal of Glaciology*, 56(196):287–296.
- Hasnain, S. I., Jose, P. G., Ahmad, S., and Negi, D. C. (2001). Character of the subglacial drainage system in the ablation area of Dokriani glacier, India, as revealed by dye-tracer studies. *Journal of Hydrology*, 248(1-4):216–223.
- Herreid, S., Pellicciotti, F., Ayala, A., Chesnokova, A., Kienholz, C., Shea, J., and Shrestha, A. (2015). Satellite observations show no net change in the percentage of supraglacial debris-covered area in northern Pakistan from 1977 to 2014. *Journal of Glaciology*, 61(227):524–536.
- Hewitt, K. (2005). The Karakoram Anomaly? Glacier Expansion and the ‘Elevation Effect,’ Karakoram Himalaya. *Mountain Research and Development*, 25(4):332–340.
- Hewitt, K. (2011). Glacier Change, Concentration, and Elevation Effects in the Karakoram Himalaya, Upper Indus Basin. *Mountain Research and Development*, 31(3):188–200.

- Heynen, M., Miles, E., Ragetti, S., Buri, P., Immerzeel, W., and Pellicciotti, F. (2016). Air temperature variability in a high elevation Himalayan catchment. *Annals of Glaciology*, 57(71):212–222.
- Hugenholtz, C. H., Moorman, B. J., Barlow, J., and Wainstein, P. A. (2008). Large-scale moraine deformation at the Athabasca Glacier, Jasper National Park, Alberta, Canada. *Landslides*, 5(3):251–260.
- Huggel, C., Kääb, A., Haerberli, W., and Teysseire, P. (2002). Remote sensing based assessment of hazards from glacier lake outbursts: a case study in the Swiss Alps. *Canadian Geotechnical Journal*, 39:316–330.
- Huss, M. and Hock, R. (2015). A new model for global glacier change and sea-level rise. *Frontiers in Earth Science*, 3(September):1–22.
- Immerzeel, W., Kraaijenbrink, P., Shea, J., Shrestha, A., Pellicciotti, F., Bierkens, M., and de Jong, S. (2014a). High-resolution monitoring of Himalayan glacier dynamics using unmanned aerial vehicles. *Remote Sensing of Environment*, 150:93–103.
- Immerzeel, W. W., Beek, L. P. H., Konz, M., Shrestha, a. B., and Bierkens, M. F. P. (2011). Hydrological response to climate change in a glacierized catchment in the Himalayas. *Climatic Change*, 110(3-4):721–736.
- Immerzeel, W. W. and Bierkens, M. F. P. (2012). Asia's water balance. *Nature Geoscience*, 5(12):841–842.
- Immerzeel, W. W., Pellicciotti, F., and Bierkens, M. F. P. (2013). Rising river flows throughout the twenty-first century in two Himalayan glacierized watersheds. *Nature Geoscience*, 6(9):742–745.
- Immerzeel, W. W., Petersen, L., Ragetti, S., and Pellicciotti, F. (2014b). The importance of observed gradients of air temperature and precipitation for modeling runoff from a glacierized watershed in the Nepalese Himalayas. *Water Resources Research*, 50:2212–2226.
- Immerzeel, W. W., van Beek, L. P. H., and Bierkens, M. F. P. (2010). Climate Change Will Affect the Asian Water Towers. *Science*, 328(5984):1382–1385.
- Iwata, S., Watanabe, O., and Fushimi, H. (1980). Surface morphology in the ablation area of the Khumbu glacier. *Seppyo*.
- Jackson, J. (2006). Fatal attraction: living with earthquakes, the growth of villages into megacities, and earthquake vulnerability in the modern world. *Philosophical Transactions of the Royal Society, Series A, Mathematical, physical, and engineering sciences*, 364(1845):1911–25.
- Jacob, T., Wahr, J., Pfeffer, W. T., and Swenson, S. (2012). Recent contributions of glaciers and ice caps to sea level rise. *Nature*, 482(7386):514–518.
- Janes, T. J. and Bush, A. B. G. (2012). The Role of Atmospheric Dynamics and Climate Change on the Possible Fate of Glaciers in the Karakoram. *Journal of Climate*, 25(23):8308–8327.

- Janke, J. R., Bellisario, A. C., and Ferrando, F. A. (2015). Classification of debris-covered glaciers and rock glaciers in the Andes of central Chile. *Geomorphology*, 241:98–121.
- Jansson, P., Hock, R., and Schneider, T. (2003). The concept of glacier storage: a review. *Journal of Hydrology*, 282(1-4):116–129.
- Jarosh, a. H. and Gudmundsson, M. T. (2012). A numerical model for meltwater channel evolution in glaciers. *The Cryosphere*, 6(2):493–503.
- Jarvis, A., Reuter, H., Nelson, A., and Guevara, E. (2008). Hole-filled SRTM for the globe Version 4, available from the CGIAR-CSI SRTM 90m Database.
- Jin, Z., Qiao, Y., Wang, Y., Fang, Y., and Yi, W. (2011). A new parameterization of spectral and broadband ocean surface albedo. *Optics Express*, 19(27):6493–6499.
- Juen, M., Mayer, C., Lambrecht, A., Han, H., and Liu, S. (2014). Impact of varying debris cover thickness on ablation: A case study for Koxkar Glacier in the Tien Shan. *Cryosphere*, 8(2):377–386.
- Kääb, A., Berthier, E., Nuth, C., Gardelle, J., and Arnaud, Y. (2012). Contrasting patterns of early twenty-first-century glacier mass change in the Himalayas. *Nature*, 488(7412):495–498.
- Kääb, A. and Haeberli, W. (2001). Evolution of a High-mountain Thermokarst Lake in the Swiss Alps. *Arctic, Antarctic and Alpine Research*, 33(September 2000):385–390.
- Kargel, J. S., Leonard, G. J., Shugar, D. H., Haritashya, U. K., Bevington, A., Fielding, E. J., Fujita, K., Geertsema, M., Miles, E. S., Steiner, J., Anderson, E., Bajracharya, S., Bawden, G. W., Breashears, D. F., Byers, A., Collins, B., Dhital, M. R., Donnellan, A., Evans, T. L., Geai, M. L., Glasscoe, M. T., Green, D., Gurung, D. R., Heijnen, R., Hilborn, A., Hudnut, K., Huyck, C., Immerzeel, W. W., Jiang, L., Jibson, R., Kääb, A., Khanal, N. R., Kirschbaum, D., Kraaijenbrink, P. D. A., Lamsal, D., Liu, S., Lv, M., McKinney, D., Nahirnick, N. K., Nan, Z., Ojha, S., Olsenholler, J., Painter, T. H., Pleasants, M., Pratima, K., Yuan, Q., Raup, B. H., Regmi, D., Rounce, D. R., Sakai, A., Shangguan, D., Shea, J. M., Shrestha, A. B., Shukla, A., Stumm, D., van der Kooij, M., Voss, K., Wang, X., Weihs, B., Wolfe, D., Wu, L., Yao, X., Yoder, M. R., Young, N., Jiang Liming, Jibson, R., Kaab, A., Khanal, N. R., Kirschbaum, D., Kraaijenbrink, P. D. A., Lamsal, D., Liu Shiyin, Lv Mingyang, McKinney, D., Nahirnick, N. K., Nan Zhuotong, Ojha, S., Olsenholler, J., Painter, T. H., Pleasants, M., KC, P., Yuan, Q., Raup, B. H., Regmi, D., Rounce, D. R., Sakai, A., Shangguan Donghui, Shea, J. M., Shrestha, A. B., Shukla, A., Stumm, D., van der Kooij, M., Voss, K., Wang Xin, Weihs, B., Wolfe, D., Wu Lizong, Yao Xiaojun, Yoder, M. R., and Young, N. (2016). Geomorphic and geologic controls of geohazards induced by Nepals 2015 Gorkha earthquake. *Science*, 351(June):1–18.
- Kattelman, R. (2003). Glacial Lake Outburst Floods in the Nepal Himalaya : A Manageable Hazard ? *Natural Hazards*, 28:145–154.
- Kayastha, R. B., Takeuchi, Y., Nakawo, M., and Ageta, Y. (2000). Practical prediction of ice melting beneath various thickness of debris cover on Khumbu Glacier, Nepal, using a positive degree-day factor. In *Debris-Covered Glaciers*, number 264, pages 71–151. IAHS Publ. no. 264.

- Kellerer-Pirklbauer, A., Lieb, G. K., Avian, M., and Gspurning, J. (2008). The response of partially debris-covered valley glaciers to climate change: The example of the pasterze glacier (Austria) in the period 1964 to 2006. *Geografiska Annaler, Series A: Physical Geography*, 90(4):269–285.
- Kienholz, C., Herreid, S., Rich, J. L., Arendt, A. A., Hock, R., and Burgess, E. W. (2015). Derivation and analysis of a complete modern-date glacier inventory for Alaska and northwest Canada. *Journal of Glaciology*, 61(227):403–420.
- Kingslake, J., Ng, F., and Sole, A. (2015). Modelling channelized surface drainage of supraglacial lakes. *Journal of Glaciology*, 61(225):185–199.
- Kirkbride, M. P. (1993). The temporal significance of transitions from melting to calving termini at glaciers in the central Southern Alps of New Zealand. *The Holocene*, 3(3):232–240.
- Kirkbride, M. P. and Deline, P. (2013). The formation of supraglacial debris covers by primary dispersal from transverse englacial debris bands. *Earth Surface Processes and Landforms*, 38(15):1779–1792.
- Kirkbride, M. P. and Warren, C. R. (1997). Calving processes at a grounded ice cliff. *Annals of Glaciology*, 24:116–121.
- Kirkbride, M. P. and Warren, C. R. (1999). Tasman Glacier, New Zealand: 20th-century thinning and predicted calving retreat. *Global and Planetary Change*, 22:11–28.
- Komori, J. (2008). Recent expansions of glacial lakes in the Bhutan Himalayas. *Quaternary International*, 184(1):177–186.
- Kotchenova, S. Y. and Vermote, E. F. (2007). Validation of a vector version of the 6S radiative transfer code for atmospheric correction of satellite data. Part II. Homogeneous Lambertian and anisotropic surfaces. *Applied Optics*, 46(20):4455–64.
- Kotchenova, S. Y., Vermote, E. F., Matarrese, R., and Klemm, Jr., F. J. (2006). Validation of a vector version of the 6S radiative transfer code for atmospheric correction of satellite data. Part I: Path radiance. *Applied Optics*, 45(26):6762.
- Kraaijenbrink, P., Meijer, S. W., Shea, J. M., Pellicciotti, F., Jong, S. M. D. E., and Immerzeel, W. W. (2016). Seasonal surface velocities of a Himalayan glacier derived by automated correlation of unmanned aerial vehicle imagery. *Annals of Glaciology*, 57(71):103–113.
- Kraus, H. (1975). An energy balance model for ablation in mountainous areas. In *Snow and Ice Symposium*, number 104.
- Lambrecht, A., Mayer, C., Hagg, W., Popovnin, V., Rezepkin, A., Lomidze, N., and Svanadze, D. (2011). A comparison of glacier melt on debris-covered glaciers in the northern and southern Caucasus. *The Cryosphere*, 5(3):525–538.
- Lejeune, Y., Bertrand, J.-M., Wagnon, P., and Morin, S. (2013). A physically based model of the year-round surface energy and mass balance of debris-covered glaciers. *Journal of Glaciology*, 59(214):327–344.

- Liang, Y.-L., Colgan, W., Lv, Q., Steffen, K., Abdalati, W., Stroeve, J., Gallaher, D., and Bayou, N. (2012). A decadal investigation of supraglacial lakes in West Greenland using a fully automatic detection and tracking algorithm. *Remote Sensing of Environment*, 123:127–138.
- Linden, P. F. (2002). Convection in the environment. In Batchelor, G., Moffatt, H., and Vorster, M., editors, *Perspectives in Fluid Dynamics: A Collective Introduction to Current Research*, pages 289 – 343. Cambridge University Press, Cambridge, UK.
- Liu, Q., Mayer, C., and Liu, S. (2013). Distribution and recent variations of supraglacial lakes on dendritic-type glaciers in the Khan Tengri-Tomur Mountains, Central Asia. *The Cryosphere Discussions*, 7(1):4545–4584.
- Liu, Q., Mayer, C., and Liu, S. (2015). Distribution and interannual variability of supraglacial lakes on debris-covered glaciers in the Khan Tengri-Tomur Mountains, Central Asia. *Environmental Research Letters*, 10:4545–4584.
- Luthje, M. and Pedersen, L. (2006). Modelling the evolution of supraglacial lakes on the West Greenland ice-sheet margin. *Journal of Glaciology*, 52(179):608–618.
- Lutz, A., Immerzeel, W., Litt, M., Bajracharya, S., and Shrestha, A. (2015). Comprehensive Review of Climate Change and the Impacts on Cryosphere, Hydrological Regimes and Glacier Lakes.
- Lutz, A. F., Immerzeel, W. W., Shrestha, A. B., and Bierkens, M. F. P. (2014). Consistent increase in High Asia’s runoff due to increasing glacier melt and precipitation. *Nature Climate Change*, 4(7):587–592.
- Mackay, S. L., Marchant, D. R., Lamp, J. L., and Head, J. W. (2014). Cold-based debris-covered glaciers: Evaluating their potential as climate archives through studies of ground-penetrating radar and surface morphology. *Journal of Geophysical Research: Earth Surface*, 119:1–36.
- Marzeion, B., Jarosch, A. H., and Hofer, M. (2012). Past and future sea-level change from the surface mass balance of glaciers. *The Cryosphere*, 6(6):1295–1322.
- Masek, J., Vermote, E., Saleous, N., Wolfe, R., Hall, F., Huemmrich, F., Gao, F., Kutler, J., and Lim, T. (2012). LEDAPS Landsat Calibration, Reflectance, Atmospheric Correction Preprocessing Code.
- Mavlyudov, B. R. (2006). Glacial karst, why it important to research. *Acta Cartologica*, 35(1):55–67.
- McMillan, M. (2007). Seasonal evolution of supra-glacial lakes on the Greenland Ice Sheet. *Earth and Planetary Science Letters*, 262:484–492.
- Ménégoz, M., Gallée, H., and Jacobi, H. W. (2013). Precipitation and snow cover in the Himalaya: From reanalysis to regional climate simulations. *Hydrology and Earth System Sciences*, 17(10):3921–3936.

- Meon, G. and Schwahz, W. (1993). Estimation of Glacier Lake Outburst Flood and its Impact on a Hydro Project in Nepal. In *Snow and Glacier Hydrology*, number 218. IAHS Publ. no. 218.
- Mihalcea, C., Brock, B. W., Diolaiuti, G., D'Agata, C., Citterio, M., Kirkbride, M. P., Cutler, M. E. J., and Smiraglia, C. (2008). Using ASTER satellite and ground-based surface temperature measurements to derive supraglacial debris cover and thickness patterns on Miage Glacier (Mont Blanc Massif, Italy). *Cold Regions Science and Technology*, 52(3):341–354.
- Mihalcea, C., Mayer, C., Diolaiuti, G., Lambrecht, A., Smiraglia, C., and Tartari, G. (2006). Ice ablation and meteorological conditions on the debris-covered area of Baltoro glacier, Karakoram, Pakistan. *Annals of Glaciology*, 43(1894):292–300.
- Miles, E. S., Pellicciotti, F., Willis, I. C., Steiner, J. F., Buri, P., and Arnold, N. S. (2016). Refined energy-balance modelling of a supraglacial pond, Langtang Khola, Nepal. *Annals of Glaciology*, 57(71):29–40.
- Mölg, T., Maussion, F., and Scherer, D. (2014). Mid-latitude westerlies as a driver of glacier variability in monsoonal High Asia. *Nature Climate Change*, 4(1):68–73.
- Mölg, T., Maussion, F., Yang, W., and Scherer, D. (2012). The footprint of Asian monsoon dynamics in the mass and energy balance of a Tibetan glacier. *The Cryosphere*, 6(6):1445–1461.
- Mountain Research Initiative EDW Working Group (2015). Elevation-dependent warming in mountain regions of the world. *Nature Climate Change*, 5(5):424–430.
- Nagai, H., Fujita, K., Nuimura, T., and Sakai, a. (2013). Southwest-facing slopes control the formation of debris-covered glaciers in the Bhutan Himalaya. *The Cryosphere*, 7(4):1303–1314.
- Nakawo, M. and Rana, B. (1999). Estimate of Ablation Rate of Glacier Ice under a Supraglacial Debris Layer. *Geografiska Annaler, Series A: Physical Geography*, 81(4):695–701.
- Nakawo, M. and Young, G. J. (1982). Estimate of glacier ablation under a debris layer from surface temperature and meteorological variables. *Journal of Glaciology*, 28(98):29–34.
- Nakawo, Masayoshi Takahashi, S. (1982). A simplified model for estimating glacier ablation under a debris layer. *Hydrological Aspects of Alpine and High Mountain Areas (Proceedings of the Exeter Symposium)*, (138):137–145.
- Nicholson, L. and Benn, D. I. (2006). Calculating ice melt beneath a debris layer using meteorological data. *Journal of Glaciology*, 52(178):463–470.
- Nicholson, L. and Benn, D. I. (2013). Properties of natural supraglacial debris in relation to modelling sub-debris ice ablation. *Earth Surface Processes and Landforms*, 38(5):490–501.
- Nie, Y., Liu, Q., and Liu, S. (2013). Glacial lake expansion in the Central Himalayas by landsat images, 1990-2010. *PLoS ONE*, 8(12):1–8.

- Nienow, P., Sharp, M., and Willis, I. (1998). Seasonal changes in the morphology of the subglacial drainage system, Haut Glacier d'Arolla, Switzerland. *Earth Surface Processes and Landforms*, 23(9):825–843.
- Nuimura, T., Fujita, K., Yamaguchi, S., and Sharma, R. R. (2012). Elevation changes of glaciers revealed by multitemporal digital elevation models calibrated by GPS survey in the Khumbu region, Nepal Himalaya, 1992–2008. *Journal of Glaciology*, 58(210):648–656.
- Ojha, S., Fujita, K., Asahi, K., Sakai, A., Lamsal, D., Nuimura, T., and Nagai, H. (2016). Glacier area shrinkage in eastern Nepal Himalaya since 1992 using high-resolution inventories from aerial photographs and ALOS satellite images. *Journal of Glaciology*, pages 1–13.
- Ostrem, G. (1959). Ice melting under a thin layer of moraine, and the existence of ice cores in moraine ridges. *Geografiska Annaler*, 41(4):228–230.
- Panday, P. K., Bulley, H., Haritashya, U., and Ghimire, B. (2012). Supraglacial Lake Classification in the Everest Region of Nepal Himalaya. In Thakur, J. K., Singh, S. K., Ramanathan, A., Prasad, M. B. K., and Gossel, W., editors, *Geospatial Techniques for Managing Environmental Resources*, pages 86–99. Springer Netherlands, Dordrecht.
- Paul, F. (2015). Revealing glacier flow and surge dynamics from animated satellite image sequences: examples from the Karakoram. *The Cryosphere Discussions*, 9(2):2597–2623.
- Pellicciotti, F., Stephan, C., Miles, E., Herreid, S., Immerzeel, W. W., and Bolch, T. (2015). Mass-balance changes of the debris-covered glaciers in the Langtang Himal, Nepal, 1974–99. *Journal of Glaciology*, 61(226):1–14.
- Pfeffer, W. T., Arendt, A. a., Bliss, A., Bolch, T., Cogley, J. G., Gardner, A. S., Hagen, J.-O., Hock, R., Kaser, G., Kienholz, C., Miles, E. S., Moholdt, G., Mölg, N., Paul, F., Radić, V., Rastner, P., Raup, B. H., Rich, J., Sharp, M. J., and The Randolph Consortium (2014). The Randolph Glacier Inventory: a globally complete inventory of glaciers. *Journal of Glaciology*, 60(221):537–552.
- Pottakkal, J. G., Ramanathan, A., Singh, V. B., Sharma, P., Azam, M. F., and Linda, A. (2014). Characterization of subglacial pathways draining two tributary meltwater streams through the lower ablation zone of Gangotri glacier system, Garhwal Himalaya, India. *Current Science*, 107(4):613–621.
- Pratap, B., Dobhal, D., Mehta, M., and Bhambri, R. (2015). Influence of debris cover and altitude on glacier surface melting: a case study on Dokriani Glacier, central Himalaya, India. *Annals of Glaciology*, 56(70):9–16.
- Quincey, D., Richardson, S., Luckman, a., Lucas, R., Reynolds, J., Hambrey, M., and Glasser, N. (2007). Early recognition of glacial lake hazards in the Himalaya using remote sensing datasets. *Global and Planetary Change*, 56(1-2):137–152.
- Quincey, D. J., Braun, M., Glasser, N. F., Bishop, M. P., Hewitt, K., and Luckman, A. (2011). Karakoram glacier surge dynamics. *Geophysical Research Letters*, 38(18):1–6.

- Racoviteanu, A. E., Arnaud, Y., Williams, M. W., and Manley, W. F. (2015). Spatial patterns in glacier characteristics and area changes from 1962 to 2006 in the Kanchenjunga-Sikkim area, eastern Himalaya. *Cryosphere*, 9(2):505–523.
- Radić, V., Bliss, A., Beedlow, a. C., Hock, R., Miles, E., and Cogley, J. G. (2014). Regional and global projections of twenty-first century glacier mass changes in response to climate scenarios from global climate models. *Climate Dynamics*, 42(1-2):37–58.
- Ragetti, S., Bolch, T., and Pellicciotti, F. (2016). Heterogeneous glacier thinning patterns over the last 40 years in Langtang Himal. *The Cryosphere Discussions*, in review.
- Ragetti, S., Pellicciotti, F., Bordoy, R., and Immerzeel, W. W. (2013). Sources of uncertainty in modeling the glaciological response of a Karakoram watershed to climate change. *Water Resources Research*, 49(9):6048–6066.
- Ragetti, S., Pellicciotti, F., Immerzeel, W. W., Miles, E. S., Petersen, L., Heynen, M., Shea, J. M., Stumm, D., Joshi, S., and Shrestha, A. (2015). Unraveling the hydrology of a Himalayan catchment through integration of high resolution in situ data and remote sensing with an advanced simulation model. *Advances in Water Resources*, 78(0):94–111.
- Rangwala, I. and Miller, J. R. (2012). Climate change in mountains: A review of elevation-dependent warming and its possible causes. *Climatic Change*, 114(3-4):527–547.
- Ranzi, R., Grossi, G., Iacovelli, L., and Taschner, S. (2004). Use of multispectral ASTER images for mapping debris-covered glaciers within the GLIMS project. *IGARSS 2004. 2004 IEEE International Geoscience and Remote Sensing Symposium*, 2(C):1144–1147.
- Reid, T. and Brock, B. (2014). Assessing ice-cliff backwasting and its contribution to total ablation of debris-covered Miage glacier, Mont Blanc massif, Italy. *Journal of Glaciology*, 60(219):3–13.
- Reid, T. D. and Brock, B. W. (2010). An energy-balance model for debris-covered glaciers including heat conduction through the debris layer. *Journal of Glaciology*, 56(199):903–916.
- Reid, T. D., Carenzo, M., Pellicciotti, F., and Brock, B. W. (2012). Including debris cover effects in a distributed model of glacier ablation. *Journal of Geophysical Research*, 117(D18):1–15.
- Reynolds, J. (2000). On the formation of supraglacial lakes on debris-covered glaciers. In *Debris-Covered Glaciers*, number 264, pages 153–161.
- Reynolds, J. M. (1999). Glacial hazard assessment at Tsho Rolpa, Rolwaling, Central Nepal. *Quarterly Journal of Engineering Geology*, 32:209–214.
- Reznichenko, N., Davies, T., Shulmeister, J., and McSaveney, M. (2010). Effects of debris on ice-surface melting rates: an experimental study. *Journal of Glaciology*, 56(197):384–394.
- Richardson, S. D. and Reynolds, J. M. (2000). Degradation of ice-cored moraine dams : implications for hazard development. In *Debris-covered glaciers : proceedings of an international workshop held at University of Washington in Seattle, Washington, USA*, number 264, pages 187 – 197.

- Röhl, K. (2006). Thermo-erosional notch development at fresh-water-calving Tasman Glacier, New Zealand. *Journal of Glaciology*, 52(177):203–213.
- Röhl, K. (2008). Characteristics and evolution of supraglacial ponds on debris-covered Tasman Glacier, New Zealand. *Journal of Glaciology*, 54(188):867–880.
- Rounce, D. R. and McKinney, D. C. (2014). Debris thickness of glaciers in the Everest Area (Nepal Himalaya) derived from satellite imagery using a nonlinear energy balance model. *The Cryosphere Discussions*, 8(1):1317–1329.
- Rounce, D. R., Quincey, D. J., and McKinney, D. C. (2015). Debris-covered glacier energy balance model for Imja–Lhotse Shar Glacier in the Everest region of Nepal. *The Cryosphere*, 9:1–16.
- Rowan, A. V., Egholm, D. L., Quincey, D. J., and Glasser, N. F. (2015). Modelling the feedbacks between mass balance, ice flow and debris transport to predict the response to climate change of debris-covered glaciers in the Himalaya. *Earth and Planetary Science Letters*, 430:427–438.
- Russell-Head, D. (1980). The melting of free-drifting icebergs. *Annals of Glaciology*, 1:119–122.
- Sakai, A. (2012). Glacial lakes in the Himalayas: A review on formation and expansion processes. *Global Environmental Research*, 16:23–30.
- Sakai, A. and Fujita, K. (2010). Formation conditions of supraglacial lakes on debris-covered glaciers in the Himalaya. *Journal of Glaciology*, 56(195):177–181.
- Sakai, A., Nakawo, M., and Fujita, K. (1998). Melt rate of ice cliffs on the Lirung Glacier, Nepal Himalayas, 1996. *Bulletin of Glacier Research*, 16(October):57–66.
- Sakai, A., Nakawo, M., and Fujita, K. (2002). Distribution Characteristics and Energy Balance of Ice Cliffs on Debris-Covered Glaciers, Nepal Himalaya. *Arctic, Antarctic, and Alpine Research*, 34(1):12.
- Sakai, A., Nishimura, K., Kadota, T., and Takeuchi, N. (2009). Onset of calving at supraglacial lakes on debris-covered glaciers of the Nepal Himalaya. *Journal of Glaciology*, 55(193):909–917.
- Sakai, A., Takeuchi, N., Fujita, K., and Nakawo, M. (2000). Role of supraglacial ponds in the ablation process of a debris-covered glacier in the Nepal Himalayas. In *Debris-Covered Glaciers*, number 264, pages 119–130.
- Salerno, F., Thakuri, S., D’Agata, C., Smiraglia, C., Manfredi, E. C., Viviano, G., and Tartari, G. (2012). Glacial lake distribution in the Mount Everest region: Uncertainty of measurement and conditions of formation. *Global and Planetary Change*, 92-93:30–39.
- Schauwecker, S., Rohrer, M., Huggel, C., Kulkarni, A., Ramanathan, A. L., Salzmann, N., Stoffel, M., and Brock, B. (2015). Remotely sensed debris thickness mapping of Bara Shigri Glacier, Indian Himalaya. *Journal of Glaciology*, 61(228):675–688.

- Scherler, D., Bookhagen, B., and Strecker, M. R. (2011a). Hillslope-glacier coupling: The interplay of topography and glacial dynamics in High Asia. *Journal of Geophysical Research: Earth Surface*, 116(March):1–21.
- Scherler, D., Bookhagen, B., and Strecker, M. R. (2011b). Spatially variable response of Himalayan glaciers to climate change affected by debris cover. *Nature Geoscience*, 4(3):156–159.
- Selmes, N., Murray, T., and James, T. D. (2011). Fast draining lakes on the Greenland Ice Sheet. *Geophysical Research Letters*, 38(15):1–5.
- Shaw, T., Brock, B., Fyffe, C., Pellicciotti, F., Rutter, N., and Diotri, F. (2016). Air temperature distribution and energy balance modelling of a debris-covered glacier. *Journal of Glaciology*, 62(23):185–198.
- Shea, J. M., Immerzeel, W. W., Wagnon, P., Vincent, C., and Bajracharya, S. (2015a). Modelling glacier change in the Everest region, Nepal Himalaya. *The Cryosphere*, 9:1105–1128.
- Shea, J. M., Wagnon, P., Immerzeel, W. W., Biron, R., Brun, F., and Pellicciotti, F. (2015b). A comparative high-altitude meteorological analysis from three catchments in the Nepalese Himalaya. *International Journal of Water Resources Development*, 31(2):174–200.
- Shrestha, A., Agrawal, N., Althman, B., Bajracharya, S., Maréchal, J., and van Oort, B. (2015). The Himalayan Climate and Water Atlas: Impact of climate change on water resources in five of Asia's major river basins. Technical report, ICIMOD, GRID-Arendal, and CICERO.
- Shrestha, A. B., Eriksson, M., Mool, P., Ghimire, P., Mishra, B., and Khanal, N. R. (2010). Glacial lake outburst flood risk assessment of Sun Koshi basin, Nepal. *Geomatics, Natural Hazards and Risk*, 1(2):157–169.
- Shugar, D. H. and Clague, J. J. (2011). The sedimentology and geomorphology of rock avalanche deposits on glaciers. *Sedimentology*, 58(7):1762–1783.
- Shukla, A. and Qadir, J. (2016). Differential response of glaciers with varying debris cover extent: evidence from changing glacier parameters. *International Journal of Remote Sensing*, 37(11):2453–2479.
- Singh, K. K., Kulkarni, A. V., and Mishra, V. D. (2010). Estimation of Glacier Depth and Moraine Cover Study using Ground Penetrating Radar (GPR) in the Himalayan Region. *Journal of the Indian Society of Remote Sensing*, 38:1–9.
- Steiner, J. and Pellicciotti, F. (2016). On the variability of air temperature over a debris covered glacier, Nepalese Himalaya. *Annals of Glaciology*, 57(71):1–13.
- Steiner, J. J. F., Pellicciotti, F., Buri, P., Miles, E. S. E., Immerzeel, W. W., Reid, T. T. D., and Steiner, C. J. F. (2015). Modelling ice-cliff backwasting on a debris-covered glacier in the Nepalese Himalaya. *Journal of Glaciology*, 61(229):889–907.
- Sugiyama, S., Fukui, K., Fujita, K., Tone, K., and Yamaguchi, S. (2013). Changes in ice thickness and flow velocity of Yala Glacier, Langtang Himal, Nepal, from 1982 to 2009. *Annals of Glaciology*, 54(64):157–162.

- Sundal, A. V., Shepherd, A., Nienow, P., Hanna, E., Palmer, S., and Huybrechts, P. (2009). Evolution of supra-glacial lakes across the Greenland Ice Sheet. *Remote Sensing of Environment*, 113(10):2164–2171.
- Suzuki, R., Fujita, K., and Ageta, Y. (2007). Spatial distribution of thermal properties on debris-covered glaciers in the Himalayas derived from ASTER data. *Bulletin of Glaciological Research*, 24:13–22.
- Swithinbank, C. (1950). The origin of dirt cones on glaciers. *Journal of Glaciology*, 1(8):461–465,439.
- Takeuchi, N., Sakai, A., Shiro, K., Fujita, K., and Masayoshi, N. (2012). Variation in Suspended Sediment Concentration of Supraglacial Lakes on Debris-covered Area of the Lirung Glacier in the Nepal Himalayas. *Global Environmental Research*, 16:95–104.
- Taschner, S. and Ranzi, R. (2002). Comparing the opportunities of Landsat-TM and Aster data for monitoring a debris covered glacier in the Italian Alps within the GLIMS project. *IEEE International Geoscience and Remote Sensing Symposium*, 2(C):8–10.
- Taylor, P. D. and Feltham, D. (2004). A model of melt pond evolution on sea ice. *Journal of Geophysical Research: Oceans*, 109(C12).
- Tedesco, M., Lüthje, M., Steffen, K., Steiner, N., Fettweis, X., Willis, I., Bayou, N., and Banwell, A. (2012). Measurement and modeling of ablation of the bottom of supraglacial lakes in western Greenland. *Geophysical Research Letters*, 39(2).
- Thakuri, S., Salerno, F., Smiraglia, C., Bolch, T., D'Agata, C., Viviano, G., and Tartari, G. (2014). Tracing glacier changes since the 1960s on the south slope of Mt. Everest (central Southern Himalaya) using optical satellite imagery. *Cryosphere*, 8(4):1297–1315.
- Thompson, S., Benn, D. I., Mertes, J., and Luckman, A. (2016). Stagnation and mass loss on a Himalayan debris-covered glacier: processes, patterns and rates. *Journal of Glaciology*, pages 1–19.
- Thompson, S. S., Benn, D. I., Dennis, K., and Luckman, A. (2012). A rapidly growing moraine-dammed glacial lake on Ngozumpa Glacier, Nepal. *Geomorphology*, 145-146:1–11.
- Watanabe, O., Iwata, S., and Fushimi, H. (1986). Topographic characteristics in the ablation area of the khumbu glacier, nepal himalaya. *Annals of Glaciology*, 8:177–180.
- Watanabe, T., Dali, L., and Shiraiwa, T. (1998). Slope denudation and the supply of debris to cones in Langtang Himal, Central Nepal Himalaya. *Geomorphology*, 26(1-3):185–197.
- Watanabe, T., Kameyama, S., and Sato, T. (1995). Imja Glacier dead-ice melt rates and changes in a supra-glacial lake, 1989-1994, Khumbu Himal, Nepal: Danger of lake drainage. *Mountain Research and Development*, 15(4):293–300.
- Watson, C., Quincey, D., Carrivick, J., and Smith, M. (2016). The dynamics of supraglacial ponds in the Everest region, central Himalaya. *Global and Planetary Change*, 142:14–27.

- Weeks, W. and Campbell, W. (1973). Icebergs as a Fresh Water Source: An Appraisal. *Journal of Glaciology*, 12(65):207–233.
- Werder, M. A., Bauder, A., Funk, M., and Keusen, H. R. (2010). Hazard assessment investigations in connection with the formation of a lake on the tongue of Unterer Grindelwaldgletscher, Bernese Alps, Switzerland. *Natural Hazards and Earth System Sciences*, 10(2):227–237.
- Werder, M. A., Hewitt, I. J., Schoof, C. G., and Flowers, G. E. (2013). Modeling channelized and distributed subglacial drainage in two dimensions. *Journal of Geophysical Research: Earth Surface*, 118(4):2140–2158.
- Wessels, R. L., Kargel, J. S., and Kieffer, H. H. (2002). ASTER measurement of supraglacial lakes in the Mount Everest region of the Himalaya. *Annals of Glaciology*, 34(1):399–408.
- Westoby, M. J., Glasser, N. F., Hambrey, M. J., Brasington, J., Reynolds, J. M., and Hassan, M. A. A. M. (2014). Reconstructing historic glacial lakeoutburst floods through numerical modelling and geomorphological assessment: Extreme events in the himalaya. *Earth Surface Processes and Landforms*, 39(12):1675–1692.
- Wilson, A. M., Williams, M. W., Kayastha, R. B., and Racoviteanu, A. (2016). Use of a hydrologic mixing model to examine the roles of meltwater, precipitation and groundwater in the Langtang River basin, Nepal. *Annals of Glaciology*, 57(71):155–168.
- Wiltshire, A. J. (2014). Climate change implications for the glaciers of the Hindu Kush, Karakoram and Himalayan region. *Cryosphere*, 8(3):941–958.
- Wu, Z., Zhang, S., and Liu, S. (2013). Optimal antenna of ground penetrating radar for depicting the debris thickness and structure of the Koxkar Glacier, Tianshan, China. *Journal of Earth Science*, 24(5):830–842.
- Xin, W., Shiyin, L., Han, H., Jian, W., and Qiao, L. (2011). Thermal regime of a supraglacial lake on the debris-covered Koxkar Glacier, southwest Tianshan, China. *Environmental Earth Sciences*, 67(1):175–183.
- Xu, J., Grumbine, R. E., Shrestha, A., Eriksson, M., Yang, X., Wang, Y., and Wilkes, A. (2009). The melting Himalayas: cascading effects of climate change on water, biodiversity, and livelihoods. *Conservation biology : the journal of the Society for Conservation Biology*, 23(3):520–30.
- Yamada, T. (1998). Glacier Lake and its Outburst Flood in the Nepal Himalaya.
- Yao, X., Liu, S., Sun, M., Wei, J., and Guo, W. (2012). Volume calculation and analysis of the changes in moraine-dammed lakes in the north Himalaya: a case study of Longbasaba lake. *Journal of Glaciology*, 58(210):753–760.
- Ye, Q., Bolch, T., Naruse, R., Wang, Y., Zong, J., Wang, Z., Zhao, R., Yang, D., and Kang, S. (2015). Glacier mass changes in Rongbuk catchment on Mt. Qomolangma from 1974 to 2006 based on topographic maps and ALOS PRISM data. *Journal of Hydrology*, 530:273–280.

- Zelazowski, P., Sayer, A. M., Thomas, G. E., and Grainger, R. G. (2011). Reconciling satellite-derived atmospheric properties with fine-resolution land imagery: Insights for atmospheric correction. *Journal of Geophysical Research*, 116(D18):1–15.
- Zhang, Y., Fujita, K., Liu, S., Liu, Q., and Nuimura, T. (2011). Distribution of debris thickness and its effect on ice melt at Hailuogou glacier, southeastern Tibetan Plateau, using in situ surveys and ASTER imagery. *Journal of Glaciology*, 57(206):1147–1157.
- Zhao, L., Ding, R., and Moore, J. C. (2014). Glacier volume and area change by 2050 in high mountain Asia. *Global and Planetary Change*, 122:197–207.
- Zhu, Z., Wang, S., and Woodcock, C. E. (2015). Improvement and expansion of the Fmask algorithm: cloud, cloud shadow, and snow detection for Landsats 4–7, 8, and Sentinel 2 images. *Remote Sensing of Environment*, 159:269–277.

# **Appendix A**

## **Supplemental Tables and Figures**

Table A.1 Summary of the 197 Landsat scenes assessed, and the 172 chosen for analysis in Chapter 3. Shown for all 197 scenes are the scene ID, data of acquisition, level of processing, sensor, % cloud cover over the whole scene, data quality, and the file processing data, all provided from the USGS. The 172 scenes chosen for processing also show the % of Langtang Valley's debris-covered glacier area that was observable, snow-covered, and ponded, and the count of individual ponds  $N$ .

SceneID	Date Acquired	Level	Sensor	% Cloud	Quality	File Date	% DCG area			$N$ Ponds
							Observable	Snow	Pond	
LE71410401999228SGS00	16-Aug-1999	L1T	ETM	60	9	30-Nov-2013	74.05	2.01	1.07	59
LE71410401999244AGS00	01-Sep-1999	L1G	ETM	81	9	30-Nov-2013				
LE71410401999340SGS00	06-Dec-1999	L1T	ETM	37	9	12-Jan-2014	89.98	65.13	0.00	2
LE71410402000023EDC00	23-Jan-2000	L1T	ETM	10	9	12-Jan-2014	92.36	73.83	0.00	0
LE71410402000167SGS00	15-Jun-2000	L1T	ETM	29	9	30-Nov-2013				
LE71410402000199EDC00	17-Jul-2000	L1T	ETM	41	9	30-Nov-2013	96.60	1.82	1.15	82
LE71410402000247SGS00	03-Sep-2000	L1T	ETM	77	9	30-Nov-2013	72.74	0.87	1.10	79
LE71410402000279SGS00	05-Oct-2000	L1T	ETM	12	9	12-Jan-2014	98.75	2.92	0.97	85
LE71410402000327EDC00	22-Nov-2000	L1T	ETM	1	9	05-Dec-2013	92.43	3.17	0.27	65
LE71410402001073SGS00	14-Mar-2001	L1T	ETM	33	9	12-Jan-2014	94.12	70.47	0.00	2
LE71410402001153SGS00	02-Jun-2001	L1T	ETM	50	9	30-Nov-2013	74.49	7.21	1.98	105
LE71410402001185SGS00	04-Jul-2001	L1T	ETM	38	9	30-Nov-2013	75.64	1.85	1.47	68
LE71410402001233SGS00	21-Aug-2001	L1T	ETM	74	9	30-Nov-2013				
LE71410402001265SGS03	22-Sep-2001	L1T	ETM	9	9	30-Nov-2013	99.22	2.07	0.97	84
LE71410402001297SGS00	24-Oct-2001	L1T	ETM	1	9	22-Nov-2013	98.04	3.38	0.52	66
LE71410402001361SGS00	27-Dec-2001	L1T	ETM	2	9	12-Jan-2014	84.07	5.24	0.00	99
LE71410402002044SGS00	13-Feb-2002	L1T	ETM	11	9	12-Jan-2014	99.22	97.95	0.00	0
LE71410402002060SGS00	01-Mar-2002	L1T	ETM	8	9	12-Jan-2014	99.29	96.56	0.00	0
LE71410402002076PFS00	17-Mar-2002	L1T	ETM	32	9	12-Jan-2014	93.81	81.76	0.03	3
LE71410402002124PFS00	04-May-2002	L1T	ETM	20	9	30-Nov-2013	99.99	51.54	0.21	22
LE71410402002188SGS00	07-Jul-2002	L1T	ETM	38	9	30-Nov-2013				
LE71410402002220SGS00	08-Aug-2002	L1T	ETM	60	9	30-Nov-2013	66.82	0.35	0.54	32
LE71410402002284SGS00	11-Oct-2002	L1T	ETM	28	9	12-Jan-2014	99.51	79.67	0.20	23
LE71410402002332SGS00	28-Nov-2002	L1T	ETM	1	9	12-Jan-2014	91.97	25.49	0.46	49
LE71410402003047SGS02	16-Feb-2003	L1T	ETM	35	9	12-Jan-2014	96.84	91.61	0.00	0
LE71410402003063SGS00	04-Mar-2003	L1T	ETM	31	9	12-Jan-2014	98.07	92.91	0.00	1
LE71410402003207ASN02	26-Jul-2003	L1T	ETM	75	9	12-Jan-2014				
LE71410402003223ASN01	11-Aug-2003	L1G	ETM	80	9	12-Jan-2014	73.29	2.63	1.05	61
LE71410402003239ASN01	27-Aug-2003	L1T	ETM	89	9	12-Jan-2014				
LE71410402003271ASN01	28-Sep-2003	L1T	ETM	15	9	12-Jan-2014	84.46	4.46	0.91	57
LE71410402003287ASN01	14-Oct-2003	L1T	ETM	0	9	26-Dec-2013	85.22	14.38	0.93	66
LE71410402003335SGS01	01-Dec-2003	L1T	ETM	1	9	12-Jan-2014	78.62	2.71	0.28	83
LE71410402004082ASN01	22-Mar-2004	L1T	ETM	4	9	12-Jan-2014	84.35	7.31	1.67	121
LE71410402004098ASN01	07-Apr-2004	L1T	ETM	63	9	12-Jan-2014	69.16	68.97	0.00	0
LE71410402004146PFS01	25-May-2004	L1T	ETM	35	9	12-Jan-2014	85.06	16.49	0.96	72
LE71410402004178ASN01	26-Jun-2004	L1T	ETM	34	9	12-Jan-2014	42.99	0.69	1.38	46
LE71410402004194ASN01	12-Jul-2004	L1T	ETM	79	9	12-Jan-2014				
LE71410402004226PFS01	13-Aug-2004	L1G	ETM	90	9	12-Jan-2014				
LE71410402004242PFS02	29-Aug-2004	L1T	ETM	59	9	12-Jan-2014	63.89	0.23	0.59	36
LE71410402004258PFS01	14-Sep-2004	L1T	ETM	15	9	12-Jan-2014	83.35	0.61	1.07	66
LE71410402004274PFS02	30-Sep-2004	L1T	ETM	48	9	12-Jan-2014	65.85	2.07	0.00	23
LE71410402004290PFS01	16-Oct-2004	L1T	ETM	21	9	12-Jan-2014	86.80	62.98	0.07	9
LE71410402004306PFS00	01-Nov-2004	L1T	ETM	2	9	12-Jan-2014	81.81	9.65	0.26	30
LE71410402004338PFS00	03-Dec-2004	L1T	ETM	2	9	12-Jan-2014	78.37	12.83	0.03	31
LE71410402004354PFS00	19-Dec-2004	L1T	ETM	1	9	12-Jan-2014	74.37	3.66	0.25	101
LE71410402005004PFS00	04-Jan-2005	L1T	ETM	5	9	12-Jan-2014	68.84	43.59	0.00	20
LE71410402005036EDC00	05-Feb-2005	L1T	ETM	20	9	12-Jan-2014	85.41	92.46	0.00	0
LT51410402005044BKT00	13-Feb-2005	L1T	TM	26	7	12-Jan-2014	99.21	92.33	0.01	4
LE71410402005052PFS00	21-Feb-2005	L1T	ETM	6	9	12-Jan-2014	84.24	77.67	0.00	3
LE71410402005068PFS00	09-Mar-2005	L1T	ETM	5	9	12-Jan-2014	84.68	65.20	0.02	4
LE71410402005084PFS00	25-Mar-2005	L1T	ETM	5	9	12-Jan-2014	86.75	98.34	0.00	0
LE71410402005100PFS00	10-Apr-2005	L1T	ETM	55	9	12-Jan-2014	86.56	83.92	0.00	0
LE71410402005116PFS00	26-Apr-2005	L1T	ETM	51	9	12-Jan-2014	82.10	30.32	0.47	37
LE71410402005132PFS00	12-May-2005	L1T	ETM	46	9	12-Jan-2014	85.94	17.77	0.70	66
LE71410402005244PFS00	01-Sep-2005	L1T	ETM	46	9	12-Jan-2014				
LE71410402005276PFS00	03-Oct-2005	L1T	ETM	18	9	12-Jan-2014	49.35	1.04	2.28	64
LE71410402005308PFS00	04-Nov-2005	L1T	ETM	23	9	12-Jan-2014	84.75	97.29	0.03	5

Table A.2 Summary of the 197 Landsat scenes assessed, and the 172 chosen for analysis in Chapter 3. Shown for all 197 scenes are the scene ID, data of acquisition, level of processing, sensor, % cloud cover over the whole scene, data quality, and the file processing data, all provided from the USGS. The 172 scenes chosen for processing also show the % of Langtang Valley's debris-covered glacier area that was observable, snow-covered, and ponded, and the count of individual ponds  $N$ .

SceneID	Date Acquired	Level	Sensor	% Cloud	Quality	File Date	% DCG area			
							Observable	Snow	Pond	$N$ Ponds
LT51410402005316BKT00	12-Nov-2005	L1T	TM	13	7	12-Jan-2014	96.61	92.36	2.14	70
LE71410402005324SGS00	20-Nov-2005	L1T	ETM	25	9	12-Jan-2014	82.78	83.43	0.45	53
LE71410402005340PFS00	06-Dec-2005	L1T	ETM	3	9	12-Jan-2014	76.65	55.38	0.23	29
LE71410402005356PFS00	22-Dec-2005	L1T	ETM	30	9	12-Jan-2014				
LE71410402006087PFS00	28-Mar-2006	L1T	ETM	32	9	12-Jan-2014	77.42	96.08	0.00	1
LE71410402006119PFS00	29-Apr-2006	L1T	ETM	18	9	12-Jan-2014	86.48	96.41	0.05	5
LE71410402006151PFS00	31-May-2006	L1T	ETM	30	9	12-Jan-2014	78.77	9.88	1.74	98
LE71410402006231PFS01	19-Aug-2006	L1G	ETM	81	9	12-Jan-2014				
LE71410402006247PFS00	04-Sep-2006	L1T	ETM	46	9	12-Jan-2014	79.78	1.37	4.37	88
LE71410402006263PFS02	20-Sep-2006	L1T	ETM	62	9	12-Jan-2014				
LE71410402006279PFS00	06-Oct-2006	L1T	ETM	2	9	12-Jan-2014	86.60	27.82	1.51	152
LT51410402006287BKT00	14-Oct-2006	L1T	TM	12	7	12-Jan-2014	98.93	15.10	2.31	179
LE71410402006295PFS00	22-Oct-2006	L1T	ETM	60	9	12-Jan-2014	86.44	96.29	0.02	2
LT51410402006303BKT00	30-Oct-2006	L1T	TM	18	7	12-Jan-2014	98.56	23.41	0.81	123
LE71410402006311PFS00	07-Nov-2006	L1T	ETM	22	9	12-Jan-2014	84.33	23.29	0.06	8
LE71410402006327PFS00	23-Nov-2006	L1T	ETM	3	9	12-Jan-2014	78.54	13.50	0.03	29
LE71410402006359SGS00	25-Dec-2006	L1T	ETM	3	9	12-Jan-2014	73.81	24.54	0.09	47
LE71410402007026SGS00	26-Jan-2007	L1T	ETM	1	9	12-Jan-2014	77.29	9.47	0.27	105
LE71410402007058SGS00	27-Feb-2007	L1T	ETM	5	9	12-Jan-2014	84.99	98.86	0.00	0
LE71410402007074SGS00	15-Mar-2007	L1T	ETM	28	9	12-Jan-2014	85.30	44.43	0.00	0
LE71410402007090SGS00	31-Mar-2007	L1T	ETM	15	9	12-Jan-2014	84.27	68.43	0.42	56
LE71410402007106SGS00	16-Apr-2007	L1T	ETM	13	9	12-Jan-2014	85.05	30.52	1.31	84
LE71410402007234PFS00	22-Aug-2007	L1T	ETM	45	9	12-Jan-2014	70.28	11.14	1.17	53
LE71410402007266PFS00	23-Sep-2007	L1T	ETM	14	9	12-Jan-2014				
LE71410402007330SGS00	26-Nov-2007	L1T	ETM	1	9	12-Jan-2014	78.62	24.93	0.35	51
LE71410402007346PFS00	12-Dec-2007	L1T	ETM	30	9	12-Jan-2014	78.91	87.24	0.00	0
LE71410402007362SGS00	28-Dec-2007	L1T	ETM	2	9	12-Jan-2014	72.85	19.06	0.20	80
LE71410402008013PFS00	13-Jan-2008	L1T	ETM	4	9	11-Jan-2014	76.67	23.55	0.02	70
LE71410402008045EDC00	14-Feb-2008	L1T	ETM	4	9	11-Jan-2014	83.33	48.42	0.01	22
LE71410402008061SGS00	01-Mar-2008	L1T	ETM	7	9	11-Jan-2014	84.91	24.98	1.75	101
LE71410402008077SGS00	17-Mar-2008	L1T	ETM	23	9	11-Jan-2014	86.02	42.44	0.05	14
LE71410402008125SGS00	04-May-2008	L1T	ETM	82	9	11-Jan-2014	61.44	62.18	0.11	10
LE71410402008141SGS00	20-May-2008	L1T	ETM	51	9	11-Jan-2014	44.32	6.99	1.11	40
LE71410402008157PFS00	05-Jun-2008	L1T	ETM	35	9	11-Jan-2014	68.03	3.90	2.01	85
LE71410402008173ASN00	21-Jun-2008	L1T	ETM	60	9	11-Jan-2014	52.11	2.07	1.59	59
LE71410402008237SGS00	24-Aug-2008	L1T	ETM	59	9	11-Jan-2014	40.37	0.11	2.01	45
LE71410402008253SGS00	09-Sep-2008	L1T	ETM	23	9	11-Jan-2014	71.98	0.45	0.98	60
LE71410402008269SGS00	25-Sep-2008	L1T	ETM	72	9	11-Jan-2014				
LE71410402008301SGS00	27-Oct-2008	L1T	ETM	1	9	11-Jan-2014	86.92	6.38	1.26	78
LE71410402008317SGS00	12-Nov-2008	L1T	ETM	2	9	11-Jan-2014	82.69	4.14	1.67	99
LE71410402008333SGS00	28-Nov-2008	L1T	ETM	1	9	11-Jan-2014	78.26	2.48	0.33	84
LE71410402008349SGS00	14-Dec-2008	L1T	ETM	1	9	11-Jan-2014	76.26	1.91	0.13	131
LE71410402008365SGS00	30-Dec-2008	L1T	ETM	3	9	11-Jan-2014	74.53	4.00	0.01	71
LE71410402009015PFS00	15-Jan-2009	L1T	ETM	2	9	11-Jan-2014	76.46	6.80	0.06	89
LT51410402009023KHC00	23-Jan-2009	L1T	TM	1	9	12-Jan-2014	86.20	3.29	2.19	186
LE71410402009031EDC00	31-Jan-2009	L1T	ETM	3	9	11-Jan-2014	81.41	2.81	0.21	123
LT51410402009039KHC00	08-Feb-2009	L1T	TM	1	9	03-Nov-2013				
LE71410402009047SGS00	16-Feb-2009	L1T	ETM	4	9	17-Nov-2013	86.03	7.30	0.30	83
LT51410402009055KHC00	24-Feb-2009	L1T	TM	33	9	12-Jan-2014	98.55	44.37	0.01	60
LE71410402009063SGS00	04-Mar-2009	L1T	ETM	6	9	17-Nov-2013	87.04	7.98	1.91	138
LT51410402009071KHC00	12-Mar-2009	L1T	TM	29	9	18-Dec-2013	98.52	4.58	0.72	144
LE71410402009079PFS00	20-Mar-2009	L1T	ETM	68	9	21-Nov-2013	53.24	75.13	0.00	0
LE71410402009111SGS00	21-Apr-2009	L1T	ETM	23	9	23-Nov-2013	83.54	9.37	1.21	99
LE71410402009127SGS00	07-May-2009	L1T	ETM	1	9	29-Nov-2013	84.38	3.65	1.27	86
LT51410402009135KHC00	15-May-2009	L1T	TM	49	9	17-Nov-2013	99.95	85.27	1.00	91
LE71410402009159ASN00	08-Jun-2009	L1T	ETM	25	9	02-Dec-2013	85.61	23.72	1.66	91

Table A.3 Summary of the 197 Landsat scenes assessed, and the 172 chosen for analysis in Chapter 3. Shown for all 197 scenes are the scene ID, data of acquisition, level of processing, sensor, % cloud cover over the whole scene, data quality, and the file processing data, all provided from the USGS. The 172 scenes chosen for processing also show the % of Langtang Valley's debris-covered glacier area that was observable, snow-covered, and ponded, and the count of individual ponds  $N$ .

SceneID	Date Acquired	Level	Sensor	% Cloud	Quality	File Date	% DCG area			$N$ Ponds
							Observable	Snow	Pond	
LT51410402009167KHC00	16-Jun-2009	L1T	TM	18	9	26-Nov-2013	99.12	3.61	2.82	185
LT51410402009199KHC00	18-Jul-2009	L1T	TM	48	9	02-Dec-2013	44.57	0.24	3.20	66
LT51410402009215KHC00	03-Aug-2009	L1T	TM	56	9	30-Nov-2013				
LT51410402009231KHC00	19-Aug-2009	L1T	TM	34	9	30-Nov-2013	94.63	0.54	2.51	145
LT51410402009247KHC00	04-Sep-2009	L1T	TM	52	9	30-Nov-2013				
LE71410402009255SGS00	12-Sep-2009	L1T	ETM	34	9	08-Dec-2013	87.25	8.65	1.47	90
LE71410402009271SGS00	28-Sep-2009	L1T	ETM	49	9	07-Dec-2013	70.81	2.35	3.33	90
LT51410402009279KHC00	06-Oct-2009	L1T	TM	62	9	11-Dec-2013				
LE71410402009287SGS00	14-Oct-2009	L1T	ETM	25	9	25-Dec-2013	88.88	37.77	1.13	79
LT51410402009295KHC00	22-Oct-2009	L1T	TM	27	9	05-Dec-2013	98.65	18.23	2.77	161
LE71410402009303EDC00	30-Oct-2009	L1T	ETM	1	9	17-Dec-2013	85.53	11.67	1.22	72
LT51410402009311KHC00	07-Nov-2009	L1T	TM	26	9	22-Nov-2013	95.38	7.45	1.66	144
LE71410402009319SGS00	15-Nov-2009	L1T	ETM	54	9	13-Dec-2013	40.71	47.07	0.00	1
LT51410402009327KHC00	23-Nov-2009	L1T	TM	45	9	25-Dec-2013	93.42	34.34	0.77	133
LE71410402009335SGS00	01-Dec-2009	L1T	ETM	5	9	11-Jan-2014	81.61	16.88	0.29	70
LT51410402009343KHC01	09-Dec-2009	L1T	TM	30	9	05-Dec-2013	87.52	9.71	0.53	171
LE71410402009351SGS00	17-Dec-2009	L1T	ETM	56	9	11-Jan-2014	84.84	19.66	0.00	52
LE71410402010002SGS00	02-Jan-2010	L1T	ETM	22	9	11-Jan-2014	77.52	39.65	0.00	5
LE71410402010018SGS00	18-Jan-2010	L1T	ETM	3	9	11-Jan-2014	76.81	9.51	0.03	86
LT51410402010026KHC00	26-Jan-2010	L1T	TM	53	9	12-Jan-2014	94.75	99.70	0.00	0
LE71410402010034SGS00	03-Feb-2010	L1T	ETM	3	9	11-Jan-2014	79.87	9.55	0.01	75
LT51410402010042KHC00	11-Feb-2010	L1T	TM	31	9	12-Jan-2014	97.59	97.30	0.01	4
LE71410402010050PFS00	19-Feb-2010	L1T	ETM	18	9	11-Jan-2014	82.80	81.09	0.00	1
LT51410402010058KHC00	27-Feb-2010	L1T	TM	58	9	12-Jan-2014	98.58	66.62	0.03	28
LE71410402010066SGS00	07-Mar-2010	L1T	ETM	3	9	11-Jan-2014	82.90	55.67	0.09	20
LE71410402010082PFS02	23-Mar-2010	L1T	ETM	6	9	11-Jan-2014	83.55	22.09	1.49	116
LT51410402010090KHC00	31-Mar-2010	L1T	TM	44	9	12-Jan-2014	100.00	99.99	0.00	0
LT51410402010106KHC00	16-Apr-2010	L1T	TM	27	9	05-Dec-2013	99.38	8.22	2.52	172
LE71410402010130PFS00	10-May-2010	L1T	ETM	30	9	11-Jan-2014	86.96	32.47	0.92	64
LE71410402010162ASN00	11-Jun-2010	L1T	ETM	3	9	11-Jan-2014	88.37	1.08	1.41	61
LE71410402010178SGS00	27-Jun-2010	L1G	ETM	83	9	11-Jan-2014				
LE71410402010210ASN00	29-Jul-2010	L1T	ETM	76	9	11-Jan-2014	84.93	0.19	1.27	88
LE71410402010274SGS00	01-Oct-2010	L1T	ETM	41	9	11-Jan-2014	87.35	2.34	1.99	88
LE71410402010306PFS00	02-Nov-2010	L1T	ETM	15	9	11-Jan-2014	88.24	14.98	0.05	14
LE71410402010338PFS00	04-Dec-2010	L1T	ETM	1	9	26-Dec-2013	78.49	3.31	0.03	79
LE71410402010354PFS00	20-Dec-2010	L1T	ETM	2	9	27-Dec-2013	76.83	1.49	0.00	101
LE71410402011005PFS00	05-Jan-2011	L1T	ETM	4	9	27-Dec-2013	78.64	50.09	0.01	29
LE71410402011069PFS00	10-Mar-2011	L1T	ETM	20	9	30-Dec-2013	87.90	85.93	0.00	0
LE71410402011085PFS00	26-Mar-2011	L1T	ETM	69	9	03-Jan-2014	88.07	34.99	0.11	17
LE71410402011101PFS00	11-Apr-2011	L1T	ETM	42	9	11-Jan-2014	88.86	44.90	0.09	9
LE71410402011117ASN00	27-Apr-2011	L1T	ETM	60	9	11-Jan-2014	53.71	75.23	0.56	13
LE71410402011133PFS00	13-May-2011	L1T	ETM	32	9	11-Jan-2014	83.97	15.78	1.86	112
LE71410402011213PFS00	01-Aug-2011	L1G	ETM	83	9	11-Jan-2014				
LE71410402011229PFS00	17-Aug-2011	L1T	ETM	73	9	11-Jan-2014	78.76	9.21	1.79	70
LT51410402011237KHC00	25-Aug-2011	L1T	TM	27	9	30-Nov-2013				
LE71410402011245PFS00	02-Sep-2011	L1T	ETM	58	9	11-Jan-2014				
LT51410402011253KHC00	10-Sep-2011	L1T	TM	67	9	30-Nov-2013	96.53	3.28	1.38	107
LE71410402011277PFS00	04-Oct-2011	L1T	ETM	24	9	11-Jan-2014	85.10	35.79	1.95	187
LE71410402011293PFS00	20-Oct-2011	L1G	ETM	45	9	11-Jan-2014	74.62	35.77	0.64	70
LE71410402011309PFS00	05-Nov-2011	L1T	ETM	55	9	11-Jan-2014	80.64	22.87	0.28	43
LE71410402011325PFS00	21-Nov-2011	L1T	ETM	2	9	11-Jan-2014	81.79	9.64	0.88	82
LE71410402011341PFS00	07-Dec-2011	L1T	ETM	1	9	11-Jan-2014	77.94	3.89	0.62	78
LE71410402011357PFS00	23-Dec-2011	L1T	ETM	5	9	11-Jan-2014	64.12	4.66	0.05	113
LE71410402012040PFS00	09-Feb-2012	L1T	ETM	95	9	11-Jan-2014	69.01	52.79	0.00	0
LE71410402012056PFS00	25-Feb-2012	L1T	ETM	36	9	11-Jan-2014	80.27	69.79	0.03	16
LE71410402012072PFS00	12-Mar-2012	L1T	ETM	19	9	11-Jan-2014	78.55	33.28	0.06	25
LE71410402012088PFS00	28-Mar-2012	L1T	ETM	21	9	11-Jan-2014	86.86	50.23	0.10	14
LE71410402012104PFS00	13-Apr-2012	L1T	ETM	23	9	11-Jan-2014	86.86	99.58	0.01	1

Table A.4 Summary of the 197 Landsat scenes assessed, and the 172 chosen for analysis in Chapter 3. Shown for all 197 scenes are the scene ID, data of acquisition, level of processing, sensor, % cloud cover over the whole scene, data quality, and the file processing data, all provided from the USGS. The 172 scenes chosen for processing also show the % of Langtang Valley's debris-covered glacier area that was observable, snow-covered, and ponded, and the count of individual ponds  $N$ .

SceneID	Date Acquired	Level	Sensor	% Cloud	Quality	File Date	% DCG area			$N$ Ponds
							Observable	Snow	Pond	
LE71410402012120PFS00	29-Apr-2012	L1T	ETM	63	9	11-Jan-2014	75.15	34.77	0.59	17
LE71410402012136PFS00	15-May-2012	L1T	ETM	37	9	11-Jan-2014	76.77	21.75	0.84	63
LE71410402012152PFS00	31-May-2012	L1T	ETM	39	9	11-Jan-2014	81.42	3.29	2.21	99
LE71410402012168PFS00	16-Jun-2012	L1T	ETM	29	9	11-Jan-2014	79.02	0.40	1.45	50
LE71410402012280PFS00	06-Oct-2012	L1T	ETM	2	9	11-Jan-2014	89.03	0.87	0.79	53
LE71410402012296PFS00	22-Oct-2012	L1T	ETM	1	9	11-Jan-2014	86.33	1.28	1.07	60
LE71410402012312PFS00	07-Nov-2012	L1T	ETM	1	9	11-Jan-2014	84.75	1.15	0.51	55
LE71410402012328PFS00	23-Nov-2012	L1T	ETM	3	9	11-Jan-2014	76.71	0.84	0.25	83
LE71410402012344PFS00	09-Dec-2012	L1T	ETM	2	9	11-Jan-2014	78.15	0.82	0.16	108
LE71410402012360PFS00	25-Dec-2012	L1T	ETM	3	9	11-Jan-2014	75.51	2.84	0.00	85
LE71410402013010EDC02	10-Jan-2013	L1T	ETM	2	9	11-Jan-2014				
LE71410402013042PFS00	11-Feb-2013	L1T	ETM	6	9	11-Jan-2014	85.32	97.63	0.18	16
LE71410402013058PFS00	27-Feb-2013	L1T	ETM	15	9	11-Jan-2014	89.05	99.00	0.02	5
LE71410402013074PFS00	15-Mar-2013	L1T	ETM	17	9	11-Jan-2014	87.70	93.06	0.00	1
LE71410402013090EDC00	31-Mar-2013	L1T	ETM	20	9	11-Jan-2014	87.78	83.52	0.07	9
LE71410402013106PFS00	16-Apr-2013	L1T	ETM	46	9	11-Jan-2014	87.64	81.35	0.07	11
LE71410402013122PFS00	02-May-2013	L1T	ETM	66	9	11-Jan-2014				
LE71410402013154PFS00	03-Jun-2013	L1T	ETM	42	9	11-Jan-2014	83.60	27.99	2.14	125
LE71410402013170PFS00	19-Jun-2013	L1G	ETM	82	9	11-Jan-2014				
LE71410402013250SG100	07-Sep-2013	L1T	ETM	59	9	11-Jan-2014	82.98	0.36	0.79	65
LE71410402013266SG100	23-Sep-2013	L1T	ETM	47	9	11-Jan-2014	84.91	0.38	1.43	67
LE71410402013282SG101	09-Oct-2013	L1T	ETM	39	9	11-Jan-2014	86.91	1.94	0.71	54
LE71410402013298SG100	25-Oct-2013	L1T	ETM	5	9	11-Jan-2014	87.19	89.71	0.10	22
LE71410402013314EDC00	10-Nov-2013	L1T	ETM	51	9	10-Nov-2013	84.31	79.68	0.03	4
LE71410402013330EDC00	26-Nov-2013	L1T	ETM	2	9	26-Nov-2013	82.85	61.59	0.52	74
LE71410402013346EDC00	12-Dec-2013	L1T	ETM	3	9	12-Dec-2013	80.11	41.49	0.05	54

Table A.5 Pond energy-balance model results for the level A runs, including pond, pond area  $A_p$ , mean shortwave energy flux  $\overline{I_{net}}$ , mean longwave energy flux  $\overline{L_n}$ , mean sensible heat flux  $\overline{H}$ , mean latent heat flux  $\overline{E}$ , mean net surface energy balance  $\overline{Q}$ , mean subaqueous bare-ice and subdebris ( $\overline{v_i}$  and  $\overline{v_d}$ ) melt rates, and mean and peak pond discharge ( $\overline{V_d}$  and  $\dot{V}_{d,max}$ ). All values are for the 35-day common period of 4 May to 8 June, 2014, with  $\alpha = 0.08$ .

Run	Pond	$m^2$ $A_p$	$W m^{-2}$ $I_n$	$W m^{-2}$ $L_n$	$W m^{-2}$ $H$	$W m^{-2}$ $E$	$W m^{-2}$ $Q$	$m d^{-1}$ $\overline{v_i}$	$m d^{-1}$ $\overline{v_d}$	$m^3 s^{-1}$ $\overline{V_d}$	$m^3 s^{-1}$ $\dot{V}_{d,max}$
A1	C	198	177	3	14	-10	187	0.01784	0.00026	0.0062	0.044
A2	C	198	175	-2	14	-10	180	0.01784	0.00026	0.0060	0.040
A3	C	170	202	-6	13	19	234	0.01837	0.00025	0.0064	0.035
A4	C	170	202	-6	13	12	223	0.01837	0.00025	0.0063	0.035
A5	C	170	202	-5	10	-17	192	0.01764	0.00025	0.0058	0.031
A1	D	419	213	-5	14	-22	203	0.03611	0.00040	0.0068	0.077
A2	D	419	220	-8	14	-22	207	0.03611	0.00040	0.0071	0.079
A3	D	419	233	-13	13	9	246	0.03611	0.00040	0.0091	0.080
A4	D	419	233	-13	13	6	239	0.03611	0.00040	0.0090	0.080
A5	D	419	233	-13	10	-24	208	0.03525	0.00040	0.0081	0.082
A4	I	554	234	-11	12	10	246	0.02156	0.00024	0.020	0.21
A5	I	554	234	-11	10	-19	214	0.02067	0.00024	0.019	0.21
A4	J	13113	207	-8	12	-8	205	0.03563	0.00041	0.27	2.2
A5	J	13113	207	-8	9	-36	175	0.03490	0.00041	0.23	2.1

Table A.6 Modelled melt for the level A runs, including pond, pond area  $A_p$ , cumulative surface energy balance  $\Sigma(Q_n A_p)$ , subaqueous bare-ice and subdebris melt ( $MW_i$  and  $MW_d$ ), cumulative discharge energy  $\Sigma D$ , total melt energy  $\Sigma Ex$ , specific melt rate  $\frac{\Sigma Ex}{A_p \Delta t}$ , and local and englacial portions of melt energy. All values are for the 35-day common period of 4 May to 8 June, 2014, with  $\alpha = 0.08$ .

Run	Pond	$m^3$ $\Sigma(Q_n A_p)$	$m^3$ $MW_i$	$m^3$ $MW_d$	$m^3$ $\Sigma D$	$m^3$ $\Sigma Ex$	$m d^{-1}$ $\frac{\Sigma Ex}{A_p \Delta t}$	% Local	% Englacial
A1	C	357	41	1	310	353	0.051	12%	88%
A2	C	344	41	1	297	340	0.049	13%	87%
A3	C	363	31	1	329	361	0.061	9%	91%
A4	C	373	31	1	338	370	0.062	9%	91%
A5	C	321	29	1	287	318	0.053	10%	90%
A1	D	802	685	2	48	734	0.050	93%	7%
A2	D	818	685	2	64	750	0.051	91%	9%
A3	D	950	685	2	202	889	0.061	77%	23%
A4	D	959	685	2	196	882	0.060	78%	22%
A5	D	834	668	2	89	759	0.052	88%	12%
A4	I	1193	577	1	551	1129	0.058	51%	49%
A5	I	1041	554	1	425	980	0.051	57%	43%
A4	J	28036	17889	85	8107	26081	0.057	69%	31%
A5	J	23875	17510	85	4363	21958	0.048	80%	20%

Table A.7 Pond energy-balance model results for the level A runs with  $\alpha = 0.12$ , including pond, pond area  $A_p$ , mean shortwave energy flux  $\overline{I_n}$ , mean longwave energy flux  $\overline{L_n}$ , mean sensible heat flux  $\overline{H}$ , mean latent heat flux  $\overline{E}$ , mean net surface energy balance  $\overline{Q}$ , mean subaqueous bare-ice and subdebris ( $\overline{v_i}$  and  $\overline{v_d}$ ) melt rates, and mean and peak pond discharge ( $\overline{V_d}$  and  $\dot{V}_{dmax}$ ). All values are for the 35-day common period of 4 May to 8 June, 2014.

Run	Pond	$\text{m}^2$ $A_p$	$\text{W m}^{-2}$ $I_n$	$\text{W m}^{-2}$ $L_n$	$\text{W m}^{-2}$ $H$	$\text{W m}^{-2}$ $E$	$\text{W m}^{-2}$ $Q$	$\text{m d}^{-1}$ $\overline{v_i}$	$\text{m d}^{-1}$ $\overline{v_d}$	$\text{m}^3 \text{s}^{-1}$ $\overline{V_d}$	$\text{m}^3 \text{s}^{-1}$ $\dot{V}_{dmax}$
A1	C	198	170	3	14	-10	179	0.018	0.00026	0.0059	0.042
A2	C	198	168	-2	14	-10	172	0.018	0.00026	0.0057	0.038
A3	C	170	194	-6	13	19	225	0.018	0.00025	0.0061	0.034
A4	C	170	194	-6	13	12	214	0.018	0.00025	0.0060	0.034
A5	C	170	194	-5	10	-17	183	0.018	0.00025	0.0055	0.030
A1	D	419	204	-5	14	-22	194	0.036	0.00040	0.0064	0.074
A2	D	419	210	-8	14	-22	197	0.036	0.00040	0.0066	0.075
A3	D	419	223	-13	13	9	236	0.036	0.00040	0.0086	0.076
A4	D	419	223	-13	13	6	229	0.036	0.00040	0.0085	0.076
A5	D	419	223	-13	10	-24	198	0.035	0.00040	0.0075	0.078
A4	I	554	224	-11	12	10	236	0.022	0.00024	0.019	0.20
A5	I	554	224	-11	10	-19	204	0.021	0.00024	0.017	0.20
A4	J	13113	198	-8	12	-8	196	0.036	0.00041	0.25	2.1
A5	J	13113	198	-8	9	-36	166	0.035	0.00041	0.22	2.0

Table A.8 Modelled melt for the level A runs with  $\alpha = 0.12$ , including pond, pond area  $A_p$ , cumulative surface energy balance  $\Sigma(Q_n A_p)$ , subaqueous bare-ice and subdebris melt ( $\text{MW}_i$  and  $\text{MW}_d$ ), cumulative discharge energy  $\Sigma D$ , total melt energy  $\Sigma Ex$ , specific melt rate  $\frac{\Sigma Ex}{A_p \Delta t}$ , and local and englacial portions of melt energy. All values are for the 35-day common period of 4 May to 8 June, 2014.

Run	Pond	$\text{m}^3$ $\Sigma(Q_n A_p)$	$\text{m}^3$ $\text{MW}_i$	$\text{m}^3$ $\text{MW}_d$	$\text{m}^3$ $\Sigma D$	$\text{m}^3$ $\Sigma Ex$	$\text{m d}^{-1}$ $\frac{\Sigma Ex}{A_p \Delta t}$	% Local	% Englacial
A1	C	342	41	1	295	338	0.049	13%	87%
A2	C	329	41	1	282	325	0.047	13%	87%
A3	C	349	31	1	315	347	0.058	9%	91%
A4	C	358	31	1	323	355	0.060	9%	91%
A5	C	306	29	1	272	303	0.051	10%	90%
A1	D	765	685	2	11	697	0.048	98%	2%
A2	D	780	685	2	26	712	0.049	96%	4%
A3	D	910	685	2	163	849	0.058	81%	19%
A4	D	918	685	2	155	841	0.057	82%	18%
A5	D	793	668	2	48	718	0.049	93%	7%
A4	I	1144	577	1	501	1080	0.056	54%	46%
A5	I	992	554	1	375	930	0.048	60%	40%
A4	J	26853	17889	85	6924	24898	0.054	72%	28%
A5	J	22693	17510	85	3180	20775	0.045	85%	15%

Table A.9 Results for model levels B-D for the common period and full period. Shown for the common period are model evaluation period  $\Delta t$  (days), total mean pond area  $\Sigma \overline{A_p}$  ( $\text{m}^2$ ), total excess surface energy balance  $\Sigma(Q_n A_p)$  ( $\text{m}^3$  ice melt), mean surface energy balance  $Q$  ( $\text{W m}^{-2}$ ), mean shortwave energy balance  $I_n$  ( $\text{W m}^{-2}$ ), and mean sensible  $H$  and latent  $E$  heat fluxes ( $\text{W m}^{-2}$ ). Shown for the full period are model evaluation period  $\Delta t$  (days), total mean pond area  $\Sigma \overline{A_p}$  ( $\text{m}^2$ ), and total excess surface energy balance  $\Sigma(Q_n A_p)$  ( $\text{m}^3$  ice melt).

Run	Pond	Altitude	Common Period								Full Period		
			$\Delta t$	$A_p$	$\frac{\Sigma(Q_n A_p)}{A_p \delta t}$	$Q_n$	$I_n$	$L_n$	$H$	$E$	$\Delta t$	$A_p$	$\frac{\Sigma(Q_n A_p)}{A_p \delta t}$
C1	A	4057	35	6	12	190	209	-8	13	-27	182	3	45
C2	A	4057	35	6	15	235	226	-17	13	10	171	8	72
D1	A	4057	35	7	13	190	209	-8	13	-27	182	7	82
D2	A	4057	35	154	360	235	226	-17	13	10	171	154	2113
B1	C	4074	35	198	357	187	177	3	14	-10	90	122	716
B2	C	4074	35	198	344	180	175	-2	14	-10	90	122	702
B3	C	4076	35	170	363	234	202	-6	13	19	108	207	891
B4	C	4076	35	170	373	223	202	-6	13	12	108	207	948
B5	C	4076	35	170	321	192	202	-5	10	-17	108	207	830
C1	C	4074	35	230	364	160	176	-3	13	-28	182	279	2739
C2	C	4077	35	230	502	218	201	-7	13	8	171	288	3688
D1	C	4074	35	217	340	160	176	-3	13	-28	182	217	2197
D2	C	4077	35	945	2046	218	201	-7	13	8	171	945	12639
B1	D	4095	35	419	802	203	213	-5	14	-22	116	394	3548
B2	D	4095	35	419	818	207	220	-8	14	-22	116	394	3597
B3	D	4095	35	419	950	246	233	-13	13	9	116	394	3944
B4	D	4095	35	419	959	239	233	-13	13	6	116	394	4209
B5	D	4095	35	419	834	208	233	-13	10	-24	116	394	3795
C1	D	4095	35	356	688	199	219	-6	13	-30	182	270	3271
C2	D	4095	35	356	843	241	231	-12	13	7	171	294	4088
D1	D	4095	35	379	738	199	219	-6	13	-30	182	379	4383
D2	D	4095	35	501	1198	241	231	-12	13	7	171	501	7144
C1	F	4144	35	197	372	195	223	-9	12	-34	182	121	1499
C2	F	4144	35	197	459	237	233	-11	12	2	171	137	1886
D1	F	4144	35	218	416	195	223	-9	12	-34	182	218	2466
D2	F	4144	35	121	284	237	233	-11	12	2	171	121	1703
C1	G	4141	35	16	25	169	191	-2	12	-34	182	9	100
C2	G	4141	35	16	33	218	214	-12	12	2	171	17	155
D1	G	4141	35	18	29	169	191	-2	12	-34	182	18	176
D2	G	4141	35	257	558	218	214	-12	12	2	171	257	3418
C1	H	4158	35	36	67	194	219	-5	12	-35	182	20	248
C2	H	4158	35	36	78	224	217	-7	12	0	171	26	319
D1	H	4158	35	40	76	194	219	-5	12	-35	182	40	447
D2	H	4158	35	132	294	224	217	-7	12	0	171	132	1794
B4	I	4190	35	554	1193	246	234	-11	12	10	99	452	4013
B5	I	4190	35	554	1041	214	234	-11	10	-19	99	452	3607
D2	I	4190	35	885	1997	227	227	-10	12	-3	171	885	12105
B4	J	4207	35	13113	28036	205	207	-8	12	-8	52	10940	31394
B5	J	4207	35	13113	23875	175	207	-8	9	-36	52	10940	26696
D2	J	4207	35	3982	8252	209	207	-7	12	-5	171	3982	50997
D2	K	4251	35	1046	2247	216	227	-14	11	-9	171	1046	13738
D2	L	4245	35	1405	2898	208	210	-7	11	-9	171	1405	17918
D2	M	4257	35	852	1680	199	205	-10	11	-10	171	852	10737
D2	N	4254	35	414	802	195	199	-7	11	-10	171	414	5090
D2	O	4254	35	2004	3957	199	206	-11	11	-9	171	2004	25004
D2	P	4253	35	877	1761	202	208	-10	11	-9	171	877	11031

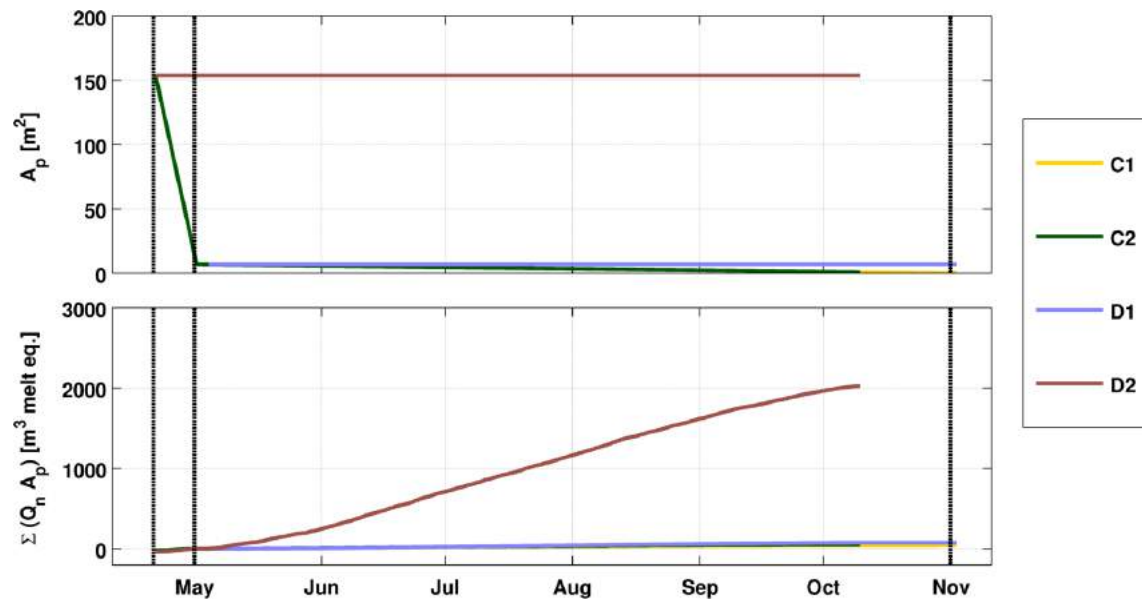


Fig. A.1 Comparison of pond area (top) and cumulative surface energy balance (bottom) for pond A across all model runs, showing that different approximations of area control cumulative energy balance, and can be a strong source of error. For pond area, run C1 plots beneath C2. For cumulative SEB, all data series begin with 0 on May 1, the date of UAV observation. Vertical dashed lines are the orthoimage dates, and all shown model runs are for  $\alpha = 0.08$ .

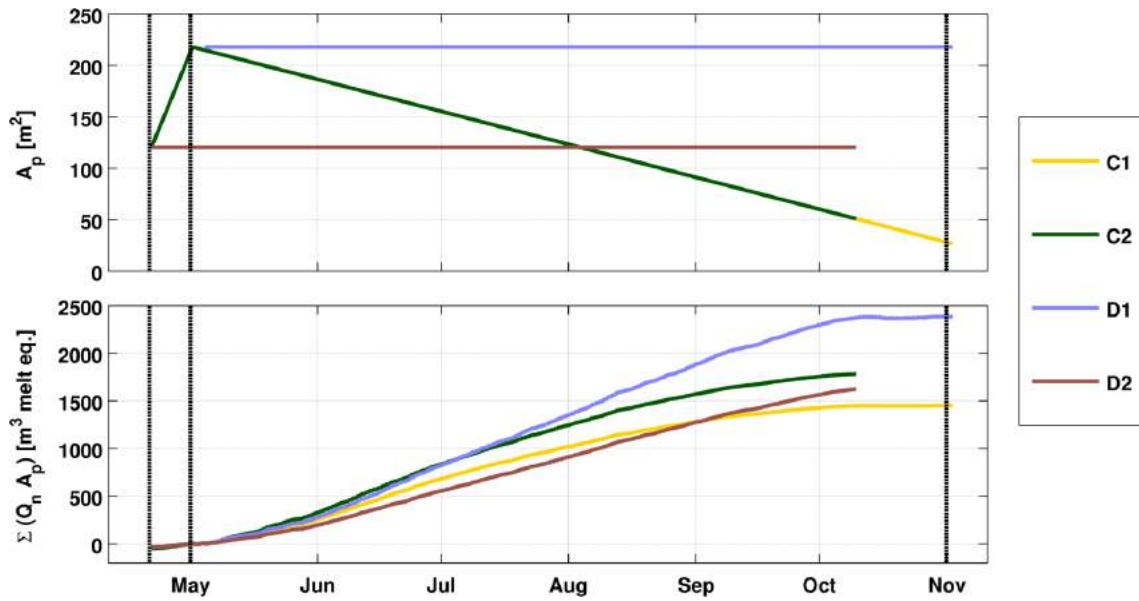


Fig. A.2 Comparison of pond area (top) and cumulative surface energy balance (bottom) for pond F across all model runs. In this case the distinct representations of pond area produce similar values of  $\Sigma(Q_n A_p)$ . For pond area, run C1 plots beneath C2. For cumulative SEB, all data series begin with 0 on May 1, the date of UAV observation. Vertical dashed lines are the orthoimage dates, and all shown model runs are for  $\alpha = 0.08$ .

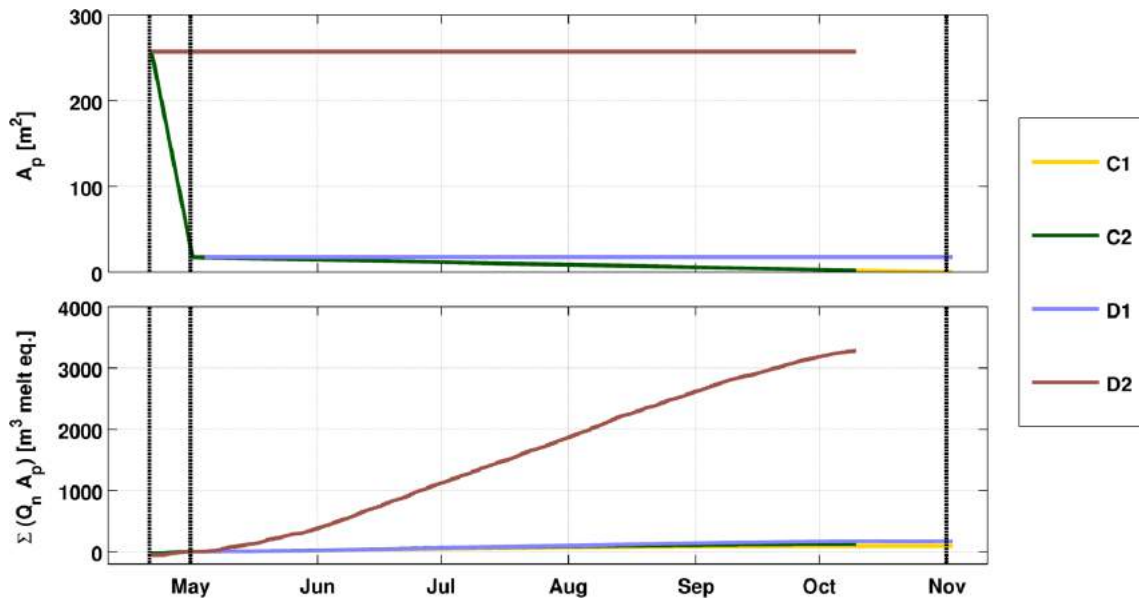


Fig. A.3 Comparison of pond area (top) and cumulative surface energy balance (bottom) for pond G across all model runs, showing that different approximations of area control cumulative energy balance, and can be a strong source of error. For pond area, run C1 plots beneath C2. For cumulative SEB, all data series begin with 0 on May 1, the date of UAV observation. Vertical dashed lines are the orthoimage dates, and all shown model runs are for  $\alpha = 0.08$ .

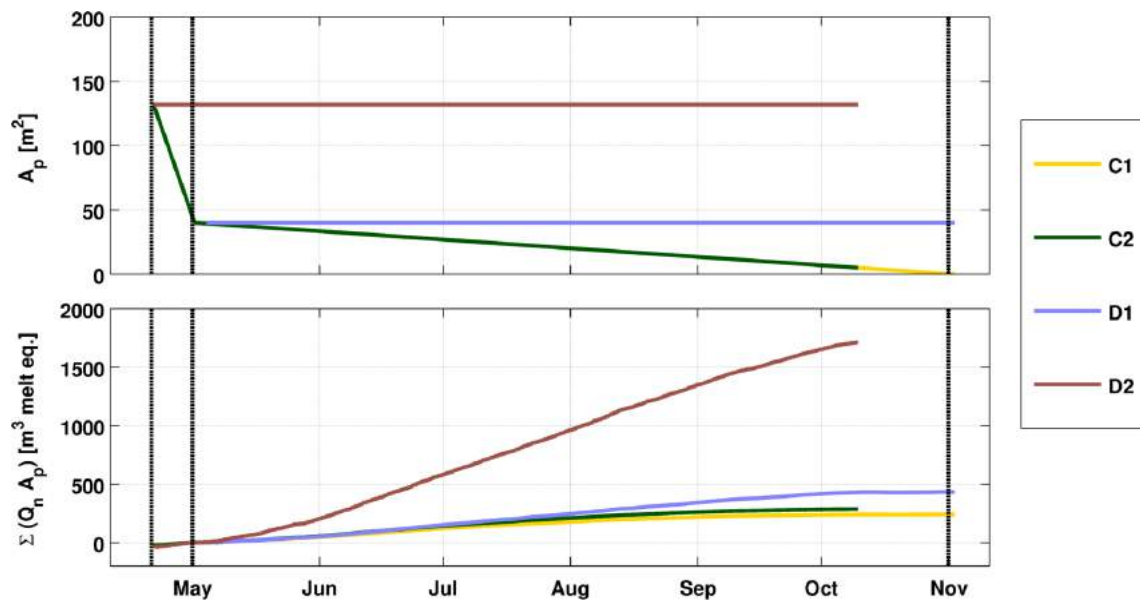


Fig. A.4 Comparison of pond area (top) and cumulative surface energy balance (bottom) for pond H across all model runs, showing that different approximations of area control cumulative energy balance, and can be a strong source of error. For pond area, run C1 plots beneath C2. For cumulative SEB, all data series begin with 0 on May 1, the date of UAV observation. Vertical dashed lines are the orthoimage dates, and all shown model runs are for  $\alpha = 0.08$ .

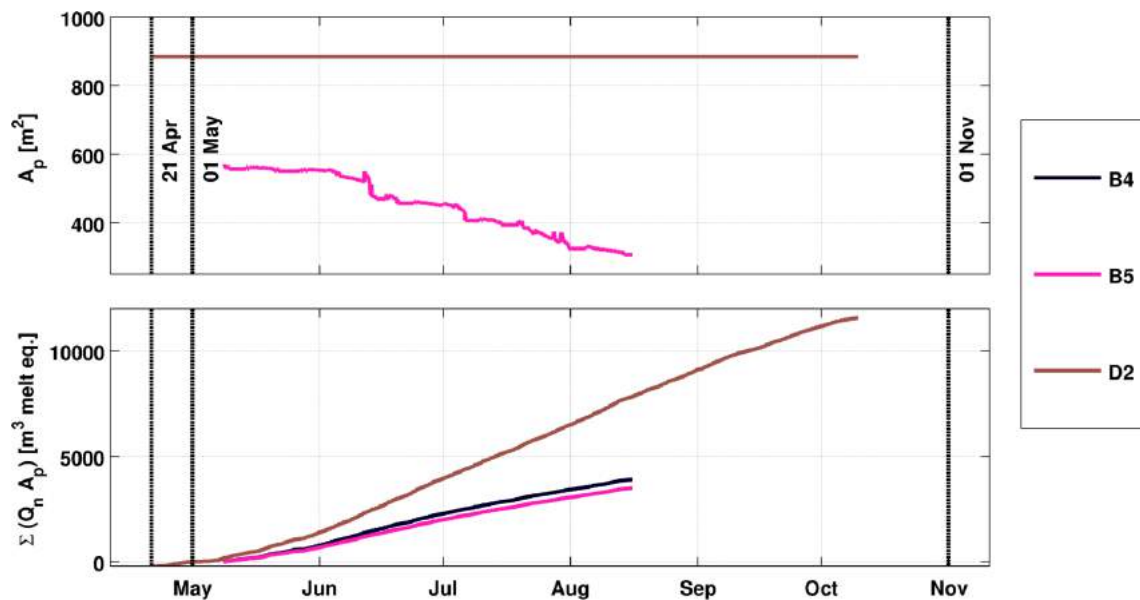


Fig. A.5 Comparison of pond area (top) and cumulative surface energy balance (bottom) for pond I across all model runs, showing that different approximations of area control cumulative energy balance, and can be a strong source of error. For cumulative SEB, all data series begin with 0 on May 1, the date of UAV observation. Vertical dashed lines are the orthoimage dates, and all shown model runs are for  $\alpha = 0.08$ .

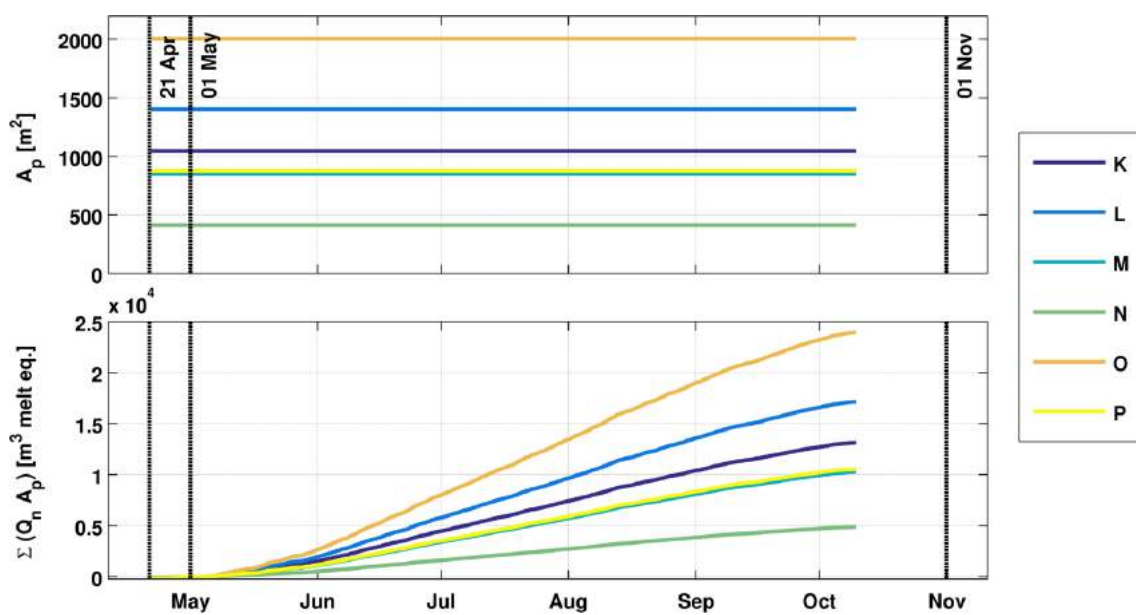


Fig. A.6 Comparison of pond area (top) and cumulative surface energy balance (bottom) for ponds K-P across, which could only be evaluated with model D2. For cumulative SEB, runs B1-B5 are nearly indistinguishable, and all lineseries begin with 0 on May 1, the date of UAV observation. Vertical dashed lines are the orthoimage dates, and all shown model runs are for  $\alpha = 0.08$ .